Lagrangian properties of turbulent channel flow: a numerical study

Juan Ignacio Polanco

N° d'ordre NNT : 2019LYSE1043

THÈSE DE DOCTORAT DE L'UNIVERSITÉ DE LYON

opérée au sein de

l'Université Claude Bernard Lyon 1

École Doctorale N° 162

Mécanique, Énergétique, Génie civil, Acoustique (MEGA)

Spécialité de doctorat : Mécanique des Fluides

Soutenue publiquement le 22/03/2019, par :

Juan Ignacio POLANCO

Lagrangian properties of turbulent channel flow: a numerical study

---

Devant le jury composé de :

MATAS Jean-Philippe	Professeur des Universités, Université Lyon 1	Président
BEC Jérémie	Directeur de recherche, CNRS	Rapporteur
SCHMITT François	Directeur de recherche, CNRS	Rapporteur
ABBAS Micheline	Maître de Conférences, INP Toulouse	Examinatrice
MORDANT Nicolas	Professeur des Universités, Université Grenoble Alpes	Examinateur
VINKOVIC Ivana	Professeure des Universités, Université Lyon 1	Directrice de thèse
BOURGOIN Mickaël	Directeur de recherche, CNRS	Invité

UNIVERSITÉ CLAUDE BERNARD – LYON 1

Président de l'Université	**M. le Professeur Frédéric FLEURY**
Président du Conseil Académique	M. le Professeur Hamda BEN HADID
Président du Conseil d'Administration	M. le Professeur Didier REVEL
Vice-président du Conseil Formation et Vie Universitaire	M. le Professeur Philippe CHEVALIER
Vice-président de la Commission Recherche	M. Fabrice VALLÉE
Directeur Général des Services	M. Alain HELLEU

COMPOSANTES SANTÉ

Faculté de Médecine Lyon Est – Claude Bernard	Directeur : M. le Professeur J. ETIENNE
Faculté de Médecine et de Maïeutique Lyon Sud – Charles Mérieux	Directeur : Mme la Professeure C. BURILLON
Faculté d'Odontologie	Directeur : M. le Professeur D. BOURGEOIS
Institut des Sciences Pharmaceutiques et Biologiques	Directeur : Mme la Professeure C. VINCIGUERRA
Institut des Sciences et Techniques de la Réadaptation	Directeur : M. le Professeur Y. MATILLON
Département de formation et Centre de Recherche en Biologie Humaine	Directeur : Mme la Professeure A-M. SCHOTT

COMPOSANTES ET DÉPARTEMENTS DE SCIENCES ET TECHNOLOGIE

Faculté des Sciences et Technologies	Directeur : M. F. DE MARCHI
Département Biologie	Directeur : M. le Professeur F. THEVENARD
Département Chimie Biochimie	Directeur : Mme C. FELIX
Département GEP	Directeur : M. Hassan HAMMOURI
Département Informatique	Directeur : M. le Professeur S. AKKOUCHE
Département Mathématiques	Directeur : M. le Professeur G. TOMANOV
Département Mécanique	Directeur : M. le Professeur M. BUFFAT
Département Physique	Directeur : M. le Professeur J-C PLENET
UFR Sciences et Techniques des Activités Physiques et Sportives	Directeur : M. Y. VANPOULLE
Observatoire des Sciences de l'Univers de Lyon	Directeur : M. B. GUIDERDONI
Polytech Lyon	Directeur : M. le Professeur E. PERRIN
Ecole Supérieure de Chimie Physique Electronique	Directeur : M. G. PIGNAULT
Institut Universitaire de Technologie de Lyon 1	Directeur : M. le Professeur C. VITON
Ecole Supérieure du Professorat et de l'Education	Directeur : M. le Professeur A. MOUGNIOTTE
Institut de Science Financière et d'Assurances	Directeur : M. N. LEBOISNE

Lagrangian properties of turbulent channel flow: a numerical study

Abstract The Lagrangian perspective, describing a flow from the trajectories of fluid tracers, is a natural framework for studying dispersion phenomena in turbulent flows. In wall-bounded turbulence, the motion of fluid tracers is affected by mean shear and by strong inhomogeneity and anisotropy near walls. We investigate the Lagrangian properties of a turbulent channel flow using direct numerical simulations at a moderate Reynolds number. Lagrangian acceleration statistics are compared to particle tracking experiments performed in parallel to this work. As in homogeneous isotropic turbulence (HIT), the acceleration components along Lagrangian paths decorrelate over time scales representative of the smallest scales of the flow, while the acceleration norm stays correlated for much longer. The persistence of small-scale anisotropy far from the wall is demonstrated in the form of a non-zero cross-correlation between acceleration components. As a result of the average fluxes of kinetic energy in wall turbulence, tracers initially located close to the wall travel and spread over longer distances when tracked backwards in time than forwards. The relative dispersion of tracer pairs is finally investigated. At short times, pair separation is ballistic for all wall distances. As in HIT, relative dispersion is time asymmetric, with tracers separating faster when tracked backwards in time. At longer times, mean shear dominates leading to rapid separation in the mean flow direction. A ballistic cascade model previously proposed for HIT is adapted to inhomogeneous flows.

Keywords turbulence, Lagrangian description, wall turbulence, channel flow, direct numerical simulation, dispersion, acceleration

---

Propriétés lagrangiennes d'un écoulement de canal turbulent : une étude numérique

Résumé La perspective lagrangienne, décrivant un écoulement selon les trajectoires de traceurs fluides, est une approche naturelle pour étudier les phénomènes de dispersion dans les écoulements turbulents. En turbulence de paroi, le mouvement des traceurs est influencé par le cisaillement moyen et par une forte inhomogénéité et anisotropie en proche paroi. On étudie les propriétés lagrangiennes d'un écoulement de canal turbulent par simulation numérique directe à un nombre de Reynolds modéré. Les statistiques d'accélération lagrangienne sont comparées aux expériences de suivi de particules réalisées en parallèle à ce travail. Comme en turbulence homogène isotrope (THI), les composantes d'accélération le long des trajectoires lagrangiennes se décorrèlent sur des temps comparables aux plus petites échelles de l'écoulement, tandis que la norme de l'accélération reste corrélée plus longtemps. La persistance d'anisotropie à petite échelle loin de la paroi est constatée par l'existence d'une corrélation croisée non nulle entre deux composantes de l'accélération. On montre que, en conséquence des flux moyens d'énergie cinétique en turbulence de paroi, près des parois les traceurs se déplacent et s'étalent sur des plus grandes distances quand ils sont suivis en arrière dans le temps qu'en avant. La dispersion relative de paires de traceurs est aussi étudiée. Aux temps courts, la séparation des paires est balistique pour toutes les distances à la paroi. Comme en THI, les traceurs se séparent plus rapidement lorsqu'ils sont suivis en arrière dans le temps. Aux temps plus longs, le cisaillement moyen accélère la séparation dans la direction de l'écoulement moyen. Un modèle de cascade balistique initialement proposé pour la THI est adapté aux écoulements inhomogènes.

Mots-clés turbulence, description lagrangienne, turbulence de paroi, écoulement de canal, simulation numérique directe, dispersion, accélération

Remerciements

Durant cette thèse j'ai eu le plaisir et la chance d'interagir avec de nombreuses personnes qui ont influencé d'une manière ou d'une autre les travaux présentés ici.

Je voudrais tout d'abord remercier Ivana Vinkovic de m'avoir motivé à faire cette thèse, et d'avoir eu la flexibilité d'adapter le sujet (qui en principe devait porter sur la dispersion de particules au dessus d'une canopée végétale) à la situation et à mes intérêts. J'ai beaucoup apprécié nos réunions improvisées en traversant le Parc de la Tête d'Or à vélo le matin. Je lui suis aussi très reconnaissant de m'avoir encouragé à présenter mes travaux dans différents congrès au niveau local et international.

Je remercie Mickaël Bourgoin d'avoir suivi une partie de mes travaux de thèse, pour nos discussions toujours très éclairantes et agréables, et plus particulièrement pour ses commentaires sur une version préliminaire de ce manuscrit. J'ai eu aussi le grand plaisir de collaborer avec Nick Stelzenmuller et Nicolas Mordant, que je remercie pour les nombreux échanges et discussions dont mes travaux ont beaucoup bénéficié. Je remercie également les autres membres du projet ANR LTIF, Romain Volk, Mikhael Gorokhovski, Peter Huck et Alexis Barge, pour leurs idées et suggestions lors des réunions de projet.

Merci aux membres du jury, en particulier aux rapporteurs Jérémie Bec et François Schmitt, pour leur disponibilité ainsi que pour leurs commentaires positifs et très constructifs envers mes travaux de thèse.

Cette thèse n'aurait pas eu lieu sans l'intervention d'Emmanuel Mignot lorsque j'étais au Chili. Je le remercie chaleureusement pour ses précieux conseils, pour les nombreuses discussions informelles tout au long de cette thèse, et plus généralement pour son hospitalité et amitié.

Merci à Serge Simoëns d'avoir soutenu, en tant que responsable du groupe Fluides Complexes et Transferts au LMFA, mes déplacements à plusieurs congrès. Je le remercie aussi pour nos discussions intéressantes, pour m'avoir aidé à obtenir un bureau à Écully, et en général pour son soutien et sa bonne humeur.

Je remercie Marc Buffat d'avoir mis à disposition une version du code NadiaSpectral pour utilisation et modification dans le cadre de cette thèse. Merci à Christophe Pera pour l'administration du centre de calcul P2CHPD à l'Université Lyon 1 et pour sa disponibilité à répondre à mes questions.

Merci à tous mes collègues doctorants et post-doctorants que j'ai rencontrés sur les trois sites du LMFA. En ordre plus ou moins chronologique, je remercie Wenchao de m'avoir aidé à démarrer avec le code DNS. Merci Dimitri, Sylvie et Vincent pour la bonne ambiance. Je remercie aussi Donato, Robert, Aleksandr (pour les chocolats!), Andrea, Cenk, Henri et Corentin. Merci Rafik pour le soutien et les conseils dans la dernière partie de ma thèse. Merci Tom pour les commentaires très opportuns à

quelques jours de ma soutenance.

Gracias al grupo de chilenos (y prácticamente chilenos) en Lyon por los buenos momentos: Fran, Carol, Manu, Eve, Carlos, Clau y Antoine. Gracias Marielle por ser una amiga increíble y una gran influencia en los últimos casi dos años. Agradezco también a mi familia por su apoyo constante y por aceptar tenerme tan lejos.

Je remercie finalement le gouvernement chilien d'avoir financé cette thèse dans le cadre du programme CONICYT Becas Chile. Mes travaux ont également bénéficié du soutien de l'Agence Nationale de la Recherche dans le cadre du projet ANR LTIF, ainsi que de plusieurs allocations de ressources informatiques au CINES.

Contents

Abstract / Résumé v

Remerciements vii

Contents ix

List of Figures xiii

List of Tables xvii

Nomenclature xix

Abbreviations xxiii

Operators xxv

1 Introduction 1

1.1 Lagrangian description of turbulent flows . . . 1
1.1.1 Eulerian and Lagrangian formulations . . . 2
1.1.2 Lagrangian properties of isotropic turbulent flows . . . 5
1.1.3 Lagrangian stochastic models . . . 7
1.1.4 Lagrangian intermittency . . . 10
1.1.5 Lagrangian acceleration . . . 11
1.1.6 Anisotropic and inhomogeneous flows . . . 14
1.2 Wall-bounded turbulence . . . 16
1.2.1 Turbulent channel flow . . . 16
1.2.2 Scales of wall-bounded turbulence . . . 21
1.2.3 Mean velocity profile . . . 21
1.2.4 Coherent structures . . . 23
1.3 Lagrangian investigations of wall turbulence . . . 28
1.3.1 Channel flow . . . 28
1.3.2 Pipe and boundary layer flows . . . 31
1.4 Objectives and outline . . . 32

2 Numerical methods 35

2.1 Direct numerical simulations . . . 35
2.1.1 General aspects of spectral methods . . . 36
2.1.2 Application to channel flow simulations . . . 39
2.1.2.1 Variational formulation . . . 40

2.1.2.2 Choice of trial and test functions . . . 40
2.1.2.3 Temporal discretisation . . . 44
2.1.2.4 Sequence of an iteration . . . 44
2.1.2.5 Computation of the acceleration field . . . 45
2.1.3 Parallelisation strategy . . . 46
2.1.3.1 Domain decomposition . . . 46
2.1.3.2 Parallel file I/O . . . 47
2.1.4 Parameters and validation of the Eulerian solver . . . 50
2.1.4.1 Simulation parameters . . . 50
2.1.4.2 Eulerian two-point auto-correlations . . . 51
2.1.4.3 Velocity statistics . . . 53
2.1.4.4 Acceleration statistics . . . 54
2.1.5 Conclusion . . . 56
2.2 Lagrangian tracking of fluid particles . . . 57
2.2.1 Governing equations and time discretisation . . . 58
2.2.2 Interpolation of Eulerian fields . . . 58
2.2.2.1 Interpolation methods . . . 59
2.2.2.2 Evaluation and choice of interpolation scheme . . . 62
2.2.2.3 Note on fluid particle accelerations . . . 66
2.2.3 Implementation details and parallel strategy . . . 67
2.2.4 Validation against Eulerian statistics . . . 68
2.2.5 Conclusion . . . 69
2.3 General conclusion . . . 70

3 Lagrangian statistics of acceleration **71**
3.1 Experimental setup . . . 71
3.1.1 Channel flow . . . 72
3.1.2 Particles and PTV system . . . 73
3.2 Velocity and acceleration profiles . . . 74
3.2.1 Velocity profiles . . . 74
3.2.2 Acceleration profiles . . . 74
3.3 Lagrangian description of wall-bounded flows . . . 77
3.4 Lagrangian acceleration correlations . . . 79
3.4.1 Acceleration auto-correlations . . . 80
3.4.2 Acceleration cross-correlations . . . 82
3.4.3 Acceleration magnitude . . . 84
3.5 Lagrangian time scales . . . 85
3.6 Acceleration PDFs . . . 90
3.7 Conclusion . . . 93

4 Single-particle dispersion **95**
4.1 Mean wall-normal particle displacement . . . 96
4.2 Mean streamwise particle displacement . . . 98

4.3 Mean-square dispersion: theory and definitions . . . 100
4.3.1 Single-particle dispersion in isotropic flows . . . 101
4.3.2 Mean-square dispersion at short times . . . 102
4.4 Lagrangian power and velocity-acceleration covariance . . . 103
4.5 Mean-square dispersion in the channel . . . 106
4.5.1 Mean-square streamwise displacement . . . 106
4.5.2 Mean-square streamwise dispersion . . . 108
4.5.3 Mean-square wall-normal displacement . . . 109
4.5.4 Mean-square spanwise dispersion . . . 111
4.6 Conclusion . . . 111

5 Relative dispersion of particle pairs **115**
5.1 Introduction . . . 116
5.1.1 Relative dispersion in isotropic turbulent flows . . . 116
5.1.2 Relative dispersion in shear and wall-bounded flows . . . 118
5.2 Particle pair datasets . . . 119
5.3 Mean-square separation . . . 122
5.3.1 Short-time dispersion . . . 124
5.3.2 Structure functions S_2 and S_{au} . . . 125
5.3.3 Ballistic time scale . . . 129
5.3.4 Normalised mean-square separation . . . 131
5.3.5 Temporal asymmetry . . . 134
5.3.6 Influence of the initial separation . . . 135
5.4 Mean shear influence . . . 137
5.4.1 Decomposition of the mean-square separation . . . 137
5.4.2 Short-time dispersion . . . 139
5.4.3 Temporal asymmetry . . . 141
5.5 Relative dispersion tensor . . . 143
5.5.1 Short-time dispersion . . . 145
5.5.2 Intermediate and long-time dispersion . . . 145
5.5.3 Time evolution of cross-term Δ_{xy} . . . 146
5.6 Ballistic dispersion model . . . 146
5.6.1 Ballistic cascade model in isotropic turbulence . . . 147
5.6.2 Ballistic cascade model in inhomogeneous turbulence . . . 148
5.6.3 Application to turbulent channel flow . . . 152
5.6.4 Discussion and perspectives . . . 154
5.7 Conclusion . . . 155

6 Conclusion and perspectives **159**

A Single-point statistics at $Re_\tau = 1440$ **163**
A.1 Velocity and acceleration statistics . . . 163
A.2 Dissipation and turbulent scales . . . 165

B Mean Lagrangian dynamics of kinetic energy **167**
B.1 Total kinetic energy budget 167
B.2 Lagrangian dynamics of the turbulent kinetic energy 169
B.2.1 Decomposition of $\overline{\mathrm{D}k/\mathrm{D}t}$ 169
B.2.2 Turbulent kinetic energy budget 172
B.2.3 Profiles at $Re_\tau = 1440$ 172

Bibliography **175**

List of Figures

1.1 Schematic of a Lagrangian trajectory. 2
1.2 Visualisation of grid-generated turbulence. 4
1.3 Lagrangian and Eulerian velocity time series. 5
1.4 Lagrangian velocity auto-correlation function. 6
1.5 Lagrangian intermittency in isotropic turbulence. 10
1.6 Lagrangian acceleration in laboratory experiments. 12
1.7 Structure of the acceleration vector in turbulent flows. 13
1.8 Channel flow geometry and coordinate system. 17
1.9 Mean velocity profile in turbulent boundary layer. 23
1.10 Coherent motions in wall turbulence. 24
1.11 Near-wall streaks in channel flow DNS. 25
1.12 Visualisation of near-wall vortices in channel flow DNS. 26
1.13 Conceptual model of hairpin vortex packets. 27
1.14 Visualisation of VLSMs in turbulent channel flow. 28

2.1 Domain decomposition configurations. 47
2.2 Two-point velocity and acceleration auto-correlations. 52
2.3 Mean and variance velocity profiles. 54
2.4 Mean and variance acceleration profiles. 55
2.5 Skewness and flatness acceleration profiles. 56
2.6 Schematic of an interpolation cell. 60
2.7 Assessment of different interpolation schemes for a single particle. . . 64
2.8 Lagrangian acceleration auto-correlations & interpolation schemes. . . 65
2.9 Acceleration of a single fluid particle over time. 66
2.10 Wall-normal bins for computation of Lagrangian statistics. 68
2.11 Acceleration variance and skewness: Eulerian/Lagrangian comparison. 69

3.1 Sketch of the turbulent channel flow experiment at LEGI. 72
3.2 Mean and variance velocity profiles. 75
3.3 Mean and variance acceleration profiles. 76
3.4 Sample high-acceleration particle trajectories. 77
3.5 Illustration of the Lagrangian averaging procedure. 78
3.6 Lagrangian auto-correlations of acceleration. 80
3.7 Sample particle trajectories projected on a y-z plane. 81
3.8 Lagrangian cross-correlations of acceleration. 82
3.9 Lagrangian acceleration cross-correlation ρ^a_{xy}. 83
3.10 Schematic of a particle approaching the wall. 84

3.11 Estimation of Lagrangian velocity time scales in the experiment. 86
3.12 Lagrangian velocity and acceleration time scales. 87
3.13 Lagrangian acceleration time scales normalised by τ_η. 88
3.14 Lagrangian time scale ratios. 89
3.15 Taylor-scale Reynolds number in the channel at $Re_\tau = 1440$. 90
3.16 Acceleration probability distribution functions. 91
3.17 Skewness of acceleration components. 92
3.18 Joint PDF of streamwise and wall-normal acceleration. 93

4.1 Mean wall-normal tracer displacement. 97
4.2 Mean streamwise tracer displacement. 99
4.3 Mean streamwise velocity $\langle v_x \rangle(y_0, \tau)$. 100
4.4 Mean velocity-acceleration product across the channel. 104
4.5 Streamwise mean-square displacement. 107
4.6 Streamwise mean-square dispersion. 108
4.7 Wall-normal mean-square dispersion 110
4.8 Spanwise mean-square dispersion 111

5.1 Schematic of particle pair datasets. 120
5.2 Sample trajectories of two particle pairs. 121
5.3 Backward and forward mean-square change of separation. 123
5.4 Structure functions $S_2(y, \boldsymbol{r})$ and $S_{au}(y, \boldsymbol{r})$. 126
5.5 Characteristic ballistic time scales for spanwise separations. 130
5.6 Normalised backward and forward mean-square change of separation. 132
5.7 Local scaling exponents of the mean-square change of separation. . . . 133
5.8 Difference between backward and forward mean-square separation. . 134
5.9 Forward mean-square change of separation for different initial configurations. 136
5.10 Mean-square change of separation due to the fluctuating flow. 138
5.11 Local scaling exponents of the mean-square separation by the fluctuating flow. 141
5.12 Difference between backward and forward mean-square separation by the fluctuating flow. 142
5.13 Difference between backward and forward mean-square separation by the fluctuating flow by separation component. 143
5.14 Relative dispersion tensor. 144
5.16 Modelled and computed velocity structure functions. 151
5.17 Inhomogeneous ballistic cascade model compared to DNS results. . . . 152
5.18 Trajectories of modelled particle pairs. 153
5.19 Modelled mean-square separation in each direction. 154

A.1 Velocity statistics: Eulerian/Lagrangian comparison. 163
A.2 Acceleration statistics: Eulerian/Lagrangian comparison. 164
A.3 Dissipation and Kolmogorov scales in the channel. 166

B.1 Mean kinetic energy budget. 169
B.2 Mean Lagrangian derivative of the turbulent kinetic energy. 173

List of Tables

2.1 Numerical parameters for channel flow DNS. 51
2.2 Performance of interpolation schemes. 63

5.1 Particle pair datasets. 120

Nomenclature

Notation	Description
$\boldsymbol{a}$	fluid or particle acceleration
a_0	constant for dissipation-range Lagrangian velocity structure function D_2
a_n	spectral coefficient
B	additive constant for logarithmic law of the wall
C_0	constant for inertial-range Lagrangian velocity structure function D_2
C_2	Kolmogorov constant for inertial-range Eulerian velocity structure function S_2
D	separation distance between two particles ($= \lvert\boldsymbol{D}\rvert$)
$\boldsymbol{D}$	separation vector between two particles
D_p	Lagrangian p-th order velocity structure function ($= \langle\lvert\boldsymbol{v}(t+\tau) - \boldsymbol{v}(t)\rvert^p\rangle$)
d_p	spherical particle diameter
E	total kinetic energy ($= \overline{\boldsymbol{u}^2}/2$)
$\boldsymbol{e}_0$	initial orientation of a particle pair
$\boldsymbol{e}_i$	Cartesian unit vector
$\boldsymbol{F}$	Non-linear and forcing terms of the Navier-Stokes equations ($= -(\boldsymbol{\nabla} \times \boldsymbol{u}) \times \boldsymbol{u} - \boldsymbol{f}$)
$\boldsymbol{f}$	Forcing term in Navier-Stokes equations
F^a	acceleration flatness
g	Richardson's constant
G_p	mean streamwise pressure gradient ($= -\partial\overline{p}/\partial x$)
h	channel half-width
$\mathbb{i}$	imaginary unit ($= \sqrt{-1}$)
k	turbulent kinetic energy ($= \overline{\boldsymbol{u}'^2}/2$)

Notation	Description
$\mathcal{P}$	turbulent kinetic energy production term ($= -\overline{u'_x u'_y}\frac{\mathrm{d}U}{\mathrm{d}y}$)
p	fluid pressure
$\boldsymbol{\nabla} p_0$	mean pressure gradient
$\boldsymbol{R}$	change of separation between two particles ($= \boldsymbol{D} - \boldsymbol{D}_0$)
Re	centreline Reynolds number ($= U_0 h/\nu$)
Re_b	bulk Reynolds number ($= U_b h/\nu$)
Re_λ	Taylor-scale Reynolds number ($= k\sqrt{20/(3\nu\varepsilon)}$)
Re_τ	friction Reynolds number ($= u_\tau h/\nu$)
S_2	total Eulerian second-order velocity structure function ($= \overline{[\boldsymbol{u}(\boldsymbol{x}+\boldsymbol{r}) - \boldsymbol{u}(\boldsymbol{x})]^2}$)
S^a	acceleration skewness
S_{au}	total Eulerian mixed velocity-acceleration structure function ($= \overline{[\boldsymbol{u}(\boldsymbol{x}+\boldsymbol{r}) - \boldsymbol{u}(\boldsymbol{x})][\boldsymbol{a}(\boldsymbol{x}+\boldsymbol{r}) - \boldsymbol{a}(\boldsymbol{x})]}$)
S_{ij}	Eulerian second-order velocity structure function tensor ($= \overline{[u_i(\boldsymbol{x}+\boldsymbol{r}) - u_i(\boldsymbol{x})][u_j(\boldsymbol{x}+\boldsymbol{r}) - u_j(\boldsymbol{x})]}$)
St	Stokes number ($= \tau_p/\tau_\eta$)
St_ν	Stokes number based on viscous time ($= \tau_p^+ = \tau_p/\tau_\nu$)
t_0	ballistic time scale in pair dispersion ($= S_2/\lvert S_{au}\rvert$)
T_a	Lagrangian acceleration time scale
T_L	Lagrangian integral time scale
T_n	Chebyshev polynomial
U	mean streamwise velocity
$\boldsymbol{u}$	fluid velocity
U_0	mean centreline velocity
U_b	bulk velocity
u_n	trial function in spectral methods
u_τ	friction velocity ($= \sqrt{\tau_w/\rho}$)
V	space of test functions
$\boldsymbol{v}$	particle velocity
W	space of trial functions
w	weight function in spectral methods
$\boldsymbol{x}$	particle position
Δ_{ij}	relative dispersion tensor ($= \langle R_i(t) R_j(t) \rangle$)

Notation	Description
Π	Lagrangian power ($= \boldsymbol{v} \cdot \boldsymbol{a}$)
Π_{in}	input power per unit mass
Ω	spatial domain
α	persistence parameter (ballistic pair dispersion model)
δ	boundary layer thickness
$\delta(x)$	Dirac delta function
δ_{ij}	Kronecker delta function
δ_ν	viscous length ($= \nu/u_\tau$)
ε	mean turbulent energy dissipation rate ($= \nu\overline{(\partial_j u_i')(\partial_j u_i')}$)
ε_T	total energy dissipation rate ($= \nu\overline{(\partial_j u_i)(\partial_j u_i)}$)
ζ_p	scaling exponent of inertial-range Lagrangian velocity structure function D_p
η	Kolmogorov length scale ($= (\nu^3/\varepsilon)^{1/4}$)
κ	von Kármán constant for logarithmic law of the wall
ν	fluid kinematic viscosity
ρ	fluid density
$\rho_E(y, \boldsymbol{r})$	Eulerian two-point correlation
$\rho_{ij}(\tau; y_0)$	Lagrangian correlation
ρ_p	particle density
σ_u^2	velocity variance $\overline{u_i'^2}$ (isotropic flows only)
τ_p	particle relaxation time ($= \rho_p d_p^2/(18\rho\nu)$)
τ_w	wall shear stress ($= \rho\nu \, \mathrm{d}U/\mathrm{d}y\big\vert_{y=0}$)
τ_η	Kolmogorov time scale ($= \sqrt{\nu/\varepsilon}$)
τ_ν	viscous time ($= \nu/u_\tau^2$)
$\boldsymbol{\omega}$	fluid vorticity ($= \boldsymbol{\nabla} \times \boldsymbol{u}$)
ϕ_i	test function in spectral methods

Abbreviations

Notation	Description
CFL	Courant-Friedrichs-Lewy condition
DNS	direct numerical simulation
FFT	fast Fourier transform
HIT	homogeneous isotropic turbulence
HSF	homogeneous shear flow
I/O	input/output
LES	large eddy simulation
LSM	large scale motion
MPI	Message Passing Interface
MWR	method of mean weighted residuals
PDF	probability density function
PTV	particle-tracking velocimetry
SDE	stochastic differential equation
TKE	turbulent kinetic energy
VLSM	very large scale motion

Operators

Notation	Description
$\langle f, g \rangle$	inner product between two functions
X^*	complex conjugate
$\dfrac{\mathrm{D}}{\mathrm{D}t}$	Lagrangian derivative (along fluid particle paths)
$\overline{X}$	Eulerian mean
$\langle X \rangle$	Lagrangian mean
X^+	quantity scaled in wall units (by u_τ and ν)

1 Introduction

The present work concerns the characterisation of a turbulent channel flow from a Lagrangian perspective. In this chapter, fundamental aspects of the Lagrangian properties of turbulent flows and of wall-bounded turbulence are presented. The Lagrangian description is introduced in section 1.1 along with relevant investigations on the Lagrangian properties of turbulence. Then, section 1.2 introduces the channel flow geometry and parameters, followed by an overview of the properties of wall-bounded turbulent flows. In section 1.3, relevant Lagrangian studies of wall-bounded turbulent flows are reviewed. Finally, the objectives of this work and the structure of this document are outlined in section 1.4.

1.1 Lagrangian description of turbulent flows

In the Lagrangian framework, a fluid flow is described in terms of the trajectories of fluid particles (or *tracers*) that follow the flow. A fluid particle is understood as an indivisible fluid element, of infinitesimal size in the macroscopic continuum approximation implied by the Navier–Stokes equations. The Lagrangian approach may describe the evolution of fluid properties such as its velocity or temperature along the trajectories of fluid particles.

The Lagrangian description is naturally linked to the problem of mixing and dispersion of species (e.g. contaminants) by fluid flows. Under certain conditions, the transport of such species (or *scalars*) immersed in a fluid can be assimilated to the dispersion of fluid particles. For this, the scalar must be *passive*, i.e. its presence must have no influence on the motion of the carrying fluid. Moreover, it must faithfully follow the fluid velocity field. This requires the scalar to be composed of particles smaller than the typical distance over which the fluid velocity field changes, and to have a density similar to that of the fluid [108, p. 580]. Finally, the scalar molecular diffusion must be negligible. This last requirement is generally satisfied in turbulent flows, as turbulence is much more efficient at diffusing species than molecular agitation.

The Lagrangian perspective and its application to turbulent flows are introduced in the following sections. In section 1.1.1, the Lagrangian formalism is introduced in relation to the Eulerian description of the flow and to the relevant equations of motion. Some basic Lagrangian properties of turbulent flows are then introduced in section 1.1.2. In section 1.1.3, two simple stochastic models for the dynamics of tracer particles are presented and linked to the Lagrangian properties of turbulence. This also serves as an introduction to the classical framework used in the study of turbulent flows. Evidence of the intermittency of Lagrangian velocity increments in isotropic turbulent

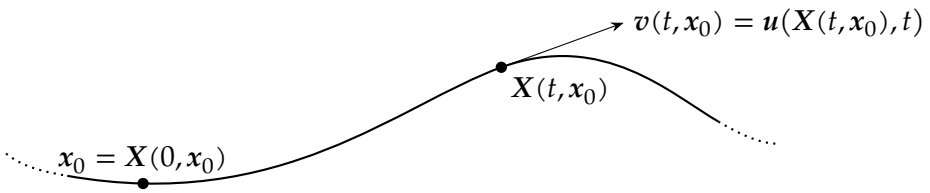

Figure 1.1. Schematic of a Lagrangian trajectory.

flows is presented in section 1.1.4. These results are extended in section 1.1.5 to the case of the Lagrangian acceleration, whose dynamics are associated to that of vortex filaments in turbulence. Finally, some remarks are made in section 1.1.6 regarding the Lagrangian properties of anisotropic turbulent flows.

1.1.1 Eulerian and Lagrangian formulations

The Lagrangian viewpoint is usually contrasted with the Eulerian approach, in which flow properties are probed at fixed locations of the spatial domain. Although it is arguably more intuitive to describe a flow by looking at the trajectories of fluid tracers, the Eulerian approach has been historically more popular among investigators for several reasons. Experimentally, it is simpler to measure flow properties at fixed locations. As an example, hot-wire probes are commonly used to measure velocity fluctuations at fixed points in space in turbulent laboratory flows at relatively low implementation and operation costs. In comparison, Lagrangian velocity measurements are much more challenging, with requirements including (i) small neutrally-buoyant particles behaving as passive tracers, (ii) the capability to identify and track individual particles over sufficiently long times, and (iii) high sampling rates ensuring that measured trajectories are smooth enough to be numerically differentiated (evidently, this last requirement is even more critical for acceleration measurements) [205]. From a theoretical perspective, the equations governing the motion of fluid flows are naturally written in the Eulerian frame, in terms of spatial fields (e.g. velocity, pressure) and their spatial gradients. Numerically, these fields are typically computed on a fixed (Eulerian) spatial grid, enabling the numerical estimation of their gradients appearing in the governing equations.

In the Eulerian description, the fluid velocity field $\boldsymbol{u} = (u_x, u_y, u_z)$ is a function of position and time, $\boldsymbol{u} = \boldsymbol{u}(\boldsymbol{x}, t)$. Here, the subscripts x, y and z denote the three Cartesian components of the velocity vector. By contrast, the tracer velocity $\boldsymbol{v}$ in the Lagrangian frame is parametrised by the initial tracer position $\boldsymbol{x}_0$ at $t = 0$ (which uniquely identifies the tracer), and by the elapsed time t, as illustrated by fig. 1.1. The trajectory of a Lagrangian particle, $\boldsymbol{X}(t, \boldsymbol{x}_0)$, is then linked to the Eulerian velocity field $\boldsymbol{u}(\boldsymbol{x}, t)$ by

$$\frac{\partial \boldsymbol{X}(t, \boldsymbol{x}_0)}{\partial t} = \boldsymbol{v}(t, \boldsymbol{x}_0) = \boldsymbol{u}(\boldsymbol{X}(t, \boldsymbol{x}_0), t), \qquad \boldsymbol{X}(0, \boldsymbol{x}_0) = \boldsymbol{x}_0. \tag{1.1}$$

In this work, we assume that the Eulerian velocity field obeys the incompressible

Navier–Stokes equations,

$$\boldsymbol{\nabla} \cdot \boldsymbol{u} = 0, \tag{1.2a}$$

$$\frac{\mathrm{D}\boldsymbol{u}}{\mathrm{D}t} = \frac{\partial \boldsymbol{u}}{\partial t} + (\boldsymbol{u} \cdot \boldsymbol{\nabla})\boldsymbol{u} = -\frac{1}{\rho}\boldsymbol{\nabla} p + \nu \nabla^2 \boldsymbol{u} + \boldsymbol{f}, \tag{1.2b}$$

where $p(\boldsymbol{x}, t)$ is the pressure field required to satisfy the incompressibility constraint (1.2a), and $\boldsymbol{f}(\boldsymbol{x}, t)$ is a forcing term that may represent the action of an external force (e.g. a large-scale mechanism driving the flow). The fluid density ρ and kinematic viscosity ν are supposed constant throughout the physical domain. In eq. (1.2b), $\mathrm{D}/\mathrm{D}t = \partial_t + (\boldsymbol{u} \cdot \boldsymbol{\nabla})$ is the material (or Lagrangian) derivative operator, representing the temporal variation of a quantity along a Lagrangian path.

The Eulerian and Lagrangian formulations contain the same information about a fluid flow, and in theory, it is possible to transform back and forth between the two descriptions. For instance, knowing the evolution of the Eulerian velocity field $\boldsymbol{u}(\boldsymbol{x}, t)$ over $t \in [0, T]$, the trajectory of a Lagrangian particle $\boldsymbol{X}(t, \boldsymbol{x}_0)$ starting from any given position $\boldsymbol{x}_0$, can be fully described over the same time interval. Conversely, since fluid particles (as mathematical objects) cover the whole fluid domain at all times, knowing the instantaneous velocity of all tracers at time t is equivalent to knowing the Eulerian velocity field $\boldsymbol{u}(\boldsymbol{x}, t)$ at that time.

In practice, it is challenging to transform back and forth between the two formulations. Experimentally, a turbulent flow can be studied by seeding particles behaving as Lagrangian tracers into the flow. If the particle concentration is high enough, it becomes possible to reconstruct the Eulerian velocity field based on subsequent particle snapshots, provided they are performed over a short temporal window. This is the principle of the particle image velocimetry technique [3]. However, due to the high particle concentration required, it is virtually impossible to identify individual particles and track them over long times using this approach. To obtain a true Lagrangian characterisation of the flow, lower tracer particle concentrations must be used, enabling particles to be individually tracked over time.[1] However, the capability to accurately reconstruct instantaneous Eulerian fields is lost as a consequence. Similarly, in numerical simulations, the most common approach to a Lagrangian description of the flow (and the one used in this work, as described in section 2.2) is to resolve the governing equations in an Eulerian reference frame, from which the resulting velocity field is then estimated at the positions of Lagrangian particles seeded into the simulation. Due to computational constraints, the number of seeded particles is typically insufficient for recovering Eulerian fields from Lagrangian data.

The equivalence of the Lagrangian and Eulerian frameworks does not imply that flow properties evolve equally at a fixed point in space and along a fluid particle path. In a stationary flow (in which $\partial_t \boldsymbol{u} = \boldsymbol{0}$), the velocity of a fluid particle may change over time despite the stationarity of the Eulerian velocity field. A simple example in two dimensions is the stationary velocity field induced by a point vortex (as illustrated

[1] This is the basis of the particle tracking velocimetry (PTV) method. See section 3.1 for more details.

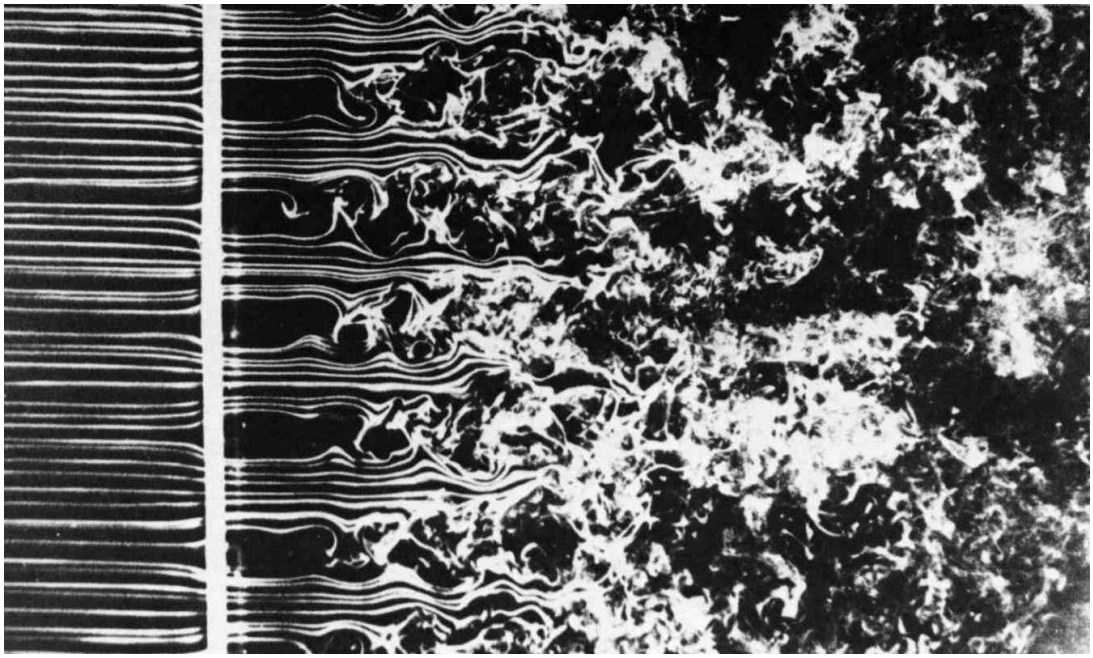

Figure 1.2. Visualisation of grid-generated turbulence using smoke wires. Reproduced from Van Dyke [185]. Photograph by T. Corke and H. Nagib.

later in fig. 1.7a). In this velocity field, a fluid particle moves in a circular orbit about the vortex. Although the magnitude of the particle velocity stays constant, its direction changes (periodically) over time.

The difference between both descriptions is particularly significant in turbulent flows, which are characterised by motions occurring over a hierarchy of scales. In three-dimensional turbulent flows, the large-scale motions are typically determined by the particular mechanism by which turbulence is generated. A classical example is the uniform flow passing through a fixed grid made of solid rods, as seen in fig. 1.2. Behind the grid, turbulent motions (or *eddies*) are generated with sizes comparable to the spacing between the rods. The classical picture of the energy cascade describes the generation of smaller-scale eddies from the initial motions at the scale of the grid, eventually leading to the decay of turbulent motion. In other words, turbulent kinetic energy is transferred from the large-scale eddies to small-scale motions. Ultimately, very small eddies are dissipated as they reach a characteristic size at which viscous effects become important.

As seen in fig. 1.2, eddies of different size spatially coexist. In other words, large-scale turbulent motions also advect smaller-scale structures. As postulated by Tennekes [176], this implies that the high-frequency temporal variations of the flow at a fixed point in space are not only given by the rapidly varying small-scale motions, but also by the advection (or *sweeping*) of these motions by the random large-scale eddies. As a result, the temporal variations of the velocity that are observed in the Eulerian frame are even faster (i.e. have a shorter time scale) than the characteristic rate of change of

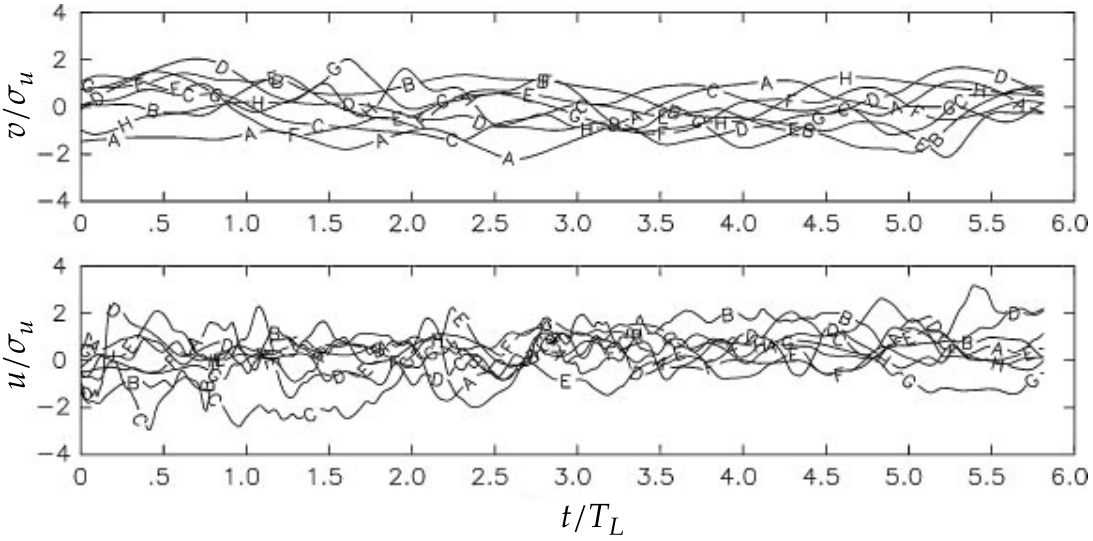

Figure 1.3. Comparison between Lagrangian (top) and Eulerian (bottom) velocity time series. Each line represents a different sample. Data was obtained from isotropic turbulence direct numerical simulations at a Taylor-scale Reynolds number $Re_\lambda = 140$ [204]. (In isotropic turbulent flows, $Re_\lambda = \sigma_u \lambda / \nu$ where σ_u is the magnitude of the velocity fluctuations, $\lambda = (15\nu\sigma_u^2/\varepsilon)^{1/2}$ the Taylor microscale, and ε the mean energy dissipation rate per unit mass [177].) Values are normalised by σ_u and the Lagrangian integral time scale T_L. Reproduced from Yeung [205].

the small-scale motions. This is not the case for the temporal fluctuations observed in the Lagrangian reference frame, which are not affected by random sweeping. This is qualitatively confirmed in fig. 1.3, where Eulerian and Lagrangian velocity time series are compared. The sharper temporal variations of the Eulerian data are a consequence of random sweeping. For this reason, the Lagrangian description is generally considered to be more appropriate to describe the temporal evolution of turbulent flows [180].

1.1.2 Lagrangian properties of isotropic turbulent flows

In the following we introduce some relevant aspects of the dynamics of Lagrangian particles in turbulent flows. Due to their complexity and chaotic behaviour, an exact treatment of turbulent flows is impractical and a statistical approach is needed to describe the flow. For now, the discussion is limited to turbulent flows which are statistically homogeneous and isotropic, i.e. their statistical properties (such as the velocity probability density function (PDF)) do not depend on the sampled location, and are invariant with respect to spatial rotations (e.g. all velocity components share the same statistics). Moreover, the turbulence is assumed to be statistically stationary, i.e. its statistical properties do not vary with time. This requires a large-scale forcing of the flow in order to compensate for the dissipation of energy at small scales. Finally,

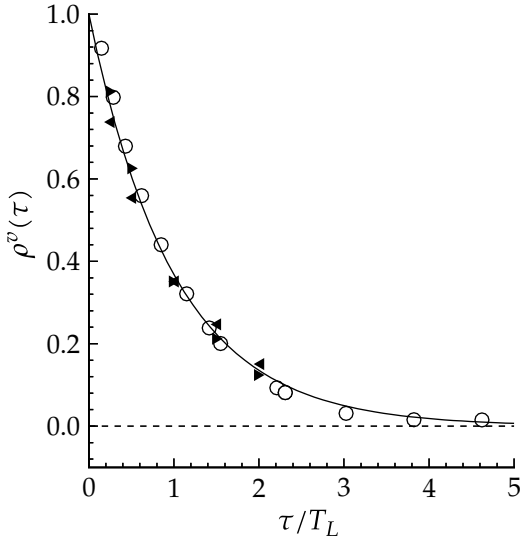

Figure 1.4. Lagrangian velocity auto-correlation function in isotropic turbulence. Filled symbols, experimental data of Sato and Yamamoto [152] at $Re_\lambda = 46$ and 66; open circles, DNS data of Yeung and Pope [206] at $Re_\lambda = 90$; solid line, Langevin model $\rho^v(\tau) = \exp(-\tau/T_L)$. Reproduced from Pope [137].

the average fluid velocity is taken as zero throughout space.[2]

An important quantity for characterising the time evolution of a turbulent flow is the Lagrangian velocity auto-correlation function,

$$\rho^v(\tau) = \frac{\langle v_i(t, \boldsymbol{x}_0)\, v_i(t+\tau, \boldsymbol{x}_0)\rangle}{\sigma_u^2}, \tag{1.3}$$

where repeated indices, representing Cartesian coordinates, do not imply summation. Due to isotropy, the three velocity components have the same auto-correlation $\rho^v(\tau)$. The Lagrangian mean $\langle\cdot\rangle$ represents an ensemble average among Lagrangian trajectories, and $\sigma_u^2 = \langle v_i^2\rangle$ is the velocity variance. By ergodicity, due to statistical stationarity and homogeneity, the Lagrangian mean is equivalent here to an average among all initial locations $\boldsymbol{x}_0$ and times t.

Typical Lagrangian velocity auto-correlation functions obtained in homogeneous isotropic turbulence (HIT) are shown in fig. 1.4. The curves decrease roughly exponentially indicating that Lagrangian particles lose memory of their velocity over time. The auto-correlation function provides an estimate of the characteristic time over which a fluid particle loses memory of its instantaneous velocity. Traditionally, this

[2]Statistical homogeneity and stationarity imply that the average velocity $\boldsymbol{U}$ is constant in space and time. Therefore, a Galilean reference frame moving with velocity $\boldsymbol{U}$ can be chosen in which the average velocity is effectively zero.

characteristic time is quantified by the Lagrangian integral time scale,

$$T_L = \int_0^\infty \rho^v(\tau)\,\mathrm{d}\tau\,. \tag{1.4}$$

In his classical work, Taylor [175] linked the statistics of fluid particle dispersion in turbulent flows with the Lagrangian velocity auto-correlation ρ^v and the Lagrangian integral time scale T_L. Namely, he showed that the mean-square fluid particle displacement is given by [177, p. 225]

$$\langle \delta x_i^2 \rangle(\tau) \equiv \langle (X_i - x_{0i})^2 \rangle(\tau) = 2\sigma_u^2 \tau \int_0^\tau \left(1 - \frac{s}{\tau}\right) \rho^v(s)\,\mathrm{d}s\,, \tag{1.5}$$

where x_{0i} and X_i are the i-th components of the initial and instantaneous particle positions, respectively. It is readily shown that at very long times ($\tau \gg T_L$), eq. (1.5) is approximated by

$$\langle \delta x_i^2 \rangle(\tau) \approx 2\sigma_u^2 T_L \tau. \tag{1.6}$$

Therefore, at sufficiently long times, the mean-square displacement grows linearly in time. This suggests that at long times, the motion of fluid particles in turbulent flows is analogous to Brownian motion (where $\langle \delta x_i^2 \rangle(\tau) = 2D\tau$), with an effective turbulent diffusion coefficient $D_T = \sigma_u^2 T_L$.

1.1.3 Lagrangian stochastic models

Here we briefly introduce two simple stochastic models predicting the dynamics of fluid particles in HIT. The development and application of Lagrangian stochastic models are beyond the scope of this work. The aim is just to provide an additional motivation for the Lagrangian description of turbulent flows, and to introduce some important concepts that are further discussed in the following sections. Lagrangian stochastic models are commonly used for predicting the dispersion of species (pollen, contaminants) in atmospheric flows [194] as well as in the ocean [90, 187]. As shown in the following, the study of the Lagrangian properties of turbulent flows can serve to improve and feed these models with relevant parameters.

Langevin equation One of the simplest Lagrangian stochastic models is the Langevin equation, which models the velocity of a particle undergoing Brownian motion. In statistically stationary HIT, the Langevin equation may be expressed as a stochastic differential equation (SDE) for the velocity increment $\mathrm{d}v$ [139],

$$\mathrm{d}v(t) = -\frac{v(t)}{T_L}\,\mathrm{d}t + \left(\frac{2\sigma_u^2}{T_L}\right)^{1/2} \mathrm{d}W(t), \qquad \mathrm{d}x(t) = v(t)\,\mathrm{d}t, \tag{1.7}$$

where $x(t)$ and $v(t)$ are the particle position and velocity in a given direction, and $W(t)$ is a Wiener process. That is, the increment $\mathrm{d}W(t) = W(t + \mathrm{d}t) - W(t)$ is Gaussian with zero mean and variance $\mathrm{d}t$, and non-overlapping increments are independent

of each other [187]. The Langevin model assumes the particle position and velocity to be jointly Markovian, and is thus considered a first-order model [153]. This is equivalent to assuming that the particle acceleration a is delta-correlated in time, i.e. $\langle a(t)\, a(t+\tau)\rangle = \langle a(t)^2\rangle\, \delta(\tau)$ where δ is the Dirac delta. According to eq. (1.7), the velocity increment $\mathrm{d}v$ is the sum of a deterministic drift term $(-v\,\mathrm{d}t/T_L)$ causing the velocity to relax to zero, and a Gaussian diffusion term with zero mean and variance $2\sigma_u^2\,\mathrm{d}t/T_L$ [137].

The stochastic process $v(t)$ generated by eq. (1.7), called the Ornstein–Uhlenbeck process, is continuous, statistically stationary and Gaussian, with zero mean, and variance $\langle v(t)^2\rangle = \sigma_u^2$ [139]. Its auto-correlation function is exponential, $\rho^v(\tau) = \exp(-|\tau|/T_L)$, and its integral time scale is T_L. In fig. 1.4, the exponential auto-correlation associated to this process is shown to correctly describe velocity auto-correlation data in turbulent flows. However, as noted by Pope [137], the exponential curve predicted by the model is incorrect at very short times ($\tau \ll T_L$), since the derivative of the auto-correlation function at $\tau = 0$ should vanish (instead of being negative) due to statistical stationarity. Indeed, from eq. (1.3), it can be shown that

$$\left.\frac{\mathrm{d}\rho^v(\tau)}{\mathrm{d}\tau}\right|_{\tau=0} = \frac{1}{2\sigma_u^2}\left\langle \frac{\partial v_i^2}{\partial t}(t,\boldsymbol{x}_0)\right\rangle = \frac{1}{2\sigma_u^2}\frac{\partial}{\partial t}\langle v_i^2(t,\boldsymbol{x}_0)\rangle, \tag{1.8}$$

which is necessarily zero since statistics are time-invariant.

In high-Reynolds numbers turbulent flows, the Lagrangian integral time scale T_L appearing in eq. (1.7) can be related to other properties of the turbulent flow by assuming that the Langevin equation is consistent with Kolmogorov's K41 similarity theory [83]. To introduce the implications of K41 theory on Lagrangian turbulence statistics and their connection to the Langevin equation, we first define the Lagrangian second-order velocity structure function,

$$D_2(\tau) = \langle [v(t+\tau) - v(t)]^2\rangle = \langle [\Delta_\tau v(t)]^2\rangle, \tag{1.9}$$

which is nothing else than the variance of the Lagrangian velocity increments $\Delta_\tau v(t) = v(t+\tau) - v(t)$ over a fixed time delay τ.

K41 theory predicts that, when τ is much larger than the characteristic time scale of the dissipative motions τ_η and much smaller than the Lagrangian time scale T_L, the Lagrangian structure function is independent of viscosity and of the precise mechanism of energy injection, and it only depends on τ and on the mean turbulent energy dissipation rate denoted by ε. The range $\tau_\eta \ll \tau \ll T_L$ is called the *inertial range*,[3] and τ_η is the Kolmogorov time scale defined as $\tau_\eta = (\nu/\varepsilon)^{1/2}$.

Under the assumptions of K41 theory, dimensional arguments then lead to the prediction that

$$D_2(\tau) = C_0\varepsilon\tau \quad \text{for} \quad \tau_\eta \ll \tau \ll T_L, \tag{1.10}$$

[3] Our formulation is somewhat unusual in that Kolmogorov's similarity theory is most often presented and applied in the Eulerian reference frame. In particular, the inertial range is typically introduced in terms of characteristic *lengths* as opposed to *time* scales.

with C_0 a non-dimensional constant supposed universal, i.e. independent of the Reynolds number and of the turbulence generation mechanism. At the present time, there is no conclusive evidence confirming the universality of the Kolmogorov constant C_0, although its value tends to plateau at $C_0 \approx 7$ at high Reynolds numbers [180]. This is discussed in some more detail in section 3.5.

The K41 prediction can be matched to that of the Langevin equation [137],

$$D_2(\tau) = 2\sigma_u^2 \tau / T_L \quad \text{for} \quad \tau \ll T_L, \tag{1.11}$$

leading to the estimation of the Lagrangian integral time scale as $T_L = 2\sigma_u^2/(C_0\varepsilon)$. Since it has no concept of a *short* time scale comparable to τ_η, the Langevin equation assumes eq. (1.11) to be valid for any arbitrarily short time lag τ. In other words, according to the Langevin equation, the inertial range extends up to infinitesimally small time lags. In turbulent flows, this corresponds to the infinite Reynolds number limit.[4]

Second-order stochastic model As discussed above, the Langevin equation is inappropriate to capture the Lagrangian dynamics at very short times comparable to the Kolmogorov time scale τ_η. To account for finite Reynolds number effects, Sawford [153] proposed a second-order stochastic model which, in contrast to the first-order Langevin model, considers the particle position, velocity and acceleration as jointly Markovian. For this, Sawford's model introduces the Kolmogorov time scale τ_η as a second model variable, in addition to the Lagrangian integral time scale T_L, in order to account for *dissipation range* ($\tau \ll \tau_\eta$) statistics. In the model, the acceleration SDE is expressed as

$$\mathrm{d}a(t) = -\alpha_1 a(t)\,\mathrm{d}t - \alpha_2 \int_0^t a(s)\,\mathrm{d}s\,\mathrm{d}t + \sqrt{2\alpha_1\alpha_2\sigma_u^2}\,\mathrm{d}W(t), \tag{1.12}$$

and the velocity and position are obtained by successive integrations of the acceleration $a(t)$. The parameters α_1 and α_2 are related to the integral and Kolmogorov time scales. They are defined so that the model matches the Lagrangian structure functions $D_2(\tau)$ predicted by K41 theory both in the dissipation and inertial ranges. In the dissipation range, the K41 prediction is given by [109, p. 359]

$$D_2(\tau) = a_0 \varepsilon^{3/2} \nu^{-1/2} \tau^2 \quad \text{for} \quad \tau \ll \tau_\eta. \tag{1.13}$$

The non-dimensional parameter a_0 is equal to the acceleration variance $\langle a(t)^2 \rangle$ normalised by ε and ν. As with C_0, K41 theory predicts that a_0 is a universal constant for high Reynolds numbers flows. As discussed in section 3.5, currently available data suggests that a_0 actually strongly varies with Reynolds number. The velocity auto-correlation function $\rho^v(\tau)$ resulting from Sawford's second-order model is expressed as the difference between two exponentials, and by construction (since dissipation scales are properly accounted for), its derivative correctly vanishes at $\tau = 0$.

[4] The empirical law of finite energy dissipation states that ε remains finite at vanishing viscosity [55]. Therefore, in the limit of infinite Reynolds number ($\nu \to 0$), the Kolmogorov time scale $\tau_\eta = (\nu/\varepsilon)^{1/2}$ tends to zero.

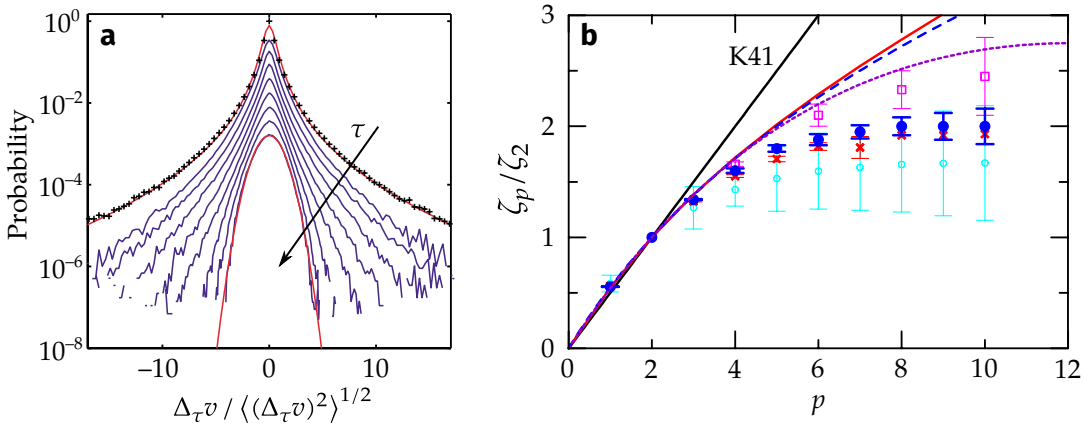

Figure 1.5. Lagrangian intermittency in isotropic turbulence. (a) PDF of velocity increments $\Delta_\tau v$ from experiments at $Re_\lambda = 740$, for time lags $100\tau/T_L = 1.3$, 2.7, 5.4, 11.2, 22.4, 44, 89.3 and 174. The curves are displayed with a vertical shift for clarity. Crosses correspond to a model prediction. Reproduced from Mordant et al. [114]. (b) Extended self-similarity estimates of the scaling exponent ratio ζ_p/ζ_2 in the inertial range. Markers correspond to different simulations and experiments: blue filled circles, Sawford and Yeung [157] ($Re_\lambda = 38-1000$); magenta squares, Benzi et al. [16] ($Re_\lambda = 600$); red crosses, Mordant et al. [118] ($Re_\lambda = 75-1000$); cyan open circles, Xu et al. [197] ($Re_\lambda = 200-815$). The black solid line represents the K41 prediction $\zeta_p = p/2$. Other lines correspond to different model predictions. Reproduced from Sawford and Yeung [157].

1.1.4 Lagrangian intermittency

Experimental and numerical Lagrangian studies of turbulent flows have shown that the Lagrangian velocity increments $\Delta_\tau v$, introduced in section 1.1.3, are actually highly intermittent at small time lags τ [180]. That is, fluid particles, in very rare occasions, see abrupt changes in their velocity over short time spans. This is manifested by PDFs of velocity increments $\Delta_\tau v$ which are strongly non-Gaussian when τ is small (fig. 1.5a), with heavy, stretched exponential tails corresponding to rare events associated to very intense velocity increments [115, 118, 157]. This intermittency is not captured by the simple Lagrangian stochastic models introduced in section 1.1.3.

Equivalently, intermittency is reflected in a departure from Kolmogorov K41 theory, which predicts that the Lagrangian velocity structure function of order p should scale as

$$D_p(\tau) \equiv \langle |\Delta_\tau v(t)|^p \rangle \sim (\varepsilon\tau)^{p/2}, \qquad p = 1, 2, 3, \ldots, \tag{1.14}$$

for inertial-range time increments τ. Attempts have been made to determine the actual scaling exponents ζ_p (such that $D_p(\tau) \sim \tau^{\zeta_p}$) from Lagrangian turbulence data, and to compare them with the K41 prediction $\zeta_p = p/2$. For the particular case $p = 2$, it has been argued [26] that as a consequence of the linear dependence of $D_2(\tau)$ on ε in eq. (1.14), the scaling exponent ζ_2 is not affected by intermittency, i.e. $\zeta_2 = 1$ as

predicted by K41 theory.[5]

At the finite Reynolds numbers of laboratory experiments and simulations, clear power laws $D_p(\tau) \sim \tau^{\zeta_p}$ are generally not observed [118]. Therefore, to determine the ζ_p exponents from available data, researchers have resorted to the extended self-similarity procedure first introduced in the context of Eulerian structure functions [17]. In the present context, this corresponds to estimating the scaling exponents ζ_p from curves of $D_p(\tau)$ plotted against $D_2(\tau)$ instead of against τ. This immediately leads to estimates of the scaling exponent ratios ζ_p/ζ_2. In addition, the assumption that $D_2(\tau) \sim \tau$ in the inertial range (i.e. $\zeta_2 = 1$) may be used to determine the other scaling exponents ζ_p. Extended self-similarity has resulted in relatively robust scaling exponents reproduced in various numerical and experimental settings [14, 19, 22, 24, 118, 197]. As shown in fig. 1.5b, the consensus is that the K41 predictions do not hold for Lagrangian structure functions of order higher than 2, confirming the intermittency of Lagrangian velocity increments in turbulent flows.

1.1.5 Lagrangian acceleration

The Lagrangian velocity increments $\Delta_\tau v$ are evidently related to the Lagrangian particle acceleration, which is obtained from $\Delta_\tau v$ in the limit of small τ. We have observed above that the Lagrangian velocity increments become more and more intermittent as the time lag τ is reduced. From this, it can be anticipated that the acceleration is a highly intermittent quantity in turbulent flows.[6]

Lagrangian accelerations were first measured in turbulent laboratory flows by Voth et al. [190]. Soon after, it was observed that the acceleration of fluid particles is very intermittent, and characterised by highly non-Gaussian PDFs with long stretched exponential tails [89, 189] as seen in fig. 1.6a. As expected, the shape of the acceleration PDFs resembles that of the velocity increments $\Delta_\tau v$ for small τ (fig. 1.5a). The inset of fig. 1.6a shows the flatness factor $\langle a^4 \rangle / \langle a^2 \rangle^2$, representing the departure of the acceleration distribution from Gaussianity. The large flatness values, which can be contrasted to the value of 3 associated to a Gaussian distribution, quantify the high intermittency of the acceleration, as they indicate that extreme accelerations much higher than the standard deviation occur relatively frequently in turbulent flows.

High-acceleration events in turbulent flows have been linked to fluid particles being trapped in helical motions such as the one visualised in fig. 1.6b. In the figure, the size of the helical loops is about 15η (where $\eta = (\nu^3/\varepsilon)^{1/4}$ is the Kolmogorov length scale associated to the smallest scales of turbulent motion), while changes of orientation occur over periods of the order of the Kolmogorov time scale τ_η [189]. This suggests that changes of acceleration occur very rapidly and are associated to small-scale turbulent

[5] As noted by Xu et al. [197], this is analogous to the case of the third-order Eulerian velocity structure function $S_3(r) = \overline{[u_\parallel(\boldsymbol{x}+\boldsymbol{r}) - u_\parallel(\boldsymbol{x})]^3}$ (where $u_\parallel = (\boldsymbol{u}\cdot\boldsymbol{r})/r$ and $r = |\boldsymbol{r}|$), with the difference that there is an *exact* expression for $S_3(r)$ in the limit of infinite Reynolds number, namely Kolmogorov's four-fifths law $S_3(r) = -\frac{4}{5}\varepsilon r$ [55, 84].

[6] Chronologically, the intermittency of the acceleration was studied before that of the Lagrangian velocity increments.

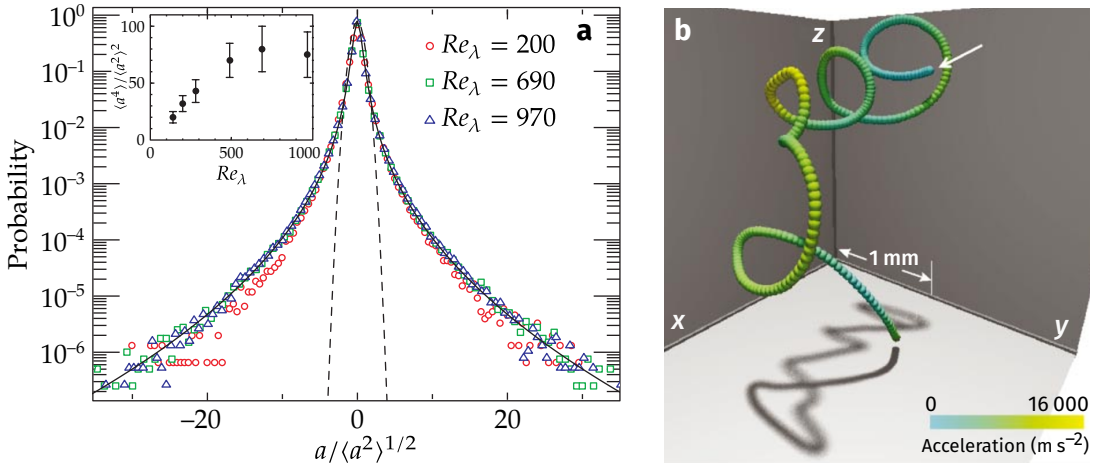

Figure 1.6. Lagrangian acceleration in laboratory experiments. (a) PDFs of acceleration normalised by its standard deviation at different Reynolds numbers. Dashed line, Gaussian distribution with unit variance; solid line, fit of $Re_\lambda = 970$ data. Inset: flatness of the acceleration distribution, $\langle a^4\rangle/\langle a^2\rangle^2$, as a function of Re_λ. Reproduced from La Porta et al. [89]. (b) Trajectory of a high-acceleration spherical tracer particle (diameter 46 μm) in a turbulent flow at $Re_\lambda = 970$. Colours represent the acceleration magnitude. Reproduced from Voth et al. [189].

structures close to the dissipation range. These structures can be identified as the intense, elongated vortex filaments of diameter of order η, which are a signature of small-scale intermittency in turbulent flows [164, 171].

Intuitively, a fluid particle rotating in helical motion experiences a centripetal acceleration towards the centre of rotation. Centripetal accelerations are associated to changes of orientation of a particle trajectory. Hence, it may be speculated that vortex filaments contribute to the intermittency of acceleration by inducing high-magnitude centripetal accelerations associated to sharp changes of orientation of trapped fluid particles. This hypothesis was examined by Toschi et al. [179], who compared the PDF of the centripetal acceleration, $a_c = |\boldsymbol{a} \times \boldsymbol{v}|/|\boldsymbol{v}|$, with that of the longitudinal acceleration (aligned with the velocity $\boldsymbol{v}$), $a_l = (\boldsymbol{a} \cdot \boldsymbol{v})/|\boldsymbol{v}|$. They found the centripetal component to be much more intermittent than the longitudinal one, in support of the above hypothesis.

If we again suppose that the acceleration of a tracer trapped in a vortical structure is mainly determined by a centripetal component, the above picture also suggests that, as the tracer circulates in helical motion, its acceleration vector continuously changes direction (as it is mainly directed towards the vortex axis) while the acceleration magnitude changes more slowly. To illustrate this idea, we come back to the simple two-dimensional point vortex model briefly mentioned in section 1.1.1. A point vortex induces a velocity field, in polar coordinates, $\boldsymbol{u} = (\Gamma/2\pi r)\boldsymbol{e}_\theta$, where Γ is the vortex circulation. The circular path of a fluid particle in this velocity field is depicted in fig. 1.7a. In this ideal example, the fluid particle acceleration only has a centripetal component which is constant in magnitude, i.e. its speed $|\boldsymbol{v}|$ stays constant while the orientation of displacement changes steadily. Moreover, the orientation of the

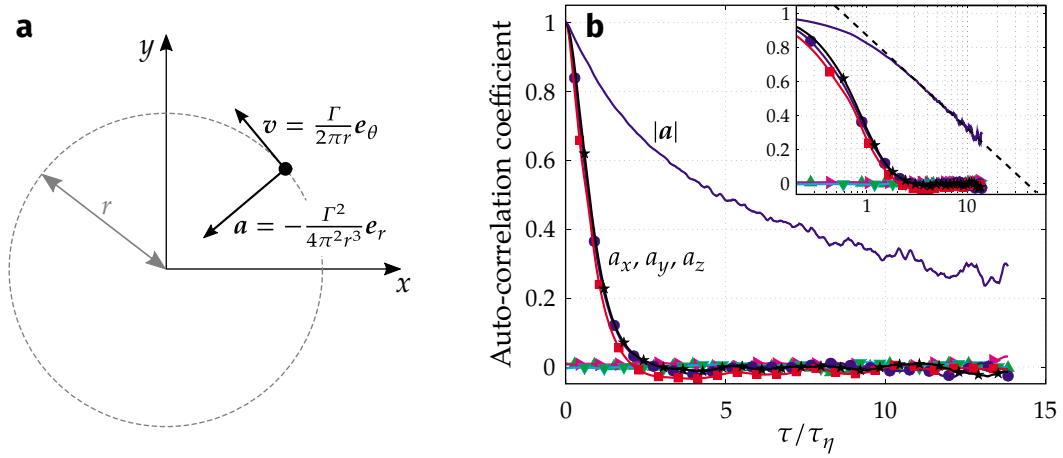

Figure 1.7. Structure of the acceleration vector in turbulent flows. (a) Lagrangian path induced by a point vortex in two dimensions. The vorticity field is of the form $\boldsymbol{\omega}(\boldsymbol{x}) = \Gamma\delta(\boldsymbol{x})\boldsymbol{e}_z$, where Γ is the vortex circulation and δ is the Dirac delta. Fluid particles travel in circular orbits. The Lagrangian velocity and acceleration have constant magnitudes but varying orientations over time. (b) Auto-correlation of acceleration magnitude $|\boldsymbol{a}|$ (solid line) and of the acceleration components a_x, a_y and a_z (●, ★, ■). Triangles (▲, ▶, ▼) represent cross-correlations between acceleration components. The flow is driven by two counter-rotating disks in a cylindrical tank at $Re_\lambda = 690$. Inset: same curves in semi-logarithmic scale. Reproduced from Mordant et al. [117].

acceleration vector clearly changes over time as the tracer rotates about the vortex. Point vortices have already been used to describe the Lagrangian dynamics of turbulence. An example is the work of Rast and Pinton [144], who introduced a model of interacting point vortices to explain the Lagrangian intermittency of turbulence.

The above simple model may serve as an explanation for the observation that in turbulent flows, the Lagrangian acceleration magnitude $|\boldsymbol{a}|$ stays correlated for much longer than the components of the acceleration vector [93, 117, 206]. As seen in fig. 1.7b, the acceleration components completely decorrelate over a time comparable to τ_η, suggesting that their dynamics are governed by the small-scale turbulent motions (as also hinted by the trajectory in fig. 1.6b). The much longer decorrelation time of $|\boldsymbol{a}|$, comparable to T_L [203], indicates that the rapid variations of the acceleration components correspond to changes of orientation of the acceleration vector, likely due to the action of vortex filaments and similar small-scale structures.

The trapping events described above are also expected to have an influence on the Lagrangian velocity increments at finite time lag τ, and thus on the structure functions discussed in section 1.1.4. The effect of such events has been analysed by filtering out their contributions to the Lagrangian structure functions $D_p(\tau)$ [24], and by comparing the statistics to those obtained for heavy inertial particles [14], which are usually expelled from small-scale helical motions due to their inertia.[7] These studies

[7] In other words, the response time of the heavy inertial particles (quantified by the Stokes number) is too large compared to the characteristic period of the small-scale helical motions, which is comparable

found that trapping events enhance intermittency of Lagrangian velocity increments for time lags up to $10\tau_\eta$, which helped explain discrepancies between the scaling exponents estimated from numerical simulations and experiments [14].

1.1.6 Anisotropic and inhomogeneous flows

Most of the Lagrangian investigations cited above have been performed in nominally isotropic turbulent flows. We first make some precisions regarding the statistical isotropy of those flows. Numerical studies of HIT are generally performed using direct numerical simulation (DNS), in which the Navier–Stokes equations (1.2) are solved up to the smallest scales of motion. The physical domain is a triply periodic box, i.e. a cube with periodic boundary conditions. This enables the use of pseudo-spectral methods by decomposing the velocity field into Fourier modes (see section 2.1.1 for details). To ensure the statistical stationarity of the flow, i.e. to compensate for the energy dissipated at the small scales, a large-scale forcing, corresponding to the $\boldsymbol{f}$ term in eq. (1.2b), must be applied. For the flow to be isotropic, the forcing term, which can be stochastic, is chosen as statistically isotropic. Still, some weak anisotropy usually persists due to the inherent anisotropy of the cubical grid. For instance, small differences may be observed for two-point statistics computed along a line parallel to the grid (say, parallel to the x axis) and along a diagonal of the cube [49].

The case of laboratory experiments is more complex, as the unavoidable presence of solid boundaries and the forcing mechanism invariantly introduce some anisotropy into the flow. The aim is for these anisotropy-generating features to be far enough from the measurement region where the flow is analysed, so that the small-scale statistics can be considered as isotropic in that region. The experiments cited in the previous sections were all conducted in von Kármán swirling flows between two coaxial counter-rotating disks in a cylindrical tank [116, 190]. This choice of flow is particularly convenient as it allows for very high Reynolds numbers in a confined geometry. In fig. 1.7b, the auto-correlation curves associated to the three acceleration components (x and y are parallel to the disks; z is the axial direction) display very similar results indicating that the flow is nearly isotropic. The isotropy is also supported by the vanishing cross-correlations between acceleration components. As shown later in section 3.4, things are very different in highly anisotropic flows. Nevertheless, some anisotropy may still persist in the measurements. For instance, using the same von Kármán experimental apparatus as in [190], Ouellette et al. [129] showed that the second-order Lagrangian structure function D_2 was clearly anisotropic. Namely, for all time lags τ, computing $D_2(\tau)$ from the x and y velocity components, parallel to the disks, resulted in larger values than the statistics associated to the z component.

In conclusion, even in controlled settings such as the experimental installations referenced above, it is very difficult to avoid anisotropy in real flows. Practical flows found in natural and industrial applications are much more complex than ideal isotropic flows due to several factors which may include – to only name a few – temporal variability,

to τ_η. Hence, the particles are not 'fast' enough to respond to the solicitations of small vortex filaments.

the presence of solid boundaries, and global rotation of the system. We finish this section by introducing arguably the simplest possible anisotropic flow, which can serve as a starting point to study the effects of anisotropy in turbulence.

Homogeneous shear flow Different canonical flows have been devised to understand the effects of large-scale anisotropy in turbulence. Here, we only mention homogeneous shear flow (HSF) due to its simplicity and its relevance for the present study. In HSF, an unidirectional mean velocity field is imposed of the form

$$U(y) = Sy, \tag{1.15}$$

where U is the mean velocity in the x (*streamwise*) direction, y is the *cross-stream* coordinate along which the mean velocity varies, and S is a constant mean shear rate, $S = \mathrm{d}U/\mathrm{d}y$. HSF is statistically homogeneous, i.e. turbulence statistics are invariant under spatial translations (for instance, the magnitude of the velocity fluctuations is the same for all y). It is therefore a simpler variant of wall-bounded turbulence (section 1.2), as it is characterised by mean shear but in the absence of wall confinement. However, HSF is not really statistically stationary, as length scales continuously grow in the streamwise direction [177, p. 230].

The dispersion of tracer particles in turbulent HSF was considered theoretically by Corrsin [44], who suggested that at asymptotically long times, the mean-square tracer displacement in the streamwise direction grows as [108, p. 558]

$$\langle \delta x^2 \rangle(\tau) = \frac{2}{3} S^2 \overline{u_y'^2} T_{L,y} \tau^3 \quad \text{for} \quad \tau \gg T_{L,y}, \tag{1.16}$$

where $T_{L,y}$ is the Lagrangian integral time scale associated to the cross-stream velocity component u_y. This can be contrasted to Taylor's prediction in HIT, $\langle \delta x^2 \rangle(\tau) \sim \tau$ [eq. (1.6)], showing that mean shear greatly enhances dispersion. To understand the effect of mean shear on dispersion, one may consider a group of fluid particles initially located on the $y = 0$ plane. Over time, due to turbulent fluctuations, tracers will spread in the cross-stream direction, and thus will be located in regions of different mean streamwise velocity U. At that point, mean shear will rapidly spread the particles in the streamwise direction, leading to a large variability of their streamwise displacements at long times.

Corrsin's estimation assumes the statistical stationarity of the flow. However, as mentioned above, HSF is not stationary, and the global kinetic energy content actually grows at long times. For this reason, DNS results have shown that the mean-square streamwise displacement asymptotically grows slightly faster than τ^3 [165, 169]. Both Squires and Eaton [169] and Shen and Yeung [165] also considered the Lagrangian velocity correlations, which, as described in section 1.1.2, are linked to the dispersive properties of the flow. They observed that the streamwise velocity component stays correlated for longer along Lagrangian paths than the other two components. In addition, Yeung [203] showed that Lagrangian acceleration correlations are nearly

isotropic in HSF, consistently with the idea of a return to isotropy at the small scales.

The present work deals with a Lagrangian description of wall-bounded turbulent flows. Some fundamental aspects of wall turbulence are introduced in section 1.2. Compared to turbulent HSF, wall-bounded turbulence is more complex since it is not only anisotropic but also inhomogeneous in the direction normal to the wall, and the presence of the wall limits the possible motions in the wall-normal direction. Moreover, the near-wall dynamics are dominated by inherently anisotropic coherent motions as described in section 1.2.4. As a consequence of inhomogeneity, the Lagrangian description of the flow is more complex since an additional dependence of Lagrangian statistics on distance from the wall must be considered. The Lagrangian description of wall-bounded turbulence is discussed in more detail in section 3.3.

1.2 Wall-bounded turbulence

A large number of turbulent flows in nature and industrial applications are subject to the presence of walls or solid boundaries. Wall-bounded turbulence is highly inhomogeneous and anisotropic, adding more complexity to the relatively simple description of turbulence initiated by Kolmogorov. Therefore, understanding and modelling wall-bounded turbulent flows is a fundamental challenge in turbulence research. To this day, much effort has gone into understanding wall-bounded flows. Different low-order formulations and modelling approaches have been proposed. In this regard, some current trends have been recently reviewed by McKeon [104], Jiménez [77], and Marusic and Monty [103]. However, no clear consensus still exists on appropriate models for predicting wall effects in practical flows.

In this work, we consider a turbulent channel flow between two smooth parallel plates. Channel flow is one of the canonical settings for studying wall turbulence, along with pipes of circular cross-section and boundary layer flows over a single flat plate. These flows share some of the same features and, due to their relative simplicity, they are particularly convenient for the study of wall turbulence.

In section 1.2.1 we describe the channel flow geometry, including its statistical symmetries and relevant physical definitions. The different regions that are classically distinguished in wall-bounded turbulence are then briefly introduced in section 1.2.2. This is followed in section 1.2.3 by a characterisation of the mean velocity profile in each of these regions. Finally, section 1.2.4 gives an overview of the coherent motions typically found in wall-bounded turbulence.

1.2.1 Turbulent channel flow

We consider the turbulent flow in a channel between two parallel walls with infinite extent. A Cartesian coordinate system is introduced, with x and z the wall-parallel directions, and y the direction normal to the walls. The flow is driven by an imposed constant pressure gradient $\boldsymbol{\nabla} p_0$ aligned with the x direction, resulting in an unidirectional average flow. Consequently, x is referred to as the *streamwise* direction, while y

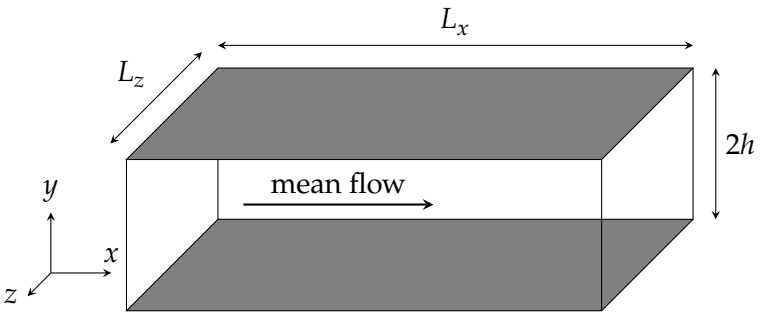

Figure 1.8. Channel flow geometry and coordinate system.

and z are respectively the *wall-normal* and *spanwise* directions. For numerical purposes, the infinite domain in x and z is modelled as a periodic domain of period L_x and L_z in each respective direction, as depicted in fig. 1.8. On the two walls, the flow velocity vanishes due to no-slip boundary conditions. The separation between the two walls is $2h$, with $y = 0$ and $y = 2h$ their respective positions. As a consequence, the domain of interest is $\Omega = [0, L_x] \times [0, 2h] \times [0, L_z]$.

Statistical symmetries The turbulent velocity field $\boldsymbol{u}(\boldsymbol{x}, t)$ in the channel is governed by the incompressible Navier–Stokes equations (1.2). The symmetry of the flow implies that statistics do not depend on the spanwise coordinate z (i.e. the flow is statistically homogeneous in that direction). The flow is studied once it has achieved a fully developed state, in which statistics are independent of time and of the streamwise coordinate x. The flow is therefore statistically stationary and is inhomogeneous only in the wall-normal direction. In particular, Eulerian single-point single-time statistics only depend on y, and the Eulerian mean velocity field writes $\overline{\boldsymbol{u}(\boldsymbol{x}, t)} = \overline{\boldsymbol{u}}(y)$. The notation $\overline{(\cdot)}$ represents an Eulerian average, that is, an ensemble average of a physical quantity over infinite repetitions of the flow, on a set of one or more fixed points in space $\{\boldsymbol{x}_i\}$ and time points $\{t_j\}$. Due to homogeneity and stationarity, this ensemble average can be replaced by an average over time and over the periodic directions x and z.

Mean velocity field As a consequence of flow symmetry, the spanwise mean velocity component $\overline{u_z}$ is zero. The same is true for the wall-normal component $\overline{u_y}$, as can be shown by ensemble-averaging the continuity equation (1.2a) along with the impermeability condition ($u_y = 0$) at the walls. Therefore, the mean velocity is expressed as

$$\overline{u_i}(y) = U(y)\delta_{ix}, \tag{1.17}$$

where $U(y)$ is the mean streamwise velocity and δ_{ij} is the Kronecker delta. The mean velocity field is zero at the walls due to no-slip conditions, and maximum at the channel centreline located at $y = h$.

External pressure gradient The externally applied pressure gradient $\boldsymbol{\nabla} p_0$ drives the flow in the channel. For convenience, we choose to include $\boldsymbol{\nabla} p_0$ in the forcing term of the Navier–Stokes equations as $\boldsymbol{f} = \boldsymbol{\nabla} p_0 / \rho$ [eq. (1.2b)]. With this choice of notation, the pressure field $p(\boldsymbol{x}, t)$ appearing in the momentum equation (1.2b) is effectively periodic and statistically homogeneous in x and z. By ensemble-averaging eq. (1.2b), it can be shown [137, p. 266] that, for the flow to be homogeneous in x, then p_0 must be necessarily independent of y. Then, its gradient can be written as $\boldsymbol{\nabla} p_0 = \frac{\mathrm{d}p_0}{\mathrm{d}x} \boldsymbol{e}_x = -G_p \boldsymbol{e}_x$ where $\boldsymbol{e}_x$ is the unit vector in the streamwise direction, and G_p is the constant magnitude of the external pressure gradient, which is positive for a flow moving on average in the positive x direction.

Energy injection and dissipation To the imposed mean pressure gradient is associated a steady energy injection into the large-scale flow, which corresponds to the work performed by the imposed pressure gradient. The mean kinetic energy injection rate (or *mean input power*) per unit mass is given by (see appendix B.1 for more details)

$$\Pi_{\text{in}} = \frac{G_p U_b}{\rho}, \tag{1.18}$$

where the *bulk velocity* is defined as

$$U_b = \frac{1}{2h} \int_0^{2h} U(y) \, \mathrm{d}y \,. \tag{1.19}$$

In a statistically stationary flow, the input power Π_{in} must be exactly compensated by the global kinetic energy dissipation rate per unit mass,

$$\varepsilon_b = \frac{1}{2h} \int_0^{2h} \varepsilon_T(y) \, \mathrm{d}y \,, \tag{1.20}$$

where the *total kinetic energy dissipation rate* is defined as

$$\varepsilon_T(y) = \nu \overline{\frac{\partial u_i}{\partial x_j} \frac{\partial u_i}{\partial x_j}}. \tag{1.21}$$

Here and in the rest of this document, repeated indices imply summation over the components x, y and z unless noted otherwise.

In high Reynolds number flows, most of the kinetic energy is dissipated by the turbulent fluctuations. The *turbulent kinetic energy dissipation rate* is similarly defined as

$$\varepsilon(y) = \nu \overline{\frac{\partial u_i'}{\partial x_j} \frac{\partial u_i'}{\partial x_j}}, \tag{1.22}$$

where primes denote a fluctuation from the Eulerian mean, $u_i'(\boldsymbol{x}, t) = u_i(\boldsymbol{x}, t) - \overline{u_i}(y)$. A comparison between total and turbulent dissipation rates in a turbulent channel flow is provided in appendix A.2 (fig. A.3a).

Centreline Reynolds number The Reynolds number in the channel can be defined based on the mean centreline velocity $U_0 = U(h)$,

$$Re = \frac{U_0 h}{\nu}. \tag{1.23}$$

The Reynolds number characterises the importance of inertia relative to viscous dissipation within the flow. These effects are respectively represented by the non-linear term $(\boldsymbol{u}\cdot\boldsymbol{\nabla})\boldsymbol{u}$ and the viscous term $\nu\nabla^2\boldsymbol{u}$ in the momentum equation (1.2b). At low Reynolds number, the flow is laminar and the fluid velocity is given by the plane Poiseuille flow solution to the Navier–Stokes equations,

$$u_i(\boldsymbol{x}) = U_0(1-\tilde{y}^2)\delta_{ix}, \tag{1.24}$$

with $\tilde{y} = (y-h)/h$ and $U_0 = G_p h^2/(2\rho\nu)$. Linear stability theory predicts that plane Poiseuille flow becomes unstable at $Re = 5772$ [124], meaning that above this threshold, infinitesimal flow perturbations are amplified and the flow eventually becomes turbulent. However, due to the non-linearity of the Navier–Stokes equations, finite-amplitude perturbations can induce transition to turbulence at much lower Reynolds numbers [99]. Recently, the global instability threshold above which self-sustained turbulence can persist has been estimated at $Re \approx 840$ [151, 183]. Slightly above this threshold, turbulence may coexist with laminar flow, for example in the form of localised turbulent spots [38]. Uniform turbulence, as opposed to laminar-turbulent coexistence, is only possible beyond a critical value of $Re \approx 1600$ [99].

Viscous scales To achieve global equilibrium of forces in a stationary channel flow, the force applied by the mean pressure gradient to accelerate the fluid must be compensated by the mean wall shear stress τ_w decelerating the fluid at the walls. This balance writes (see e.g. [96])

$$G_p = \frac{\tau_w}{h}, \tag{1.25}$$

where the mean wall shear stress is given by

$$\tau_w = \rho\nu \left.\frac{\mathrm{d}U}{\mathrm{d}y}\right|_{y=0}. \tag{1.26}$$

The mean wall shear stress τ_w and the viscosity ν are the most relevant parameters for describing the dynamics of the near-wall region in wall-bounded turbulence. It is therefore appropriate to rescale physical quantities by combinations of these two parameters. The relevant velocity scale near the wall is the *friction velocity*,

$$u_\tau = \sqrt{\frac{\tau_w}{\rho}}, \tag{1.27}$$

while the associated *viscous time* and *length scales* are respectively

$$\tau_\nu = \frac{\nu}{u_\tau^2} \qquad \text{and} \qquad \delta_\nu = \frac{\nu}{u_\tau}. \tag{1.28}$$

Throughout this work, the superscript + is used to indicate non-dimensional quantities normalised by the viscous scales defined above. Such a quantity is said to be given in *wall* (or *viscous*) *units*.

Friction Reynolds number As an alternative to the centreline Reynolds number Re, the *friction Reynolds number* can be defined from the viscous scales,

$$Re_\tau = \frac{u_\tau h}{\nu}. \tag{1.29}$$

The friction Reynolds number is more relevant than Re when discussing the near-wall dynamics of wall turbulence. Moreover, it allows for a comparison with other wall-bounded flows, where Re_τ is defined similarly. In pipe and boundary layer flows, h is replaced by the pipe radius R and the boundary layer thickness δ, respectively [167].

At the present time, the highest friction Reynolds number achieved by DNS of turbulent channel flow is $Re_\tau = 8000$ by Yamamoto and Tsuji [199], using high-order finite difference schemes with a $8640 \times 4096 \times 6144$ spatial grid resolution. Compared to pipe and spatially developing boundary-layer flows, the channel flow setting is particularly suitable for numerical studies due to the simplicity of its geometry, which (unlike pipe flow) can be represented naturally using a Cartesian reference frame. Moreover, the homogeneity of channel flows in the streamwise direction allows for periodic boundary conditions and thus Fourier decomposition of the velocity field in that direction. Homogeneity also increases the convergence rate of Eulerian statistics, as these can be computed from spatial averages in the streamwise direction, in addition to averages in the spanwise direction and in time.

In laboratory experiments, the situation of channel flow compared to other wall-bounded geometries is the opposite. Channel flow experiments are particularly challenging due to the need of (i) a long development region upstream of the measurement section, and (ii) a high aspect ratio between the channel spanwise width W and the wall-normal size $2h$ to ensure a statistically two-dimensional flow far from the spanwise walls [210]. The minimum required aspect ratio $W/(2h)$ has been estimated to be 7 [46, 112]. The largest Reynolds numbers achieved in channel flow experiments are $Re_\tau \approx 4000$ in Melbourne [112] and 4800 in Erlangen [209]. In this regard, higher Reynolds numbers can be achieved in other wall-bounded geometries such as pipe and boundary-layer flows. Some notable examples of circular pipe flow experiments capable of very high Reynolds numbers are the Princeton superpipe [72] and the CICLoPE facility in Bologna [123], which have respectively achieved air flows at $Re_\tau \approx 98\,000$ and $Re_\tau \approx 40\,000$, as well as the Hi-Reff facility in Japan [56] reaching up to $Re_\tau \approx 53\,000$ in a water pipe flow. As for boundary layers, some recent high-Reynolds number measurements include include the High-Reynolds-Number Boundary Layer Wind Tunnel

(HRNBLWT) in Melbourne [8] (up to $Re_\tau \approx 22\,800$), and the atmospheric surface layer measurement campaigns in the Surface Layer Turbulence and Environmental Science Test (SLTEST) in Utah's salt flats [74] (up to $Re_\tau \sim 6 \times 10^5$).

1.2.2 Scales of wall-bounded turbulence

Wall-bounded turbulent flows are classically described as being composed of two main regions that follow different scalings [102, 177]. Very close to the wall (for wall distances $y \ll h$), in the so-called *inner region*, viscous stress is important and even dominant, and the viscous length $\delta_\nu = \nu/u_\tau$ and friction velocity u_τ are the appropriate parameters for scaling flow quantities. Conversely, in the *outer region* sufficiently far from the wall ($y \gg \delta_\nu$), direct viscous effects become negligible (as in unbounded turbulent flows) and the appropriate characteristic length scale is the channel half-height h (or the boundary-layer thickness δ, in the case of flat-plate boundary layers). Classically, the characteristic velocity scale in the outer region is u_τ as in the inner layer, since u_τ determines the inner boundary condition for the outer flow [101]. However, there is currently no consensus on this choice, and other scales such as U_0 and $(U_0 - u_\tau)$ have also been proposed [80, 102].

The friction Reynolds number defined in eq. (1.29) can be written as the length scale ratio $Re_\tau = h/\delta_\nu$, and thus represents the separation between outer and inner scales in wall turbulence. Provided that this scale separation is sufficiently large, i.e. at high Reynolds numbers, an intermediate *overlap region* (also called the *logarithmic layer* due to the predicted shape of the mean velocity profile, as described in section 1.2.3) exists in the range $\delta_\nu \ll y \ll h$, connecting the inner and outer regions.

The above picture of scale separation is clearly reminiscent of the spectral structure of turbulence, in which viscous effects are negligible except at the smallest scales of motion (at which kinetic energy is dissipated), and an intermediate inertial range exists between the largest and the dissipative scales. In fact, in analogy to the turbulent energy cascade, the dynamics of the flow in the logarithmic region has been interpreted as a cascade of momentum towards the wall by a self-similar hierarchy of eddies [76]. The wall acts as a momentum sink, similar to the way the dissipative scales act as a sink of kinetic energy in the turbulent energy spectrum [177].

1.2.3 Mean velocity profile

The above picture of the different regions of wall turbulence has implications on the expected shape of the mean velocity profile $U(y)$ in each region.

In the inner region, the mean velocity profile only depends on the wall distance y and on the scaling parameters u_τ and δ_ν. Dimensional analysis then implies that

$$U^+ = f(y^+) \quad \text{for} \quad y \ll h, \tag{1.30}$$

where $U^+ = U/u_\tau$ and $y^+ = y/\delta_\nu$, and f is a universal function supposed independent of Reynolds number [57]. The inner region is usually divided into the *viscous sublayer*,

where the mean velocity profile is $U^+ = y^+$, and the *buffer layer*, where the profile is no longer linear. The viscous sublayer extends from the wall to about $y^+ = 5$. The buffer layer connects the viscous sublayer with the logarithmic layer.

In the outer region, the appropriate length scale is h, and the mean velocity profile is defined in terms of the velocity defect $U_0 - U$. The mean velocity profile then takes the form of the velocity-defect law,

$$U_0^+ - U^+ = g\left(\frac{y}{h}\right) \quad \text{for} \quad y \gg \delta_\nu. \tag{1.31}$$

The velocity profile in the logarithmic region is obtained by matching the asymptotic inner profile (1.30) when $y^+ \to \infty$, with the asymptotic outer profile (1.31) when $y/h \to 0$ [177, p. 154]. The result is the *logarithmic law of the wall*,

$$U^+ = \frac{1}{\kappa} \ln y^+ + B \quad \text{for} \quad \delta_\nu \ll y \ll h, \tag{1.32}$$

where κ is the von Kármán constant and B is called the additive constant.

Both κ and B are expected to be universal constants. However, it is well accepted that their values actually depend on the type of flow [101, 120]. In channel flow experiments at Re_τ up to 4000, Monty [112] estimated $\kappa = 0.389$ and $B = 4.23$. These results are consistent with the more recent channel flow DNS results by Lee and Moser [94] at $Re_\tau = 5200$ and by Yamamoto and Tsuji [199] at $Re_\tau = 8000$, who respectively obtained $\kappa = 0.384$ and 0.387, and $B = 4.27$ and 4.21. At lower Reynolds numbers, a distinctive logarithmic region is not clearly identified due to the weaker scale separation between δ_ν and h, and the estimated values of κ and B are larger. For instance, at $Re_\tau \approx 1000$, available numerical and experimental results suggest that $\kappa \approx 0.4$ and $B \approx 5$ in channel flows [120]. The extent of the logarithmic layer, where the mean velocity profile approximately has the form (1.32), is classically estimated as $30 < y^+ < 0.15\,Re_\tau$, and therefore, to observe a decade of logarithmic velocity profile, $Re_\tau > 2000$ is required [167].

A mean velocity profile measured in a boundary layer experiment at $Re_\tau = 20\,000$ in the Melbourne wind tunnel [150] is plotted in fig. 1.9. Also shown is the profile obtained from our channel flow DNS at $Re_\tau = 1440$ ($Re \approx 33\,800$ based on the centreline velocity U_0), described later in section 2.1.4. As a result of the large Reynolds number, two decades of logarithmic layer are observed in the experimental profile. This can be contrasted with the moderate Reynolds number of our DNS, in which slightly less than a decade is expected according to the above stated criterion (since $0.15\,Re_\tau = 216 < 300$).

The experimental profile in fig. 1.9 starts at $y^+ \approx 10$, and data closer to the wall is seemingly unavailable. This is explained by the high Reynolds number of the experiment and the technical limitations of the measurement apparatus. As the Reynolds number increases, the viscous length δ_ν becomes smaller. In the conditions of the experiment, the viscous length is only 17.2 µm at $Re_\tau = 20\,000$ [150], and thus the whole inner region is about half a millimetre. Therefore, very high resolution probes

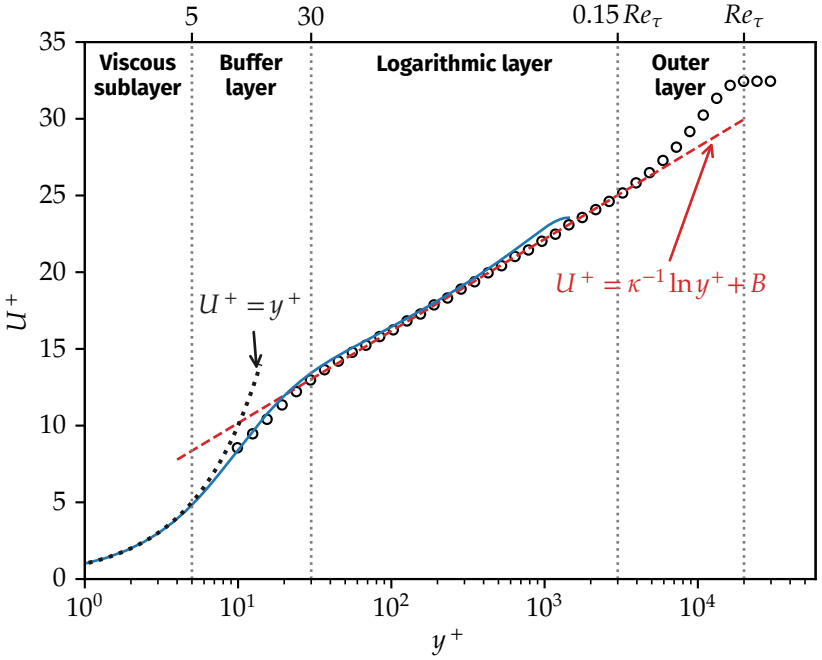

Figure 1.9. Mean velocity profile scaled in wall units. Experimental data (circles) is from a flat-plate boundary layer flow at $Re_\tau = 20\,000$ by Samie et al. [150]. Solid line, channel flow DNS at $Re_\tau = 1440$. Dashed line, logarithmic law (1.32) with parameters fitting the experimental data, $\kappa = 0.384$ and $B = 4.17$ [150]. Dotted line, linear profile $U^+ = y^+$. The vertical dotted lines delimit the different regions of the flow at the Reynolds number of the experimental data.

are needed to measure the flow in the near-wall region. Namely, they use nanoscale thermal anemometry probes specifically manufactured for the measurement of high Reynolds number wall-bounded flows [184].

1.2.4 Coherent structures

Thus far we have briefly introduced wall-bounded flows in a statistical sense, namely in terms of the most basic statistical quantity which is the mean velocity profile $U(y)$. This statistical approach is appropriate considering the random nature of turbulent flows. In wall turbulence, an alternative *structural* description of wall-bounded flows has also caught much interest. This description views the flow as a collection of interacting *organised motions* or *coherent structures* that greatly contribute to the flow dynamics. Taken to the extreme, the structural view can be applied as an attempt to describe a wall-bounded turbulent flow in a deterministic manner [77].

The concept of a coherent structure is controversial since it has no precise definition, although it is clear that their study has helped improve the understanding of wall turbulence [101]. Coherent structures can be roughly defined as turbulent motions with a spatial and temporal persistence, and which contribute importantly to the transport of momentum, mass and heat [101].

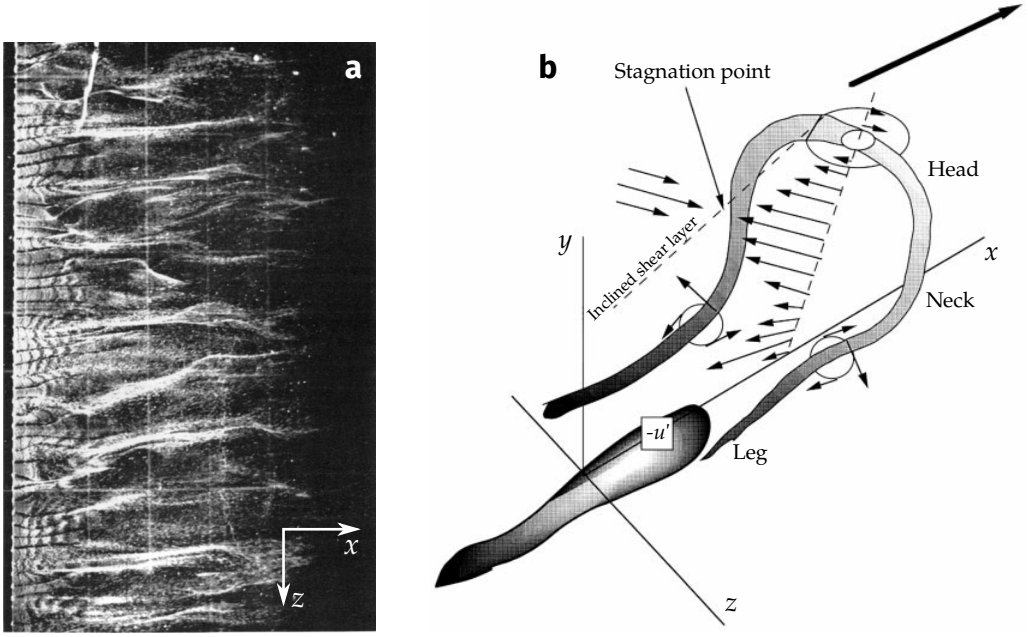

Figure 1.10. Coherent motions in wall turbulence. (a) Visualisation of low-speed streaks in boundary layer on a wall-parallel plane at $y^+ = 4.3$ using hydrogen bubbles generated along an upstream wire (left of the image). Reproduced from Kline et al. [82]. (b) Conceptual model of a wall-attached hairpin vortex and its induced motion. Reproduced from Adrian et al. [2].

Smits et al. [167] classify coherent structures into four main types. The first two are near-wall streaks and hairpin vortices, which have been known to exist and have been studied for several decades. The other two, large scale motions (LSMs) and very large scale motions (VLSMs), have been observed more recently as they are characteristic of high Reynolds number wall turbulence, and due to their significant size, their study requires large spatial observation windows and simulation domains.

Near-wall streaks One of the first experimental observations of coherent structures in wall turbulence was by Kline et al. [82], who used small hydrogen bubbles to visualise low-speed streaks in a boundary layer very near the wall. Figure 1.10a shows one of their observations in the viscous sublayer. It can be seen that despite the dominance of viscous shear in that region, the flow there is not laminar, but characterised by spatial fluctuations and unsteadiness. The concentration of bubbles in the form of elongated streaks indicates the existence of a fluctuating spanwise velocity u_z that displaces the bubbles uniformly generated along an upstream wire. The streaks were identified by Kline et al. as regions of low-speed streamwise flow relative to the mean velocity (i.e. of negative streamwise fluctuation u'_x). Their average spanwise spacing was found to be $\Delta z^+ \approx 100$ in the buffer layer. Subsequent studies revealed that this value is independent of Reynolds number and of the type of wall-bounded flow [4, 170], although it increases with wall distance away from the viscous sublayer [102].

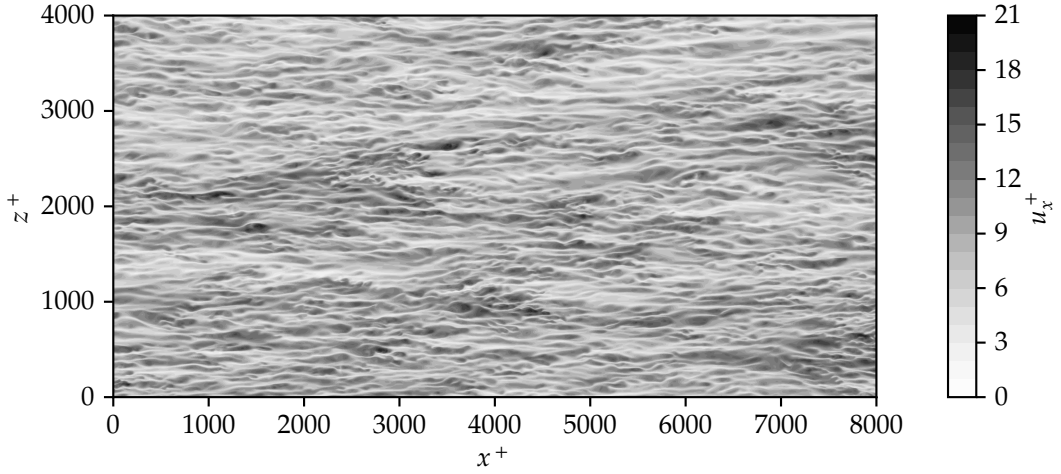

Figure 1.11. Instantaneous streamwise velocity at $y^+ = 9.7$ obtained from channel flow DNS at $Re_\tau = 1440$.

Similar near-wall streaks in our channel flow simulations, which display roughly the same spanwise spacing $\Delta z^+ \approx 100$, are visible in the instantaneous streamwise velocity field shown in fig. 1.11.

Near-wall streaks have been associated to *bursting* events, which are described by streaks oscillating in the wall-normal direction with increasing intensity until they are lifted away from the wall and eventually break down into smaller-scale motions [4, 137]. Bursting events have been further characterised as a sequence of increasingly stronger *ejections* of slow fluid away from the wall, as opposed to individual ejection events [4]. To satisfy continuity, ejections must be necessarily compensated by motion of fluid towards the wall [137], a mechanism referred to as *sweeps*. Since the average flow is faster away from the wall, sweeps most often bring relatively fast fluid towards the wall, thus locally increasing the streamwise velocity gradient and wall shear stress.

Both sweeps and ejections have been linked to the action of *quasi-streamwise vortices* (QSVs), which are elongated vortical structures almost aligned with the streamwise coordinate, but slightly tilted in the wall-normal direction at a positive angle. Ejections are induced by pairs of counter-rotating QSVs on either side of a low-speed streak. QSVs are typically found in the buffer layer and their average diameter is of 40 viscous units, that is, comparable to the size of the buffer region. As noted by Marusic and Adrian [102], this similarity is no coincidence as QSVs dominate the dynamics of the buffer layer and determine its average structure. The streamwise length of the QSVs greatly varies from about 100 to 10 000 viscous units. The characteristic length of the induced near-wall streaks is of the order of 1000 viscous units [130], which coincides with the peak of the spectrum of the streamwise velocity fluctuations (u'_x) along the streamwise direction in the buffer layer [102].

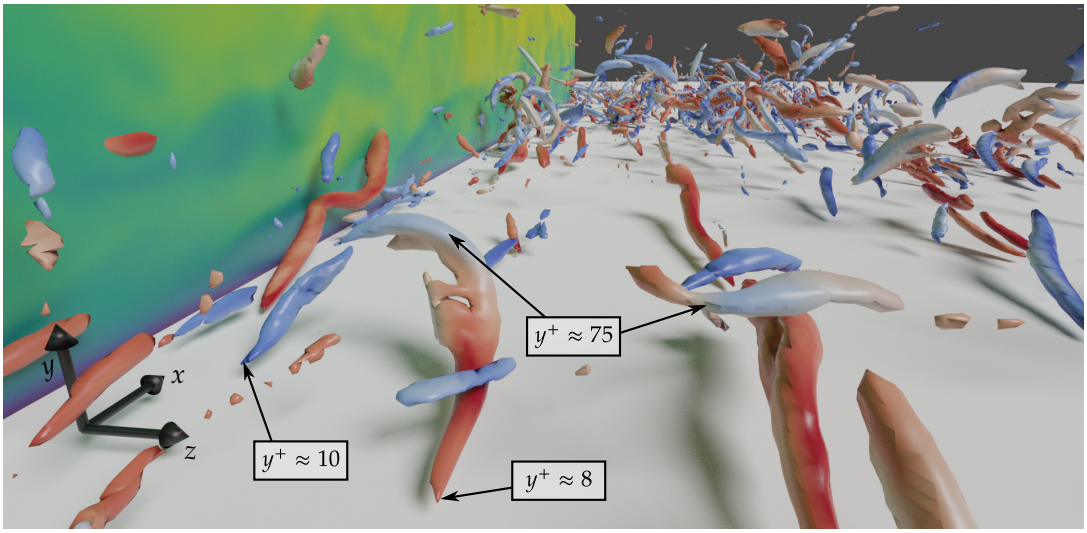

Figure 1.12. Visualisation of near-wall vortices in channel flow DNS at $Re_\tau = 1440$. Vortices are identified using isocontours of the second invariant of the velocity gradient tensor at the level $Q^+ = 0.05$ [73]. Isocontours are coloured by the streamwise vorticity (red, $\omega_x > 0$; blue, $\omega_x < 0$). The plane on the left is an instantaneous slice of the streamwise velocity field. Rendered with Blender (`www.blender.org`).

Hairpin vortices Away from the buffer layer, the most significant coherent motions are *hairpin vortices* such as the one sketched in fig. 1.10b. These are formed by pairs of QSVs that lift up from the wall and merge forming a loop [102]. Hence QSVs are often the legs of hairpin vortices, and represent their extension into the inner region of the flow. The head of a hairpin vortex is typically located above $y^+ \approx 100$. Remarkably, the hairpin vortex cross-section size has been found to scale with the Kolmogorov length scale η, which increases with wall distance (see e.g. fig. A.3a in appendix A.2). Concretely, the typical diameter of the legs and of the head section is close to 16η, a value that presents little variation with wall distance [62]. This is similar to the case of vortex filaments in HIT, whose diameter distribution scales with η [78]. The existence of hairpin vortices has been a subject of long controversy, although relatively recent works such as the flat-plate boundary layer DNS of Wu and Moin [195] seem to confirm their ubiquitous presence in wall-bounded turbulence. A collection of near-wall vortical motions from our DNS are visualised in fig. 1.12 using the Q criterion [73], which identifies zones of strongly rotating fluid. Besides some QSVs with negative and positive streamwise vorticity very near the wall, a broken hairpin vortex is visible in the foreground (centre left), as well as some vortices elongated along the spanwise direction (centre right) which may correspond to heads of hairpin vortices.

As sketched in fig. 1.10b, hairpin vortices induce a fluctuating flow around them. In the buffer layer, the hairpin vortex is a pair of counter-rotating QSVs which, as mentioned above, induces an ejection of the slow fluid between them. As it extends into the logarithmic region, the hairpin vortex is inclined by about 45° relative to the

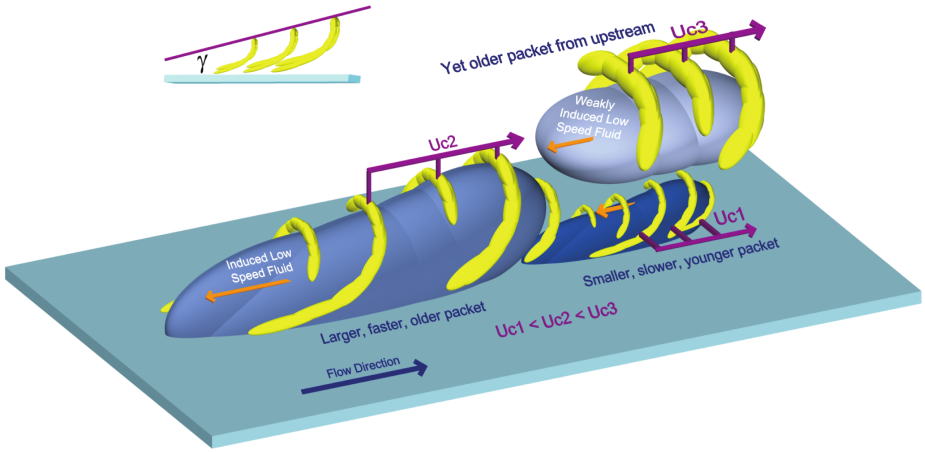

Figure 1.13. Conceptual model of wall-attached hairpin vortex packets proposed by Adrian et al. [2]. Reproduced from Adrian [4].

wall. The whole loop of the vortex, including the neck and the head, induce a negative fluctuating velocity field below the vortex head.

Large scale motions There has been evidence in the last few decades that hairpin vortices tend to group in streamwise succession, effectively forming hairpin vortex *packets* (HVPs) that travel at the same convective velocity [4, 167]. These packets are a predominant form of large scale motion, and have streamwise sizes of up to 3δ (in channels, the boundary layer thickness δ is comparable to the channel half-width h). HVPs extend deeply into the logarithmic layer and sometimes reach the outer region of the flow. Due to the accumulation of their individual effects, they can induce large regions of coherent velocity referred to as uniform momentum zones [4]. The observations of HVPs are summarised by the conceptual model in fig. 1.13, which depicts three different packets moving at different convective velocities, each consisting of several hairpin vortices, and each inducing a low-speed region beneath their structure.

Very large scale motions In the logarithmic layer, it has been observed that the streamwise spectrum of u'_x presents two peaks, one associated to LSMs (of size $\mathcal{O}(\delta)$), and the other associated to larger structures of size $\mathcal{O}(10\delta)$ [10, 61] classified as VLSMs. This has been reproduced in the three canonical wall-bounded flows. In the particular case of channel flow, Monty et al. [111] observed long meandering structures with streamwise lengths of up to about $25h$ at $Re_\tau \approx 3200$ (fig. 1.14). As in many experiments, their observations were obtained using fixed hot-wire probes and thus rely on Taylor's frozen turbulence hypothesis, in which velocity time series are converted into spatial data by assuming that velocity fluctuations u'_i are much weaker than the mean velocity U [137]. Taylor's hypothesis loses accuracy as the apparent size of the detected spatial structures increases, casting some doubt on the observed VLSMs [101].

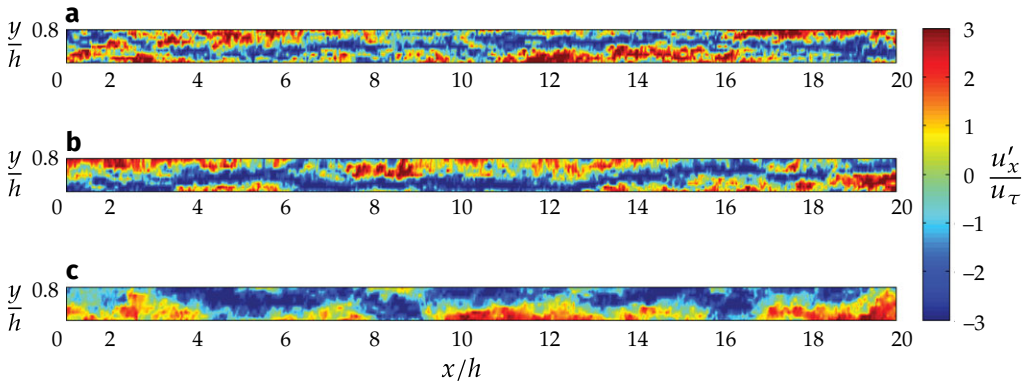

Figure 1.14. Visualisation of VLSMs in turbulent channel flow at $Re_\tau = 3178$. Colours represent streamwise velocity fluctuations u'_x scaled in wall units. Wall distances are (a) $y = 0.08h$, (b) $y = 0.14h$ and (c) $y = 0.56h$. Reproduced from Monty et al. [111].

However, the results are consistent with other studies. For instance, from channel flow DNS at $Re_\tau \approx 550$ in a very large domain ($L_x = 60\pi h$, $L_z = 6\pi h$), Lozano-Durán and Jiménez [95] showed that non-negligible amounts of turbulent kinetic energy were associated to structures of streamwise wave length $\lambda_x \approx 100h$, in support of the existence of very large structures in channel flow turbulence.

1.3 Lagrangian investigations of wall turbulence

The objective of the present study is to describe a wall-bounded turbulent flow from a Lagrangian perspective. This section reviews relevant investigations that have been performed on this issue in the past. We focus on studies concerning tracer particles, while inertial particle investigations are beyond the scope of this review. Chronologically, the first Lagrangian investigations of wall turbulence were performed in channel flows using numerical simulations. A selection of these studies are introduced in section 1.3.1. To our knowledge, besides the recent work of Stelzenmuller [173] performed in parallel to our study (their work is partially presented in chapter 3), experimental Lagrangian studies of turbulent channel flows have not been attempted. This is not the case in pipe and boundary layer flows, where the few existent Lagrangian studies are predominantly experimental. Investigations in these two geometries are briefly reviewed in section 1.3.2.

1.3.1 Channel flow

An early numerical study of the Lagrangian statistics of wall-bounded flows was performed by Deardorff and Peskin [47] in 1970 using large eddy simulation (LES) in a channel flow geometry. Due to the computational resources available at the time, they tracked 480 tracer particles on a numerical grid of resolution $24 \times 14 \times 20$. They discussed Lagrangian velocity auto-correlations, as well as one- and two-particle dis-

persion statistics. In particular, they observed that mean shear greatly accelerates the relative separation of particle pairs. Moreover, they found that two-particle Lagrangian velocity correlations were more persistent than single-particle ones.

Channel flow DNS became feasible much later, with the first simulations reported by Kim et al. [81] in 1987 at $Re_\tau = 180$. Soon after, Bernard et al. [20] considered the Lagrangian trajectories in channel flow DNS at nearly the same Reynolds number. They followed a mostly graphical approach, in which they related images of Lagrangian paths, tracked over relatively short times, with sweeps and ejections near the wall. Later, Lagrangian tracking of fluid particles in turbulent channel flow was performed by Kontomaris et al. [85] at a low Reynolds number, $Re_b = 2hU_b/\nu \approx 4500$ based on the bulk velocity U_b. They mainly focused on the numerical methods, but also considered the mean-square dispersion of tracers $\langle \delta x_i'^2 \rangle(\tau)$ released from the channel centre. They compared their results to Taylor's theory for isotropic turbulence predicting $\langle \delta x_i'^2 \rangle(\tau) \sim \tau$ at asymptotically long times [eq. (1.6)]. Here, $\delta x_i' = \delta x_i - \langle \delta x_i \rangle$ is the displacement fluctuation relative to the displacement averaged among all particles, $\langle \delta x_i \rangle$. Kontomaris et al. found that only the spanwise displacement δz asymptotically follows Taylor's prediction. In the streamwise direction, the mean-square dispersion grows much faster due to the effect of mean shear. Their result is qualitatively consistent with the fast growth of the mean-square dispersion predicted in HSF [eq. (1.16)]. In the wall-normal direction, the authors found that the mean-square dispersion slows down at long times due to the walls limiting the motion of tracers in that direction.

With the objective of characterising the inhomogeneity of Lagrangian statistics in turbulent channel flows, Choi et al. [41] tracked fluid particles in a DNS at $Re_\tau = 200$ and 400. They computed Lagrangian auto-correlations of velocity and acceleration components. Near the wall, they observed that the streamwise velocity decorrelates more slowly along Lagrangian paths, followed by the spanwise and the wall-normal components. As in HIT [206], the acceleration components decorrelate over short time lags $\tau \approx 2\tau_\eta$, with the exception of the streamwise acceleration in the inner region where it presented a much longer correlation time. The authors associated the observed near-wall behaviour to the effect of quasi-streamwise vortices. Choi et al. also considered the mean-square displacement $\langle \delta x_i^2 \rangle$ of tracers released from different channel locations. In contradiction with theoretical predictions in HSF, the authors found that $\langle \delta x^2 \rangle$ grows asymptotically as τ^2 and not as τ^3, concluding that the effect of mean shear on dispersion is minimal. In fact, the analogy of channel flow with HSF is only reasonable as long as tracers stay within one half of the domain. Once tracers cross the channel centreline, the direction of mean shear is reversed and the asymptotic behaviour differs from HSF. Finally, Choi et al. examined the second-order Lagrangian velocity structure function $D_2(\tau)$ [eq. (1.9)] associated to the three velocity components, from which they estimated the supposedly universal constants a_0 and C_0. The normalised acceleration variance a_0 was only weakly anisotropic and, consistently with HIT, it increased with the local Taylor-scale Reynolds number Re_λ. Meanwhile, the D_2 curves computed at different wall distances did not display the linear scaling predicted by K41 theory in the inertial range [eq. (1.10)], which can be explained by the lack of scale separation at their Reynolds number.

Lagrangian acceleration As an extension to the work of Choi et al. [41], Lee et al. [93] performed channel flow DNS at Re_τ between 100 and 400 focusing on the behaviour of the acceleration near the walls. The authors observed that, as in HIT, the Lagrangian acceleration is highly intermittent. This was quantified by the acceleration flatness, which was close to 15 away from the viscous sublayer. Perhaps surprisingly, this value changed little with Reynolds number, in contrast with HIT where the flatness shows strong Reynolds number dependence especially for low values of Re_λ (see inset of fig. 1.6a). Lee et al. further linked the intermittency of acceleration near the wall to the action of quasi-streamwise vortices and hairpin vortices inducing helical particle motions associated to strong centripetal accelerations, in analogy to the effect of vortex filaments in HIT.

The study of acceleration in near-wall turbulence was later extended by Yeo et al. [202] using channel flow DNS at Re_τ between 180 and 600. Their approach was purely Eulerian, as their statistics were computed from the acceleration field obtained as

$$\boldsymbol{a} = -\frac{1}{\rho}\boldsymbol{\nabla} p + \nu\nabla^2\boldsymbol{u} = \boldsymbol{a}^I + \boldsymbol{a}^S, \tag{1.33}$$

where $\boldsymbol{a}^I$ and $\boldsymbol{a}^S$ are respectively called the irrotational and the solenoidal acceleration. In isotropic turbulence, the solenoidal component is generally negligible and the acceleration is dominated by $\boldsymbol{a}^I$ [64, 188]. As shown by Yeo et al. [202], the solenoidal term $\boldsymbol{a}^S$ becomes important in the viscous sublayer, where it has a larger variance than $\boldsymbol{a}^I$. However, the intermittency of the acceleration in that region, where the flatness factor exceeds 100, is still dominated by extreme values of the irrotational term $\boldsymbol{a}^I$. The authors associated the strong intermittency in the viscous sublayer to the effect of vortical structures near the wall.

Dispersion and stochastic models Besides the analysis of Kontomaris et al. [85] and Choi et al. [41] discussed above, other authors have considered the dispersion of tracers in turbulent channel flows using DNS, especially in relation with the application of Lagrangian stochastic models to predict dispersion statistics. For instance, Mito and Hanratty [105] incorporated spatially-varying Lagrangian time scales obtained from a channel flow DNS to a Langevin equation adapted to inhomogeneous turbulence. The proposed model was compared to channel flow DNS at $Re_\tau = 150$ and 300. For tracers released from different wall-normal locations, the model accurately reproduced the single-particle dispersion PDFs evaluated at later times, except for particles released very close to the wall.

More recently, Kuerten and Brouwers [88] performed channel flow DNS at $Re_\tau = 950$. They computed Lagrangian velocity and wall-normal tracer dispersion statistics as a function of initial wall distance y_0, and compared their results to an inhomogeneous Langevin model they proposed. The model used as input parameters Eulerian quantities computed from their DNS, namely the dissipation profile $\varepsilon(y)$, the mean velocity profile $U(y)$ and the Reynolds stress tensor $\overline{u_i' u_j'}(y)$, as well as the Kolmogorov constant C_0 which they chose as equal to 6 to fit their DNS results. Near the wall ($y_0^+ < 100$),

significant deviation was observed between computed and modelled velocity auto-correlation functions, especially for the streamwise velocity component. The authors attributed this difference to the limited Reynolds number of the DNS, which did not allow for a large separation of scales required for the application of Kolmogorov's hypothesis (which are implied in their stochastic model). Regarding tracer diffusion, the model underpredicted the wall-normal mean-square dispersion $\langle \delta y'^2 \rangle$ close to the wall and overpredicted it near the channel centre. The authors tracked fluid particles over a relative short time $T^+ = 190$, shorter than the time required for Lagrangian velocity auto-correlations to decay to zero. As a consequence, they were unable to characterise the long-time dispersion limit from their DNS results.

Particle pair dispersion As mentioned above, the relative dispersion of particle pairs in channel flow was considered in the early work of Deardorff and Peskin [47] using LES, where they showed that mean shear greatly enhances the relative separation of particle pairs in the streamwise direction. Concretely, they observed that the streamwise mean-square particle separation $\langle D_x^2 \rangle$ (where $\boldsymbol{D} = \boldsymbol{x}^B - \boldsymbol{x}^A$ is the separation vector between two particles) grew approximately as τ^3 at long times. They attempted to relate this observation to Richardson's law [146], which predicts $\langle \boldsymbol{D}^2 \rangle \sim \varepsilon \tau^3$ in turbulent flows (see section 5.1.1 for details), by arguing that mean shear generates dissipation.

The feasibility of DNS in the last few decades has facilitated the study of relative dispersion of tracer pairs in turbulent flows. However, relevant investigations in channel flows (and in wall-bounded flows in general) are to our knowledge almost non-existent. In this context, we can only cite the relatively recent work of Pitton et al. [134], who analysed the relative dispersion of tracers and heavy inertial particles in a channel flow DNS at $Re_\tau = 150$. Their work, as well as the relevant DNS work of Shen and Yeung [165] in HSF, is discussed in more detail in section 5.1.2.

1.3.2 Pipe and boundary layer flows

The initial Lagrangian investigations of wall turbulence were performed using numerical simulations of turbulent channel flows, as described above. The other two canonical wall-bounded flows have been considered in later years. In a turbulent pipe flow, Walpot et al. [192] computed Lagrangian velocity auto- and cross-correlations using both particle-tracking velocimetry (PTV) and DNS, with the aim of determining the drift tensor coefficients appearing in an anisotropic variant of the Langevin equation (1.7). To estimate the value of the Kolmogorov constant C_0, they also considered the second-order velocity structure functions associated to each velocity component. They found that C_0 decreases with wall distance and depends on the considered velocity component, which they attributed to their relatively low Reynolds number, $Re_b = U_b D/\nu \leq 10\,300$ based on the bulk velocity U_b and the pipe diameter D. In the same experimental apparatus and at the same Reynolds number, Oliveira et al. [122] considered Lagrangian velocity and acceleration correlations for tracers and inertial particles. They found that the acceleration of inertial particles decorrelated more slowly

than that of fluid tracers, while the latter present a decorrelation time comparable to the Kolmogorov time scale τ_η.

Lagrangian properties of turbulent boundary layers have also been studied experimentally. Although it concerns inertial particles, it is worth mentioning the work of Gerashchenko et al. [58] due to its significance. They performed PTV to investigate the effects of mean shear on the acceleration statistics of heavy inertial particles in a flat-plate boundary layer. The authors measured two components of the particle trajectories using a single high-speed camera that moved at the mean flow velocity. They reported acceleration PDFs and related acceleration moments, and found that close to the wall, the acceleration mean and variance are larger in magnitude, and the acceleration PDFs become more skewed and narrower. The latter observation was attributed to the increasing Stokes number and mean shear as the wall is approached. A few years later, Schröder et al. [162] performed 3D PTV using tracer particles, combined with time-resolved tomographic PIV in a turbulent boundary layer at $Re_\tau \approx 800$. This enabled the measurement of three-dimensional Lagrangian and Eulerian fields. They observed that Lagrangian acceleration PDFs in the logarithmic region of the flow are long-tailed and almost symmetric, with slight differences observed among acceleration components. More recently, Schröder et al. [163] applied the novel Shake-The-Box PTV technique [160], which allows for higher particle seeding densities, to a boundary layer flow at $Re_\tau = 929$. Owing to the high number of seeding particles, they were able to reconstruct the Eulerian velocity field and near-wall coherent structures from Lagrangian particle data.

1.4 Objectives and outline

Some fundamental Lagrangian properties of turbulent flows are introduced in section 1.1, mainly focusing on the case of homogeneous isotropic turbulence. Then, a short overview of wall-bounded turbulence is given in section 1.2, highlighting some of the current questions which revolve mostly around high Reynolds number effects in wall-bounded flows. This overview is presented from a fundamentally Eulerian perspective, in coherence with the vast majority of the relevant studies available on the subject. In section 1.3, some previous attempts to link the Lagrangian description with wall-bounded turbulence are presented.

The aim of the present work is to apply the Lagrangian framework to the description of a moderate Reynolds number wall-bounded turbulent flow. Specifically, a channel flow geometry is chosen for its simplicity from a numerical simulation standpoint, and also due to the availability of Lagrangian data from channel flow experiments that were performed in parallel to this work (the experimental setup is described in section 3.1). A moderate friction Reynolds number matching that of the experiments, $Re_\tau = 1440$, is chosen for the ensemble of the results presented in this thesis. In light of the discussion in section 1.1.1, we believe that the Lagrangian description can complement the more usual Eulerian description of wall-bounded turbulent flows and contribute to a better understanding of their dynamics. In particular, it can provide

an alternative characterisation of the coherent motions introduced in section 1.2.4, as well as improving the understanding of the dispersive properties of wall turbulence. Furthermore, it can provide necessary input data for existing Lagrangian stochastic models such as those introduced in section 1.1.3.

The higher Reynolds of the present investigation compared to the Lagrangian studies referenced in section 1.3 can lead to a better understanding of highly turbulent wall-bounded flows. At this Reynolds number, a larger scale separation between inner and outer motions of the wall-bounded flow is available. As a consequence, a clear logarithmic region that is absent in low Reynolds number flows begins to appear (as seen in fig. 1.9). In particular, a larger region of the flow is dominated by mean shear, which is expected to have an impact on dispersion statistics in the channel.

Another aspect of wall-bounded turbulence that has remained almost unexplored until now is the backwards in time Lagrangian dynamics. That is, the past behaviour of fluid particles given a chosen *final* condition at a reference time t_0 (which by abuse of language we refer to as the *initial* time). As an example illustrating the importance of such an effort, the backward dispersion of particle pairs is relevant to describe turbulent mixing phenomena, since it concerns the coalescence of trajectories originating from different locations [158]. A fraction of the present study is devoted to characterise the difference between forwards and backwards in time Lagrangian statistics in wall turbulence.

The numerical approach applied in this work is described in chapter 2, where the pseudo-spectral channel flow DNS method and the Lagrangian particle tracking algorithms are detailed and validated. Lagrangian acceleration statistics from channel flow experiments and from our DNS are presented in chapter 3, and contrasted to previously existent studies in isotropic turbulence and in turbulent channel flows at lower Reynolds numbers. In chapter 4, we present statistics of single-tracer dispersion in channel flows focusing on the temporal asymmetry of dispersion statistics. These results are extended to statistics of relative dispersion of tracer pairs in chapter 5. Finally, general conclusions and perspectives for future investigations are given in chapter 6.

As a final remark, the present work is limited to the dynamics of ideal Lagrangian tracers in wall turbulence. The study of inertial particles [9, 180, 191], characterised by a finite size and often by a density different to that of the fluid, is beyond the scope of this work. Nevertheless, an important motivation for future work is to extend the results presented in the following chapters to the case of inertial particles. In this context, collaborative work has resulted in a publication on the acceleration dynamics of elongated spheroidal particles in moderate Reynolds number channel flow turbulence [127].

2 Numerical methods

Lagrangian aspects of wall-bounded turbulence are studied in this work by means of turbulent channel flow direct numerical simulation (DNS) combined with Lagrangian particle tracking. This chapter introduces the numerical methods that are employed to solve the governing equations of the fluid flow, followed by a presentation of the Lagrangian particle tracking algorithms.

In section 2.1, the pseudo-spectral method used to numerically solve the incompressible Navier–Stokes equations and its application to channel flow are first described (sections 2.1.1 and 2.1.2). The solver implementation in terms of a massively parallel DNS code is then presented (section 2.1.3). The simulation parameters used in this work are then introduced, and Eulerian velocity and acceleration statistics are validated in the case of channel flow simulations at $Re_\tau = 1440$ (section 2.1.4).

Section 2.2 describes the Lagrangian particle tracking algorithms, starting with the equations governing the fluid particle dynamics and their temporal discretisation (section 2.2.1). Then, different interpolation schemes for evaluating Eulerian fields at the particle positions are assessed, and a choice is made according to accuracy and efficiency considerations (section 2.2.2). This is followed by details on the implementation of the particle tracking algorithms within the parallel solver (section 2.2.3). Some resulting Lagrangian statistics are validated against their equivalent Eulerian counterparts (section 2.2.4).

Finally, section 2.3 is devoted to general conclusions on the presented numerical methods.

2.1 Direct numerical simulations

The incompressible Navier–Stokes equations (1.2) are resolved in an infinite channel geometry by DNS using NadiaSpectral,[1] an in-house C++ code developed by Marc Buffat at the Laboratoire de Mécanique des Fluides et d'Acoustique (LMFA) [35]. In this section, the mathematical formulation of the channel flow DNS approach is presented. This is followed by a description of its implementation and the parallelisation strategy used to efficiently solve the resulting discrete system in high-performance computing clusters. The physical and numerical parameters used throughout this work to numerically solve the Navier–Stokes equations are then introduced. The solver and the choice of parameters are validated by comparison of Eulerian velocity and acceleration statistics against DNS results found in the literature.

[1] For a description, examples, and relevant publications, see https://perso.univ-lyon1.fr/marc.buffat/NadiaSpectral/index.html.

2.1.1 General aspects of spectral methods

Spectral and pseudo-spectral methods are known for their high accuracy. For well-behaved solutions, e.g. in the absence of discontinuities, the error of a spectral method decreases exponentially with the number of spatial degrees of freedom (as N^{-N}, where N is the number of degrees of freedom). This is sometimes referred to as the *exponential convergence* of spectral methods [31]. In comparison, finite difference methods are characterised by an algebraic convergence, which is asymptotically much slower than for spectral methods. For instance, second-order finite difference schemes are characterised by an error that decreases as N^{-2}. Such second-order schemes are still used (see [133] for a recent example of a high Reynolds number channel flow DNS). More interestingly for practical problems where high accuracy is not required, the number of degrees of freedom needed in a 3D spectral simulation to obtain a moderately accurate solution is typically an order of magnitude lower than in finite difference methods [31, 37, 107], resulting in a significant reduction of memory requirements.

In a spectral method, the solution to the partial differential equation

$$Hu(x) = f(x) \quad \text{for } x \in \Omega, \tag{2.1}$$

where H is a differential operator, is approximated as a weighted sum of basis functions,

$$\tilde{u}(x) = \sum_{n=0}^{N} a_n u_n(x), \tag{2.2}$$

where a_n are the weights or *spectral coefficients*. The basis (or *trial*) functions u_n are global in the sense that they are defined over the entire spatial domain, and are infinitely differentiable. In contrast, finite difference methods are expressed in terms of local basis functions, typically low-order piecewise polynomials. The goal of a spectral method is to determine the coefficients a_n that, according to some criterion, best match the exact solution of the governing equations (2.1). This requirement is typically expressed as an optimisation problem, in which the optimal coefficients are those that minimise the residual

$$R(x; \boldsymbol{a}) = H\tilde{u}(x) - f(x), \tag{2.3}$$

where $\boldsymbol{a} = [a_0 \; a_1 \; \cdots \; a_N]^T$ is the vector of spectral coefficients.

Most strategies for minimising the residual may be written in terms of the method of mean weighted residuals (MWR) [53], in which $N+1$ equations of the form

$$\langle \phi_i, R \rangle = 0, \quad i = 0, 1, \ldots, N \tag{2.4}$$

need to be simultaneously satisfied [31]. The functions $\phi_i(x)$ are called *test* functions, while the inner product between two complex functions f and g is defined by

$$\langle f, g \rangle = \int_\Omega f(x)\, g^*(x)\, w(x)\, \mathrm{d}x\,, \tag{2.5}$$

with $w(x)$ a non-negative weight function, and g^* the complex conjugate of g. Spectral

methods are usually classified according to the choice of test functions. Canuto et al. [37] identify three families of spectral methods:

- in **collocation methods** (also called **pseudo-spectral methods**) the governing equations are satisfied exactly on a chosen set of *collocation* points $\{x_i\}$ (or equivalently, the residual is zero at those points). In this case, the test functions are given by the Dirac delta function centred at each of the collocation points, $\phi_i(x) = \delta(x - x_i)$;
- in **Galerkin methods**, the test functions are the same as the trial functions, $\phi_i(x) = u_i(x)$, and they individually satisfy the boundary conditions. In the more general case where trial and test functions differ, the method is said to be of **Petrov–Galerkin** type;
- **Tau methods** are similar to Galerkin methods, except that test functions do not need to satisfy the boundary conditions of the problem. Therefore, boundary conditions must be enforced by an additional set of equations.

Generally, the set of trial functions u_n is chosen to be an orthogonal basis with respect to the inner product (2.5), i.e.

$$\langle u_m, u_n \rangle = \Phi_n^2 \delta_{mn}, \tag{2.6}$$

where the Φ_n are normalisation constants and δ is the Kronecker delta function. When the trial functions are orthogonal, the spectral coefficient associated to a given mode u_n can be simply evaluated as

$$a_n = \langle u_n, \tilde{u} \rangle / \langle u_n, u_n \rangle = \langle u_n, \tilde{u} \rangle / \Phi_n^2. \tag{2.7}$$

The system of equations (2.4) obtained from the MWR method establishes that the approximation $\tilde{u}$ is solution of the *weak form* of the governing equation (2.1),

$$\langle \phi_i, Hu \rangle = \langle \phi_i, f \rangle, \quad i = 0, 1, \dots, N, \tag{2.8}$$

which is obtained by taking the inner product between eq. (2.1) and each of the test functions ϕ_i. The weak form (2.8) is also called the variational formulation of problem (2.1). If the differential operator H is linear, then the weak form may be written as the matrix equation

$$M_{ij} a_j = \hat{f}_i, \quad i = 0, 1, \dots, N, \tag{2.9}$$

where $M_{ij} = \langle \phi_i, Hu_j \rangle$ and $\hat{f}_i = \langle \phi_i, f \rangle$, which can then be solved to obtain the spectral coefficients a_n.

Fourier series In spectral methods, the most commonly used trial function bases are Fourier series and Chebyshev polynomials. The Fourier series expansion of a periodic

function f may be written as

$$f(x) = \sum_{n=-\infty}^{\infty} a_n e^{2\mathbb{i}\pi n/L}, \tag{2.10}$$

where L is the period and $\mathbb{i} = \sqrt{-1}$. Fourier series are typically used when periodic boundary conditions need to be satisfied, since every Fourier basis function is periodic of period L (or a fraction thereof). The corresponding Fourier coefficients are given by

$$a_n = \frac{1}{L}\int_0^L f(x)e^{-2\mathbb{i}\pi n/L}\,\mathrm{d}x\,. \tag{2.11}$$

According to definition (2.6), the Fourier basis functions are orthogonal given a constant weight function, e.g. $w(x) = 1$.

Chebyshev polynomials Chebyshev polynomials are often used in non-periodic problems. They are related to Fourier series (more specifically to Fourier *cosine* series) by a change of variable. Consequently, they share most of the properties of Fourier series [31]. The Chebyshev series of a function defined on the interval $[-1, 1]$ is

$$f(x) = \sum_{n=0}^{\infty} a_n T_n(x), \tag{2.12}$$

where the Chebyshev polynomials T_n are the unique polynomials satisfying

$$T_n(\cos\theta) = \cos(n\theta). \tag{2.13}$$

The Chebyshev basis is orthogonal given the weight function $w(x) = 1/\sqrt{1-x^2}$, with $\langle T_0, T_0\rangle = \pi$ and $\langle T_n, T_n\rangle = \pi/2$ for $n \neq 0$.

Pseudo-spectral evaluation In numerical applications, Fourier and Chebyshev series are truncated to their first N elements. For non-linear problems, the matrix elements M_{ij} in the Galerkin method are usually computed using numerical integration of quantities evaluated over a set of *collocation* points. In this case, Galerkin methods are also referred to as *pseudo-spectral* due to their equivalence with collocation methods [31]. With Fourier and Chebyshev series, the numerical integration is more efficient when using the fast Fourier transform (FFT) algorithm [43], provided the collocation points are chosen adequately. For Fourier series, the collocation points are equidistant, i.e.

$$x_n = \frac{nL}{N}, \quad n = 0, \dots, N-1. \tag{2.14}$$

In the case of Chebyshev polynomials, either the 'roots' (or Gauss–Chebyshev) grid,

$$x_n = \cos\left[\frac{(2n+1)\pi}{2N}\right], \quad n = 0, \dots, N-1, \tag{2.15}$$

or the 'extrema' (or Gauss–Lobatto) grid,

$$x_n = \cos\left[\frac{n\pi}{N-1}\right], \quad n = 0, \dots, N-1, \tag{2.16}$$

may be chosen. The latter is usually preferred when boundary conditions need to be specified, since it includes the endpoints $x = \pm 1$.

2.1.2 Application to channel flow simulations

The NadiaSpectral code solves the Navier–Stokes equations (1.2) in a channel flow geometry using the Petrov–Galerkin method first proposed by Moser et al. [119]. The method is briefly presented by Canuto et al. [37] and described in more detail by Pasquarelli et al. [131], Godeferd and Lollini [59] and Buffat et al. [35]. The approach consists in choosing a space of divergence-free (or *solenoidal*) trial functions $\boldsymbol{u}_n$ which vanish on solid boundaries, so that the approximate velocity field automatically satisfies the incompressibility condition (1.2a) and no-slip boundary conditions on the walls. Moreover, an appropriate selection of the space of test functions $\boldsymbol{\phi}_i$ leads to the elimination of the fluctuating pressure field from the weak form of the governing equations.

An important feature of the present formulation is that, as described by Buffat et al. [35], the velocity field is decomposed into two L^2-orthogonal vector fields respectively defined in terms of the wall-normal velocity component u_y and the wall-normal vorticity component ω_y. This makes the formulation particularly adapted for the study of transition to turbulence in wall-bounded flows, since the two terms of the decomposition are related to the Orr–Sommerfeld and Squire equations in linear stability theory [161].

We first write the Navier–Stokes equations in the periodic channel as

$$\boldsymbol{\nabla} \cdot \boldsymbol{u} = 0, \qquad \text{in } \Omega, \tag{2.17a}$$

$$\frac{\partial \boldsymbol{u}}{\partial t} + (\boldsymbol{\nabla} \times \boldsymbol{u}) \times \boldsymbol{u} + \frac{1}{2}\boldsymbol{\nabla}|\boldsymbol{u}|^2 = -\frac{1}{\rho}\boldsymbol{\nabla} p + \nu \nabla^2 \boldsymbol{u} + \boldsymbol{f} \qquad \text{in } \Omega, \tag{2.17b}$$

where the solution domain[2] is $\Omega = [0, L_x] \times [-1, 1] \times [0, L_z]$. The forcing term is given here by the mean streamwise pressure gradient driving the flow, $\boldsymbol{f} = -\boldsymbol{\nabla} p_0 / \rho$, while the fluctuating pressure p, required to keep the flow incompressible, is periodic in x and z. The non-linear term is written in its rotation form [37], $(\boldsymbol{u} \cdot \boldsymbol{\nabla})\boldsymbol{u} = (\boldsymbol{\nabla} \times \boldsymbol{u}) \times \boldsymbol{u} + \boldsymbol{\nabla}|\boldsymbol{u}|^2/2$. Equations (2.17) are complemented by no-slip boundary conditions on the walls, i.e. $\boldsymbol{u} = \boldsymbol{0}$ at $y = \pm 1$.

[2] For simplicity of the presentation, the wall-normal bounds are set in this section to $y \in [-1, 1]$ (as they are actually set in the numerical implementation) instead of the range $y \in [0, 2h]$ used in the rest of this document.

2.1.2.1 Variational formulation

In the following, the Navier–Stokes equations are written under their weak form. The space of trial and test functions are respectively defined by (see Pasquarelli et al. [131] for a more rigorous definition)

$$W = \left\{ \boldsymbol{u} \colon \Omega \to \mathbb{R}^3, \text{ periodic in } (x,z) \mid \boldsymbol{u} = \boldsymbol{0} \text{ at } y = \pm 1 \text{ and } \boldsymbol{\nabla} \cdot \boldsymbol{u} = 0 \right\}, \tag{2.18}$$

$$V = \left\{ \boldsymbol{\phi} \colon \Omega \to \mathbb{R}^3, \text{ periodic in } (x,z) \mid \boldsymbol{\phi} = \boldsymbol{0} \text{ at } y = \pm 1 \text{ and } \boldsymbol{\nabla} \cdot (w\boldsymbol{\phi}) = 0 \right\}, \tag{2.19}$$

where $w(\boldsymbol{x})$ is the weight function associated to the inner product (2.5). Note that trial and test functions are now three-component vector functions, and they both satisfy no-slip boundary conditions at the walls. Unlike trial functions, test functions are not divergence-free; only their product by the weight function w is.

The variational formulation of (2.17b) then writes

$$\text{find } \boldsymbol{u} \in W \text{ such that } \left\langle \boldsymbol{\phi}, \frac{\partial \boldsymbol{u}}{\partial t} \right\rangle = \nu \left\langle \boldsymbol{\phi}, \nabla^2 \boldsymbol{u} \right\rangle + \langle \boldsymbol{\phi}, \boldsymbol{F} \rangle \quad \forall \boldsymbol{\phi} \in V, \tag{2.20}$$

where $\boldsymbol{F} = -(\boldsymbol{\nabla} \times \boldsymbol{u}) \times \boldsymbol{u} - \boldsymbol{\nabla} p_0/\rho$ includes the non-linear and forcing terms. Both the periodic pressure term and the potential part of the non-linear term vanish when projected onto the space of test functions V. Indeed, using integration by parts along with definition (2.5) and setting $P = p + |\boldsymbol{u}|^2/2$,

$$\langle \boldsymbol{\phi}, \boldsymbol{\nabla} P \rangle = -\int_\Omega P \, \boldsymbol{\nabla} \cdot (w\boldsymbol{\phi}) \, \mathrm{d}V + \int_{\partial\Omega} wP(\boldsymbol{\phi} \cdot \boldsymbol{n}) \, \mathrm{d}S, \tag{2.21}$$

where $\partial\Omega$ represents the domain boundaries, and $\boldsymbol{n}$ is the unitary normal on each boundary, pointing outwards of the domain. As a consequence of definition (2.19), the first integral is zero since $w\boldsymbol{\phi}$ is divergence-free, while the second one vanishes due to $\boldsymbol{\phi}$ satisfying impermeability conditions at $y = \pm 1$ and periodic conditions in x and z (this also requires periodicity of the weight function w).

2.1.2.2 Choice of trial and test functions

Following the method of Moser et al. [119], trial and test function basis are first written in terms of Fourier series in the periodic directions x and z,

$$\boldsymbol{u}_{ijk}(x,y,z) = \boldsymbol{u}_j^{ik}(y) \, e^{\mathbb{i}(\alpha_i x + \beta_k z)}, \tag{2.22}$$

$$\boldsymbol{\phi}_{ijk}(x,y,z) = \boldsymbol{\phi}_j^{ik}(y) \, e^{\mathbb{i}(\alpha_i x + \beta_k z)}, \tag{2.23}$$

where $\alpha_i = 2\pi i/L_x$ and $\beta_k = 2\pi k/L_z$ are respectively the streamwise and spanwise Fourier wave numbers, and $\boldsymbol{u}_j^{ik}$ and $\boldsymbol{\phi}_j^{ik}$ are complex vector functions that still need to be defined. Their definitions must be consistent with the requirements of spaces W

and V, namely

$$\boldsymbol{u}_j^{ik}(\pm 1) = 0 \quad \text{and} \quad \boldsymbol{\nabla} \cdot \left[\boldsymbol{u}_j^{ik} \, e^{\mathbb{i}(\alpha x + \beta z)} \right] = 0, \tag{2.24a}$$

$$\boldsymbol{\phi}_j^{ik}(\pm 1) = 0 \quad \text{and} \quad \boldsymbol{\nabla} \cdot \left[w \, \boldsymbol{\phi}_j^{ik} \, e^{\mathbb{i}(\alpha x + \beta z)} \right] = 0. \tag{2.24b}$$

As discussed in section 2.1.1, the orthogonality of the Fourier basis functions is achieved by taking a constant weight function in the inner product (2.5). Consequently, the weight function $w(\boldsymbol{x})$ is here taken to be constant in x and z, so that the inner product between functions in Ω is explicitly written as

$$\langle f, g \rangle = \int_0^{L_x} \int_0^{L_z} \int_{-1}^{1} f(x,y,z) \, g^*(x,y,z) \, w(y) \, \mathrm{d}y \, \mathrm{d}z \, \mathrm{d}x \, . \tag{2.25}$$

Furthermore, trial and test function spaces are truncated to $N_x \times (N_y + 1) \times N_z$ modes, with N_x and N_z even numbers. As a result, the velocity field is expanded as

$$\boldsymbol{u}(x,y,z,t) = \sum_{i=-N_x/2}^{N_x/2-1} \sum_{k=-N_z/2}^{N_z/2-1} \sum_{j=0}^{N_y} a_j^{ik}(t) \, \boldsymbol{u}_j^{ik}(y, \alpha_i, \beta_k) \, e^{\mathbb{i}(\alpha_i x + \beta_k z)}, \tag{2.26}$$

where the a_j^{ik} are the unknown spectral coefficients of the expansion. By plugging expansion (2.26) into the variational formulation (2.20), and as a consequence of the orthogonality of the Fourier basis functions under the inner product (2.25), one finds $N_x \times N_z$ uncoupled systems of equations

$$\boldsymbol{A}^{ik} \frac{\mathrm{d}\boldsymbol{a}^{ik}}{\mathrm{d}t} = \nu \boldsymbol{B}^{ik} \boldsymbol{a}^{ik} + \boldsymbol{f}^{ik}, \tag{2.27}$$

where $\boldsymbol{a}^{ik} = [a_0^{ik} \; a_1^{ik} \; \cdots \; a_{N_y}^{ik}]^T$ is the vector of unknown spectral coefficients associated to the Fourier mode (α_i, β_k); and $\boldsymbol{A}^{ik}$ and $\boldsymbol{B}^{ik}$ are $(N_y + 1) \times (N_y + 1)$ matrices with elements

$$A_{lj}^{ik} = \left\langle \boldsymbol{\phi}_l^{ik}, \boldsymbol{u}_j^{ik} \right\rangle, \tag{2.28}$$

$$B_{lj}^{ik} = \left\langle \boldsymbol{\phi}_l^{ik}, \frac{\mathrm{d}^2 \boldsymbol{u}_j^{ik}}{\mathrm{d}y^2} - \sigma^2 \boldsymbol{u}_j^{ik} \right\rangle, \tag{2.29}$$

where $\sigma = \sqrt{\alpha_i^2 + \beta_k^2}$ is the norm of the wall-parallel Fourier wave number. The vector $\boldsymbol{f}^{ik}$ in eq. (2.27) accounts for the contribution of the non-linear and forcing terms.

From this point on, the indices i and k associated to wall-parallel Fourier wave numbers are dropped for clarity. It is desirable to define functions $\boldsymbol{u}_j$ and $\boldsymbol{\phi}_l$ yielding sparse matrices $\boldsymbol{A}$ and $\boldsymbol{B}$, so that the system (2.27) can be efficiently inverted numerically. The strategy is to choose quasi-orthogonal bases so that the inner product $\langle \boldsymbol{\phi}_l, \boldsymbol{u}_j \rangle$ is non-zero only when the indices l and j are 'close enough', thus yielding banded matrices.

As a consequence of the incompressibility constraint, the velocity field can be de-

composed into two independent vector fields (instead of three in the compressible case). The same is true for trial and test functions, since they must satisfy the solenoidal constraints in eq. (2.24). Consequently, Moser et al. [119] proposed to split the basis $\boldsymbol{u}_j(y)$ into two orthogonal bases $\{\boldsymbol{u}_j^+, \boldsymbol{u}_j^-\}$, and similarly $\boldsymbol{\phi}_l(y)$ into $\{\boldsymbol{\phi}_l^+, \boldsymbol{\phi}_l^-\}$. The decomposition is such that the orthogonality conditions $\langle \boldsymbol{\phi}_l^+, \boldsymbol{u}_j^- \rangle = 0$ and $\langle \boldsymbol{\phi}_l^-, \boldsymbol{u}_j^+ \rangle = 0$ are also met. As a result of this decomposition, the system (2.27) is effectively split into two independent systems,

$$\boldsymbol{A}^+ \frac{\mathrm{d}\boldsymbol{a}^+}{\mathrm{d}t} = \nu \boldsymbol{B}^+ \boldsymbol{a}^+ + \boldsymbol{f}^+ \quad \text{and} \quad \boldsymbol{A}^- \frac{\mathrm{d}\boldsymbol{a}^-}{\mathrm{d}t} = \nu \boldsymbol{B}^- \boldsymbol{a}^- + \boldsymbol{f}^-, \tag{2.30}$$

for each Fourier mode (α, β). Hence, a total of $2 \times N_x \times N_z$ linear systems needs to be inverted.

The choice of the above decompositions is not unique. Buffat et al. [35] proposed to decompose the velocity field into two vector fields $\boldsymbol{u}^{os}$ and $\boldsymbol{u}^{sq}$ that are expressed in terms of the wall-normal velocity u_y and the wall-normal vorticity ω_y. The fields are solenoidal and orthogonal with respect to the L^2 inner product,

$$\boldsymbol{u} = \boldsymbol{u}^{os} + \boldsymbol{u}^{sq} \quad \text{with} \quad \boldsymbol{\nabla} \cdot \boldsymbol{u}^{os} = \boldsymbol{\nabla} \cdot \boldsymbol{u}^{sq} = 0 \quad \text{and} \quad \int_\Omega \boldsymbol{u}^{os} \cdot \boldsymbol{u}^{sq} \, \mathrm{d}V = 0, \tag{2.31}$$

and satisfy the constraints

$$(\boldsymbol{\nabla} \times \boldsymbol{u}^{os}) \cdot \boldsymbol{e}_y = 0, \quad \boldsymbol{u}^{sq} \cdot \boldsymbol{e}_y = 0 \quad \text{and} \quad \overline{\boldsymbol{u}^{sq}}(y) = \boldsymbol{0}. \tag{2.32}$$

These requirements express that $\boldsymbol{u}^{os}$ has zero wall-normal vorticity while $\boldsymbol{u}^{sq}$ has zero wall-normal velocity. Additionally, to satisfy orthogonality, the average of $\boldsymbol{u}^{sq}$ over wall-parallel planes vanishes. The superscripts *os* and *sq* are a reference to the Orr–Sommerfeld and Squire equations, which respectively describe the response of the wall-normal velocity and the wall-normal vorticity components to an infinitesimal perturbation of a laminar viscous shear flow [161].

In terms of trial functions, the decomposition of Buffat et al. [35] translates into modes

$$\boldsymbol{u}_j^+(y) = \begin{pmatrix} \mathbb{i}\alpha v_j'(y)/\sigma^2 \\ v_j(y) \\ \mathbb{i}\beta v_j'(y)/\sigma^2 \end{pmatrix} \quad \text{and} \quad \boldsymbol{u}_j^-(y) = \begin{pmatrix} -\mathbb{i}\beta \omega_j(y)/\sigma^2 \\ 0 \\ \mathbb{i}\alpha \omega_j(y)/\sigma^2 \end{pmatrix} \tag{2.33}$$

for non-zero wall-parallel wave numbers $\sigma = \sqrt{\alpha^2 + \beta^2}$. Here, $v_j(y)$ and $\omega_j(y)$ are functions associated to the wall-normal velocity and wall-normal vorticity, respectively, and primes denote differentiation with respect to y. It is readily verified that the two bases are orthogonal in the geometrical sense, i.e. $\boldsymbol{u}_j^+ \cdot \boldsymbol{u}_j^- = 0$, and that both respect the constraints of eq. (2.24a) provided that the boundary conditions

$$v_j(\pm 1) = v_j'(\pm 1) = \omega_j(\pm 1) = 0 \tag{2.34}$$

are met. Up to multiplication factors σ for $\boldsymbol{u}_j^+$ and $\mathbb{i}\sigma$ for $\boldsymbol{u}_j^-$, the decomposition (2.33) is the same as the one proposed by Moser et al. [119]. With respect to the original decomposition, an advantage of the present formulation is that it can be physically interpreted in terms of wall-normal velocity and vorticity modes.

Analogously to the trial functions, the test function decomposition writes

$$\boldsymbol{\phi}_l^+(y) = \begin{pmatrix} \mathbb{i}\alpha[w(y)Q_l(y)]'/[w(y)\sigma^2] \\ Q_l(y) \\ \mathbb{i}\beta[w(y)Q_l(y)]'/[w(y)\sigma^2] \end{pmatrix} \quad \text{and} \quad \boldsymbol{\phi}_l^-(y) = \begin{pmatrix} -\mathbb{i}\beta P_l(y)/\sigma^2 \\ 0 \\ \mathbb{i}\alpha P_l(y)/\sigma^2 \end{pmatrix}, \tag{2.35}$$

where $Q_l(y)$ and $P_l(y)$ must satisfy the boundary conditions

$$Q_l(\pm 1) = [wQ_l]'(\pm 1) = P_l(\pm 1) = 0 \tag{2.36}$$

for the constraints (2.24b) to be satisfied.

Noting that the vectors defined in eqs. (2.33) and (2.35) are ill-defined when $\alpha = \beta = 0$, the zero wave number case is treated differently. In this case, the spectral coefficients give the velocity field averaged over the two periodic directions. Since the average field must satisfy no-slip boundary conditions and the average wall-normal velocity must vanish on each wall-parallel plane, the vectors are chosen as

$$\boldsymbol{u}_j^+ = \begin{pmatrix} \omega_j(y) \\ 0 \\ 0 \end{pmatrix}, \quad \boldsymbol{u}_j^- = \begin{pmatrix} 0 \\ 0 \\ \omega_j(y) \end{pmatrix}, \quad \boldsymbol{\phi}_l^+ = \begin{pmatrix} P_l(y) \\ 0 \\ 0 \end{pmatrix} \quad \text{and} \quad \boldsymbol{\phi}_l^- = \begin{pmatrix} 0 \\ 0 \\ P_l(y) \end{pmatrix}, \tag{2.37}$$

consistently with Moser et al. [119].

To summarise, trial and test vectors are written in terms of the weight function $w(y)$, along with functions $v_j(y), \omega_j(y), Q_l(y)$ and $P_l(y)$ satisfying boundary conditions (2.34) and (2.36). As proposed by Moser et al. [119], these functions are chosen in terms of Chebyshev polynomials,

$$\begin{aligned} v_j(y) &= (1-y^2)^2 T_j(y), \quad \omega_j(y) = (1-y^2)T_j(y), \\ Q_l(y) &= \frac{1}{4}\left[\frac{T_{l+4}(y)}{(l+2)(l+3)} - \frac{2T_{l+2}(y)}{(l+1)(l+3)} + \frac{T_l(y)}{(l+2)(l+1)}\right], \\ P_l(y) &= \frac{T_l(y) - T_{l+2}(y)}{2(l+1)}, \end{aligned} \tag{2.38}$$

and the weight is taken as the Chebyshev weight function $w(y) = 1/\sqrt{1-y^2}$. With this choice of functions, the matrices $\boldsymbol{A}^+$ and $\boldsymbol{A}^-$ in eq. (2.30) have respectively 7 and 4 non-zero diagonals. Moreover, since they are expressed in terms of integrals of products between Chebyshev polynomials, matrix coefficients can be calculated analytically, thus eliminating quadrature errors [35]. Since Chebyshev polynomials T_n have even

symmetry for n even, and odd symmetry for n odd, each of the two $(N_y+1)\times(N_y+1)$ systems in eq. (2.30) is further split into two decoupled systems of roughly half the size.

2.1.2.3 Temporal discretisation

The linear systems (2.30) are integrated in time using a semi-implicit second-order finite-difference scheme with a constant time step Δt. At each iteration, the unsteady term is approximated by a first-order forward difference $\partial \boldsymbol{u}/\partial t \approx (\boldsymbol{u}^{n+1}-\boldsymbol{u}^n)/\Delta t$, where $\boldsymbol{u}^n$ is the known velocity field at time $t^n = n\Delta t$ and $\boldsymbol{u}^{n+1}$ is the unknown velocity field at time t^{n+1}. The viscous term is treated by an implicit second-order Crank–Nicolson scheme, $\nu\nabla^2\boldsymbol{u} \approx \nu\nabla^2(\boldsymbol{u}^n+\boldsymbol{u}^{n+1})/2$, while the non-linear terms are approximated by an explicit second-order Adams–Bashforth scheme, $\boldsymbol{F} \approx (3\boldsymbol{F}^n - \boldsymbol{F}^{n-1})/2$. As a result, the systems (2.30) are discretised as

$$\left(\boldsymbol{A} - \frac{\Delta t}{2}\nu\boldsymbol{B}\right)\boldsymbol{a}^{n+1} = \left(\boldsymbol{A} + \frac{\Delta t}{2}\nu\boldsymbol{B}\right)\boldsymbol{a}^n + \frac{\Delta t}{2}\left(3\boldsymbol{f}^n - \boldsymbol{f}^{n-1}\right), \tag{2.39}$$

where the + and − superscripts have been omitted. Note that this discretisation requires the additional storage of the non-linear terms at time t^{n-1}.

The numerical linear stability threshold associated to the use of a second order Adams–Bashforth scheme is given by the Courant-Friedrichs-Lewy (CFL) condition

$$\mathrm{CFL} = \pi\Delta t\left[\frac{N_x \max|u_x|}{L_x} + \frac{N_y \max|u_y|}{2} + \frac{N_z \max|u_z|}{L_z}\right] < 1, \tag{2.40}$$

where u_x, u_y and u_z are the three velocity components, and the maxima are taken over the ensemble of $N_x \times N_y \times N_z$ collocation points [35].

2.1.2.4 Sequence of an iteration

At each time iteration, the non-linear term $-(\boldsymbol{\nabla}\times\boldsymbol{u})\times\boldsymbol{u}$ is evaluated pseudo-spectrally in physical space and then decomposed using Fourier expansions in the x and z directions and Chebyshev polynomials in y. This requires a total of 9 FFTs, one for each spatial direction and one for each vector component. Since the computation of the non-linear term in physical space introduces aliasing of the spectral coefficients, Orszag's two-thirds rule [31, 125] is then applied in the Fourier directions to eliminate aliasing error. Then, the forcing term $\boldsymbol{f} = -\boldsymbol{\nabla}p_0/\rho$ is added in spectral space and the result is advanced in time according to the Adams–Bashforth scheme introduced above. Finally, the viscous and unsteady terms are evaluated in spectral space, and the linear systems introduced above are inverted to obtain the spectral coefficients of the velocity field $\boldsymbol{u}^{n+1}$. Using 9 inverse FFTs, the velocity field is recovered in physical space, enabling the evaluation of the non-linear terms at the next iteration.

2.1.2.5 Computation of the acceleration field

An important part of the physical analysis performed in this work is dedicated to the study of the acceleration of fluid tracers in turbulent channel flows. As described later in section 2.2, the Lagrangian acceleration of a fluid tracer is determined by interpolation of the acceleration field $\boldsymbol{a}(\boldsymbol{x}, t)$, described in the Eulerian reference frame, at the instantaneous tracer position. By definition, the fluid acceleration is the material derivative of the velocity field, i.e. its derivative along fluid particle paths,

$$\boldsymbol{a} = \frac{\mathrm{D}\boldsymbol{u}}{\mathrm{D}t} = \frac{\partial \boldsymbol{u}}{\partial t} + (\boldsymbol{u} \cdot \boldsymbol{\nabla})\boldsymbol{u}, \tag{2.41}$$

and corresponds to both the left-hand side and the right-hand side of the momentum equation (2.17b).

Since the pseudo-spectral solver does not explicitly compute the pressure field, we obtain the acceleration from the left-hand side of the momentum equation, both for consistency with the solver and for performance concerns. Considering that the rotational term $(\boldsymbol{\nabla} \times \boldsymbol{u}) \times \boldsymbol{u}$ is already calculated by the simulation at each iteration (computed in physical space, then transformed to spectral space), only the unsteady term (or *local* acceleration) $\partial \boldsymbol{u}/\partial t$ and the potential term $\boldsymbol{\nabla}|\boldsymbol{u}|^2/2$ remain to be explicitly computed. The unsteady term is discretised in time using a second-order central difference scheme. As a result, the acceleration field at iteration n is estimated as

$$\boldsymbol{a}^n = \frac{\boldsymbol{u}^{n+1} - \boldsymbol{u}^{n-1}}{2\Delta t} + \frac{1}{2}\boldsymbol{\nabla}|\boldsymbol{u}^n|^2 + (\boldsymbol{\nabla} \times \boldsymbol{u}^n) \times \boldsymbol{u}^n. \tag{2.42}$$

To minimise the number of required FFTs, the three terms are first added in spectral space and then transformed back to physical space. The potential term is obtained by first computing $|\boldsymbol{u}|^2$ in physical space, then transforming to spectral space (requiring 3 FFTs), and finally computing its gradient. The rotational term is already stored by the simulation in spectral space in dealiased form, as well as the velocity fields $\boldsymbol{u}^{n-1}$ and $\boldsymbol{u}^{n+1}$, hence they can be readily summed. Before transforming back to physical space (9 additional FFTs), the spectral coefficients are dealiased to prevent aliasing errors from the computation of the non-linear term $\boldsymbol{\nabla}|\boldsymbol{u}|^2$. This method requires the additional storage of the velocity field $\boldsymbol{u}^{n-1}$ between two subsequent simulations to preserve the temporal continuity of the acceleration field.

Putting aside the specificities of our DNS solver, it is worth discussing whether it would be preferable to compute the acceleration field from the right-hand side of eq. (2.17b) as opposed to its left-hand side. In high-Reynolds number HIT, it is well known that the pressure gradient contribution to the acceleration (the irrotational component $\boldsymbol{a}^I = -\boldsymbol{\nabla}p/\rho$) is dominant over the viscous contribution (the solenoidal component $\boldsymbol{a}^S = \nu\nabla^2\boldsymbol{u}$) [64, 109, 188]. The same has been shown to be true in wall-bounded flows, with the exception of the viscous sublayer where the solenoidal component is dominant [93, 202]. Hence, the decomposition of acceleration onto an irrotational and a solenoidal component has a clear physical interpretation, with two components that are generally uncorrelated and typically with different magnitudes. On the other hand,

the alternative decomposition of acceleration into a local acceleration $\boldsymbol{a}^L = \partial \boldsymbol{u}/\partial t$ and a convective acceleration $\boldsymbol{a}^C = (\boldsymbol{u} \cdot \boldsymbol{\nabla})\boldsymbol{u}$ was studied in HIT by Tsinober et al. [182]. The authors found that both components tend to cancel out: they are nearly anti-aligned, approximately equal in magnitude, and their individual magnitudes are much larger than that of the total Lagrangian acceleration (i.e. $|\boldsymbol{a}^L| \sim |\boldsymbol{a}^C| \gg |\boldsymbol{a}|$). A similar behaviour was observed in channel flow DNS at $Re_\tau = 720$ by Chen et al. [40]. By analysing standard deviation profiles of acceleration components, Chen et al. found that, for $y^+ > 10$, the fluctuations of local and convective acceleration were of the same magnitude, and were about an order of magnitude larger than the fluctuations of the total acceleration. To conclude, the two alternative decompositions have very different properties. From a numerical standpoint, adding two quantities that tend to cancel out may be detrimental to the numerical precision of the result, however the impact may be negligible when working with double precision floating-points, especially when the difference between $|\boldsymbol{a}^L|$ and $|\boldsymbol{a}|$ fluctuations is less than two orders of magnitude.

2.1.3 Parallelisation strategy

2.1.3.1 Domain decomposition

The NadiaSpectral solver is parallelised using the Message Passing Interface (MPI) protocol, enabling the code to run on distributed memory systems. The parallelisation strategy is presented in detail by Montagnier et al. [110] and is briefly described below. The code implements a 2D domain (or *pencil*) decomposition, in which the domain is partitioned in two Cartesian directions. Each MPI process manages the data associated to a chunk of the partition. With respect to a simpler 1D (or *slab*) decomposition, a pencil decomposition is less limited by the maximum possible number of domain chunks, or equivalently, by the maximum possible number of MPI processes. Hence, pencil decomposition is preferable when the code is executed on massively parallel computing systems. For this reason, this strategy is commonly found on modern DNS codes and related libraries.[3]

Domain decomposition is particularly challenging when global operations such as FFTs need to be performed. Commonly used FFT libraries are serial, thus requiring the operated data to be stored within a single domain chunk. This is the case of the FFTW library [54] used in NadiaSpectral. Even parallel FFT libraries such as P3DFFT [132] ultimately rely on FFTW or other sequential libraries while handling themselves the domain decomposition. Hence, in the case of a pencil-decomposed domain (say, partitioned in x and y), FFTs can only be performed in the direction in which decomposition is not applied (in z). To circumvent this issue when FFTs need to be applied in all three directions, it is necessary to deal with three different decomposition layouts in which either the x, y or z direction is not partitioned. These layouts are referred to as x-pencil, y-pencil and z-pencil schemes, respectively. Furthermore, it must be possible

[3] Some open source examples are the Incompact3d DNS code [91] and the P3DFFT parallel FFT library [132].

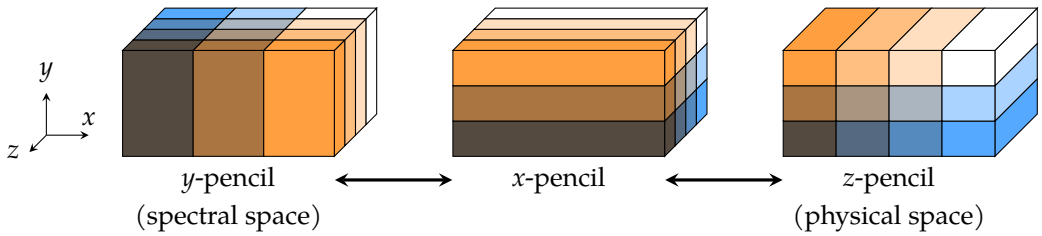

Figure 2.1. Domain decomposition configurations. Each colour represents a different MPI process.

to transpose the data from one configuration to the other, requiring time-intensive interprocess communications associated to data transfers between MPI processes.

The different decomposition layouts used in NadiaSpectral are illustrated in fig. 2.1. The code includes functions to transpose field data from a given layout to another. The transpositions are done through calls to the non-blocking MPI routines `MPI_Isend` and `MPI_Irecv`, enabling a more fine-grained control of the inter-process communications compared to `MPI_Alltoall` and its non-blocking variant `MPI_Ialltoall`. As stated above, each decomposition layout enables the evaluation of FFTs in a single direction. At a given iteration, the non-linear terms are computed in physical space in the z-pencil configuration. Then, an FFT is applied along z before transposing to the x-pencil layout, in which a second FFT is applied in the x direction. Finally, the Fourier-transformed data is transposed to the y-pencil configuration, followed by a discrete Chebyshev transform in that direction. At this point the viscous and unsteady terms can be added in spectral space, and the linear systems introduced in section 2.1.2 can be inverted. After this, the inverse process is applied to transform the spectral coefficients of the solution back to physical space.

2.1.3.2 *Parallel file I/O*

An important challenge arising with data being distributed among a large number of computing processes is that of file input/output (I/O) operations. In a DNS, saving restart data (in our case velocity fields and non-linear terms) or datasets for further post-processing or visualisation can be very time-demanding. This is especially the case in high-resolution simulations generating large amounts of data. The most straightforward approach to writing parallel data is the one-file-per-process method, in which each process independently writes the portion of data it owns to a separate file. Besides being simple to implement, this approach is usually faster than concurrently writing parallel data to a single file. However, the one-file-per-process approach does not scale well with the number of processors. Parallel file systems such as Lustre,[4] typically found on Linux computing clusters, see a decreased performance when a very large number of files is present in a single directory. In addition, it becomes cumbersome and impractical for the user to interact with the files, be it for file transfers, visualisation or post-processing [97]. Restarting a simulation using a different number of processors

[4] http://lustre.org

or a different domain decomposition layout becomes a complicated task, since data stored in the files must be merged, split or rearranged in often non-trivial ways.

An alternative to the one-file-per-process approach is writing the data from all processes to a single file. Hybrid approaches are also possible, in which process subsets share a common output file. In one possible implementation of the single-file approach, a single process is responsible for writing the data from all the processes to a file. Such a master-slave model does not scale well with the number of processes due to the increasingly high number of required communications. A different possibility is all processes writing concurrently to a shared file. This requires a high level of coordination between processes, since data needs to be written in a deterministic order that can be understood once the file is read later. With MPI, this is typically done using the MPI-IO specification, either directly or through higher-level libraries making use of MPI-IO.

Originally, NadiaSpectral used the one-file-per-process approach to write data to VTK files, allowing the direct visualisation of the results generated by each process using software such as ParaView.[5] Although the files could be easily visualised, performing other post-processing operations on a large number of VTK XML files containing binary data in a high-level programming language such as Julia [21] or Python proved to be impractical. Such operations may include estimating spatial statistics from a single flow snapshot, rearranging simulation restart files in order to run a simulation under a different number of processes, or simply determining the portion of the domain associated to a given MPI process.

For the above reasons, we have implemented an alternative solution using the HDF5 format [86], commonly used in the scientific community to store data generated by experiments and simulations. HDF5 files are self-describing, in the sense that they include not only the raw data (e.g. velocity fields) but also the associated metadata, including array dimensions, data types and byte order information. Datasets can be easily compressed using zlib[6] or other compression libraries. This is particularly convenient when storing datasets containing many zeros, as is the case of dealiased fields in spectral space. HDF5 file I/O is performed through the HDF5 libraries, which are accessible from a wide range of programming languages including those mentioned above. These libraries are readily available in common Linux distributions and in most computing clusters, and provide convenient command-line and graphical interfaces for quickly inspecting and comparing HDF5 files.

At first, the VTK output was replaced by serial HDF5 files using the original one-file-per-process approach. This greatly simplified the manipulation of simulation-generated files, although the issues associated to the large number of files remained unsolved. In a subsequent step, the option for parallel HDF5 output, in which all MPI processes write their data to a shared file, was implemented. The HDF5 libraries support parallel I/O using the MPI-IO specification mentioned above. However, parallel I/O can perform very poorly if not done carefully. In our implementation, we have applied multiple

[5] https://www.paraview.org
[6] http://zlib.net

optimisations that have enabled writing and reading times that are comparable to serial I/O, namely:

- datasets are written using collective I/O operations, in which the writes are coordinated over all MPI processes. This leads to a better performance compared to independent I/O operations;

- each process writes their own data to a single contiguous chunk in the file. This requires all the processes to deal with the same amount of data. Writing a single large chunk per process is considerably faster than writing several smaller chunks;

- by default, the HDF5 library fills a new dataset with a constant value (zero by default). Disabling this behaviour (for instance via the `H5Pset_fill_time` function) reduced the dataset writing time by one half;

- parallel file systems such as Lustre are able to perform *file striping*, in which different chunks of a file are stored on different physical or virtual storage disks. Striping of a file is defined in terms of a *stripe count*, which is the number of disks over which the file is stored, and a *stripe size*, which is the size in bytes of each file chunk. By properly adjusting these two parameters at file creation (see below for details), we have achieved a tenfold decrease of the dataset reading and writing times.

As the official HDF5 C++ interface does not currently support parallel I/O we have developed our own lightweight C++11 interface wrapping the HDF5 C libraries.[7]

We have evaluated the performance impact associated to dealing with parallel HDF5 files in comparison to serial HDF5 files after applying the above optimisations. For a $Re_\tau = 1440$ channel flow simulation using nearly 9×10^8 grid points, running on 1024 MPI processes distributed among 37 computing nodes on a Lustre file system,[8] a three-component velocity field took about 4.5 seconds to be written to a single 21 GiB parallel HDF5 file, as opposed to 2.2 seconds for the serial (one-file-per-process) case. This was achieved using a stripe count of 37 (same as the number of nodes) and a stripe size of 4 MiB, which was found to minimise the writing times. For comparison, a single iteration of flow simulation, not considering the time associated to Lagrangian particle tracking or the computation of acceleration fields, took in average 2.3 seconds. In conclusion, the present implementation is capable of reading and writing global domain data to a single file shared among all processes, with a relatively low performance penalty when compared to the one-file-per-process case, while providing a much more convenient management of the generated files after the simulation.

[7] This HDF5 C++ interface is open source and available at https://gitlab.com/jipolanco/HDF5mm.

[8] The simulations ran on the Occigen cluster administered by the Centre Informatique National de l'Enseignement Supérieur (CINES).

2.1.4 Parameters and validation of the Eulerian solver

2.1.4.1 Simulation parameters

Throughout this work, we consider a turbulent channel flow at a friction Reynolds number $Re_\tau = 1440$. In this section, the choice of numerical parameters for simulating this case are presented. The relevant parameters determining the accurate prediction of channel flow turbulence are the domain size, the number of spectral modes in each spatial direction (or equivalently, the spacing between collocation points) and the time step. The domain size needs to be sufficiently large to allow the formation of large-scale coherent structures typically found in wall-bounded turbulence. The grid spacing and the time step must be small enough to capture the velocity variations at the smallest turbulent length and time scales, at which turbulent energy is dissipated. Moreover, their combination must respect the CFL condition (2.40) to ensure the numerical stability of the DNS solver.

The choice of numerical parameters for the considered Reynolds number are listed in table 2.1. Also shown for reference is a lower Reynolds number case, $Re_\tau = 180$, that has been used for testing purposes. Included in the table are the domain dimensions, L_x, L_y and L_z; the number of spectral modes before dealiasing, N_x, N_y and N_z; the grid spacing and simulation time step in wall units, Δx^+, Δy^+, Δz^+ and Δt^+; and the CFL number for each simulation. Since the distribution wall-normal grid points is not uniform, both the minimum (at the walls) and the maximum (at the channel centre) values of Δy^+ are given.

Turbulent channel flows at $Re_\tau = 180$ have been extensively studied by DNS in the last 30 years. The numerical parameters of our DNS at this Reynolds number are coherent with most recent studies. For comparison, the seminal work of Kim et al. [81] used a larger domain ($L_x = 4\pi h$, $L_z = 2\pi h$) but at a coarser grid resolution ($\Delta x^+ \approx 12$, $\Delta y^+_{\text{min}} \approx 0.05$, $\Delta z^+ \approx 7$). More recently published DNS at the same Reynolds numbers have increased the grid resolution to values closer to those found in table 2.1 (for some examples see [1, 93, 202]). Yeo et al. [202] found that, due to the high intermittency of fluid acceleration, the accurate computation of high-order acceleration statistics requires a finer spatial resolution than that typically used for the velocity. For $Re_\tau = 180$ and 600, they used a grid resolution given by $\Delta x^+ = 11.8$, $\Delta y^+_{\text{min}} = 0.05$ and $\Delta z^+ = 3.93$, which is similar if not slightly coarser than the resolution in table 2.1. At $Re_\tau = 180$, they showed this resolution to be sufficient to correctly resolve the flatness factors of the spanwise acceleration, which quantify the acceleration intermittency. Since the parameters used for the $Re_\tau = 180$ case are consistent with many contemporary studies found in the literature, validation details are only provided for the less common and more demanding $Re_\tau = 1440$ case.

In the rest of this section, a validation of the $Re_\tau = 1440$ configuration is presented. To evaluate the suitability of the chosen domain size, the spatial velocity and acceleration auto-correlations along the two periodic dimensions are analysed. Ideally, the domain should be large enough for these auto-correlations to vanish at long-enough distances. In other words, the domain should be able to represent multiple independent large-

Table 2.1. Numerical parameters for channel flow DNS.

Re_τ	Re	L_x	L_y	L_z	N_x	N_y	N_z	Δx^+	$\Delta y^+_{\text{min / max}}$	Δz^+	Δt^+	CFL
180	3280	$3\pi h$	$2h$	$\frac{4}{3}\pi h$	192	192	192	8.84	0.024 / 2.95	3.93	0.033	0.65
1440	33 800	$4\pi h$	$2h$	πh	2048	432	1024	8.81	0.038 / 10.4	4.41	0.033	0.71

scale turbulent structures within its volume. In practice, however, it is very challenging to resolve the largest structures in wall-bounded turbulence using DNS. As stated in the introduction (section 1.2.4), VLSMs in the channel can achieve lengths that are many times the channel half-height. Using hot-wire anemometry in a turbulent channel flow at $Re_\tau = 3178$, Monty et al. [111] detected the presence of coherent motions elongated in the streamwise direction, with lengths up to $25h$. These large-scale structures affect the near-wall turbulence through modulation of the near-wall cycle [167]. Lozano-Durán and Jiménez [95] discussed the effect of the domain size on channel flow DNS. Using a very large domain of dimensions $60\pi h \times 2h \times 6\pi h$ at $Re_\tau = 547$, they found that in order to capture 80 % of the streamwise turbulent kinetic energy at the channel centre, structures of longitudinal wavelength up to $\lambda_x \approx 100h$ need to fit within the simulation domain. On the other hand, they also performed two $Re_\tau = 2009$ simulations with domain sizes $2\pi h \times 2h \times \pi h$ and $8\pi h \times 2h \times 3\pi h$. They found no difference between the one-point Eulerian velocity statistics obtained from the two simulations, suggesting that a very large domain is not required for this purpose, even though the very large scales are not correctly reproduced in the smaller domain.

2.1.4.2 Eulerian two-point auto-correlations

The Eulerian two-point auto-correlation of a velocity component $u_i(\boldsymbol{x}, t)$ between two locations $\boldsymbol{x}$ and $\boldsymbol{x} + \boldsymbol{r}$ at a time t is defined by

$$\rho^u_{E,ii}(\boldsymbol{x}, \boldsymbol{r}, t) = \overline{u_i'(\boldsymbol{x}, t)\, u_i'(\boldsymbol{x} + \boldsymbol{r}, t)} \,\Big/\, \left[\overline{u_i'^2(\boldsymbol{x}, t)}\;\overline{u_i'^2(\boldsymbol{x} + \boldsymbol{r}, t)}\right]^{1/2}, \tag{2.43}$$

where $u_i' = u_i - \overline{u}_i$ is the fluctuation of u_i about its mean value. No summation is applied over repeated indices. In statistically stationary channel flow, the auto-correlation neither depends on time nor on the streamwise and spanwise positions of one of the probed locations, so that $\rho^u_{E,ii}(\boldsymbol{x}, \boldsymbol{r}, t)$ reduces to $\rho^u_{E,ii}(y, \boldsymbol{r})$ where y is the wall-normal position of the first point. The acceleration auto-correlation $\rho^a_{E,ii}(y, \boldsymbol{r})$ is defined in an analogous manner.

In fig. 2.2, two-point auto-correlations of velocity and acceleration are represented over two wall-parallel planes, $y = h/2$ and $y = h$, for spatial displacements in the streamwise ($\boldsymbol{r} = r_x \boldsymbol{e}_x$) and spanwise ($\boldsymbol{r} = r_z \boldsymbol{e}_z$) directions. Due to the symmetry of the auto-correlation function in the periodic directions, displacements are plotted over the ranges $0 \leq r_x \leq L_x/2$ and $0 \leq r_z \leq L_z/2$. On the two planes, the three acceleration components completely decorrelate over short distances relative to the domain dimensions, suggesting that the box size is large enough to correctly predict the Eulerian structure

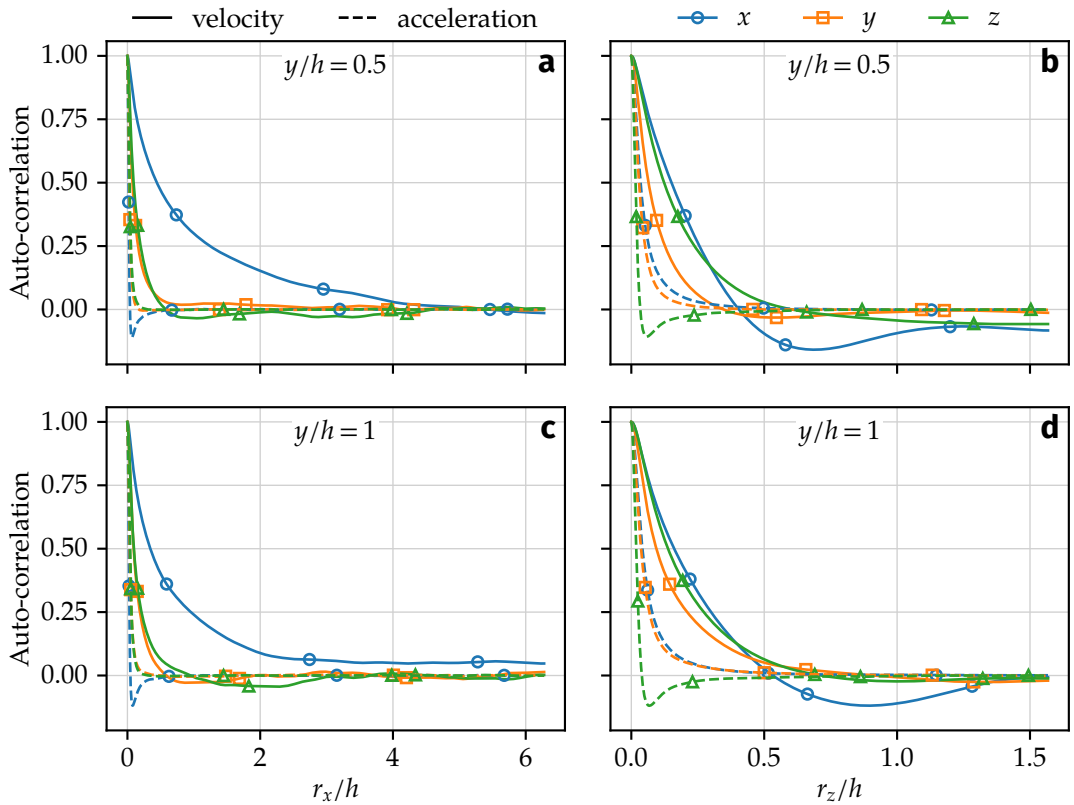

Figure 2.2. Two-point velocity and acceleration auto-correlations at $Re_\tau = 1440$. Wall-parallel planes are $y = h/2$ ($y^+ = 720$; subfigures a-b) and $y = h$ ($y^+ = 1440$; subfigures c-d). Left: auto-correlations along the streamwise direction. Right: auto-correlations along the spanwise direction. Colours and symbols represent different velocity and acceleration components.

of the acceleration field. This also shows that the acceleration is a small-scale quantity, since the variations of the fluctuating acceleration in space happen over much shorter lengths than those of the fluctuating velocity. As confirmed in section 3.4, the same is true in a Lagrangian reference frame, i.e. the acceleration of a fluid tracer varies much faster than the velocity along its trajectory. Interestingly, in all cases the longitudinal acceleration component (the one aligned with the direction of displacement) displays a weak negative auto-correlation at short offsets that is not observed for the transverse components (perpendicular to the direction of displacement). This behaviour may be explained by the effect of small-scale vortex filaments, which are responsible for high-magnitude centripetal accelerations in turbulent flows [93, 118, 179] (see also section 1.1.5). This can be better understood from the point vortex model depicted in fig. 1.7a. If the Eulerian auto-correlation is computed along a line that intersects a vortex centre, the longitudinal acceleration is the same as the centripetal acceleration, and it changes orientation from one side of the vortex to the other, thus explaining the change of sign of the correlation.

More relevant for evaluating the effects of the domain size are the velocity auto-

correlations, since velocity variations in turbulent flows happen over a wide range of scales. For streamwise displacements, fig. 2.2 shows that the wall-normal and spanwise velocity components decorrelate over short spatial offsets on the two chosen wall-parallel planes. The streamwise velocity component has a longer decorrelation distance. At $y = h/2$ (fig. 2.2a), it becomes completely decorrelated at an offset $r_x \approx 5h$, i.e. about two-fifths of the domain length in that direction. At the channel centre ($y = h$, fig. 2.2c), the streamwise velocity does not achieve a full decorrelation over the chosen domain length, even though the auto-correlation coefficient becomes smaller than 10% for offsets $r_x > 2h$. This indicates that the domain is not long enough to reproduce the largest turbulent structures that may be visible in the channel centre.

In the spanwise direction, both the streamwise and spanwise velocity components display a weak negative auto-correlation at the largest spatial offsets on the $y = h/2$ plane (fig. 2.2b), indicating that the spanwise domain size is not large enough to compute the largest turbulent structures at this distance from the wall. This is not the case at the channel centre (fig. 2.2d), where the three velocity components decorrelate over the spanwise domain size.

In conclusion, the chosen domain is sufficiently large to reproduce acceleration fluctuations in channel flow, which are inherently small-scale quantities. On the other hand, the Eulerian structure of the velocity field may not exactly represent the very large-scale structure of a real wall-bounded flow, even though the degree of coherence at the large scales remains very low. For the purposes of this study, this is not a critical issue since fluid tracers mostly see the local flow structure while being swept by the mean flow and the large-scale turbulent motion. The only potential issue is with the relative dispersion of particle pairs, since our simulations may not accurately reproduce certain situations where two particles belong to two independent large-scale motions.

2.1.4.3 *Velocity statistics*

To validate the accuracy of the velocity and acceleration fields in our $Re_\tau = 1440$ simulations, one-point statistics are compared in this section to other channel flow simulations found in the literature.

Velocity statistics are compared to those obtained by Hu et al. [69] from channel flow DNS at the same Reynolds number, $Re_\tau = 1440$. Hu et al. used a spectral method based on Fourier and Chebyshev expansions. The non-linear terms were discretised in time using a third-order Runge–Kutta scheme. In their DNS, the domain size was nearly the same as in our DNS in the streamwise direction ($L_x = 12h$), while it was almost twice as large in the spanwise direction ($L_z = 6h$). However, their spatial discretisation was almost twice as coarse in both wall-parallel directions, with $\Delta x^+ = 16.88$ and $\Delta z^+ = 8.44$. Mean and variance velocity profiles are compared in fig. 2.3. To illustrate the Reynolds number effects on velocity statistics, also added to the comparison are the channel flow simulations by Hoyas and Jiménez [67] at $Re_\tau = 950$ and 2000. For their high Reynolds number case, Hoyas and Jiménez applied Fourier expansions in the wall-parallel direction and seven-point compact differences in the wall-normal direction, along with a third-order Runge–Kutta scheme for time discretisation the

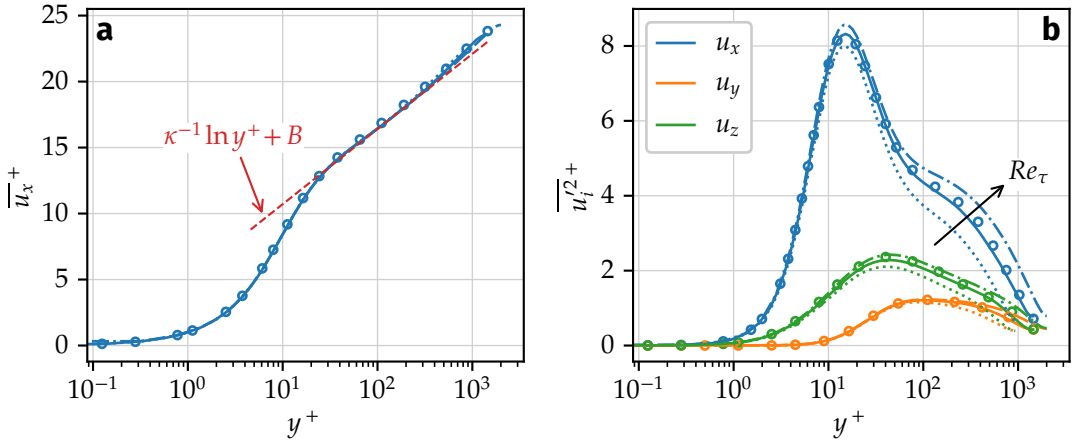

Figure 2.3. Mean and variance velocity profiles along the channel width. Comparison between the present DNS at $Re_\tau = 1440$ (solid lines) and the DNS by Hu et al. [69] ($Re_\tau = 1440$, circles) and by Hoyas and Jiménez [67] ($Re_\tau = 950$, dotted lines; $Re_\tau = 2000$, dash-dotted lines). On the left, the red dashed line represents the log law $\overline{u_x}^+ = \kappa^{-1}\ln y^+ + B$ with $\kappa = 0.404$ and $B = 5.016$.

non-linear terms.

The mean streamwise velocity from the different simulations (fig. 2.3a) collapses to a single profile characteristic of wall-bounded turbulent flows. The velocity profile is nearly logarithmic in the range $40 \lesssim y^+ \lesssim 600$, as shown by the fit of the law of the wall $\overline{u_x}^+ = \kappa^{-1}\ln y^+ + B$ where κ is the von Kármán constant (section 1.2.3). Regarding the velocity variance (fig. 2.3b), a clear Reynolds number effect is observed when comparing the profiles from different simulations. As expected, wall-scaled velocity fluctuations become more intense far from the wall as the Reynolds number is increased. Slight differences are found between the two $Re_\tau = 1440$ DNSs, which may be explained by the coarser grid resolution used in the simulations by Hu et al. [69]. In all cases, the streamwise velocity fluctuations are the most intense throughout the channel, followed by the spanwise and finally the wall-normal velocity. Each variance profile presents a single peak located in the near-wall region. At higher Reynolds numbers, recent experiments suggest the appearance of a secondary (or *outer*) peak in the u_x variance profile located in the logarithmic layer [101, 150].

2.1.4.4 *Acceleration statistics*

Acceleration statistics at $Re_\tau = 1440$ are discussed and compared against the channel flow DNS of Yeo et al. [202] at $Re_\tau = 600$. Yeo et al. used a spectral method with dealiased Fourier and Chebyshev expansions in the periodic and wall-normal directions, respectively. Time discretisation was based on a third-order Runge–Kutta method for the non-linear terms. In contrast to our simulations, Yeo et al. computed the fluid acceleration from the right-hand side of the momentum equation (2.17b). The discussion here is limited to the numerical accuracy of the acceleration statistics

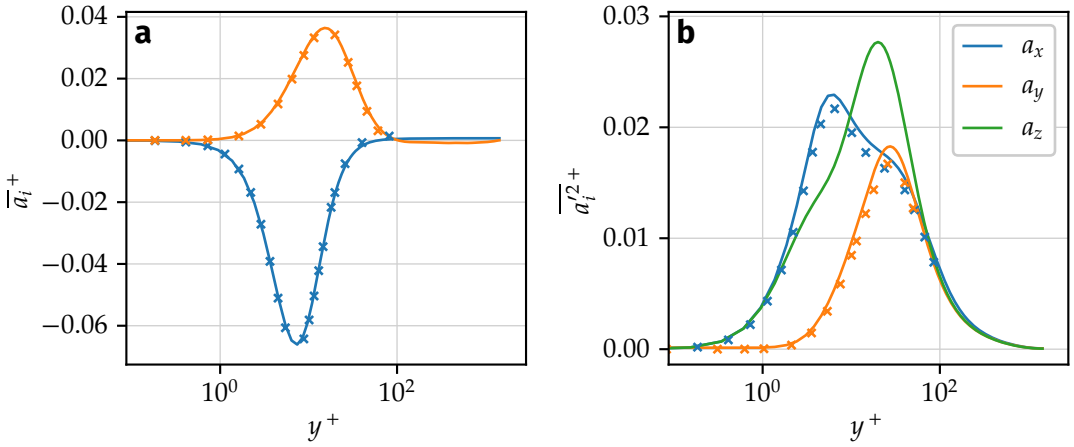

Figure 2.4. Mean and variance acceleration profiles along the channel width. Comparison between the present DNS at $Re_\tau = 1440$ (solid lines) and the DNS by Yeo et al. [202] at $Re_\tau = 600$ (crosses).

and to apparent Reynolds number effects; a physical interpretation of the profiles is deferred to chapter 3. Mean and variance acceleration profiles are plotted in wall units in fig. 2.4. The mean acceleration profiles from the two simulations (fig. 2.4a) nearly collapse, indicating that u_τ and ν are the appropriate normalisation parameters for acceleration statistics in wall turbulence, as is the case for velocity statistics. The mean acceleration components can be written as gradients of the Reynolds stresses,

$$\overline{a_x} = \frac{\mathrm{d}}{\mathrm{d}y}\overline{u_x' u_y'} \quad \text{and} \quad \overline{a_y} = \frac{\mathrm{d}}{\mathrm{d}y}\overline{u_y'^2}, \tag{2.44}$$

while the spanwise component is zero due to flow symmetry. As for the acceleration variance (fig. 2.4b), slight differences are found between the two simulations. This may be explained by a Reynolds number effect, in which acceleration fluctuations far from the wall become more intense as the flow becomes more turbulent, and is similar to the Reynolds number effect observed in the velocity profiles (fig. 2.3b). The a_z variance profiles at $Re_\tau = 600$ are not shown since they were not reported by Yeo et al. [202].

Also of interest are the acceleration skewness and flatness factors, as they are good indicators of the anisotropy and intermittency of the acceleration fluctuations. These are respectively defined as

$$S_i^a = \overline{a_i'^3} \,/\, \overline{a_i'^2}^{3/2} \quad \text{and} \quad F_i^a = \overline{a_i'^4} \,/\, \overline{a_i'^2}^{2}. \tag{2.45}$$

For $Re_\tau = 600$, Yeo et al. [202] only reported the skewness and flatness of the wall-normal acceleration, which is both the most anisotropic and the most intermittent acceleration component within the viscous sublayer. This is seen in fig. 2.5, where their results are compared against our $Re_\tau = 1440$ simulation. Both the skewness and flatness of the wall-normal acceleration agree well in the logarithmic and buffer regions of the

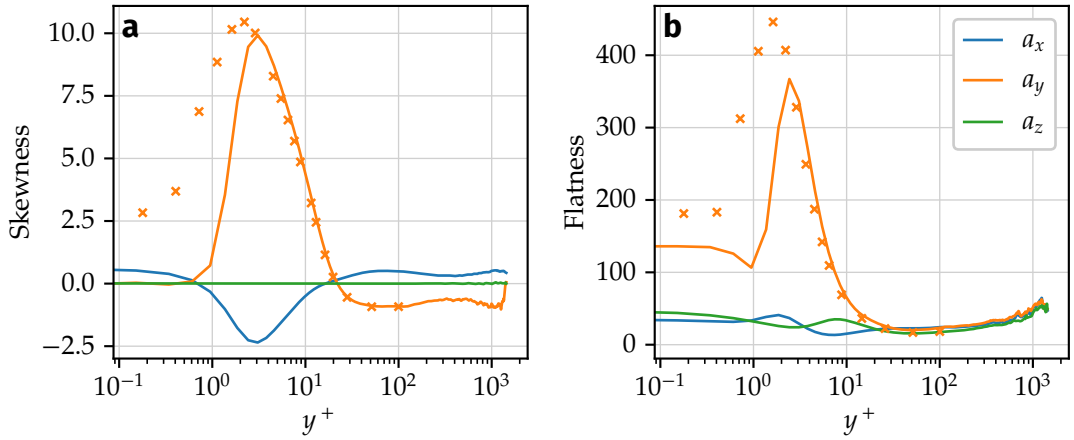

Figure 2.5. Skewness and flatness acceleration profiles along the channel width. Comparison between the present DNS at $Re_\tau = 1440$ (solid lines) and the DNS by Yeo et al. [202] at $Re_\tau = 600$ (crosses).

channel, where the statistics appear to be Reynolds-number independent. On the other hand, important differences are observed in the viscous sublayer for $y^+ < 3$, where their DNS predicts higher skewness and flatness values despite their lower Reynolds number. This disagreement may be explained by the difference in the spatial resolution of both simulations or by the different approaches to computing the acceleration field (from the pressure gradient and viscous terms by Yeo et al.). Further tests of sensibility to the numerical parameters are required to clearly identify the source of disagreement. Nevertheless, the acceleration field away from the viscous sublayer, most relevant for the physical analysis in this work, does not appear to be affected by these accuracy issues.

2.1.5 Conclusion

The pseudo-spectral Galerkin method used to numerically solve the Navier–Stokes equations in a periodic channel is described in this section. The velocity field is decomposed into Fourier expansions in the two periodic directions and Chebyshev polynomials in the wall-normal direction. Through an appropriate selection of test and trial functions, the method eliminates the pressure term from the weak form of the Navier–Stokes equations.

The domain decomposition strategy for parallelisation of the solver using MPI is described. A pencil decomposition method is applied, in which the domain is partitioned in two Cartesian directions, allowing the computation of FFTs in the third direction locally within each MPI process. To fully transform a field from physical to spectral space or back, transposition of data between different pencil decomposition configurations is performed, requiring communication-intensive data exchange operations between MPI processes. A parallel I/O approach, for saving Eulerian solution fields to data files shared among all processes, has been implemented and optimised. The approach

takes advantage of the capabilities of parallel file systems, while greatly simplifying the handling of Eulerian solution files generated by highly parallel simulations, and has a low performance penalty relative to the less convenient one-file-per-process approach.

The physical and numerical parameters of the Eulerian solver used for the simulations presented in this work are introduced. To evaluate the appropriateness of the chosen domain size at $Re_\tau = 1440$, two-point auto-correlations of velocity and acceleration components along the periodic directions are analysed. The domain is large enough to correctly resolve the acceleration field, which is to be expected since acceleration is an inherently small-scale quantity. On the other hand, the streamwise velocity component fails to completely decorrelate within the extent of the domain, indicating that very large-scale flow structures (VLSMs) may not be accurately resolved. This is not expected to visibly affect the Lagrangian dynamics of the flow which are at the core of this work, since tracers are mostly affected by the local flow structure while being swept by the large-scale motions.

Finally, one-point velocity and acceleration statistics obtained at $Re_\tau = 1440$ are validated against results from other channel flow DNSs found in the literature. Velocity statistics agree well with the results by Hu et al. [69] at the same Reynolds number. Acceleration statistics are compared to the simulations by Yeo et al. [202] at a lower Reynolds number, $Re_\tau = 600$. Mean and variance profiles agree well between both simulations, with slight differences in the variances which are attributed to the effect of the Reynolds number. Since acceleration is a highly intermittent quantity in wall-bounded turbulent flows, higher order statistics, namely the skewness and flatness factors, are also of interest. In the viscous sublayer of the channel, important differences are found between both DNSs. These are likely caused by differences in the numerical methods or in the spatial resolutions, although further tests are required to identify the exact source of inaccuracy. These issues do not appear to affect the acceleration statistics in the region away from the viscous sublayer, most relevant for tracer dispersion and the present work.

2.2 Lagrangian tracking of fluid particles

Lagrangian flow statistics are computed from the trajectories of fluid particles (or *tracers*) that follow the fluid flow. In the DNS, particles are spawned in the numerical domain at an initial time. Their positions and other properties are then updated over time according to the Eulerian fields computed by the solver. In the following, the numerical methods used for determining the particle properties at each iteration are introduced. Different interpolation schemes used to evaluate field data at particle positions are examined, and their influence on Lagrangian statistics are assessed. Details on the implementation of Lagrangian tracking algorithms are then briefly discussed. Finally, generated Lagrangian particle data is validated by comparison with one-point Eulerian statistics of the flow.

2.2.1 Governing equations and time discretisation

The position of a particle at a given time t is uniquely determined by its position $\boldsymbol{x}_0$ at an initial time t_0 and by its velocity history between t_0 and t. By definition, the velocity of a Lagrangian particle is equal to the velocity of the fluid at the instantaneous particle position. Hence, the position $\boldsymbol{X}$ of the particle over time satisfies the evolution equation

$$\frac{\partial \boldsymbol{X}(t, \boldsymbol{x}_0)}{\partial t} = \boldsymbol{u}(\boldsymbol{X}(t, \boldsymbol{x}_0), t), \qquad \boldsymbol{X}(t_0, \boldsymbol{x}_0) = \boldsymbol{x}_0, \tag{2.46}$$

where $\boldsymbol{u}(\boldsymbol{x}, t)$ is the fluid velocity field. In the rest of this document, the dependency of a particle trajectory on $\boldsymbol{x}_0$ is omitted unless stated otherwise.

In the DNS, the fluid velocity field $\boldsymbol{u}(\boldsymbol{x}, t)$ is known at each iteration. In order to determine the position of a tracer at any given iteration, first the fluid velocity is evaluated at the particle position, and secondly eq. (2.46) is integrated using an appropriate numerical scheme. Some possible interpolation schemes for performing the first step are discussed in section 2.2.2. As for the second step, a finite difference scheme is used to update the particle position based on its velocity. For consistency with the Eulerian solver (see section 2.1.2.3), an explicit second-order Adams–Bashforth scheme is applied, so that the fluid particle position at iteration $n + 1$ is obtained as

$$\boldsymbol{X}^{n+1} = \boldsymbol{X}^n + \Delta t \left(\frac{3}{2} \boldsymbol{v}^n - \frac{1}{2} \boldsymbol{v}^{n-1} \right), \tag{2.47}$$

where $\boldsymbol{v}$ is the particle velocity, Δt is the simulation time step, and the superscripted indices denote temporal iterations. The integration of the particle trajectories is performed using the same time step as the Eulerian solver.

Similarly to the velocity, fluid particle accelerations are obtained by interpolation of the fluid acceleration field, first computed in the Eulerian frame according to eq. (2.42), at the instantaneous particle positions. This choice is discussed in section 2.2.2.3 and compared to the more common approach consisting in differentiating particle velocities in time.

2.2.2 Interpolation of Eulerian fields

The choice of the interpolation scheme used for evaluating Eulerian fields (e.g. velocity, acceleration) at the particle positions is critical for the accurate calculation of the tracer trajectories and can have an important impact on the associated Lagrangian statistics. Choi et al. [41] examined different interpolation schemes and their effects on the tracer trajectories, velocities and accelerations in a pseudo-spectral turbulent channel flow DNS. They showed that schemes based on linear interpolation and on sixth-order Lagrange polynomials quickly diverge from the exact evaluation of the velocity field using its spectral coefficients, while interpolations based on Hermite polynomials are much more accurate at correctly representing the particle velocities and accelerations over time. In particular, they found that low-order interpolation schemes induce large oscillations of the particle acceleration prediction in time. This is partially explained by

the authors' choice of evaluating the particle acceleration from the temporal derivative of its velocity. In that case, the (possibly small) interpolation error carried by the velocity signal is strongly amplified when the velocity is differentiated over time.

In the following, different possible interpolation schemes are introduced and examined in the context of our $Re_\tau = 1440$ simulation. Then, a choice is made based on a trade-off between numerical accuracy and time efficiency.

2.2.2.1 Interpolation methods

Spectral interpolation Given the pseudo-spectral nature of the Eulerian flow solver, it is technically possible to evaluate an Eulerian field at any arbitrary point of the domain with *spectral* accuracy, using the spectral coefficients of the field of interest. For instance, the velocity at a given point (x, y, z) can be evaluated as

$$\boldsymbol{u}(x,y,z,t) = \sum_{i=-N_x/2}^{N_x/2-1} \sum_{k=-N_z/2}^{N_z/2-1} \sum_{j=0}^{N_y} \hat{\boldsymbol{u}}_{ijk}(t)\, T_n(y)\, e^{\mathbb{i}(\alpha_i x + \beta_k z)}, \tag{2.48}$$

where $\hat{\boldsymbol{u}}_{ijk}$ are the spectral coefficients of the velocity field decomposed into Fourier and Chebyshev polynomials, T_n is the n-th Chebyshev polynomial, and $\alpha_i = 2\pi i / L_x$ and $\beta_k = 2\pi k / L_z$ are the streamwise and spanwise Fourier wave numbers (see also section 2.1.2.2). Spectral interpolation yields the highest possible accuracy, but at an exceedingly high computational cost that makes it impractical for actual simulations. Indeed, to interpolate a field at the position of a single particle, it is necessary to evaluate several Fourier and Chebyshev basis functions at the particle position (which can be done relatively efficiently by using recurrence relations). More critically, due to the global nature of eq. (2.48), it is necessary to perform a sum over all the spectral coefficients of the field weighted by the evaluated basis functions. As the spectral coefficients are typically distributed over all the computing processes in a parallel simulation, this requires intensive communications between processes. Needless to say, this approach becomes very slow when the number of particles is large, as the same operations need to be applied for each particle. For this reason, to our knowledge this approach is never used in spectral codes other than to evaluate the accuracy of faster interpolation methods.

Trilinear interpolation In contrast, trilinear interpolation is one of the fastest means to estimate three-dimensional field data at an arbitrary location, albeit at the cost of poor accuracy. It requires the data to be known on a regular grid in physical space. To determine the value of a field $u(\boldsymbol{x})$ at a point $\boldsymbol{x} = (x, y, z)$, the values of u at the 8 vertices of the cell where the point is located are needed, as represented in fig. 2.6. A trilinear interpolation can be constructed as a composition of 7 subsequent one-dimensional linear interpolations. First, four linear interpolations are performed in one direction (say x, i.e. along the cell edges AB, DC, EF and HG in fig. 2.6), then the results are interpolated along a second direction (e.g. along y, on the planes $ABCD$

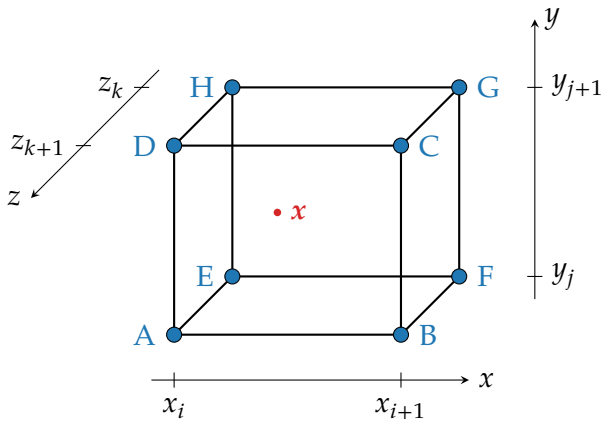

Figure 2.6. Schematic of an eight-point interpolation cell used for trilinear and Hermite interpolations.

and *EFGH*). A last interpolation along the third direction gives the approximate value at $\boldsymbol{x}$. This interpolation is said to be first-order accurate since, along each direction, the interpolated function is approximated by a first-order polynomial (the *interpolant*), whose coefficients are such that the interpolant matches the actual values of u at the grid nodes.

In terms of the parallel implementation of trilinear interpolation, it is important to note that the vertices in fig. 2.6 may belong to different MPI subregions. For instance, if the domain is decomposed in the x direction, the field data associated to vertices A, D, E, and H may be stored in one MPI process, while vertices B, C, F and G may belong to a neighbouring process. When a pencil decomposition scheme is used (see section 2.1.3.1), the data in one interpolation cell may be split among up to four different processes. For this reason, previous to applying interpolations, MPI processes must exchange data with their neighbours so that they have access to the field values at the interfaces. Since the exchanges are performed locally between small groups of processes, and since the amount of exchanged data is relatively small, this operation is fast compared to other operations such as global data transpositions required by FFTs.

Hermite interpolation One possible way to improve the accuracy of trilinear interpolation is to make the interpolant match not only the values of u at the grid nodes, but also the values of the derivatives of u. This is the principle of the Hermite interpolation scheme.

Let us first consider the interpolation of an unknown function $u(x)$ defined in $x \in [x_0, x_1]$, whose values and derivatives $u' = \mathrm{d}u/\mathrm{d}x$ are known at the boundaries $x = x_0$ and x_1. The Hermite interpolant of u can be constructed as

$$\tilde{u}(x) = u(x_0)\, H_0(X) + u(x_1)\, H_1(X) + \Delta x \left[u'(x_0)\, G_0(X) + u'(x_1)\, G_1(X)\right], \qquad (2.49)$$

where the H_i and G_i are third-order polynomials, $\Delta x = x_1 - x_0$, and $X = (x - x_0)/\Delta x$. It

can be shown that, in order for $\tilde{u}$ and $\tilde{u}'$ to respectively match u and u' at the boundaries, these polynomials are necessarily given by

$$H_0(x) = (1+2x)(1-x)^2, \qquad G_0(x) = x(1-x)^2, \tag{2.50}$$

$$H_1(x) = x^2(3-2x), \qquad G_1(x) = -x^2(1-x). \tag{2.51}$$

In three dimensions, Hermite interpolation in an interval $\boldsymbol{x} = (x, y, z) \in [x_0, x_1] \times [y_0, y_1] \times [z_0, z_1]$ can be constructed in an analogous way to trilinear interpolation, by composition of subsequent 1D interpolations in the three spatial directions. This procedure leads to an interpolant of the form

$$\begin{aligned}
\tilde{u}(\boldsymbol{x}) = \sum_{i=0}^{1}\sum_{j=0}^{1}\sum_{k=0}^{1} & H_i(X)\,H_j(Y)\,H_k(Z)\,u(\boldsymbol{x}_{ijk}) + \Delta x\,G_i(X)\,H_j(Y)\,H_k(Z)\,\frac{\partial u}{\partial x}(\boldsymbol{x}_{ijk}) \\
& + \Delta y\,H_i(X)\,G_j(Y)\,H_k(Z)\,\frac{\partial u}{\partial y}(\boldsymbol{x}_{ijk}) + \Delta z\,H_i(X)\,H_j(Y)\,G_k(Z)\,\frac{\partial u}{\partial z}(\boldsymbol{x}_{ijk}) \\
& + \Delta x\Delta y\,G_i(X)\,G_j(Y)\,H_k(Z)\,\frac{\partial^2 u}{\partial x\partial y}(\boldsymbol{x}_{ijk}) + \Delta x\Delta z\,G_i(X)\,H_j(Y)\,G_k(Z)\,\frac{\partial^2 u}{\partial x\partial z}(\boldsymbol{x}_{ijk}) \\
& + \Delta y\Delta z\,H_i(X)\,G_j(Y)\,G_k(Z)\,\frac{\partial^2 u}{\partial y\partial z}(\boldsymbol{x}_{ijk}) \\
& + \Delta x\Delta y\Delta z\,G_i(X)\,G_j(Y)\,G_k(Z)\,\frac{\partial^3 u}{\partial x\partial y\partial z}(\boldsymbol{x}_{ijk}),
\end{aligned} \tag{2.52}$$

where Y, Z, Δy and Δz are defined analogously to X and Δx, and $\boldsymbol{x}_{ijk} = (x_i, y_j, z_k)$ represents one of the corners of the interpolation box (nodes A through H in fig. 2.6).

According to eq. (2.52), three-dimensional Hermite interpolations require not only the gradient of $u(\boldsymbol{x})$ to be known at the grid nodes, but also its mixed second- and third-order derivatives. This means that, previous to interpolating a scalar field, a total of 7 spatial derivatives must be computed in the DNS. If the derivatives are computed in spectral space (to preserve the spectral accuracy of the fields), this has a considerable computational cost since each derivative must be transformed back to physical space via a 3D FFT. For this reason, we also examine a *partial* Hermite interpolation scheme in which the terms in eq. (2.52) associated to the mixed derivatives are neglected, so that only the first-order gradients are computed.

As with trilinear interpolation, neighbouring MPI processes must exchange field data stored at the interface between MPI subregions. In the case of Hermite interpolation, it is necessary to exchange not only the interpolated field but also its derivatives. This represents a higher communication cost, which is however much smaller than the cost of calculating the gradients themselves. It is finally worth noting that both the computation of the derivatives and the data exchanges between neighbouring processes are done once per interpolated scalar field, while the sum in eq. (2.52) is performed once for each particle and for each field. In practice, this means that adding more particles to a simulation does not impact the computational time provided the number of particles is kept reasonably small. We have found this to be the case when tracking

nearly 5 million particles in our $Re_\tau = 1440$ simulations.

Other interpolation schemes The list of interpolation methods introduced above is not exhaustive, and other schemes have been applied in existing numerical studies. For instance, Yeung et al. have used cubic splines to interpolate the fluid velocity at the tracer positions in isotropic [157, 206] and in homogeneous shear flow DNS [165]. In channel flow DNS, Pitton et al. [134] used sixth-order Lagrange polynomials to study the dispersion of fluid and inertial particle pairs. As mentioned above, however, Lagrange polynomials were considered insufficient by Choi et al. [41] to correctly capture the fluid particle accelerations in channel flow simulations. Therefore, they settled for a hybrid between four-point (seventh-order) Hermite polynomials in the two homogeneous directions (as opposed to the two-point/third-order Hermite polynomials introduced above), and Chebyshev spectral interpolation in the wall-normal direction. Such a high-order scheme is not required in our work as our approach to compute the tracer acceleration is less sensible to interpolation error (see section 2.2.2.3 below).

Finally, van Hinsberg et al. [186] proposed an interpolation scheme based on B-splines for spectral DNS codes in periodic boxes (i.e. based on Fourier decompositions in the three spatial directions). Their approach is particularly interesting since it achieves a similar accuracy to Hermite interpolation, but without the high cost of computing field derivatives and associated FFTs. As a perspective, an interesting development would be to adapt their scheme to our channel flow DNS, perhaps by using B-splines in the homogeneous directions and another scheme (e.g. Chebyshev, Hermite) in the wall-normal direction.

2.2.2.2 *Evaluation and choice of interpolation scheme*

The interpolation methods described above are assessed in the $Re_\tau = 1440$ case (see table 2.1 for simulation parameters). For each scheme, 100 fluid particles are seeded at the same initial positions, using the same initial velocity field, and are tracked for a duration $\Delta T^+ \approx 65$. Particle data is saved at each iteration of simulation, i.e. every $\Delta t_p^+ \approx 1/30$. Such a high-frequency sampling is typically not required for Lagrangian statistics (in chapter 3 we use $\Delta t_p^+ \approx 1/3$ for acceleration statistics), but is required for capturing the spurious oscillations associated to interpolation errors.

In table 2.2, the performance of the different interpolation methods is evaluated. For local interpolation schemes (Hermite and trilinear), initialisation operations clearly have the highest impact on performance. The number of particles is expected to have a negligible influence on the computation time, even for particle numbers of the order of one million. The initialisation cost of partial Hermite interpolation is roughly 3/7 of that of full Hermite interpolation, which is consistent with the number of derivatives computed in each case. As for spectral interpolations, although they do not need an initialisation step, the cost of interpolation per particle is extremely high compared to the local schemes, rendering simulations with more than a hundred particles impractical.

Table 2.2. Average time for the interpolation of a scalar field using different interpolation schemes. *Initialisation* refers to data exchanges at the MPI partition interfaces and, for Hermite interpolations, computation of field gradients. *Interpolation* corresponds to the actual interpolation time per particle (not including initialisation time). *Total* refers to the total interpolation time for 100 particles. Times are in milliseconds. Simulations were performed on 256 processors.

	Initialisation (ms)	Interpolation (ms / particle)	Total (ms)
Spectral	0	30.5	3050
Hermite (full)	3540	5.9×10^{-6}	3540
Hermite (partial)	1533	4.0×10^{-6}	1533
Trilinear	10.6	1.2×10^{-6}	10.6

The temporal evolution of a sample tracer particle as estimated from the examined interpolation schemes is presented in fig. 2.7. In the observed time interval, both Hermite interpolations correctly reproduce the particle trajectory when compared to spectral interpolation (fig. 2.7a), while the trajectory predicted by trilinear interpolation diverges over time from the other schemes. Figure 2.7b shows the spanwise component of the particle velocity over time. This component was arbitrarily chosen, and the same observations are valid for the other velocity components. The velocity signal obtained from trilinear interpolation importantly differs from that of the other schemes, presenting high-amplitude fluctuations with a seemingly constant oscillation period which corresponds to the average time the particle needs to cross a numerical grid cell. This is demonstrated by the associated power spectrum in fig. 2.7c, where the highest peak is located at the average grid-cell-crossing frequency $f_g = V_x/\Delta x$ with V_x the time-averaged streamwise particle velocity and Δx the streamwise grid spacing in the DNS. Lower-amplitude peaks are also observed at the harmonics of f_g. This estimation of the crossing frequency is valid as long as the streamwise velocity dominates over the other components, as is generally the case in wall-bounded flows.

As illustrated by fig. 2.7b, Hermite interpolations accurately capture the particle velocity. Nevertheless, they are still subject to the same type of spurious oscillation at the frequency f_g, albeit at a significantly reduced fluctuation amplitude (fig. 2.7c). Full Hermite interpolation provides a noticeable improvement in the damping of oscillations when compared to the partial Hermite scheme, but at a considerably higher computational cost.

The above observations are also valid for the particle acceleration, whose spanwise component is examined in fig. 2.7(d-e). It is worth noting that the interpolation error associated to the velocity and the acceleration are of the same order of magnitude, as inferred by the amplitude of the peaks in the respective power spectra. As noted below in section 2.2.2.3, this is a consequence of directly interpolating the acceleration field computed in the Eulerian frame. The error in the particle acceleration is considerably higher when the acceleration is obtained as the temporal derivative of the (interpolated) particle velocity.

To estimate the effect of the different interpolation schemes on Lagrangian statistics, the Lagrangian auto-correlation of the particle acceleration components is computed

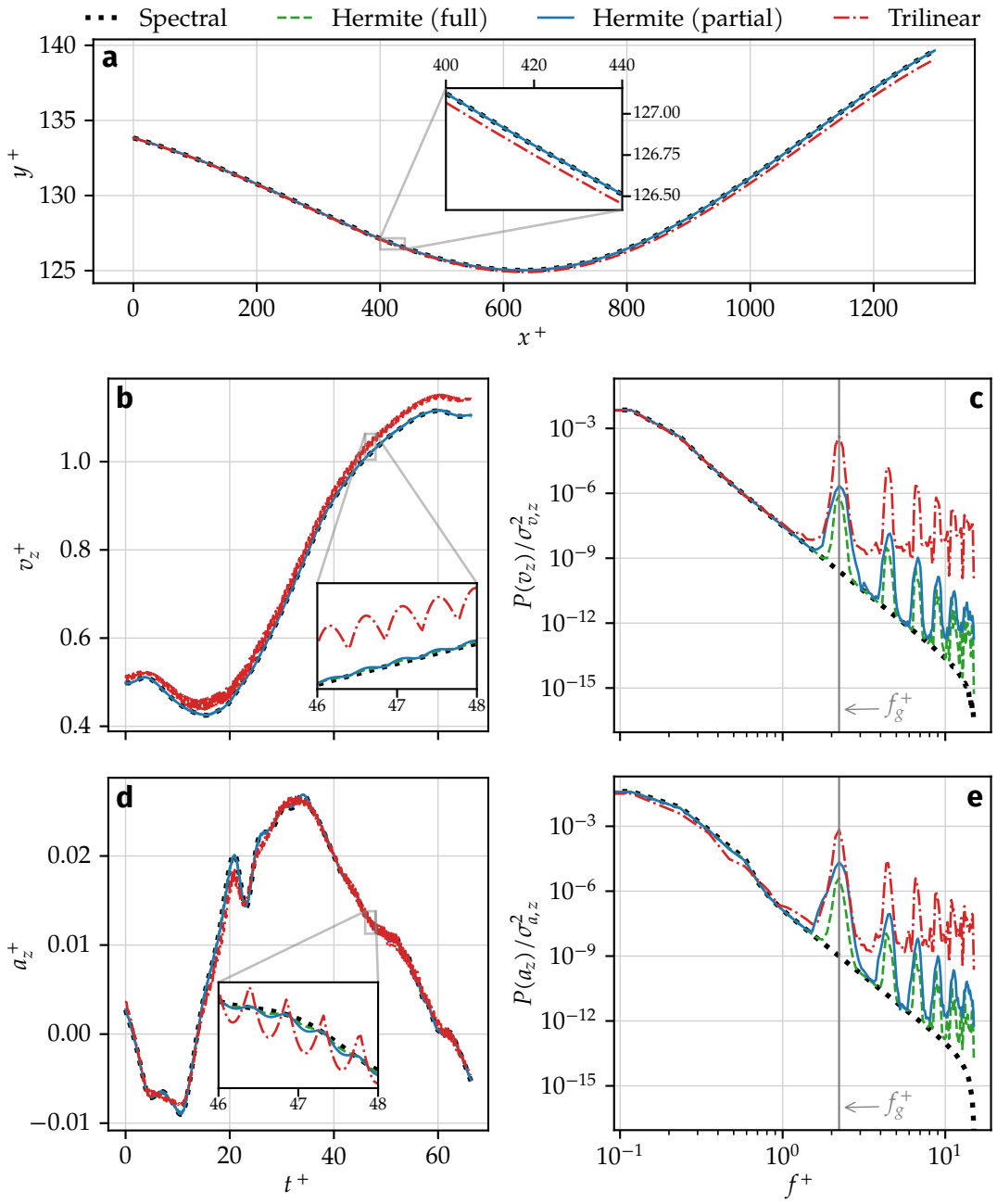

Figure 2.7. Assessment of different interpolation schemes for a single particle. (a) Particle trajectory over time, projected on a x-y plane. (b) Spanwise particle velocity over time and (c) associated power spectrum normalised by the spanwise particle velocity variance. (d-e) Same for the spanwise particle acceleration. In (c) and (e), the vertical line marks the average streamwise grid-cell-crossing frequency of the particle, $f_g = V_x/\Delta x$ (see text for details).

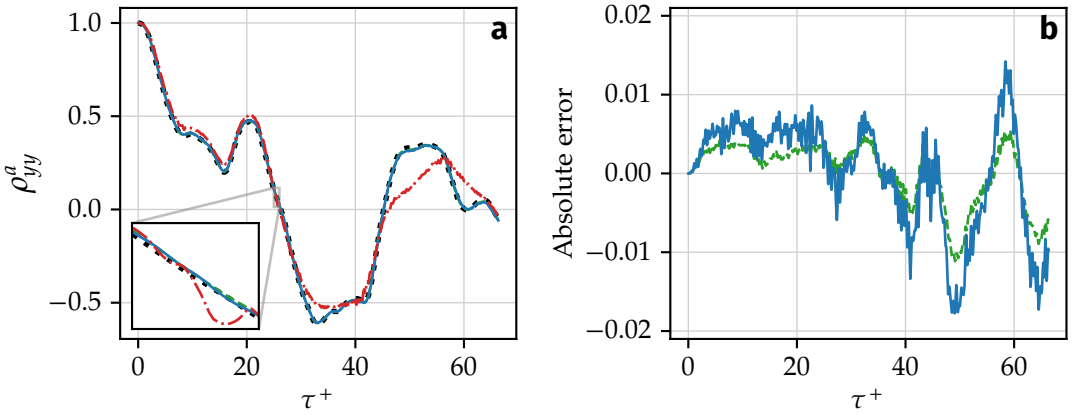

Figure 2.8. (a) Lagrangian auto-correlation of wall-normal acceleration resulting from different interpolation schemes. The inset shows an interval $\Delta t^+ = 1$. (b) Error of partial and full Hermite interpolations relative to spectral interpolation, $E(\tau) = \rho^a_{yy}(\tau) - \rho^a_{yy,\text{spectral}}(\tau)$. (See fig. 2.7 for legends.)

from the 100 particles used in the test. The Lagrangian acceleration correlation tensor is defined here as

$$\rho^a_{ij}(\tau) = \frac{\langle a'_i(t_0)\, a'_j(t_0+\tau)\rangle}{\langle a'^2_i(t_0)\rangle^{1/2}\langle a'^2_j(t_0+\tau)\rangle^{1/2}}, \tag{2.53}$$

where the Lagrangian average $\langle\cdot\rangle$ is an ensemble average performed over all particles, and the primes represent a fluctuation about the Lagrangian average, i.e. $a'_i(t) = a_i(t) - \langle a_i(t)\rangle$. This definition differs from the one used later in chapter 3 in that it does not take into account the initial particle wall distance y_0, rendering it inappropriate for a phenomenological analysis of wall-bounded flows. It is nevertheless used given the reduced number of particles in the interpolation tests. The resulting wall-normal acceleration auto-correlation is presented in fig. 2.8a. Consistently with the results of fig. 2.7, trilinear interpolation fails to correctly predict the correlations, with an error that increases over time. The gap between Hermite and spectral interpolations is almost imperceptible at all times. The error associated to the partial Hermite scheme is only slightly more pronounced than that of full Hermite interpolation (fig. 2.8b), confirming that the former is sufficiently adapted for the computation of Lagrangian correlations.

Based on the observations in this section, we choose to use the partial Hermite interpolation scheme for the simulations presented in this work, as it represents an appropriate balance between time efficiency and accuracy of the resulting Lagrangian statistics.

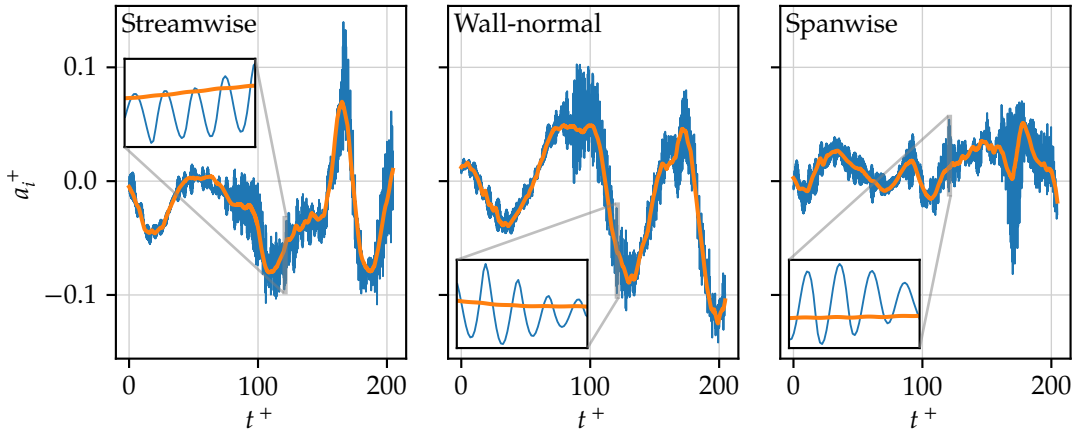

Figure 2.9. Acceleration of a single fluid particle over time in a $Re_\tau = 1440$ simulation. From left to right: streamwise, wall-normal and spanwise acceleration components. The acceleration is alternatively computed by interpolation of the acceleration field (thick orange lines) and by differentiation of the particle velocity (thin blue lines). The fluid velocity and acceleration fields are interpolated using a partial Hermite scheme. The particle is located within $y^+ \in [80, 140]$. Insets show accelerations over the temporal range $t^+ \in [120, 122]$.

2.2.2.3 Note on fluid particle accelerations

As mentioned in section 2.2.1, tracer accelerations are obtained from interpolation of the fluid acceleration first computed on the Eulerian grid. Since the tracer acceleration is simply the time derivative of its velocity, a more straightforward approach would instead be to numerically differentiate the tracer velocity over time. For instance, a centred finite difference scheme could be used, $\boldsymbol{a}^n \approx (\boldsymbol{v}^{n+1} - \boldsymbol{v}^{n-1})/(2\Delta t)$. This kind of approach is very commonly used in DNS studies of Lagrangian acceleration statistics (see for instance [157, 179, 206] in HIT and [41] in channel flow).

Figure 2.9 shows that, when using partial Hermite interpolations, the differencing approach for computing the particle acceleration leads to very high-amplitude noise in the generated particle acceleration signal. The noise is explained by an amplification of the (relatively weak) interpolation error carried by the velocity signal observed in fig. 2.7(b-c). The present acceleration signals show a clear oscillation period which is, as for the velocity, characterised by the grid-cell-crossing frequency f_g, however at an oscillation amplitude that is orders of magnitude more intense.

Similar issues were observed by Choi et al. [41] in channel flow DNS when computing fluid particle accelerations from their velocity history. As mentioned above, the authors resorted to using very high-order interpolation schemes to suppress the spurious oscillations. Using a different version of our DNS code and an independent implementation of the particle tracking algorithms, Zamansky et al. [207] found the same issues, and applied a different solution consisting in low-pass filtering the velocity signal before differentiating it. Their approach is based on a technique first proposed by Mordant et al. [113] for experimentally measured particle tracks, in which

they estimated particle accelerations from the convolution of the particle trajectories against the second derivative of a Gaussian kernel, which resulted in a low-pass filtered acceleration signal.

From a practical viewpoint, the interpolating approach can also be applied for studying the dynamics of inertial particles, since their motion may be determined by, among other forces, an added mass term written in terms of the fluid acceleration at the particle positions.

2.2.3 Implementation details and parallel strategy

The implementation of the particle tracking algorithms is consistent with the domain decomposition strategy of the Eulerian solver (see section 2.1.3.1). Namely, each MPI process manages the data associated to the particles located within its local domain subregion. The process is therefore responsible for updating the local particle properties, including position, velocity and acceleration vectors. This also means that particle data is transferred from one MPI process to another when a particle crosses the boundaries of a parallel subregion.

Regarding the in-memory structure of the particle data, there exist two common strategies referred to as *Array of Structures* (AoS) and *Structure of Arrays* (SoA). The first consists in defining a `Particle` structure that holds all the data associated to a single particle. In this case, the data from all the particles is stored in a single array of `Particle` objects. The second corresponds to storing all the particle data in a few large arrays. For instance, a single array may store the position of all particles, another their velocities, and so on. From an implementation standpoint, the AoS strategy is generally considered as more convenient, as it is naturally consistent with the object-oriented programming paradigm. On the other hand, it has been argued that the SoA strategy performs better in DNS codes due to memory locality, leading to a better use of cache and vectorisation [66].

We decide to use a hybrid approach in which some particle properties are stored in a `Particle` structure, while others are stored in separate arrays. In order to transfer particle data from one MPI process to another (when a particle crosses a parallel subregion), the particle only needs to remember a subset of its properties, which are those contained in the `Particle` structure. In our implementation, these properties are the current particle position, velocity, acceleration, as well as a unique identifier (an integer value), and three Cartesian indices identifying the current location of the particle in the Eulerian grid. To transfer particle data between processes, we define a custom MPI data type describing the structure of these fields within a `Particle` object. Data stored in separate arrays include the particle velocities at a previous iteration (for advancing particle positions; see eq. (2.47)), and, for inertial particles, the velocity and acceleration of the fluid at the position of the particles.

As a final note, the current implementation allows to track multiple independent particle sets, each having different properties, within the same simulation. For instance, it is possible to follow, at the same time, a set of fluid particles along with multiple sets of inertial particles having different Stokes numbers or using different models for

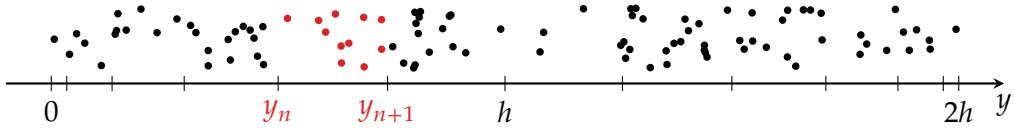

Figure 2.10. Illustration of wall-normal bins for computation of Lagrangian statistics. Dots represent randomly positioned particles. Here, bin edges follow a Gauss–Lobatto node distribution, $y_n/h = 1 - \cos(n\pi/N)$, with $N = 12$. Coloured particles belong to the same wall-normal bin $[y_n, y_{n+1})$ and count towards the statistics associated to that bin.

their equations of motion. This approach is valid as long as the particles do not have a feedback effect on the carrying flow, as in the case of a one-way coupling approximation. The implementation is very convenient for studying the effect of the very same flow on different kinds of particles, while greatly reducing the computational cost associated to the numerical solution of the Navier–Stokes equations and to the initialisation of Hermite interpolations (as these operations are shared among all the particle sets).

2.2.4 Validation against Eulerian statistics

Single-point single-time flow statistics can be computed both from the Eulerian and the Lagrangian reference frames, and both approaches yield in theory equivalent results. To validate our Lagrangian tracking algorithms, Lagrangian acceleration moments are compared to their Eulerian counterparts, which were already presented in section 2.1.4.4. This validation also serves as an introduction to some of the technicalities associated to the calculation of Lagrangian statistics.

In wall-bounded flows, single-time Lagrangian statistics depend on the instantaneous wall distance of the particles. Therefore, to compute statistics, the wall-normal coordinate is discretised into wall-normal bins as illustrated by fig. 2.10. For each temporal snapshot, every particle is assigned a wall-normal bin according to its instantaneous position, and the current particle state is used to update the statistics associated to that bin.

The choice of bin edges is arbitrary. We decide to use the same Gauss–Lobatto node distribution that is used by the DNS solver [eq. (2.16)] in order to better capture the rapid variation of the flow statistics in the near-wall region. If the particles are uniformly distributed throughout the domain, this has the disadvantage that fewer particles are found in the smaller bins near the walls, and therefore near-wall statistics take longer to converge. This issue is clearly illustrated by fig. 2.10 where only a few particles are located in the wall-adjacent bins (those with edges at $y = 0$ and $2h$).

The variance and skewness of the fluid acceleration components obtained both from Eulerian acceleration fields and from Lagrangian particle data are compared in fig. 2.11. The agreement between both approaches is generally very good, with the only exception being the skewness of the wall-normal acceleration within the viscous sublayer. This difference is explained by the lack of statistical convergence in the Lagrangian case, since, as noted above, the wall-normal bins near the wall are

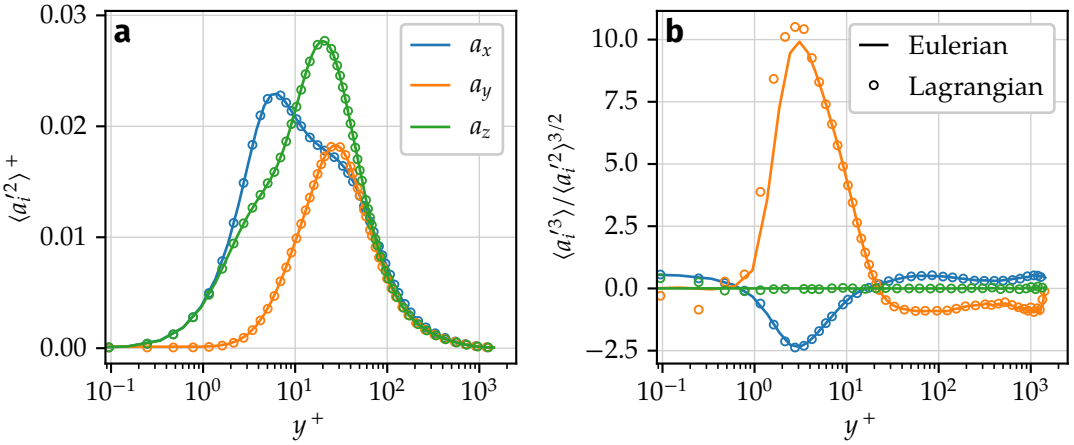

Figure 2.11. Acceleration variance (left) and skewness (right) profiles obtained from Eulerian fields and from Lagrangian particle data at $Re_\tau = 1440$.

much smaller than in the rest of the channel, leading to a lower number of samples per bin in that region. As presented in appendix A.1, similar differences are observed for the acceleration flatness (fig. A.2d), while for lower-order velocity and acceleration moments the agreement is excellent at all wall distances.

2.2.5 Conclusion

The method for tracking fluid particles in our channel flow DNS is described here. To determine the velocity and acceleration of a fluid particle, the fluid velocity and acceleration fields, known in the Eulerian reference frame, are evaluated at the instantaneous particle position using a variant of the third-order Hermite interpolation scheme. Then, a second-order Adams–Bashforth scheme is applied to advance the particle position in time based on its new velocity.

The chosen interpolation scheme, based on regular 3D Hermite interpolation but neglecting terms containing high-order field derivatives, is appropriate for the estimation of fluid particle velocities and accelerations as well as Lagrangian statistics such as acceleration auto-correlations. Furthermore, the chosen approach for evaluating the fluid particle accelerations proves to be significantly more robust to interpolation error than the more common method consisting in time-differentiating the particle velocity signal. This enables us to avoid very-high-order interpolation schemes, as well as filtering steps, that have been used in similar works to suppress high-amplitude interpolation noise.

Details on the numerical implementation are briefly discussed, including the parallel implementation and the in-memory layout of particle data. The current implementation allows to simultaneously track particle sets with different properties within the same simulation. This is convenient when analysing the dynamics of different groups of inertial particles using point-particle models with a one-way coupling approximation.

Finally, acceleration statistics obtained from Lagrangian particle data are compared

with Eulerian one-point statistics. The very good agreement between both approaches serves as a validation of the Lagrangian particle tracking implementation.

2.3 General conclusion

The pseudo-spectral method used to numerically solve the Navier–Stokes equations in a periodic channel flow geometry is described in this chapter. The velocity field is decomposed into Fourier modes in the two periodic directions and Chebyshev polynomials along the wall-normal coordinate. Through an appropriate selection of trial and test function spaces, the pressure term of the Navier–Stokes equations is eliminated. The massively parallel implementation of the method is described, including the domain decomposition strategy and its consequences in terms of global FFT operations and on-disk storage of solution files. Then, the numerical and physical parameters used for our $Re_\tau = 1440$ simulations are introduced. By analysing the decay of Eulerian velocity and acceleration auto-correlations within the numerical channel in the large Reynolds number case, the chosen domain size is shown to be adapted for studying tracer dispersion and Lagrangian flow statistics. Moreover, computed velocity and acceleration statistics are validated against DNS results at similar Reynolds numbers found in the literature [67, 69, 202].

Lagrangian particle tracking algorithms and their integration within the existing DNS code are then described. Fluid particle velocities and accelerations are estimated from interpolation of the respective Eulerian fields. For this purpose, different interpolation methods are examined. Their effects on tracer trajectories, velocities and accelerations, as well as on resulting Lagrangian statistics, are assessed. A partial third-order Hermite interpolation scheme is chosen as it represents a reasonable trade-off between time efficiency and accuracy. Implementation details are discussed including the parallelisation of particle tracking algorithms and the in-memory layout of particle data. Finally, the implementation is validated by comparison of single-point single-time Eulerian acceleration statistics with equivalent Lagrangian statistics.

3 Lagrangian statistics of acceleration

As discussed in the introduction, understanding the Lagrangian dynamics of acceleration in turbulent flows is of great importance for describing the small scales of the flow, since the components of acceleration vary very rapidly along tracer trajectories when compared to the fluid velocity. The characteristic times over which velocity and acceleration components evolve can serve as input for stochastic models aiming either at predicting the dynamics of tracer particles in fluid flows [136, 138, 153], or at predicting the unresolved subgrid-scale flow dynamics in large eddy simulations (LES) [148, 208]. From a phenomenological standpoint, the dynamics of Lagrangian acceleration is closely related to the presence of small-scale structures including vortex filaments in turbulent flows, which induce intense centripetal accelerations towards their centre of rotation [118, 179]. Analogously, in the case of wall-bounded turbulent flows, large-magnitude accelerations are often associated to quasi-streamwise vortices in the near-wall region [93, 202].

In this chapter, Lagrangian statistics of acceleration in a turbulent channel flow are presented and the associated Lagrangian time scales are characterised. The statistics are obtained both from PTV measurements performed by N. Stelzenmuller and N. Mordant in a turbulent channel flow at the Laboratoire des Écoulements Géophysiques et Industriels (LEGI) in Grenoble, France, and from our direct numerical simulations at $Re_\tau = 1440$ described in chapter 2. An important part of this chapter is adapted from our article 'Lagrangian Acceleration Statistics in a Turbulent Channel Flow' [174].

In section 3.1, the channel flow experiments performed at LEGI are presented. An initial description of the flow is given in section 3.2 in terms of Eulerian velocity and acceleration single-point statistics obtained from experiments and DNS. Section 3.3 introduces the approach for computing Lagrangian single-particle statistics in wall-bounded flows. In section 3.4, this approach is used to describe the time correlations of fluid acceleration along Lagrangian trajectories. The associated acceleration (and velocity) time scales are discussed in section 3.5. In section 3.6, the probability distribution of the acceleration components is presented in the channel and compared to the isotropic case. Finally, section 3.7 is devoted to the conclusions.

3.1 Experimental setup

The channel flow installation at LEGI consists in a closed-loop water tunnel with a 3.2 m long test section shown in fig. 3.1. The experiment is briefly described below. For more details the reader is referred to Stelzenmuller [173].

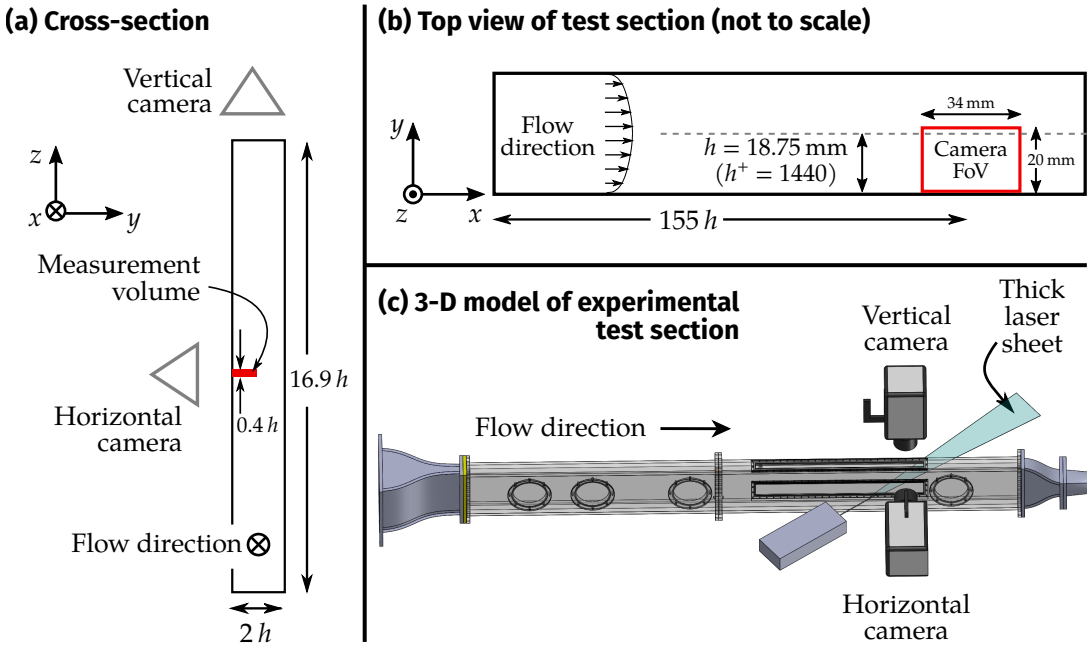

Figure 3.1. Sketch of the turbulent channel used in the experiment at LEGI. (a) Cross-section of the channel (spanwise direction is vertical), illustrating the aspect ratio 16.9:2 of the channel section as well as the positions of the two cameras. (b) Streamwise–wall-normal slice of the test section and field of view (FoV) of the vertical camera. (c) 3D rendering of the experimental setup, including the positions of the two cameras and the laser sheet used to illuminate the measurement volume. Figure adapted from Stelzenmuller [173, fig. 2.2].

3.1.1 Channel flow

Channel flow experiments are performed in a closed-loop water tunnel. The test region of the channel has a rectangular cross-section of dimensions $L_y \times L_z = 2\,h \times 16.9\,h = 37.5 \times 317\,\mathrm{mm}^2$ (fig. 3.1a). The high aspect ratio $L_z/L_y = 8.45$ enables the flow to be statistically homogeneous in the spanwise direction far from the spanwise walls, as it is superior to the aspect ratio of 7 found by Dean to be required for this purpose [46, 173]. The mean centreline velocity is $U_0 = 1.75\,\mathrm{m\,s^{-1}}$, resulting in a centreline Reynolds number of $Re \approx 31\,000$. The Reynolds number based on the friction velocity u_τ at the walls is $Re_\tau \approx 1350$.

To achieve a fully developed turbulent state, i.e. a statistically homogeneous flow in the streamwise direction, the measurement section is placed downstream of a $L = 2.9\,\mathrm{m}$ long development region (seen in fig. 3.1(b-c)). The development length, $L/h = 155$ in terms of the channel half-width h, is considered to be long enough to achieve a fully developed flow except very close to the channel centre, where the boundary layers on the two sides of the channel are not fully merged [112, 173]. The entrance of the development section is equipped with boundary layer trips to ensure the even development of the boundary layers along the two walls.

3.1.2 Particles and PTV system

In the experiment, water is chosen as the working fluid as it allows to use nearly neutrally-buoyant particles. Concretely, particles are fluorescent polystyrene spheres with diameter $d_p = 10.2\,\mu\text{m}$ and density $\rho_p = 1.05\,\text{g}\,\text{cm}^{-3}$. The particle diameter is smaller than the viscous length scale $\delta_\nu = \nu/u_\tau = 14\,\mu\text{m}$ in the present experimental conditions. Therefore, particles are expected to faithfully follow the carrying fluid, acting as fluid tracers, even in the viscous sublayer of the channel. The Stokes number of the particles is small, ranging from $St \approx 0.017$ near the wall to 9.8×10^{-4} at the channel centre [173]. Here, the Stokes number is defined as the ratio between the particle relaxation time $\tau_p = \rho_p d_p^2/(18\rho\nu)$ and the Kolmogorov time scale $\tau_\eta = (\nu/\varepsilon)^{1/2}$ describing the characteristic time of the dissipative (smallest) turbulent motions, with the mean turbulent energy dissipation rate estimated as $\varepsilon = \nu\overline{(\partial_j u_i')(\partial_j u_i')}$. Since the flow is statistically inhomogeneous in the wall-normal direction, the dissipation and its derived quantities (including the Stokes number) vary with wall distance, i.e. $\varepsilon = \varepsilon(y)$ and $St = St(y)$. In wall-bounded flows, it is also appropriate to define a Stokes number St_ν based on the viscous time scale $\tau_\nu = \nu/u_\tau^2 \approx 0.18\,\text{ms}$, yielding $St_\nu = \tau_p/\tau_\nu \approx 0.03$. The small value of the different Stokes numbers confirms that the particles are practically inertialess under the present experimental conditions.

Three-dimensional particle trajectories are measured by 3D PTV. The PTV system consists of a thick 25 W laser sheet that illuminates a $34 \times 20 \times 8\,\text{mm}^3$ region of the channel, along with two high-speed Phantom v2511 cameras with a maximum sampling frequency of 25 000 frames/s. The cameras are equipped with 180 mm and 150 mm macro lenses with optical filters tuned to the emission frequency of the fluorescent particles. The measurement volume covers about half of the channel width. Considering that particles are mainly swept away from the measurement volume by the mean streamwise velocity, the streamwise length of the illuminated area must be long enough for particles to stay in the area for a reasonably long time. The present dimensions of the measurement volume allow to capture the full decorrelation of the particle acceleration components, and close to the wall, of the particle velocity (where the mean flow is slower and the velocity decorrelates faster; see section 3.5). Particle velocities and accelerations are obtained by convolution of the trajectories against the derivatives of a Gaussian kernel, which also acts as a low-pass filter reducing measurement noise [113]. As recently discussed by Lawson et al. [92], a limitation of this method is that filtered quantities are undefined at the track ends, since the filter requires raw data to be available over a temporal window centred at the output time. Using synthetic Lagrangian particle tracking in isotropic turbulence DNS, the authors showed that this leads to a selection bias by which faster particles are under-represented, an effect that increases with the filter size. Since high accelerations are correlated with large velocities, this resulted in an underestimation of the acceleration variance in their simulations.

Fluorescent particles were chosen in the experiment to avoid two problems related to PTV measurements [173]. First, tracer particles are difficult to distinguish from microbubbles which are invariably present in the channel. By using fluorescent particles

along with adapted optical filters on the cameras, microbubbles can be eliminated from the generated PTV images. Secondly, the same optical filters also eliminate reflections of the laser light on the channel walls and thus improve contrast in the near-wall region.

Due to reflection of images on the wall and to inaccuracies related to the apparent particle size in the images, particle positions are not accurately measured in the viscous subregion and up to about 50 µm from the wall. Hence, the actual range of measurement spans over $y^+ \in [4, 1440]$, i.e. more than two decades of wall distance.

3.2 Velocity and acceleration profiles

To introduce the average Eulerian characteristics of turbulent channel flows, mean and variance velocity and acceleration profiles are presented in this section along the channel width. The statistics are obtained both from the experiment described in section 3.1 and from our DNS. As described above, DNS and experiments are performed at roughly the same Reynolds number $Re_\tau \approx 1440$.

Experimental statistics are computed from PTV-measured particle velocities and accelerations conditioned by their instantaneous wall distance. The wall-normal coordinate is discretised into bins using a similar procedure as the one described in section 2.2.4 for DNS data (see also fig. 2.10). Throughout this chapter, and unless stated otherwise, error bars on experimentally obtained statistics are estimated using the bootstrap method for a 95 % confidence interval [15, 48]. Uncertainty estimations also take into account, using a standard approach [106], the experimental precision associated to flow parameters used to report normalised statistics (e.g. ν, u_τ).

3.2.1 Velocity profiles

Figure 3.2 compares mean and variance velocity profiles from experiments and simulations. The numerical profiles have been validated earlier in section 2.1.4 against simulations at similar Reynolds numbers (see fig. 2.3). The mean velocity profile obtained from both approaches (fig. 3.2a) displays a clear logarithmic region in the range $40 \lesssim y^+ \lesssim 600$. Small departures of the experimental profile relative to the simulations are observed in the near-wall region ($y^+ < 30$) and towards the channel centre ($y^+ > 500$). These differences are within the uncertainty estimations. Pronounced differences are observed for the streamwise velocity variance profile (fig. 3.2b), in which case the experiment underestimates the u_x fluctuations at $y^+ < 50$, and in particular, fails to reproduce the variance peak at $y^+ \approx 15$. On the other hand, wall-normal and spanwise velocity variances are in good agreement between experiments and simulations at nearly all measured wall distances (with slight differences near the wall).

3.2.2 Acceleration profiles

Mean and variance acceleration profiles are shown in fig. 3.3. Similarly to the velocity profiles, acceleration statistics from our simulations have been validated in section 2.1.4

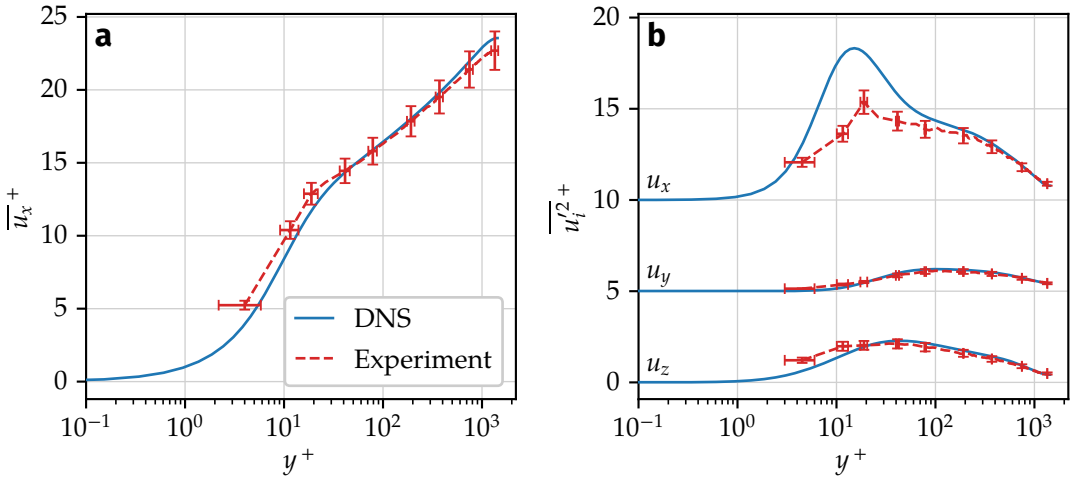

Figure 3.2. Mean and variance velocity profiles at $Re_\tau = 1440$. Comparison between experiments (dashed lines) and DNS (solid lines). Velocity variance profiles are shifted vertically for clarity. Error bars on experimental data represent a 95 % confidence interval.

against the channel flow DNS of Yeo et al. [202] at $Re_\tau = 600$ (see figs. 2.4 and 2.5). In the near-wall region, both experiments and simulations show a negative mean acceleration in the streamwise direction and a positive one in the wall-normal direction (fig. 3.3a). Far from the wall the sign of both components is inverted while being considerably weaker than near the wall. As explained in the next paragraph, near the wall the mean streamwise acceleration is mainly determined by the mean viscous stress, i.e. $\overline{a_x} \approx \nu \frac{\mathrm{d}^2 \overline{u_x}}{\mathrm{d}y^2} < 0$. As for the wall-normal acceleration, its positive value near the wall is explained by a mean pressure gradient directed towards the wall.

As noted in section 2.1.4, the mean acceleration components can be expressed in terms of the Reynolds stresses,

$$\overline{a_i} = \frac{\partial}{\partial x_j} \overline{u_i u_j} = \frac{\mathrm{d}}{\mathrm{d}y} \overline{u_i' u_y'}, \tag{3.1}$$

where the last relation is due to the statistical homogeneity of the flow in the streamwise and spanwise directions. It is readily seen from eq. (3.1) that the mean spanwise acceleration $\overline{a_z}$ is zero due to flow symmetry in that direction. Alternatively, Yeo et al. [202] studied the decomposition of the mean acceleration into an irrotational and a solenoidal contribution, which are respectively given by the mean pressure gradient and the mean viscous diffusion terms of the Reynolds-averaged Navier–Stokes equations. In the streamwise direction, when normalised by the viscous scales, this decomposition writes

$$\overline{a_x^+} = A_x^{I+} + A_x^{S+} = \frac{1}{Re_\tau} + \frac{\mathrm{d}^2 \overline{u_x^+}}{\mathrm{d}y^{+2}}. \tag{3.2}$$

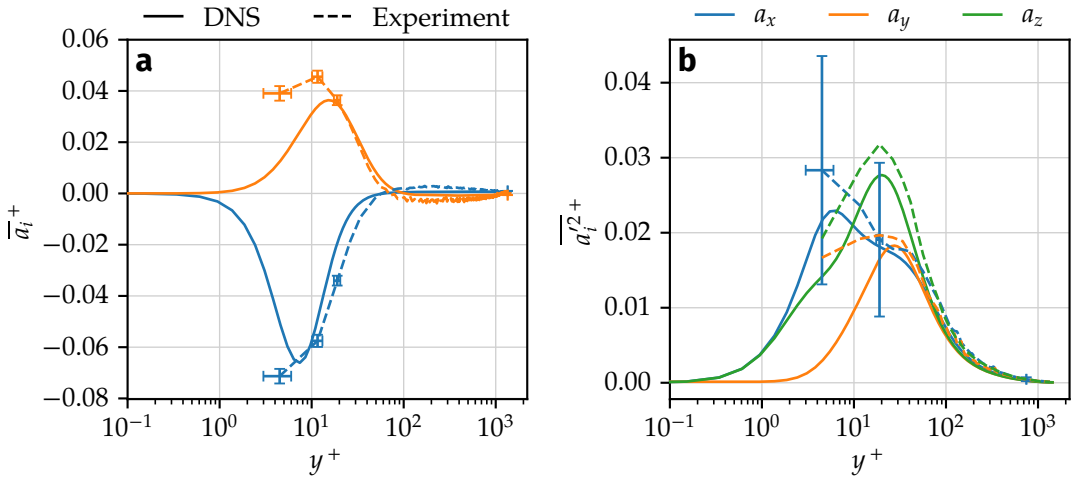

Figure 3.3. Mean and variance acceleration profiles at $Re_\tau = 1440$. Comparison between experiments (dashed lines) and DNS (solid lines). Error bars on experimental data represent a 95 % confidence interval.

Near the wall, the solenoidal term A_x^{S+} dominates [93, 202], suggesting that the negative peak of the mean streamwise acceleration at $y^+ \approx 7$ is a result of mean viscous stress near the wall. In the case of the mean wall-normal acceleration, the corresponding solenoidal term A_y^{S+} is zero (since $\overline{u_y} = 0$). Therefore, its profile is entirely determined by the mean wall-normal pressure gradient, i.e. $\overline{a_y} = -(1/\rho)\,\partial\overline{p}/\partial y$. At $y^+ < 20$, an increasingly large difference is observed between the mean wall-normal acceleration obtained from experiments and DNS. This may be explained by difficulties in the experiment to capture trajectories near the wall, as a consequence of light reflection on its surface.

Acceleration variance profiles are shown in fig. 3.3b. Qualitative agreement is found between experiments and simulations, despite large uncertainty in the experimental data near the wall. These differences are again attributed to the increasingly challenging reconstruction of experimental trajectories near the wall. Interestingly, the standard deviation of the acceleration components is more intense than the mean acceleration at all wall distances. As noted by Yeo et al. [202], the peak of $\overline{a_x'^2}$ coincides with that of $\overline{a_x}$ at $y^+ \approx 7$, and can again be explained by the effect of viscous stresses near the wall [93]. On the other hand, the peaks of wall-normal and spanwise acceleration variance are found in the outer part of the buffer layer, respectively at $y^+ \approx 30$ and 20. In that region, the presence of quasi-streamwise vortices is associated to intense centripetal accelerations towards the vortex centres [93]. The effect of these turbulent structures on particle accelerations is clearly seen in fig. 3.4, where a selection of particle trajectories subject to high accelerations near the wall is visualised. The displayed particles follow helical paths while having accelerations that are many times the acceleration standard deviation.[1]

[1] From fig. 3.3b, the highest standard deviation of an acceleration component is $a^+_{z,\mathrm{std}} \approx \sqrt{0.0275} \approx 0.17$.

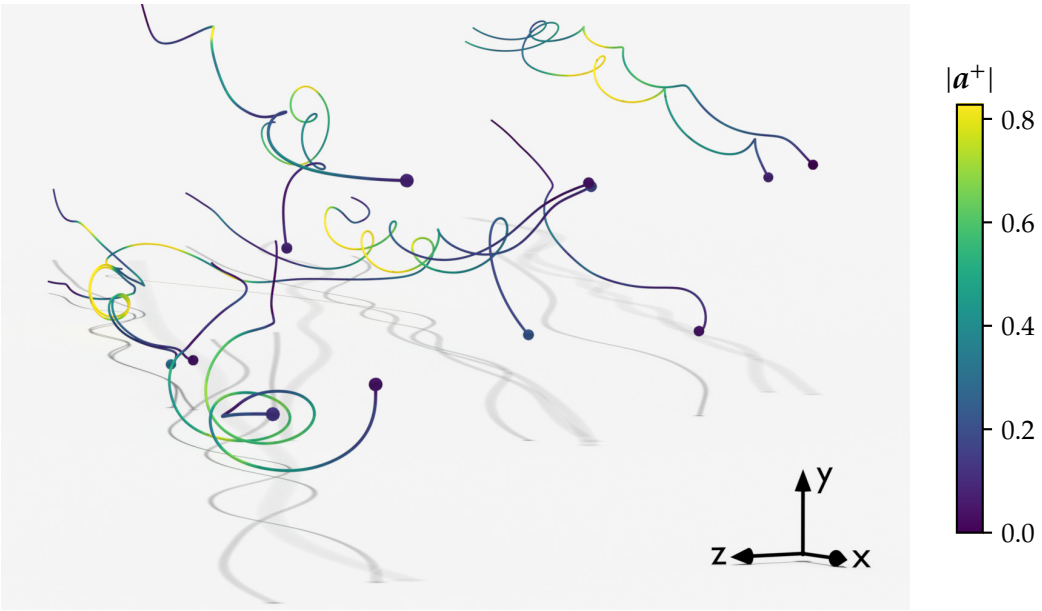

Figure 3.4. Sample high-acceleration particle trajectories obtained from DNS. Particles are located in the near-wall region ($y^+ < 200$). Trajectories are shown over $\Delta t^+ = 120$. The shadow is projected on the wall. Colours represent the norm of particle acceleration. In the experiment, $|a^+| = 1$ roughly corresponds to $430\,\mathrm{m\,s^{-2}}$. Rendered with Blender (`www.blender.org`).

3.3 Lagrangian description of wall-bounded flows

As demonstrated by fig. 3.4, Lagrangian particle tracking can reveal flow properties that are otherwise hidden in the Eulerian reference frame. To quantify Lagrangian aspects of the turbulent flow, including particle dispersion and relevant turbulent time scales, a statistical approach is appropriate. In the following, the statistical framework for characterising the flow from a Lagrangian viewpoint is introduced.

In the Lagrangian approach, the flow is described from the trajectories of fluid particles that are tracked from their initial position $\boldsymbol{x}_0$ at a reference time t_0. A Lagrangian trajectory is then parametrised by $\boldsymbol{x}_0$, t_0, and by a time delay τ relative to t_0. Hence, in the most general case, Lagrangian single-particle statistics[2] depend on the parameter set $(\boldsymbol{x}_0, t_0, \tau)$.

Lagrangian statistics have been extensively documented in statistically stationary homogeneous isotropic turbulence (HIT) or in nearly isotropic flows, as described in section 1.1. In these cases, Lagrangian statistics do not depend on the initial time t_0 due to statistical stationarity, nor on the initial position $\boldsymbol{x}_0$ due to translational invariance. Therefore, the only relevant parameter is the time delay τ. This is not the case of statistically inhomogeneous flows, where the translational invariance is lost

[2] As opposed to multi-particle quantities such as the relative particle pair dispersion statistics discussed in chapter 5. In the case of two-particle relative dispersion, an additional dependency on the initial particle separation vector must be included.

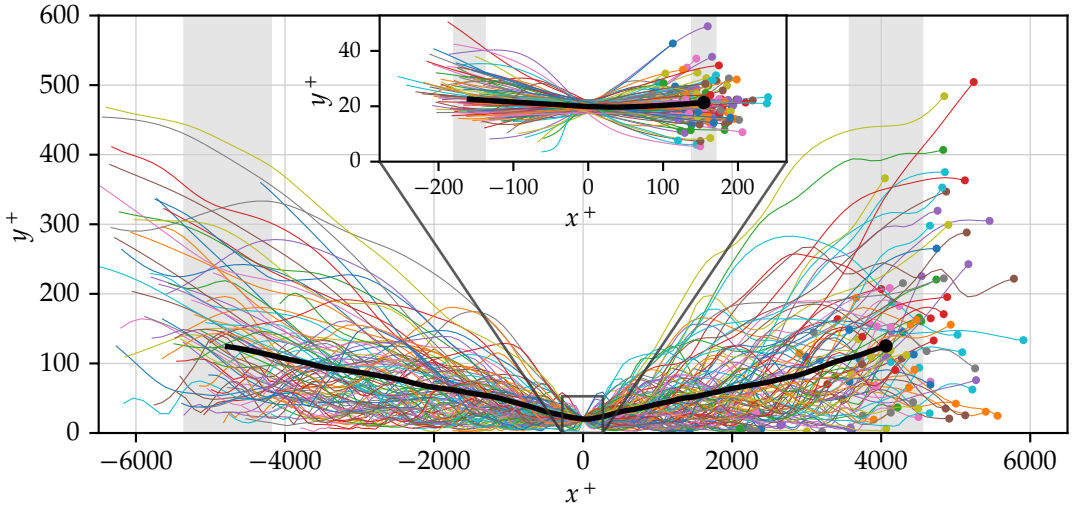

Figure 3.5. Illustration of the Lagrangian averaging procedure. The curves represent trajectories of tracer particles located at $y^+ = y_0^+ \pm 0.5\,\delta y^+$ at a reference time t_0 (here $y_0^+ = 20$ and $\delta y^+ = 5$). Trajectories are shifted in the streamwise direction so that $x(t_0) = 0$. The thick curve represents the Lagrangian-averaged particle position $\langle \boldsymbol{x} \rangle(\tau, y_0)$. The channel centre is at $y^+ = 1440$. Trajectories $\boldsymbol{x}(\boldsymbol{x}_0, t_0 + \tau)$ are shown for time lags $\tau^+ \in [-333, 333]$. The zoomed inset represents time lags $\tau^+ \in [-13, 13]$. Grey filled areas represent the spread of streamwise particle displacements at the two time extrema. Their width is the standard deviation of the streamwise displacements, $\langle \delta x'^2 \rangle^{1/2}$ (see chapter 4, section 4.5.2 for details).

and consequently the dependency on $\boldsymbol{x}_0$ must be retained. Since the turbulent channel flow considered here is statistically homogeneous in two Cartesian directions, the dependency on the initial position reduces to a dependency on the initial wall distance y_0 of the particles.

The Lagrangian averaging procedure for channel flow turbulence is illustrated in fig. 3.5 using the example of the mean particle position $\langle \boldsymbol{x} \rangle(\tau, y_0)$. The Lagrangian mean $\langle \cdot \rangle$ designates an ensemble average among the subset of particles located at y_0 at the labelling time t_0. In practice, to account for the dependency on y_0, particles located within a wall distance $y = y_0 \pm 0.5\,\delta y$ at the reference time t_0 are selected. Hence, the wall-normal coordinate is effectively discretised into wall-normal bins as described in section 2.2.4 (fig. 2.10). The bin size δy must be small enough for the Eulerian structure of the flow not to change significantly within a bin.

From fig. 3.5, a few aspects of Lagrangian dispersion in channel flow turbulence are apparent. First, tracers initially located near the wall tend on average to drift towards the channel centre at long times. Furthermore, a careful inspection of the average trajectory makes it clear that the dispersion is not symmetric in time, as tracers on average travel a longer distance when tracked backwards in time than forwards in the near-wall region. Finally, as suggested by the width of the filled areas, tracers spread over longer streamwise distances for negative time lags than positive. These aspects are discussed in more detail in chapter 4 where single-tracer dispersion is analysed in

the channel.

3.4 Lagrangian acceleration correlations

The analysis of the dynamics of tracer velocities and accelerations over time can yield important insights on the Lagrangian properties of the turbulent flow. In particular, it can serve to characterise the typical Lagrangian time scales (e.g. Lagrangian integral scales) and their relation with other quantities such as the Kolmogorov time scale τ_η. In this section, Lagrangian correlations of acceleration are described in the channel, and the evolution of the associated time scales with wall distance is characterised qualitatively from the results. Later in section 3.5, Lagrangian acceleration (and also velocity) time scales are quantified from the correlation curves and discussed.

The Lagrangian acceleration correlation tensor is defined as

$$\rho^a_{ij}(\tau, y_0) = \frac{\langle a'_i(t_0, \boldsymbol{x}_0)\, a'_j(t_0+\tau, \boldsymbol{x}_0)\rangle}{\langle a'^2_i(t_0, \boldsymbol{x}_0)\rangle^{1/2} \langle a'^2_j(t_0+\tau, \boldsymbol{x}_0)\rangle^{1/2}}, \tag{3.3}$$

where $a'_i(t_0+\tau, \boldsymbol{x}_0) = a_i(t_0+\tau, \boldsymbol{x}_0) - \langle a_i\rangle(\tau, y_0)$ is the fluctuation of the i-th acceleration component relative to its Lagrangian mean (defined in section 3.3) at a time lag τ. The initial particle position $\boldsymbol{x}_0$ is such that its wall-normal component is equal to y_0. In other words, all particles are at the same wall distance y_0 at the labelling time t_0. Hence, the tensor component ρ^a_{ij} correlates the initial acceleration fluctuation a'_i of a fluid particle located at y_0, with its acceleration fluctuation a'_j at a time lag τ.

We briefly discuss the above definition of the acceleration fluctuation a'_i. In inhomogeneous flows, the Lagrangian mean $\langle a_i\rangle(\tau, y_0)$ at non-zero time lags is fundamentally different from the Eulerian mean $\overline{a_i}(y)$. Since Lagrangian particles migrate from their initial location and diffuse for $\tau \neq 0$ (as seen in fig. 3.5), the Lagrangian mean represents an average over regions where the Eulerian flow properties can vary significantly. The Lagrangian acceleration fluctuation a'_i introduced above is calculated relative to this Lagrangian mean. An alternative approach, which has been applied in homogeneous shear flow [165] and in channel flow DNS [41], consists in defining the fluctuating velocity (or acceleration) of a fluid particle as its velocity relative to the mean Eulerian velocity at its current position, $\widetilde{v_i}(t) = v_i(t) - \overline{u_i}(\boldsymbol{x}(t))$.[3] We apply this approach later in section 5.4 to characterise the contribution of the fluctuating Eulerian velocity field to the relative separation of particle pairs. A disadvantage of this definition is that in general $\langle\widetilde{v_i}\rangle(\tau, y_0) \neq 0$, i.e. this 'fluctuation' has a non-zero average with respect to the Lagrangian mean, and therefore the statistical interpretation of $\widetilde{v_i}$ is less clear than that of v'_i. In particular, $\langle v'^2_i\rangle(\tau, y_0)$ represents the velocity variance among particles initially located at y_0 after a time τ, whereas the same is generally not true for $\langle\widetilde{v_i}^2\rangle(\tau, y_0)$. Therefore, our definition of v'_i is more consistent with the usual definition of Eulerian

[3] Here we exemplify with the Lagrangian velocity, but the same applies to the acceleration and to any other flow quantity.

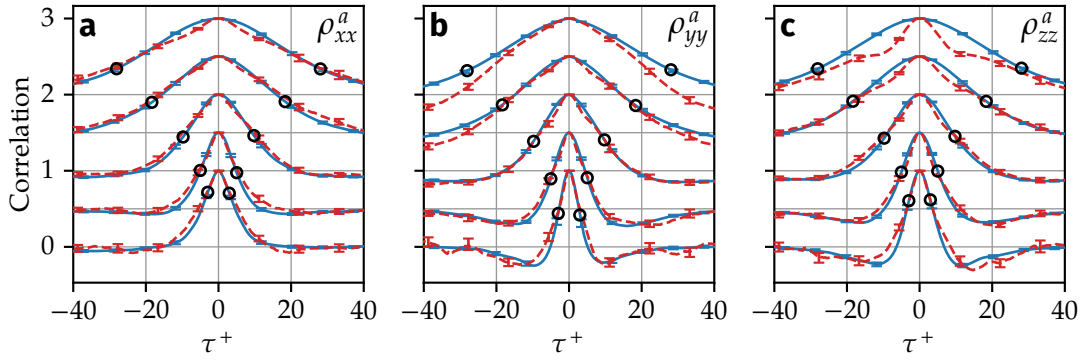

Figure 3.6. Lagrangian auto-correlations of (a) streamwise, (b) wall-normal and (c) spanwise acceleration. Comparison between experiments (red dashed lines) and DNS (blue solid lines). Circles indicate time lags $\tau = \pm\tau_\eta$. Curves are shifted vertically by increments of 0.5 for clarity. From bottom to top, the curves correspond to particles initially located at $y_0^+ = 20$, 60, 200, 600 and 1000. Horizontal grid lines show the zero-correlation level for each y_0^+. In the experiment, $\tau^+ = 1$ corresponds to 0.18 ms. Error bars on experimental and numerical data are obtained from the percentile bootstrap method with a 95 % confidence interval.

and Lagrangian correlations. In wall-bounded flows, the difference between both definitions is seen more clearly in the wall-normal velocity, which generally has a non-zero Lagrangian mean for $\tau \neq 0$ (as implied by the average wall-normal drift seen in fig. 3.5) as opposed to its Eulerian mean which is zero at all wall distances. Hence, the 'fluctuation' $\widetilde{v_y}$ is equal to the total velocity v_y which, as stated above, has a non-zero Lagrangian mean.

3.4.1 Acceleration auto-correlations

Lagrangian auto-correlations of acceleration, corresponding to the diagonal terms of ρ^a_{ij}, are shown in fig. 3.6 for different initial wall distances y_0 and for positive and negative time lags. Auto-correlations are nearly symmetric in time, e.g. $\rho^a_{xx}(-\tau, y_0) \approx \rho^a_{xx}(\tau, y_0)$, which can be explained by the time-symmetric tracer displacements in the wall-normal direction as illustrated by fig. 3.5 (and as confirmed in section 4.1).

For the three acceleration components, the decorrelation time increases significantly with wall distance as a result of the flow inhomogeneity. In all cases except for the streamwise acceleration near the wall, the decorrelation time is about two times the Kolmogorov time scale $\tau_\eta(y) = \sqrt{\nu/\varepsilon(y)}$ (circles in fig. 3.6), which characterise the temporal variations of the smallest turbulent scales at which energy is dissipated. This is consistent with DNS results in HIT, where acceleration components decorrelate after $\tau \approx 2\tau_\eta$ [118, 206], and in turbulent channel flow at lower Reynolds numbers [41]. Moreover, it is an indication of the rapidly-varying nature of the tracer acceleration and its connection to the small-scale flow dynamics. Close to the wall, the decorrelation times are also comparable to the viscous time scale $\tau_\nu = \nu/u_\tau^2$ (corresponding to $\tau^+ = 1$ in fig. 3.6), indicating the relevance of wall scales to describe small-scale quantities

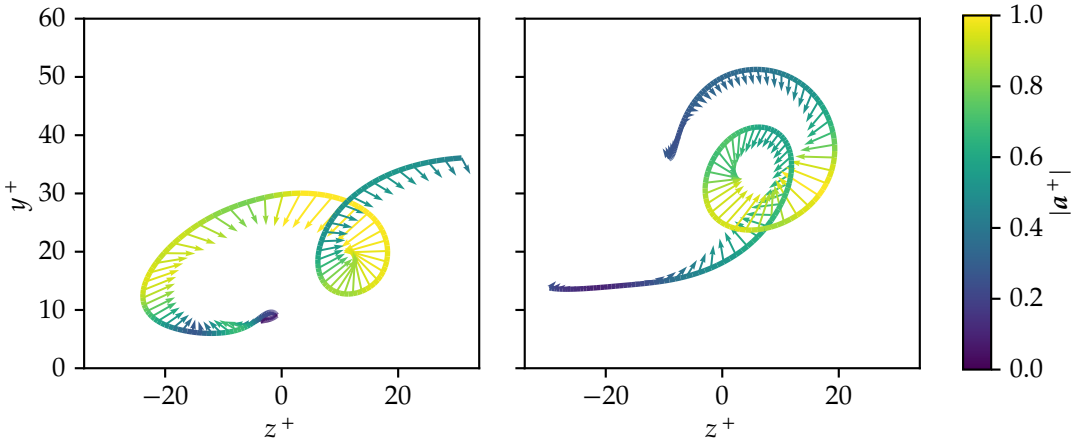

Figure 3.7. Sample particle trajectories projected on a y-z plane. Arrows represent the instantaneous particle acceleration vector. Trajectories and arrows are coloured by the acceleration norm. Trajectories are shown over $\Delta t^+ = 67$ and are shifted in z for clarity.

such as the acceleration near the wall. Lagrangian acceleration decorrelation times and their relation to other characteristic flow time scales are further discussed in section 3.5.

In general, very good agreement is found in fig. 3.6 between experimental and numerical results. Significant differences are only found very far from the wall, at $y_0^+ = 1000$, for the wall-normal and spanwise acceleration components. Differences in ρ_{zz}^a are mainly observed at short time lags, and are explained by a higher level of noise in the measurement of the spanwise component, which is a technical consequence of the way the PTV is performed, concretely due to the position of the horizontal camera [173]. As a consequence, the signal-to-noise ratio is larger for the spanwise components, and comes close to the limits of the filtering methods described in section 3.1. The short-time behaviour of the experimentally obtained ρ_{zz}^a at $y_0^+ = 1000$ thus corresponds in part to the auto-correlation of noise. In the case of ρ_{yy}^a, the differences at $y_0^+ = 1000$ may be explained by a form of statistical bias in the experiment associated to particles leaving the measurement volume at $\tau > 0$ through its wall-normal boundary located near the channel centreline (represented in fig. 3.1b). Namely, particles moving towards the centreline ($v_y > 0$) may leave the measurement volume through the wall-normal boundary, in which case they stop contributing to the statistics, while particles moving towards the wall ($v_y < 0$) stay within the measurement volume for longer times and end up having a more important weight on the statistics [173, sec. 2.4.3]. Evidently, this form of bias has a more noticeable effect when particles are initially located near the aforementioned boundary (in which case particles are more likely to exit the measurement volume), i.e. near the channel centre.

As expected, signs of flow anisotropy are mainly observed in the auto-correlations near the wall. This is visible in the form of different correlation shapes for the streamwise, wall-normal and spanwise accelerations. While ρ_{yy}^a and ρ_{zz}^a computed at $y_0^+ = 20$ become negative at $\tau \sim 2\tau_\eta$, the streamwise acceleration decorrelates more slowly and

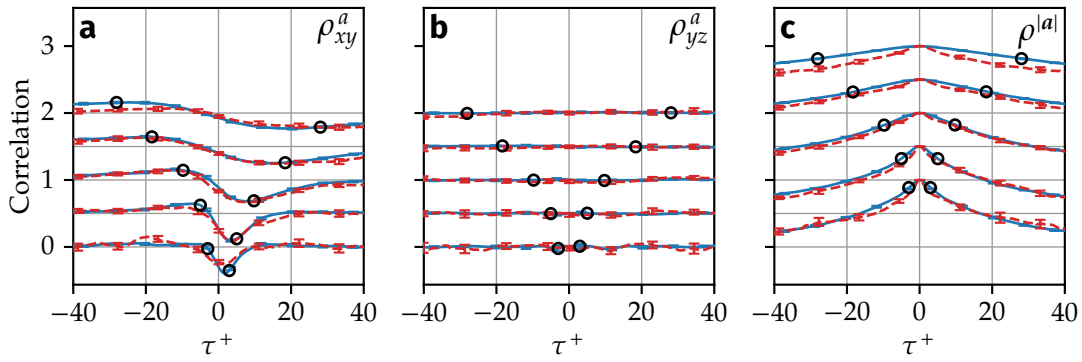

Figure 3.8. (a-b) Lagrangian cross-correlations of acceleration ρ^a_{xy} and ρ^a_{yz}. (c) Lagrangian auto-correlation of the acceleration magnitude, $\rho^{|a|}$. From bottom to top, the curves correspond to particles initially located at $y_0^+ = 20$, 60, 200, 600 and 1000. (See fig. 3.6 for details.)

does not display a significant negative correlation at longer times. This can be explained by the preferential orientation of vortices near the wall. It has been observed in HIT that vortex dynamics are responsible for high-acceleration events [118, 179]. A fluid particle in the vicinity of a vortex filament is affected by a large centripetal acceleration towards the vortex centre. Moreover, since the particle rotates about the vortex core, the centripetal acceleration changes direction when seen from a fixed reference frame. After half a rotation, the orientation of the centripetal acceleration is opposite to its initial orientation, leading to a negative auto-correlation of the centripetal acceleration at half the rotation period. Since vortex filaments do not have a preferential orientation in HIT, this affects the Lagrangian correlation of any arbitrary acceleration component. In the case of near-wall turbulence, rotational motions mainly exist in the form of elongated quasi-streamwise vortices, whose rotation axis is oriented roughly in the streamwise direction. As they rotate about these vortices, fluid particles near the wall (such as the ones visible in fig. 3.4) mostly see centripetal accelerations in the wall-normal and spanwise directions [93, 202]. This is seen more clearly in fig. 3.7, where the particle acceleration vector is projected on a plane normal to the streamwise direction for two sample particle trajectories near the wall. Therefore, mainly these two components display a negative correlation after a short time lag, while the streamwise acceleration is not affected by a systematic change of sign.

3.4.2 Acceleration cross-correlations

Due to $z \leftrightarrow -z$ symmetry, the cross-correlations containing the spanwise acceleration component are zero at all time lags. This is verified for the case of ρ^a_{yz} in fig. 3.8b. On the other hand, the cross-correlation ρ^a_{xy} between the streamwise and wall-normal acceleration components is in general different from zero in wall-bounded turbulence as shown in fig. 3.8a. Close to the wall, ρ^a_{xy} is strongly time-asymmetric, with a small positive correlation for $\tau < 0$ and a larger negative correlation which peaks at a positive time lag that scales with τ_η. As it is seen more clearly in fig. 3.9, where time

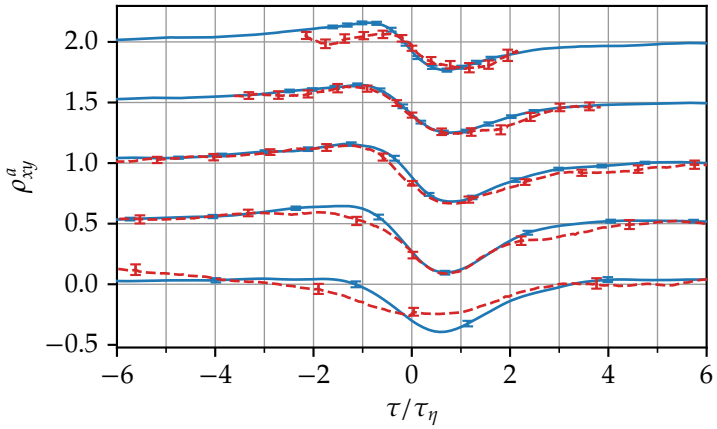

Figure 3.9. Lagrangian cross-correlation between streamwise and wall-normal acceleration components. Time delay τ is normalised with the local Kolmogorov time scale τ_η. From bottom to top, the curves correspond to particles initially located at $y_0^+ = 20$, 60, 200, 600 and 1000. (See fig. 3.6 for details.)

lags are normalised by τ_η, the value of τ/τ_η at the negative peak varies between 0.5 and 0.7. Furthermore, the change of sign of the correlation does not actually happen at $\tau = 0$, where the correlation is negative, but at a small negative time lag.[4] Note that, due to symmetry about the channel centreline, ρ^a_{xy} is necessarily zero at the channel centre. Far from the wall, this change of sign around $\tau = 0$ persists although the maximum correlation decreases, suggesting a (partial) return to isotropy. Moreover, the correlation becomes antisymmetric in time, i.e. $\rho^a_{xy}(y_0, -\tau) \approx -\rho^a_{xy}(y_0, \tau)$. The change of sign of ρ^a_{xy} at $\tau \approx 0$ suggests the idea of casualty between the two acceleration components. Concretely, in the Lagrangian frame, a given wall-normal acceleration fluctuation a'_y is on average followed by a streamwise acceleration fluctuation a'_x of the same sign, which is then followed by an opposite-sign a'_y.

The non-zero value of ρ^a_{xy} at all wall distances indicates the presence of small-scale anisotropy even in the outer layer of the channel, where wall effects are less important and a return to isotropy may be expected. To describe this anisotropy, we first note that $\rho^a_{xy}(\tau, y_0)$ describes the changes of orientation of the acceleration fluctuation vector $\boldsymbol{a}'(t_0 + \tau, \boldsymbol{x}_0)$ projected on the x-y plane. Therefore, the observed behaviour implies that there is a preferential direction of rotation of $\boldsymbol{a}'$ along a fluid particle trajectory. Moreover, as deduced from fig. 3.9, such changes of orientation of $\boldsymbol{a}'$ happen over times of the order of the Kolmogorov time scale. This implies that the anisotropy is associated with the smallest scales of turbulence. The preferential direction of rotation implied by the change of sign of ρ^a_{xy} is consistent with the direction of mean shear. The latter can be expressed in terms of the average vorticity $\overline{\omega}_z = -\,\mathrm{d}U/\mathrm{d}y$, which is negative in the lower half of the channel where the presented statistics are obtained. The present

[4] Only the lower half of the channel ($0 < y < h$) is considered in the present analysis. Due to symmetry, the same behaviour with opposite correlation signs is found in the upper half of the channel ($h < y < 2h$).

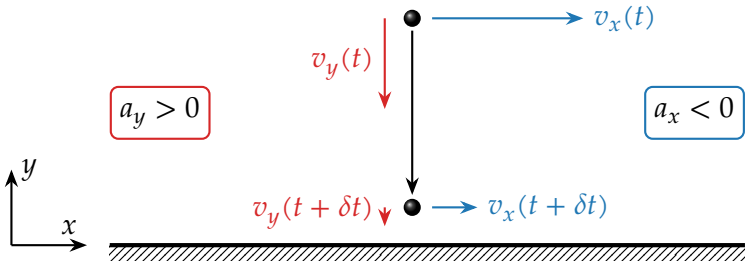

Figure 3.10. Schematic of a particle approaching the wall. As the particle approaches the wall, its streamwise velocity v_x diminishes translating into a negative streamwise acceleration. At the same time, the wall stops the particle in its motion towards the wall resulting in an acceleration towards the channel centre ($a_y > 0$).

results are consistent with evidence of small-scale anisotropy found in other turbulent flows characterised by large-scale anisotropy. For instance, from DNS of homogeneous shear flow, Pumir and Shraiman [140] found signs of small-scale anisotropy which did not decrease at increasing Reynolds number, in contradiction with Kolmogorov's local isotropy hypothesis [55, 83]. In their work, small-scale anisotropy was quantified by the skewness of the spanwise vorticity ω_z, which was shown to be of the same sign as the large-scale average vorticity. More recently, and using a similar approach, Pumir et al. [142] showed the presence of small-scale anisotropy throughout the logarithmic layer using DNS of turbulent channel flow at $Re_\tau \approx 1000$. Our results show that such small-scale anisotropy has a noticeable effect on the Lagrangian acceleration statistics. Practically, this suggests that, to account for small-scale anisotropy in shear flows, a stochastic model for the acceleration of fluid particles should aim at reproducing the observed non-zero cross-correlation ρ^a_{xy}.

At zero time lag, the correlation ρ^a_{xy} is characterised by an increasingly negative value as the wall is approached. In this special case, ρ^a_{xy} is equivalent to the Eulerian single-point single-time correlation between a_x and a_y. As illustrated by fig. 3.10, this negative correlation is partially explained by the increasing viscous effects as a tracer approaches the wall (the particle slows down in its streamwise motion, i.e. $a_x < 0$), combined with the effect of wall confinement which limits the motion of the particle towards the wall (the particle experiences an acceleration opposing this motion, i.e. $a_y > 0$). This is discussed in more detail in section 3.6 where the joint PDF between both components is studied.

3.4.3 Acceleration magnitude

We briefly comment on the auto-correlation of the acceleration magnitude $|\boldsymbol{a}|$ plotted in fig. 3.8c. From the figure, it is shown that, at all wall distances, $|\boldsymbol{a}|$ stays correlated for much longer than the acceleration components. This behaviour is consistent with results in HIT [117, 206], and it reflects that changes in the orientation of the acceleration vector occur at much faster rate than changes in its magnitude. In near-wall turbulence, this observation is again associated to the effect of streamwise vortices. While the

orientation of centripetal accelerations induced by these vortices changes at a rate comparable with the fastest scales of the flow, the centripetal acceleration magnitude varies over a much longer time scale [93].

3.5 Lagrangian time scales

From the acceleration auto-correlations described in section 3.4.1, Lagrangian time scales characterising the typical rate of change of the acceleration components can be deduced. In the following, the Lagrangian acceleration time scales are defined as

$$T_{a,i}(y_0) = \int_0^{\tau_c} \rho_{ii}^a(\tau, y_0)\,\mathrm{d}\tau\,, \tag{3.4}$$

where τ_c is the time lag at which the auto-correlation first crosses $\rho_c = 0.05$. This unusual definition can be contrasted to more common estimations of the Lagrangian time scales. On the one hand, the usual definition of the Lagrangian integral time scale T_L, in which the velocity auto-correlation is integrated for τ between zero and infinity, cannot be used for the acceleration components since their correlations generally become negative after a certain time lag (as shown in fig. 3.6). This is also the case in HIT where the integral of the acceleration auto-correlation is actually zero due to the statistical stationarity of the velocity. On the other hand, the zero-crossing time proposed e.g. by Yeung and Pope [206] can neither be used here because some correlations obtained from the experiment, especially near the channel centre, do not cross zero during the observation time. The definition eq. (3.4) works around these two issues while being equally appropriate to represent typical Lagrangian decorrelation times. In typical cases, the present definition yields roughly half the value of the more usual zero-crossing time.[5] For consistency between the different time scales, the same definition eq. (3.4) is used to estimate Lagrangian velocity (integral) time scales $T_{L,i}$, as well as the acceleration norm time scale $T_{|\boldsymbol{a}|}$. As shown in fig. 3.8c for the case of $|\boldsymbol{a}|$, these quantities stay correlated for much longer along Lagrangian paths than the acceleration components.

In the experiment, due to the limited size of the measurement volume, the full decorrelation of the velocity components and of the acceleration norm is not achieved far from the wall. This is explained by two complementary mechanisms. First, particles far from the wall spend less time within the measurement volume due to the increasing mean streamwise velocity that sweeps them away from the volume. Secondly, as seen in figs. 3.6 and 3.8 for the acceleration and confirmed below in fig. 3.12, Lagrangian decorrelation times increase with wall distance, i.e. longer particle tracks are needed to capture the full decorrelation of velocity and acceleration. For these reasons, the associated time scales are approximated in the experiment by extrapolation of the measured auto-correlation functions as illustrated by fig. 3.11. This introduces an uncertainty in the estimated time scales which increases with increased fraction of

[5] This relation would be exact had we chosen $\rho_c = 0$ instead of 0.05 (in which case τ_c would precisely be the zero-crossing time) and if the correlation function decayed linearly with time.

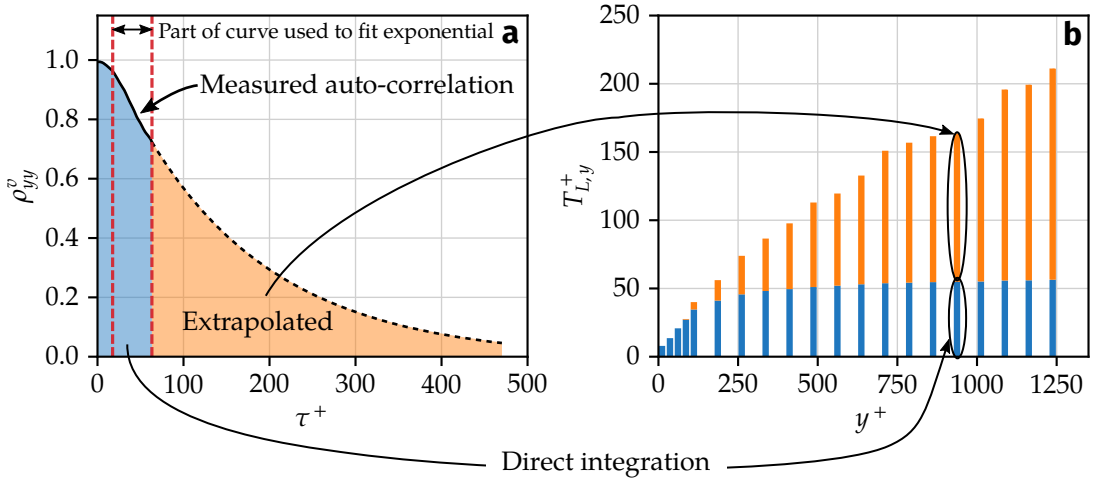

Figure 3.11. Estimation of Lagrangian velocity time scales in the experiment. In (a), the measured wall-normal velocity auto-correlation ρ^v_{yy} at $y_0^+ = 925$ is shown (solid black line) along with its exponential extrapolation at long times (dashed black line). The extrapolation is estimated from the section of the curve between the two vertical dashed lines. The filled areas under the curves are used to estimate the Lagrangian integral time scales shown in (b).

extrapolated data, or equivalently, with wall distance. Extrapolation is not required to calculate the acceleration time scales $T_{a,i}$, since the decorrelation time of the acceleration components is short enough to capture their full decorrelation (as seen in fig. 3.6). Extrapolation is neither required for DNS data as the computed Lagrangian trajectories are longer than the typical velocity decorrelation times.

Lagrangian velocity and acceleration time scales across the channel are shown in fig. 3.12 normalised in wall units. As deduced from the auto-correlation curves in fig. 3.6 and fig. 3.8c, Lagrangian acceleration time scales $T_{a,i}$ and $T_{|\boldsymbol{a}|}$ generally increase with wall distance. The same is observed for the Lagrangian integral time scales $T_{L,i}$. According to fig. 3.12a, the time scale of the acceleration norm is comparable to the integral time scales. In other words, $|\boldsymbol{a}|$ varies over long times scales characteristic of the energy-containing turbulent motions. Relative to the time scales associated to the acceleration components (fig. 3.12b), $T_{|\boldsymbol{a}|}$ is about one order of magnitude larger than $T_{a,i}$ for all wall distances.

Regarding the Lagrangian velocity time scales (fig. 3.12a), signs of anisotropy are observed at all wall distances. Concretely, the wall-normal velocity varies over shorter times than the other two components. This behaviour is observed both in experiments and DNS. As expected, the difference is more significant near the wall where the flow is strongly anisotropic. Similar observations can be made for the acceleration components (fig. 3.12b), although differences between components are mainly visible in the viscous and buffer layers. Noting that the acceleration is a small-scale quantity, the nearly isotropic behaviour far from the wall may be a sign of return to isotropy at the small scales (even though isotropy is not fully recovered as discussed above in section 3.4.2).

In section 3.4.1, it has been qualitatively observed that the acceleration components

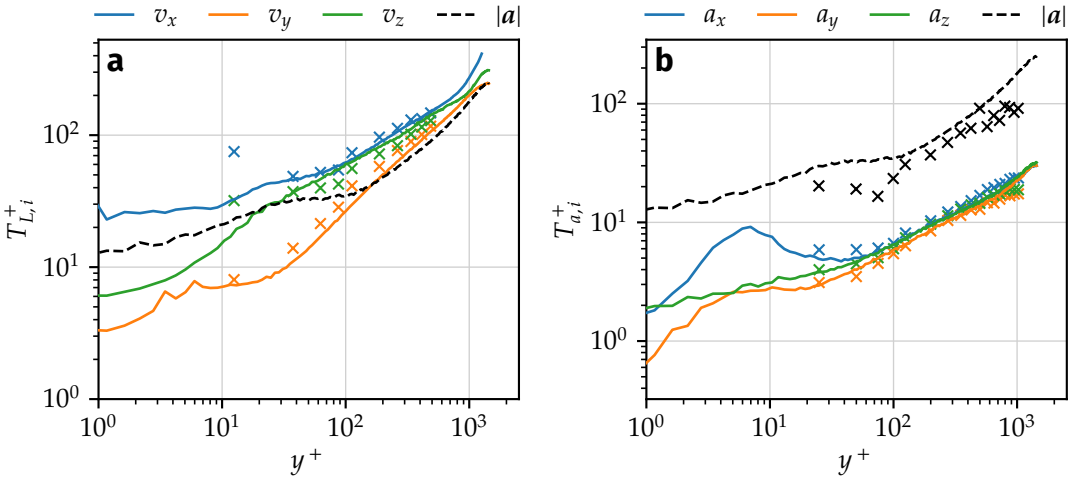

Figure 3.12. Lagrangian velocity and acceleration time scales in wall units. Experiments, crosses; DNS, solid lines. Colours represent velocity or acceleration components. The acceleration magnitude time scale $T_{|a|}$ is represented by dashed black lines.

decorrelate over time lags $\tau \sim 2\tau_\eta$ in most of the channel, similarly to the case of HIT. To quantify this, the acceleration time scales $T_{a,i}$ are plotted in fig. 3.13 normalised by the Kolmogorov time scale τ_η. We recall that, due to inhomogeneity, τ_η varies with wall distance. Its profile along the channel width is presented in the inset of fig. 3.13. The curves are consistent with our observations in section 3.4.1. Namely, the acceleration time scales are close to τ_η in the channel, except for $T_{a,x}$ near the wall which displays a much larger value. This is consistent with the slower decorrelation time of the streamwise acceleration relative to the other components in that region (fig. 3.6a), associated to the presence of coherent structures such as quasi-streamwise vortices near the wall. In the other cases, the value $T_{a,i} \approx \tau_\eta$ is consistent with a decorrelation time of approximately $2\tau_\eta$. Nevertheless, even in the logarithmic and outer regions, small differences are found between $T_{a,y}$ and the time scales associated to the other components suggesting again the presence of small-scale anisotropy far from the wall.

Since Lagrangian acceleration and velocity time scales are respectively related to the dissipative and energy-containing scales of the flow, their ratio gives an indication of the degree of scale separation in the turbulent flow. In other words, it determines the extent of the inertial range of Lagrangian time scales, $T_{a,i} \sim \tau_\eta \ll \tau \ll T_{L,i}$, over which Lagrangian statistics are supposedly independent of energy injection and dissipation mechanisms according to Kolmogorov's K41 theory [83]. In HIT it is well accepted that, for a given Reynolds number, the separation of Lagrangian scales is much weaker than that of Eulerian scales, and as a consequence, larger Reynolds numbers are required to observe universal scaling of Lagrangian statistics in the inertial range than for Eulerian statistics [180, 205]. As introduced in section 1.1.3, Sawford [153] proposed a second-order stochastic equation for the fluid particle acceleration accounting for finite Reynolds number effects by including both τ_η and the Lagrangian integral time scale T_L as model parameters. Based on this model, Sawford derived an expression

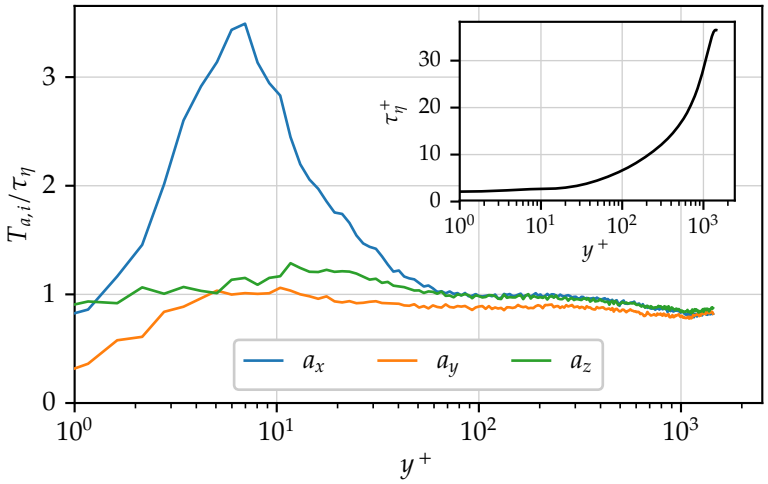

Figure 3.13. Lagrangian acceleration time scales normalised by the local Kolmogorov time scale (DNS results only). Inset: local Kolmogorov time scale in wall units.

for the ratio between these two time scales as a function of the Taylor-scale Reynolds number, $Re_\lambda = \bar{k}\sqrt{20/(3\nu\varepsilon)}$ (with $\bar{k} = \overline{u_i' u_i'}/2$ the mean turbulent kinetic energy),

$$\frac{T_L}{\tau_\eta} = \frac{2Re_\lambda}{C_0\sqrt{15}}\left(1 + \frac{\sqrt{15}}{4}\frac{C_0^2}{a_0 Re_\lambda}\right), \tag{3.5}$$

where, according to K41 scaling, a_0 and C_0 are universal dimensionless constants. In isotropic turbulence experiments and simulations, both have been found to actually increase with Reynolds number, with the former estimated as

$$a_0 = 1.9\, Re_\lambda^{0.135}/(1 + 85\, Re_\lambda^{1.135}) \tag{3.6}$$

by Sawford et al. [154] and the latter approaching $C_0 \approx 7$ at high Reynolds numbers [180]. We note that, following K41 scaling, a_0 represents the normalised acceleration variance $a_0 = \overline{a_i'^2}\sqrt{\nu/\varepsilon^3}$, while C_0 appears in the expected inertial-range form of the Lagrangian second-order velocity structure function $D_2(\tau) = \langle[v_i(t_0+\tau) - v_i(t_0)]^2\rangle$, i.e. $D_2(\tau) \approx C_0\varepsilon\tau$ for $\tau_\eta \ll \tau \ll T_L$. To present day, available experimental and numerical results have not found conclusive evidence of such an inertial-range behaviour, although a tendency is seen in favour of this prediction at increasingly high Reynolds numbers [156, 180].

The component-wise ratios between Lagrangian velocity and acceleration time scales along the channel width are shown in fig. 3.14a. In the buffer layer and logarithmic regions, the streamwise and spanwise components display nearly the same behaviour, consistently with the curves in fig. 3.12. In the logarithmic region, their ratio stays nearly constant, meaning that velocity and acceleration time scales grow at the same rate. On the other hand, the ratio between wall-normal velocity and acceleration time scales

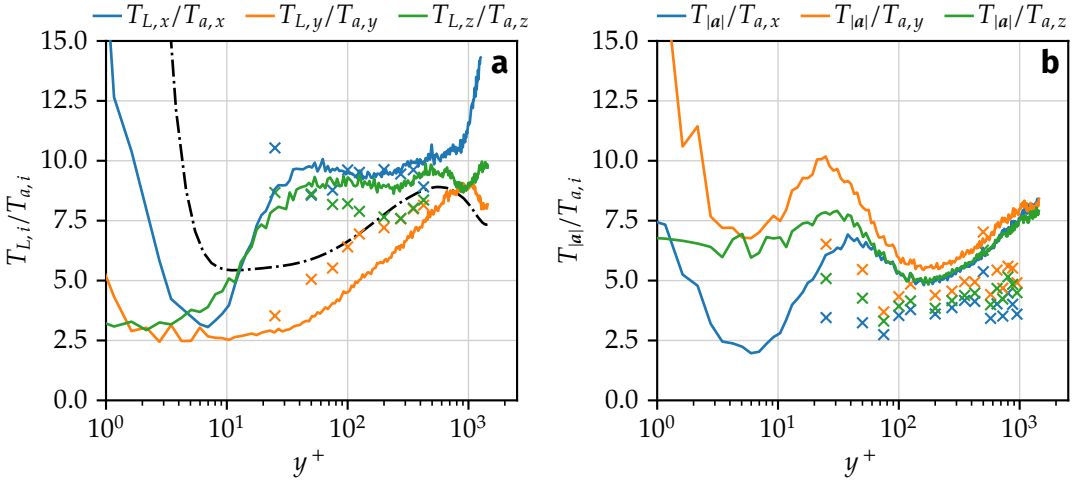

Figure 3.14. Lagrangian time scale ratios. Experiments, crosses; DNS, solid lines. (a) Ratio between the Lagrangian velocity and acceleration time scales, by component. The dash-dotted line represents the ratio $T_{L,i}/\tau_\eta$ in HIT as predicted by Sawford's second-order stochastic model [153] (eq. (3.5), with a_0 given by eq. (3.6) and $C_0 = 7$). (b) Ratio between time scales of acceleration magnitude and of the acceleration components.

is smaller than for the other components throughout the channel. This is consistent with the smaller value of the integral time scale $T_{L,y}$ relative to the other components as seen in fig. 3.12a, and it suggests that, as a result of confinement, the Lagrangian separation of scales is weaker when the wall-normal motions are considered.

Also shown in fig. 3.14a is Sawford's prediction (3.5) for isotropic turbulence. Since $T_{a,i} \approx \tau_\eta$ in most of the channel (fig. 3.13), this prediction should match the $T_{L,i}/T_{a,i}$ ratios were the model applicable to the present flow. We also note that the Taylor-scale Reynolds number appearing in eq. (3.5) varies with wall distance as a result of its dependence on $\overline{k}$ and ε. In fig. 3.15, it is shown that Re_λ increases with wall distance up to the end of the logarithmic layer, where it reaches $Re_\lambda \approx 100$ at $y^+ \approx 600$. Then it slightly decreases in the outer layer of the channel. Due to the anisotropy displayed by the Lagrangian time scales, Sawford's isotropic model cannot be expected to match the statistical data. However, the model captures the observed trends especially in the logarithmic region, where the predicted values are in between the ratios found for the different velocity and acceleration components.

As discussed above, the acceleration components and its norm change over very different time scales. Based on this observation, models for the fluid particle acceleration have been proposed treating the fast-varying orientation of acceleration and the slow-varying acceleration norm as two independent random processes obeying different stochastic equations [148, 208]. The ratios of acceleration norm to acceleration component time scales are shown in fig. 3.14b. For $y^+ > 50$, the ratios are weakly varying, and only small differences are observed between the three acceleration components. Moreover, the observed values are comparable in magnitude to the ratios between velocity and acceleration time scales (fig. 3.14a).

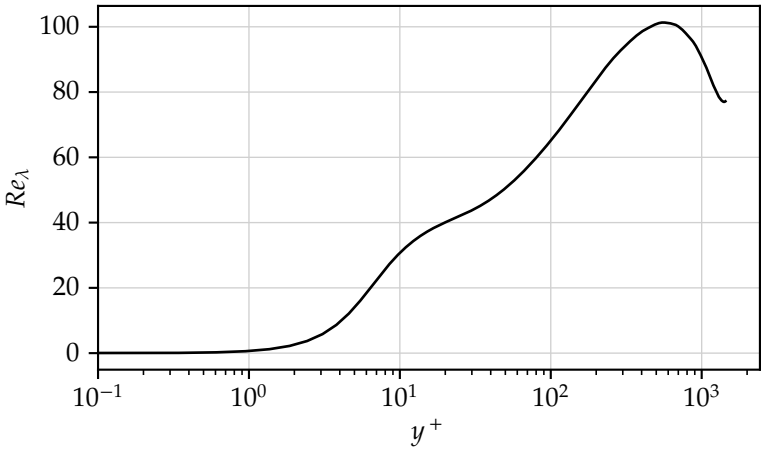

Figure 3.15. Taylor-scale Reynolds number in the channel at $Re_\tau = 1440$.

3.6 Acceleration PDFs

High-acceleration events such as the ones shown in fig. 3.4 are a form of intermittency of turbulent flows, by which tracers occasionally experience accelerations that are many times more intense than the acceleration standard deviation. In HIT, this intermittency has been associated to very long tails in the PDF of the acceleration components relative to a Gaussian distribution [89]. The same has been observed in wall turbulence at lower Reynolds numbers [202]. The intermittency of fluid particle accelerations is confirmed in the present channel flow as shown in fig. 3.16, where the PDF of the three acceleration components is plotted at different wall distances. Once again, good agreement is achieved between experiments and simulations. Superposed to the curves is the analytical expression for the acceleration PDF proposed by Mordant et al. [117] under the assumptions that the acceleration magnitude follows a log-normal probability distribution and that the acceleration vector is isotropic,

$$P(a_i) = \frac{e^{s^2/2}}{4m}\left[1 - \mathrm{erf}\left(\frac{\ln(|a_i|/m) + s^2}{\sqrt{2}s}\right)\right], \tag{3.7}$$

where m determines the variance of a_i ($m = \sqrt{3/e^{2s^2}}$ for variance 1), while s determines the shape of the PDF. As in [117], $s = 1$ is used in the figure. This expression accurately predicts the behaviour of the three acceleration components near the channel centre ($y^+ = 1200$), where the flow is nearly isotropic at the small scales. Closer to the wall, anisotropy increases and thus the prediction becomes less accurate for the streamwise and wall-normal accelerations. Surprisingly, this is not the case for the spanwise acceleration PDF which is very well represented by eq. (3.7) very near the wall, suggesting that this component is not strongly affected by anisotropy. The general agreement of the presented curves with the shape of the isotropic PDF suggests that intermittency of Lagrangian accelerations is extremely strong even at the moderate Reynolds num-

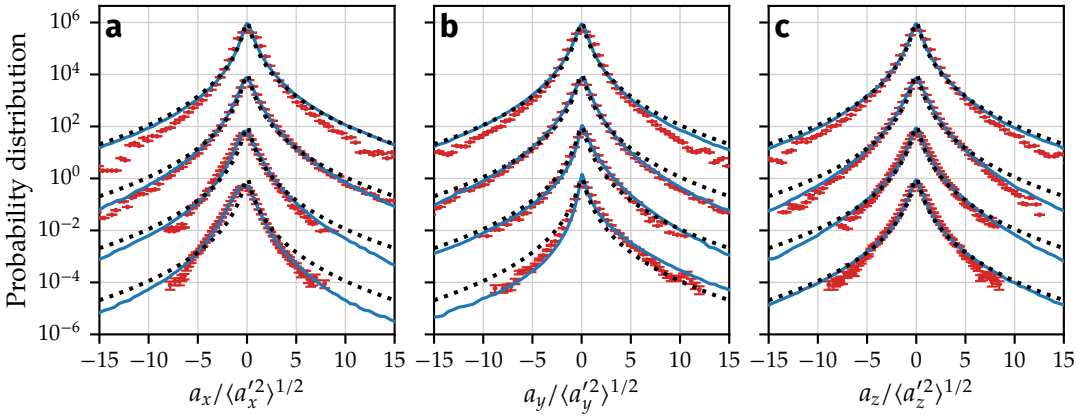

Figure 3.16. PDF of (a) streamwise, (b) wall-normal and (c) spanwise tracer acceleration. Experiments, symbols with error bars; DNS, solid lines. Dotted lines represent the analytical prediction for the acceleration PDF in HIT proposed by Mordant et al. [117] (eq. (3.7) with $m = \sqrt{3/e^{2s^2}}$ and $s = 1$). The PDFs are normalised by the standard deviation of the acceleration components. From bottom to top, the curves correspond to particles located at $y^+ = 10$, 20, 200 and 1200. The statistical convergence of the statistical data is represented by error bars proportional to $1/\sqrt{n_i}$ where n_i is the number of events in the i-th wall bin.

bers of the present wall-bounded flow, i.e. $Re_\lambda \sim 60$ to 100 in the logarithmic layer (fig. 3.15), whereas it was close to 1000 in La Porta et al. [89]. This also shows that the shape of the acceleration PDF presents some universality, not only because it is seemingly Reynolds number-independent, but also because it only weakly depends on the large-scale properties of the flow (at least in regions where anisotropy is weak).

Due to statistical symmetry, the spanwise acceleration displays a symmetric PDF at all wall distances. This is not the case for the streamwise and wall-normal accelerations, which present increasingly asymmetric behaviours as the wall is approached. Compared to the isotropic PDF, the streamwise acceleration PDF is slightly shifted and skewed towards negative accelerations near the wall. As shown earlier in fig. 3.3a, its mean is also negative for $y^+ < 60$. Conversely, the distribution of wall-normal accelerations is skewed towards positive values very near the wall, which is again consistent with the positive $\overline{a_y}$ in that region (fig. 3.3a). As shown by Yeo et al. [202], the intermittency of acceleration is explained at all wall distances by the contribution of the irrotational term $\boldsymbol{a}^I = -(1/\rho)\boldsymbol{\nabla} p$. Perhaps surprisingly, this includes the viscous sublayer where the streamwise acceleration variance is actually dominated by the solenoidal component $a_x^S = \nu\nabla^2 u_x$ [202].

The asymmetry of the streamwise and wall-normal acceleration distributions is quantified in fig. 3.17 in terms of their skewness $S_i^a = \langle a_i'^3\rangle/\langle a_i'^2\rangle^{3/2}$ along the channel width. The spanwise acceleration is not shown since its skewness is zero due to flow symmetry. The curves confirm the previous observation that very close to the wall, the a_x and a_y distributions are strongly skewed towards negative and positive values, respectively. The signs of S_x^a and S_y^a are both inverted after $y^+ \approx 20$. Their respective

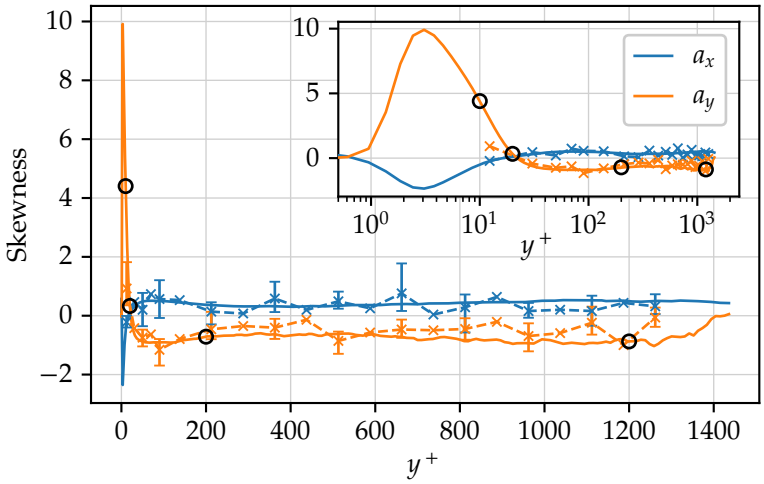

Figure 3.17. Skewness of streamwise and wall-normal acceleration components. Experiments, crosses; DNS, solid lines. Circles indicate the skewness of a_y at $y^+ = 10, 20, 200$ and 1200, where the PDFs in fig. 3.16 were obtained. In the inset, skewness profiles are represented with y^+ in logarithmic scale.

values are nearly constant and different from zero at larger wall distances and up to the channel centre. This is yet another indication of the persistence of small-scale anisotropy even near the channel centre.

The cross-correlation between the streamwise and wall-normal acceleration components discussed in section 3.4.2 suggest a significant interdependency between these two components along Lagrangian paths. Near the wall, their cross-correlation at zero time lag, equal to the normalised single-time covariance $\overline{a_x' a_y'}$, is negative. To better understand this behaviour, their joint PDF $P(a_x, a_y)$ is shown in fig. 3.18 at two wall distances, $y^+ = 15$ and 59. At $y^+ = 15$, the joint PDF has a stretched shape, showing a preference for events of negative a_x and positive a_y. These events can be associated to fluid particles moving towards the wall, as previously illustrated by fig. 3.10. These particles probe regions of decreasing mean streamwise velocity, leading on average to a streamwise deceleration of their motion ($a_x < 0$). Simultaneously, their negative wall-normal velocity is reduced due to confinement by the wall limiting their motion in that direction, resulting in a positive wall-normal acceleration ($a_y > 0$). As for particles moving away from the wall, a positive streamwise acceleration is expected as they probe regions of faster mean velocity. However, since their motion is less affected by wall confinement, their contribution to the wall-normal accelerations is less visible in the joint PDF. The conditional means $\langle a_x \,|\, a_y \rangle$ and $\langle a_y \,|\, a_x \rangle$, which are superposed to the joint PDF contours in fig. 3.18, confirm that streamwise and wall-normal accelerations are on average of opposite signs near the wall. As expected, further away from the wall ($y^+ = 59$, fig. 3.18b) the joint PDF partially loses its stretched form and the interdependency between both components becomes weaker.

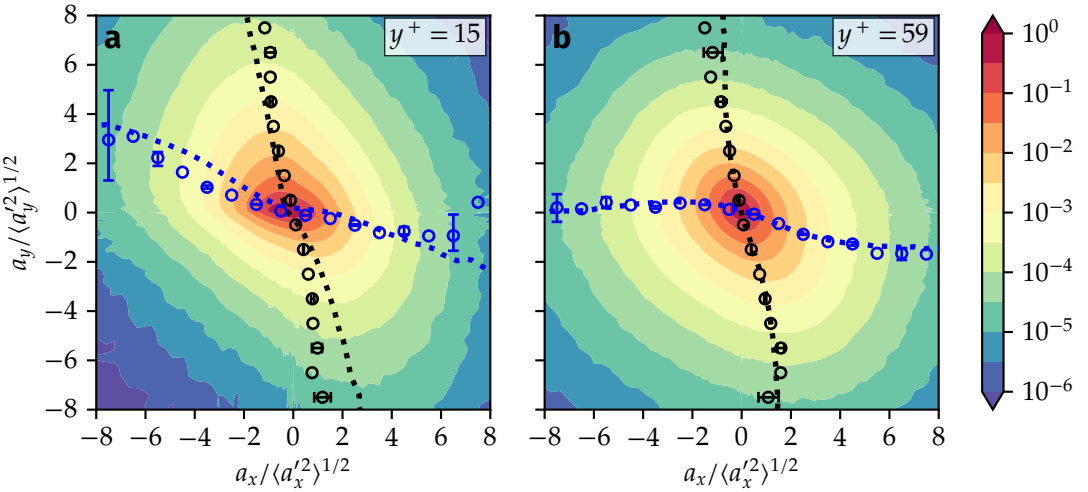

Figure 3.18. Joint PDF of streamwise and wall-normal acceleration at $y^+ = 15$ and 59 obtained from DNS. Normalised conditional means $\langle a_x \,|\, a_y\rangle/\langle a_x'^2\rangle^{1/2}$ and $\langle a_y \,|\, a_x\rangle/\langle a_x'^2\rangle^{1/2}$ are superposed to the contours using black and blue markers, respectively. Experiments, circles; DNS, dotted lines.

3.7 Conclusion

The acceleration of fluid particles in a turbulent channel flow is studied in this chapter by comparison between our DNS and the 3D PTV measurements performed by N. Stelzenmuller and N. Mordant at LEGI at nearly the same Reynolds number $Re_\tau \approx 1440$. A remarkable agreement is found between both approaches in most of the channel. Our findings are largely consistent with previous observations in homogeneous isotropic turbulence experiments and DNS and in lower Reynolds number channel flow simulations. Namely, acceleration is a highly intermittent quantity, i.e. fluid particles occasionally experience accelerations which are many times more intense than their standard deviation [89]. This intermittency translates into a substantial departure from Gaussianity of the acceleration PDFs, which present very long tails corresponding to extreme acceleration events. This is observed even at the moderate Reynolds number of the present wall-bounded flow, in which Re_λ barely exceeds a value of 100 in the logarithmic region.

The fluid acceleration presents a dual temporal behaviour, that is, the orientation of the acceleration vector changes very quickly along Lagrangian paths (its decorrelation time is comparable to the dissipation time scale τ_η), while its norm stays correlated for much longer, over times comparable to the Lagrangian integral time scales $T_{L,i}$. This has already been observed in nearly isotropic flows [117], and has been associated to the effect of vortex filaments on nearby fluid particles [118, 179]. As they rotate about one such vortex, particles see intense centripetal accelerations oriented towards the rotation axis. These vortex filaments are responsible for the intermittency of acceleration mentioned above [118]. In wall-bounded turbulence the same mechanism describes the

Lagrangian dynamics of acceleration, with the difference that near the wall, rotational motions inducing centripetal accelerations have preferential orientations mainly in the form of quasi-streamwise vortices [93, 202]. This results in rapidly varying wall-normal and spanwise acceleration components, while the streamwise acceleration stays correlated for longer times.

The present work confirms previous observations on the Lagrangian dynamics of acceleration in wall-bounded turbulence at a higher Reynolds number, and, for the first time, with support of experimental measurements. In addition, it characterises the small-scale anisotropy of the flow and its effect on Lagrangian acceleration statistics. In particular, it is shown that the Lagrangian cross-correlation between the streamwise and wall-normal accelerations is non-zero at all wall distances over time lags of the order of τ_η. This contradicts the expectation of a return to isotropy far from the wall, i.e. it confirms that small-scale anisotropy persists even near the channel centre. Furthermore, the dependency between a_x and a_y is analysed in terms of their joint PDF, which suggests a preference for negative a_x and positive a_y events close to the wall. These events are associated to particles migrating towards the wall, which are decelerated in their streamwise motion due to increasing viscous effects, and at the same time, due to wall confinement, experience a force which opposes their motion towards the wall.

The results presented in this chapter can serve as a basis for the improvement of existing stochastic models for the fluid acceleration in wall-bounded flows. The Lagrangian velocity and acceleration time scales, which are fully characterised in this work, can serve as input for such models. More importantly, to properly account for small-scale anisotropy in wall-bounded turbulence and more generally in shear flows, stochastic models for the acceleration should be able to reproduce the described dependency between acceleration components, namely the effect of coherent structures and wall confinement near the wall, as well as the shear-induced small-scale anisotropy resulting in non-zero acceleration cross-correlations.

4 Single-particle dispersion

The single-particle dispersion problem, attempting to statistically describe the trajectories of particles in turbulent flows, is arguably the most natural application of the Lagrangian approach. The statistical framework for obtaining single-particle Lagrangian statistics in turbulent channel flow has been applied in chapter 3 for characterising the dynamics of Lagrangian accelerations in the channel. In this chapter, more details are provided on the dispersion of single fluid particles in the channel, which have been qualitatively discussed in section 3.3 for the case of particles initially located near the wall.

In chapter 3, fig. 3.5 gives an intuition about the properties of particle dispersion in wall-bounded flows. Despite the low number of particles represented in the illustration, the figure suggests that tracers that are initially close to the wall tend to migrate on average towards the channel centre. This has been observed in other channel flow simulations [41, 193], and is explained by particles 'forgetting' their initial positions at very long times, resulting in a uniform particle distribution across the channel width. The same is observed when tracers are followed backwards in time, i.e. for $\tau < 0$. The latter point raises the question of whether the migration occurs at the same rate when particles are tracked backwards and forwards in time. A negative answer to this question may indicate the existence of a temporal asymmetry as a consequence of the irreversibility of the turbulent flow [196]. From fig. 3.5 alone, not much can be said regarding the time asymmetry of the mean particle migration away from the wall. On the other hand, in the streamwise direction, fig. 3.5 indicates that particles in the near-wall region travel on average a longer distance when tracked backwards ($\langle \delta x^+ \rangle \approx -4770$ at $\tau^+ = -333$) than forwards in time ($\langle \delta x^+ \rangle \approx 4060$ at $\tau^+ = 333$).

Following the above discussion, here we quantify the dynamics of fluid particle trajectories in the channel. Whenever appropriate, we emphasise on the temporal asymmetry of dispersion statistics, which is intimately linked to the Lagrangian dynamics of kinetic energy and to the irreversibility of turbulence [79, 141, 196]. In inhomogeneous flows, contrarily to the case of stationary HIT, average kinetic energy fluxes may exist across spatial regions. As discussed in this chapter, this has consequences on the temporal asymmetry of dispersion. The spatial flux of turbulent kinetic energy (TKE) and its link to dispersion have been recently studied experimentally by Huck [71] in a von Kármán flow between two counter-rotating disks in a square tank. The flow is strongly anisotropic at the geometric centre of the tank, where it has a stagnation point topology with one converging direction and two diverging directions, and where turbulence production is dominated by mean strain. To our knowledge, these questions have not been discussed in wall-bounded turbulent flows where turbulent fluctuations are produced by mean shear and where similar spatial energy fluxes exist.

The structure of this chapter is as follows. In section 4.1 the average displacement of fluid particles in the wall-normal direction is briefly described. The case of the average streamwise displacement is treated in section 4.2, where the time asymmetry discussed above is quantified and linked to the mean streamwise acceleration profile in the channel. Mean-square displacement and dispersion statistics are introduced in section 4.3, along with analytical short-time estimations relating the time asymmetry of the statistics to the mean Lagrangian power and the velocity-acceleration covariance. These two quantities are discussed in more detail in section 4.4, and their influence on short-time dispersion statistics is estimated in section 4.5 where numerical mean-square dispersion results are presented. Finally, general conclusions and perspectives are given in section 4.6.

4.1 Mean wall-normal particle displacement

We first consider the average particle drift towards the channel centre. The quantity of interest here is the average wall-normal particle position $\langle y \rangle(\tau, y_0)$, or equivalently, the average wall-normal particle displacement $\langle \delta y \rangle(\tau, y_0) = \langle y \rangle(\tau, y_0) - y_0$. At short time lags τ, the time evolution of $\langle \delta y \rangle$ is given by the Taylor expansion

$$\langle \delta y \rangle(\tau, y_0) = \langle v_y \rangle(0, y_0)\, \tau + \frac{1}{2} \langle a_y \rangle(0, y_0)\, \tau^2 + \mathcal{O}(\tau^3). \tag{4.1}$$

At $\tau = 0$, Lagrangian statistics coincide with their Eulerian counterparts evaluated at y_0. Since the mean wall-normal velocity is zero at all wall distances, eq. (4.1) reduces to

$$\langle \delta y \rangle(\tau, y_0) = \frac{1}{2} \overline{a_y}(y_0) \tau^2 + \mathcal{O}(\tau^3). \tag{4.2}$$

Near the wall, the mean wall-normal acceleration $\overline{a_y}$ is positive (fig. 3.3a), hence an average motion of the particles away from the wall is to be expected at short times. Conversely, the weakly negative mean acceleration found far from the wall (at $y^+ > 100$) predicts an average initial motion towards the wall.

Average wall-normal particle positions, conditioned by their initial wall distance y_0, are plotted in fig. 4.1a for time lags $\tau^+ \in [-3000, 3000]$. On average, all particles drift away from the wall at long times. This is consistent with the hypothesis that particles tend to forget their initial position at very long times, their distribution across the channel becoming uniform. In fig. 4.1b, forward ($\tau > 0$) and backward ($\tau < 0$) displacement curves are superposed for selected values of y_0. Also shown are mean forward displacements obtained from a longer-extent fluid particle dataset labelled DS2[1] ($\tau^+_{\max} \approx 17\,000$), which confirm that tracers on average drift towards the channel centre at long times. There is no clear difference between backward and forward mean displacements (small differences are most likely explained by the finite size of the statistical sample), indicating that the Lagrangian-averaged wall-normal

[1] This dataset was initially used for relative pair dispersion statistics and is described in more detail in chapter 5.

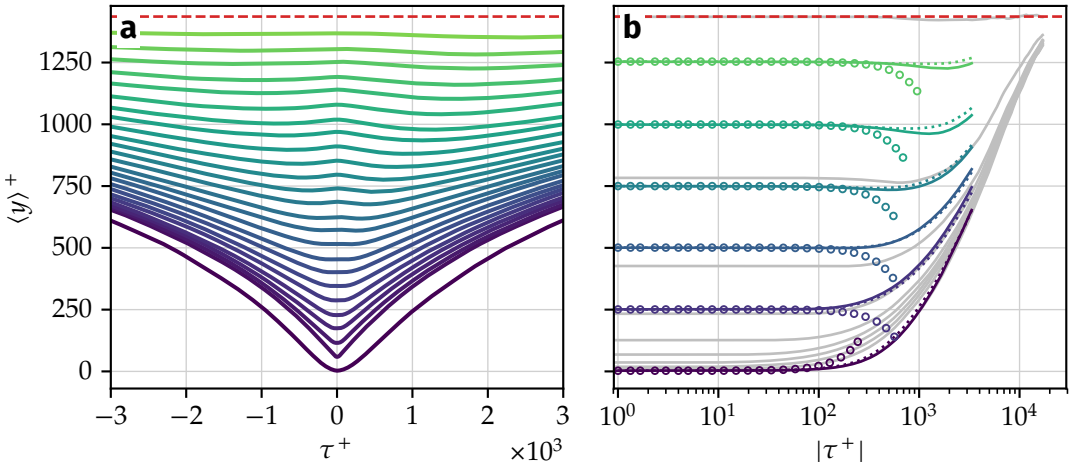

Figure 4.1. Mean wall-normal tracer displacement in the channel. (a) Average wall-normal particle position $\langle y \rangle(y_0, \tau)$ for particles initially located at varying wall distances y_0. The red dashed line represents the channel centre. (b) Detail on particle sets initially located at $y_0^+ = 3$, 250, 500, 750, 1000 and 1250 (from bottom to top). Time lag τ is represented in logarithmic scale. Dotted lines represent backward displacement ($\tau < 0$). Circles represent the short-time estimation $\langle y \rangle \approx y_0 + \overline{a_y}(y_0)\tau^2/2$ [eq. (4.2)]. Grey lines represent forward statistics obtained from the long-extent particle dataset DS2 described in chapter 5.

displacement is time-symmetric. Interestingly, near the channel centre the average trajectory is described by a weak initial displacement towards the wall, followed by a return towards the centre.

According to fig. 4.1b, on average tracers start drifting towards the channel centre after $\tau^+ \sim 100$ for particles near the wall and $\tau^+ \sim 1000$ for particles in the outer layer. As seen in sections 3.4 and 3.5, at $\tau^+ \sim 100$ the tracer acceleration components are completely decorrelated. Therefore, the mean drift towards the channel centre is not explained by the effect of the mean initial acceleration and thus by the short-time estimation (4.2), which by its nature is not valid at long times. This is confirmed in fig. 4.1b, where the circles representing eq. (4.2) do not predict the observed mean drift after $\tau^+ \sim 100$. Therefore, other mechanisms must be taken into account to explain the mean particle drift towards the channel centre.

To summarise, the zero average wall-normal velocity for all y implies that, initially, particles stay on average on their initial wall-normal plane y_0 (as seen more clearly in fig. 4.1b), and start drifting away from y_0 at a finite time $|\tau|$ as they are dispersed by the fluctuating flow. Note that the existence of an average drift at $|\tau| > 0$ implies a non-zero value of the Lagrangian average of the wall-normal velocity $\langle v_y \rangle(\tau, y_0)$, since $\langle v_y \rangle = \partial \langle y \rangle / \partial \tau$. This can be contrasted with the Eulerian average $\overline{u_y}(y)$ which is zero for all y. Fluid particles released from a given wall distance, drift on average towards the channel centre to achieve the predicted uniform particle distribution throughout the channel at very long times. The average drift is much slower than the decorrelation of the tracer acceleration, and hence the latter cannot explain the observed average

wall-normal tracer displacement.

4.2 Mean streamwise particle displacement

A similar procedure can be applied to characterise the average particle displacement in the streamwise direction, and in particular, its time asymmetry qualitatively observed in fig. 3.5. In the following we show that the average initial particle acceleration can effectively explain the short-time streamwise displacement including its time asymmetry, at least in regions where the average acceleration is relatively important.

As in section 4.1, we first consider the short-time Taylor expansion of the streamwise displacement of a particle,

$$\delta x(\tau) = v_{0x}\tau + \frac{1}{2}a_{0x}\tau^2 + \mathcal{O}(\tau^3) = v_{0x}\tau\left(1 + \frac{a_{0x}}{2v_{0x}}\tau + \mathcal{O}(\tau^2)\right), \tag{4.3}$$

where v_{0x} and a_{0x} are the particle velocity and acceleration at $\tau = 0$. It follows that the absolute streamwise displacement is

$$|\delta x|(\tau) = v_{0x}|\tau|\left(1 + \frac{a_{0x}}{2v_{0x}}\tau + \mathcal{O}(\tau^2)\right) = v_{0x}|\tau| + \frac{1}{2}a_{0x}|\tau|\tau + \mathcal{O}(\tau^3), \tag{4.4}$$

under the assumptions that the streamwise particle velocity v_{0x} is positive,[2] and that the term in the parenthesis is also positive, which can be expected for $|\tau| \ll v_{0x}/|a_{0x}|$. Equation (4.4) expresses that the particle displacement is initially described by its initial velocity followed by a correction due to its initial acceleration. More interestingly, this implies a temporal asymmetry of the particle displacement,

$$|\delta x|(\tau) - |\delta x|(-\tau) = a_{0x}|\tau|\tau + \mathcal{O}(\tau^3). \tag{4.5}$$

Equations (4.4) and (4.5) can be averaged among particles initially located at a wall distance y_0, assuming that all the particles have a positive initial streamwise velocity, to yield

$$\langle|\delta x|\rangle(\tau) = \langle v_{0x}\rangle|\tau| + \frac{1}{2}\langle a_{0x}\rangle|\tau|\tau + \mathcal{O}(\tau^3), \tag{4.6}$$

$$\langle|\delta x|\rangle(\tau) - \langle|\delta x|\rangle(-\tau) = \langle a_{0x}\rangle|\tau|\tau + \mathcal{O}(\tau^3), \tag{4.7}$$

where the dependency of the statistics on y_0 has been omitted for clarity.

Figure 4.2 presents mean streamwise displacements results for particles initially located at different wall distances y_0. In fig. 4.2a, backwards and forwards in time displacements are shown. As predicted by eq. (4.6), the mean displacement is determined at short times by the average streamwise velocity at the starting position. At long times, particles initially close to the wall accelerate on average, i.e., their average

[2] This is a very reasonable assumption in the present flow, where turbulent fluctuations are nearly always weaker than the mean streamwise velocity.

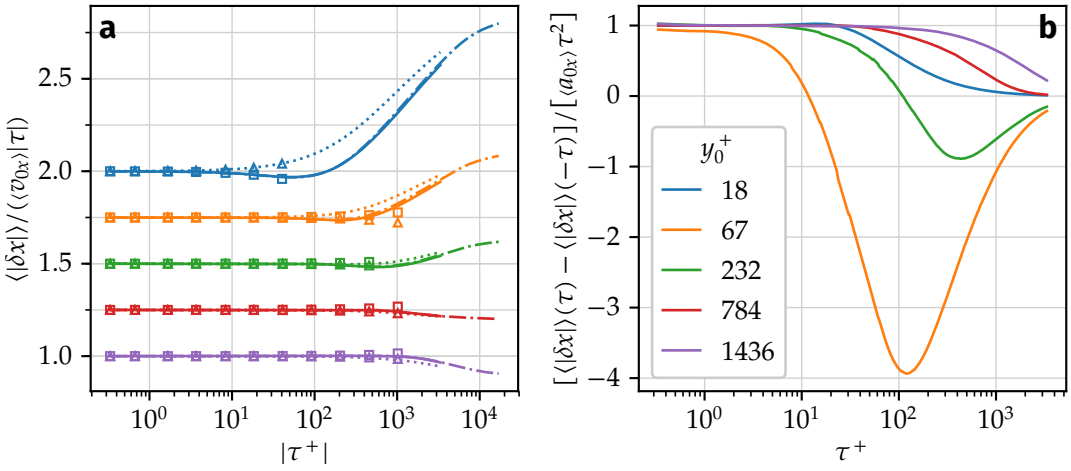

Figure 4.2. Mean streamwise tracer displacement in the channel. (a) Average streamwise displacement $\langle|\delta x|\rangle(y_0, \tau)$. Colours indicate the initial particle wall distance y_0 (see legend on the right). Curves are normalised by the displacement due to the initial mean particle velocity, $\langle v_{0x}\rangle|\tau|$. Dotted lines represent backward displacement ($\tau < 0$). Curves are shifted vertically by increments of 0.25 for clarity. Squares and triangles represent the short-time estimation $\langle|\delta x|\rangle \approx \langle v_{0x}\rangle|\tau| + \frac{1}{2}\langle a_{0x}\rangle|\tau|\,\tau$ for $\tau > 0$ and $\tau < 0$, respectively. Dash-dotted lines represent forward statistics obtained from dataset DS2. (b) Difference between mean displacements forwards and backwards in time, normalised by $\langle a_{0x}\rangle\tau^2$.

streamwise velocity $\langle v_x\rangle(\tau)$ is larger for large $|\tau|$ than at $\tau = 0$. This can be understood by considering that tracers are uniformly distributed across the channel at very long times. Under this assumption, the asymptotic mean streamwise velocity of the tracers is equal to the bulk velocity U_b in the channel [eq. (1.19)]. This is verified in fig. 4.3 where the average streamwise velocity of tracers released at different wall distances is plotted for positive time lags. Therefore, if tracers are initially labelled in a region where the mean velocity $U(y)$ is small relative to U_b, the tracers are expected to gain streamwise velocity on average at long times. Conversely, particles initially located near the channel centre decelerate on average since their initial mean streamwise velocity is higher than the bulk flow velocity.

As predicted from fig. 3.5, the mean streamwise displacement is asymmetric in time (fig. 4.2a). This is clearly visible for particles initially located near the wall, which travel longer distances when tracked backwards in time. For the initial wall distance $y_0^+ = 18$, where the mean streamwise acceleration is relatively important compared to the rest of the channel (fig. 3.3a), the initial particle acceleration is sufficient to explain this asymmetry, as seen by the good agreement at short times between our data and the estimation (4.6) (symbols in fig. 4.2a). The validity of the short time estimation is further evaluated in fig. 4.2b, where the difference between backward and forward mean displacements is plotted normalised by the estimation (4.7). According to the figure, the short-time estimation is appropriate for a characteristic duration $\tau^+ \sim 10$, which actually varies with the initial wall distance.

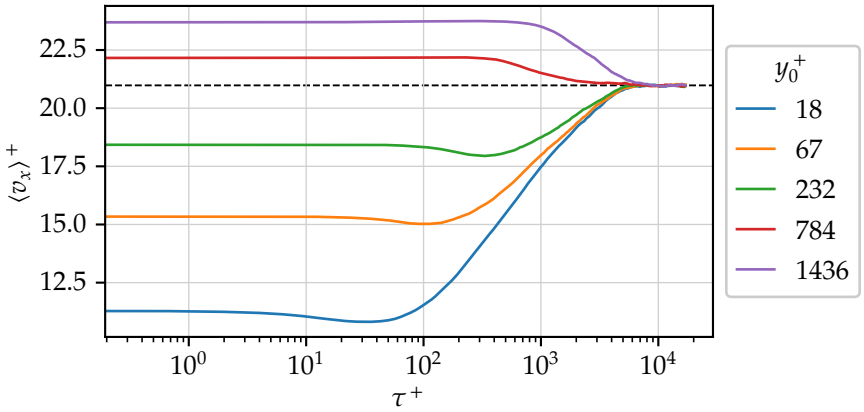

Figure 4.3. Mean streamwise tracer velocity $\langle v_x \rangle(y_0, \tau)$ for different initial particle wall distances y_0. The horizontal dashed line represents the bulk velocity in the channel, $U_b = \frac{1}{2h} \int_0^{2h} U(y)\,\mathrm{d}y$.

The analysis presented here shows that Taylor expansions are appropriate to describe the streamwise tracer displacement up to times of the order of 10 wall units. In practice, this observation may serve as an estimate for the temporal resolution required to estimate mean accelerations from mean displacement statistics, for instance in particle tracking experiments. At later times following the kinematic regime, the mean streamwise displacement is intuitively described by a tendency of the mean streamwise tracer velocity to approach the bulk velocity U_b in the channel. Therefore, tracers initially located near the wall are accelerated on average as the local mean velocity is smaller than U_b, and conversely for tracers near the channel centre.

4.3 Mean-square dispersion: theory and definitions

Above we have considered the average displacement $\langle \delta x_i \rangle$ of an ensemble of fluid particles conditioned by their initial distance from the wall. In the following sections we characterise the typical variation of the tracer displacements away from their average displacements. This is quantified by the standard deviation of the displacements or equivalently by its variance $\langle \delta x_i'^2 \rangle(\tau, y_0)$, which is referred to in the following as the *mean-square dispersion*. Here $\delta x_i'$ has the meaning of a *fluctuating* displacement relative to the mean Lagrangian displacement $\langle \delta x_i \rangle$, i.e.

$$\delta x_i'(t_0 + \tau, \boldsymbol{x}_0) = \delta x_i(t_0 + \tau, \boldsymbol{x}_0) - \langle \delta x_i \rangle(\tau, y_0) \tag{4.8}$$

$$= \int_0^t \left[v_i(t_0 + \tau, \boldsymbol{x}_0) - \langle v_i \rangle(\tau, y_0) \right] \mathrm{d}\tau\,. \tag{4.9}$$

We note that, unlike δx_i, the fluctuating displacement $\delta x_i'$ is Galilean-invariant since it can be expressed in terms of a velocity difference.

First, the case of isotropic turbulent flows is discussed in section 4.3.1, including well-established results and more recent discussions on the time asymmetry of single-

particle Lagrangian statistics. In section 4.3.2, short-time estimations for the mean-square displacement $\langle \delta x_i^2 \rangle$ and the mean-square dispersion $\langle \delta x_i'^2 \rangle$ are derived, and their time asymmetry is respectively expressed in terms of the mean Lagrangian power and the velocity-acceleration covariance. Later in section 4.4, a physical interpretation of these two quantities and their values across the channel are discussed. Finally, numerical results are presented in section 4.5 and compared to analytical predictions.

4.3.1 Single-particle dispersion in isotropic flows

In HIT, since the average displacement $\langle \delta x_i \rangle$ is zero at all times, the mean-square dispersion $\langle \delta x_i'^2 \rangle$ is the lowest-order statistic that can provide a significant description of the dispersion properties of the flow. For the same reason, in HIT no distinction is made between $\langle \delta x_i'^2 \rangle$ and the mean-square displacement $\langle \delta x_i^2 \rangle$. Moreover, due to isotropy, the displacement along a single arbitrary direction is sufficient to characterise tracer dispersion.

In turbulent flows, the time evolution of tracer dispersion is closely linked to the Lagrangian time scales of the flow. In the case of single-particle dispersion, the most important quantity is the Lagrangian integral time scale T_L characterising the typical decorrelation time of the tracer velocity fluctuations (see also section 3.5). As stated in the introduction (section 1.1.2), Taylor [175] linked the mean-square displacement $\langle \delta x_i^2 \rangle$ in a stationary system to the Lagrangian velocity auto-correlation $\rho^v(\tau)$,

$$\langle \delta x_i^2 \rangle(\tau) = 2\sigma_u^2 \tau \int_0^\tau \left(1 - \frac{s}{\tau}\right) \rho^v(s)\, \mathrm{d}s\,, \tag{4.10}$$

where $\sigma_u^2 = \overline{u_i'^2}$ is the velocity variance. At small time delays $\tau \ll T_L$, the Lagrangian velocity does not change importantly, which is reflected by an auto-correlation $\rho^v(\tau) \approx 1$. This leads to a *ballistic* growth of the mean-square displacement at short times, $\langle \delta x_i^2 \rangle(\tau) \approx \sigma_u^2 \tau^2$. On the other hand, at times $\tau \gg T_L$, particles lose memory of their initial velocities ($\rho^v(\tau) \approx 0$) and dispersion is described by Brownian motion [51]. From eq. (4.10), the asymptotic diffusive regime is given by

$$\langle \delta x_i^2 \rangle(\tau) \approx 2\sigma_u^2 T_L \tau \quad \text{for} \quad \tau \gg T_L. \tag{4.11}$$

In recent years, the question of the consequences of the time irreversibility of turbulence on Lagrangian statistics has been raised. As demonstrated by Falkovich et al. [52], single-particle Lagrangian statistics in homogeneous flows are necessarily time-symmetric provided that the statistics are invariant under Galilean transformation. An important example is the family of Lagrangian velocity structure functions $D_p(\tau) = \langle |v_i(t_0 + \tau) - v_i(t_0)|^p \rangle$ (see section 1.1.4). In statistically stationary HIT, Xu et al. [196] recently found that the irreversibility of turbulence is visible on the Lagrangian evolution of kinetic energy. They observed that fluid particles lose their kinetic energy faster than they gain it, a phenomenon they called 'flight-crash events'. Since kinetic energy is not Galilean-invariant, this does not contradict the observations by Falkovich et al. [52]. Xu et al. [196] associated their findings with a negative skewness

of the Lagrangian power $\Pi = \mathrm{D}E/\mathrm{D}t = \boldsymbol{v} \cdot \boldsymbol{a}$, where $E = |\boldsymbol{v}|^2/2$ is the fluid particle kinetic energy. We note that in HIT, the skewness is the first non-zero odd moment of Π, since the mean Lagrangian power $\overline{\Pi}$ necessarily vanishes due to stationarity (the global energy content is conserved) and homogeneity (there is no mean energy flux across spatial regions). From experimental and DNS data at Re_λ between 170 and 690, Xu et al. [196] further showed that the skewness is nearly Reynolds-number independent and is close to -0.5 in statistically stationary 3D turbulence. Furthermore, Lagrangian power fluctuations were shown by Pumir et al. [141] to be dominated by the pressure gradient force, which, although it does not exert an average work on the flow,[3] tends to redistribute energy in 3D HIT by accelerating high-velocity fluid particles and decelerating slow particles.

4.3.2 Mean-square dispersion at short times

In the rest of this chapter, the distinction is made between the *mean-square displacement* $\langle \delta x_i^2 \rangle(\tau, y_0)$ and the *mean-square dispersion* $\langle \delta x_i'^2 \rangle(\tau, y_0)$, where the fluctuating displacement $\delta x_i'$ is defined as in eq. (4.8). In the spanwise direction (as in HIT), both quantities are equal in the channel since the average displacement $\langle \delta z \rangle$ is zero due to $z \leftrightarrow -z$ symmetry. As seen in sections 4.1 and 4.2, this is generally not the case in the streamwise and wall-normal directions.

The motion of a particle at short times can be approximated by the effect of its initial velocity $\boldsymbol{v}_0 = \boldsymbol{v}(\boldsymbol{x}_0, t_0)$ and, at the second order, of its initial acceleration $\boldsymbol{a}_0 = \boldsymbol{a}(\boldsymbol{x}_0, t_0)$. The associated Taylor expansion of the short-time particle motion leads to the estimation of the mean-square displacement

$$\langle \delta x_i^2 \rangle(\tau, y_0) = \langle v_{0i}^2 \rangle \tau^2 + \langle v_{0i}\, a_{0i} \rangle \tau^3 + \mathcal{O}(\tau^4), \tag{4.12}$$

where v_{0i} and a_{0i} are the i-th components of the initial particle velocity and acceleration, respectively. In eq. (4.12) and in the rest of this chapter, summation is not implied over repeated indices. The zero-lag Lagrangian means can be replaced by their Eulerian counterparts to yield

$$\langle \delta x_i^2 \rangle(\tau, y_0) = \overline{u_i^2}(y_0) \tau^2 + \overline{u_i a_i}(y_0) \tau^3 + \mathcal{O}(\tau^4). \tag{4.13}$$

The first term on the right-hand side of eq. (4.13) indicates that, at short times, the displacement of a particle away from its initial position is given by the ballistic regime mentioned in section 4.3.1. The ballistic regime appropriately describes the mean-square particle displacement for durations over which the mean particle velocity does not change importantly, i.e. for τ much smaller than the Lagrangian integral time scale $T_{L,i}$ representing the characteristic tracer velocity decorrelation time.

[3] The work exerted by the pressure gradient at a fixed point $\boldsymbol{x}$ and time t is $W_p(\boldsymbol{x}, t) = -\boldsymbol{u}(\boldsymbol{x}, t) \cdot \boldsymbol{\nabla} p(\boldsymbol{x}, t)/\rho$. This is the contribution of the pressure gradient force to the Lagrangian power. In other words, if $W_p(\boldsymbol{x}, t) > 0$, the pressure gradient is increasing the kinetic energy of a tracer located at $\boldsymbol{x}$ at time t. In HIT, the average work $\overline{W_p}$ is zero. See also appendix B.1 and eq. (B.1).

Similarly to section 4.2, the second-order correction $\overline{u_i a_i}\tau^3$ may provide an indication of the temporal asymmetry of the dispersion at short times. From eq. (4.13), the forwards and backwards in time behaviours can be subtracted to obtain

$$\langle \delta x_i^2 \rangle(\tau, y_0) - \langle \delta x_i^2 \rangle(-\tau, y_0) = 2\overline{u_i a_i}(y_0)\tau^3 + \mathcal{O}(\tau^5). \tag{4.14}$$

Therefore, a non-zero value of $\overline{u_i a_i}$ indicates that, at short times, the dispersion is time asymmetric. As mentioned in section 4.3.1, the velocity-acceleration product $\boldsymbol{v} \cdot \boldsymbol{a}$ is equal to the Lagrangian power Π, representing the energy instantaneously gained or lost by a fluid particle with velocity $\boldsymbol{v}$ and acceleration $\boldsymbol{a}$. The mean Lagrangian power appears in the total mean-square displacement, obtained from adding the three components of eq. (4.14),

$$\langle \delta \boldsymbol{x}^2 \rangle(\tau, y_0) - \langle \delta \boldsymbol{x}^2 \rangle(-\tau, y_0) = 2\overline{\boldsymbol{u} \cdot \boldsymbol{a}}(y_0)\tau^3 + \mathcal{O}(\tau^5). \tag{4.15}$$

Hence, the mean Lagrangian power $\overline{\Pi} = \overline{\boldsymbol{u} \cdot \boldsymbol{a}}$ quantifies the short-time temporal asymmetry of the average squared tracer displacement. Equation (4.15) expresses the intuitive idea that an increase of the average particle kinetic energy is associated with an acceleration of their motion, and therefore particles tend to travel longer distances forwards than backwards in time.

It is readily shown that the following analogue equations to eqs. (4.13) to (4.15) describe the short-time behaviour of the mean-square dispersion $\langle \delta x_i'^2 \rangle$,

$$\langle \delta x_i'^2 \rangle(\tau, y_0) = \overline{u_i'^2}(y_0)\tau^2 + \overline{u_i' a_i'}(y_0)\tau^3 + \mathcal{O}(\tau^4), \tag{4.16}$$

$$\langle \delta x_i'^2 \rangle(\tau, y_0) - \langle \delta x_i'^2 \rangle(-\tau, y_0) = 2\overline{u_i' a_i'}(y_0)\tau^3 + \mathcal{O}(\tau^5), \tag{4.17}$$

$$\langle \delta \boldsymbol{x}'^2 \rangle(\tau, y_0) - \langle \delta \boldsymbol{x}'^2 \rangle(-\tau, y_0) = 2\overline{\boldsymbol{u}' \cdot \boldsymbol{a}'}(y_0)\tau^3 + \mathcal{O}(\tau^5). \tag{4.18}$$

The time asymmetry of the mean-square dispersion is therefore quantified by the velocity-acceleration covariance $\overline{\boldsymbol{u}' \cdot \boldsymbol{a}'}$, analogously to the mean Lagrangian power $\overline{\Pi}$ for the case of $\langle \delta \boldsymbol{x}^2 \rangle$. As discussed below in section 4.4, $\overline{\boldsymbol{u}' \cdot \boldsymbol{a}'}$ is related (but not exactly equal) to the average rate of change of TKE along Lagrangian paths.

4.4 Lagrangian power and velocity-acceleration covariance

In the following, the profiles of mean Lagrangian power $\overline{\boldsymbol{u} \cdot \boldsymbol{a}}$ and velocity-acceleration covariance $\overline{\boldsymbol{u}' \cdot \boldsymbol{a}'}$ appearing in eqs. (4.15) and (4.18) are presented in the channel, as well as the contributions from the three velocity and acceleration components appearing in eqs. (4.14) and (4.17).

Unlike in homogeneous flows, where there is no average flux of energy across spatial regions,[4] in wall turbulence most of the energy is injected far from the walls and dissipated by viscous shear near the walls. Indeed, as discussed in more detail in appendix B.1, the mean Lagrangian power profile $\overline{\Pi}(y)$ across the channel results

[4] There is an energy flux across spatial *scales*, i.e. the energy cascade, but this is not discussed here.

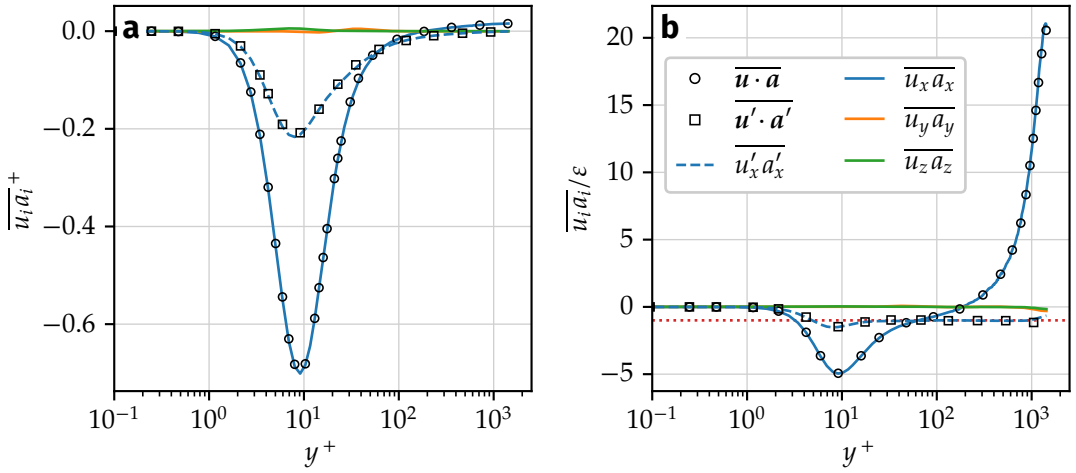

Figure 4.4. Mean velocity-acceleration product across the channel non-dimensionalised (a) in wall-units and (b) by the mean turbulent dissipation rate $\varepsilon(y)$. Solid lines represent total components $\overline{u_i a_i}$ (no summation implied). The dashed line represents the velocity-acceleration covariance $\overline{u_x' a_x'}$. Circles represent the Lagrangian power $\overline{\boldsymbol{u}\cdot\boldsymbol{a}}$ and squares represent the covariance $\overline{\boldsymbol{u}'\cdot\boldsymbol{a}'}$. In subfigure (b), the red dotted line corresponds to $\overline{u_i a_i} = -\varepsilon$. Mean fluctuating products $\overline{u_y' a_y'}$ and $\overline{u_z' a_z'}$ are not shown since they are equal to their total counterparts.

from the balance between (i) the mean input power Π_{in}, which corresponds to the average work performed by the mean pressure gradient driving the flow; (ii) the total mean energy dissipation rate $\varepsilon_T = \nu\overline{(\partial_j u_i)(\partial_j u_i)}$; and (iii) a viscous diffusion term that mainly redistributes kinetic energy from the buffer layer to the viscous subregion. Since the mean input power is proportional to the local mean streamwise velocity in the channel [eq. (B.4)], most of the energy is injected where the average velocity is higher, i.e. far from the walls. The total kinetic energy budget across the channel is plotted in fig. B.1 (appendix B.1). Due to statistical stationarity, the total energy in the system is conserved over time, and therefore the globally-averaged mean power is necessarily zero, i.e. $\int_{-h}^{h} \overline{\Pi}(y)\,\mathrm{d}y = 0$, which is verified in our simulations.

Profiles of mean Lagrangian power, as well as the contributions from the three velocity and acceleration components, are shown in fig. 4.4. The mean power is mainly determined by the streamwise velocity and acceleration components, while the other two components have a negligible contribution. This means that the mean rate of change of kinetic energy mostly describes an average increase or decrease of the fluid particle streamwise velocity. The negative peak of the mean power at $y^+ \approx 9$ indicates that fluid particles on average lose kinetic energy in the near-wall region, and as a consequence they travel on average shorter streamwise distances when tracked forwards in time. This is consistent with the observations from figs. 3.5 and 4.2. Similar behaviour of the mean Lagrangian power across the channel has been observed in the experiments by Stelzenmuller [173, sec. 3.4]. Far from the wall and up to the channel centre, the mean Lagrangian power is weakly and increasingly positive. This is more visible in fig. 4.4b, where quantities are normalised by the local mean turbulent energy dissipation rate

$\varepsilon(y)$. This suggests that fluid particles on average gain energy in that region, albeit at a much slower rate than the loss of energy near the wall.

Also shown in fig. 4.4 is the velocity-acceleration covariance $\overline{\boldsymbol{u}' \cdot \boldsymbol{a}'}$, which, as for $\overline{\boldsymbol{u} \cdot \boldsymbol{a}}$, is almost entirely determined by the streamwise fluctuations $\overline{u_x' a_x'}$. As noted above, the velocity-acceleration covariance is the analogue of the mean Lagrangian power when the mean-square dispersion $\langle \delta x_i'^2 \rangle$ is considered, as it determines its short-time temporal asymmetry. The covariance is related to the mean power via the Reynolds decomposition $\overline{u_i' a_i'} = \overline{u_i a_i} - \overline{u_i}\,\overline{a_i}$. Since the mean velocity $\overline{u_i}$ is zero in the wall-normal and spanwise directions, the components $\overline{u_y' a_y'}$ and $\overline{u_z' a_z'}$ are equal to their non-fluctuating counterparts.

From fig. 4.4 it is seen that, in the buffer layer, $\overline{\boldsymbol{u}' \cdot \boldsymbol{a}'}$ represents a non-negligible fraction of the mean Lagrangian power, accounting for about 30 % of the total loss of kinetic energy at the peak located near $y^+ = 10$. As opposed to the total power, which is weakly positive for $y^+ > 200$, the covariance is negative at all wall distances. This is seen more clearly in fig. 4.4b where data is normalised by the local mean turbulent dissipation rate $\varepsilon(y)$. Interestingly, $\overline{\boldsymbol{u}' \cdot \boldsymbol{a}'} \approx -\varepsilon$ in most of the channel. This can be explained, at least in the logarithmic region of the channel, by considering the relation between $\overline{\boldsymbol{u}' \cdot \boldsymbol{a}'}$ and the average rate of change of TKE along tracer paths derived in appendix B.2 [eq. (B.17)],

$$\overline{\frac{\mathrm{D}k}{\mathrm{D}t}}(y) = \overline{\boldsymbol{u}' \cdot \boldsymbol{a}'}(y) + \mathcal{P}(y), \tag{4.19}$$

where $k = |\boldsymbol{u}'|^2/2$ is the TKE[5] and $\mathcal{P} = -\overline{u_x' u_y'}\,\mathrm{d}U/\mathrm{d}y$ is the turbulent kinetic energy production rate [137]. In the logarithmic region, $\overline{\boldsymbol{u}' \cdot \boldsymbol{a}'}$ and $\mathcal{P}$ cancel out ensuring that, on average, fluid particles do not gain or lose TKE in that region (fig. B.2). At the same time, TKE production and dissipation rates are nearly balanced in the logarithmic region [see e.g. 94], which leads to the observed value $\overline{\boldsymbol{u}' \cdot \boldsymbol{a}'} \approx -\varepsilon$.

Alternatively, from the kinetic energy budget derived from the Navier–Stokes equations [137], it is shown in appendix B.2 that the velocity-acceleration covariance can be written as [eq. (B.25)]

$$\overline{\boldsymbol{u}' \cdot \boldsymbol{a}'} = -\varepsilon + \nu \frac{\mathrm{d}^2 \overline{k}}{\mathrm{d}y^2} - \frac{1}{\rho} \frac{\mathrm{d}}{\mathrm{d}y} \overline{u_y' p'}, \tag{4.20}$$

where the last two terms on the right-hand side represent viscous diffusion and pressure transport. The relation $\overline{\boldsymbol{u}' \cdot \boldsymbol{a}'} \approx -\varepsilon$ can be explained by these last two terms vanishing far from the wall, which has been observed away from the viscous and buffer layers in previous studies [1, 68, 100]. More generally, this relation is expected to be valid in other inhomogeneous turbulent flows. For instance, Huck et al. [70, 71] analysed in

[5] The notation k denotes in this work the *instantaneous* turbulent kinetic energy evaluated at a fixed position in space, or equivalently, the instantaneous TKE of a fluid particle. Other works, including Pope [137] referenced above, use k to denote the Eulerian average of the TKE, which is here given by $\overline{k}$.

detail the TKE budget equations in a von Kármán flow between two counter-rotating disks in a square tank. They found $\overline{\boldsymbol{u}' \cdot \boldsymbol{a}'} \approx -\varepsilon$ far from the impellers where energy is injected into the flow, and suggested that this result can provide an alternative method for estimating the local dissipation rate in inhomogeneous turbulence experiments using single-particle Lagrangian data. In particular, this approach is simpler than relying on the relation $\overline{\delta\boldsymbol{u} \cdot \delta\boldsymbol{a}} \approx -2\varepsilon$ involving relative increments of velocity and acceleration between particle pairs (see section 5.3.1 for details), which requires higher particle concentrations [70].

To summarise, in contrast with the direct relation between $\overline{\boldsymbol{u} \cdot \boldsymbol{a}}$ and the total kinetic energy E, the velocity-acceleration covariance $\overline{\boldsymbol{u}' \cdot \boldsymbol{a}'}$ does not directly represent the mean rate of change of TKE, to which it is instead related by eq. (4.19). Far from the wall, $\overline{\boldsymbol{u}' \cdot \boldsymbol{a}'}$ only represents the loss of TKE by fluid particles associated to the dissipation ε, without being counterbalanced by the TKE production term $\mathcal{P}$. In particular, this suggests that the mean-square dispersion is time-asymmetric in the logarithmic region despite the balance between production and dissipation of TKE, i.e. despite the fact that tracers on average do not gain or lose TKE in that region.

4.5 Mean-square dispersion in the channel

In this section, mean-square dispersion statistics obtained from our channel flow DNS at $Re_\tau = 1440$ are presented. Results are compared with the short-time predictions in section 4.3.2. In particular, the temporal asymmetry of mean-square dispersion statistics is evaluated in terms of the profiles of mean Lagrangian power and velocity-acceleration covariance discussed in section 4.4.

4.5.1 Mean-square streamwise displacement

The case of the streamwise displacement δx is shown in fig. 4.5. In fig. 4.5a, the mean-square displacement $\langle \delta x^2 \rangle$ is plotted compensated by the short-time ballistic regime (eq. (4.12) truncated to its first-order term) for positive and negative time lags τ. The ballistic approximation accurately describes the mean tracer motion at short times. This ballistic regime is valid over a characteristic time that increases with wall distance, consistently with the behaviour of the Lagrangian integral time scales in the channel (see section 3.5, fig. 3.12).

Following the ballistic regime, the mean-square displacement evolves differently for positive and negative time lags, demonstrating the time asymmetry of the streamwise particle motion. For tracers initially located near the wall, $\langle \delta x^2 \rangle$ grows faster backwards in time. This is consistent with the observations for the absolute streamwise displacement (fig. 4.2). In the case of $y_0^+ = 18$ and 67, the temporal asymmetry is explained at short times, up to $|\tau| \sim 10$, by the negative value of the streamwise contribution to the mean Lagrangian power $\overline{u_x a_x}$ observed in fig. 4.4. This is confirmed in fig. 4.5b, where the difference between backward and forward displacement is compensated by $2\tau^3$. Under this normalisation, the short-time estimation (4.14) predicts a short-time

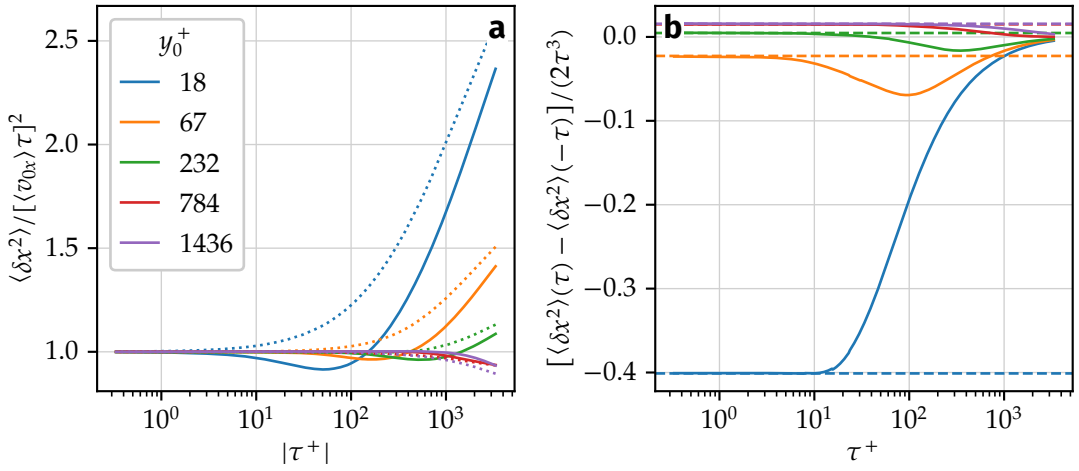

Figure 4.5. Streamwise mean-square displacement in the channel. (a) Streamwise mean-square displacement $\langle \delta x^2 \rangle$ compensated by the ballistic short-time approximation $\langle \delta x^2 \rangle \approx \langle v_{0x}^2 \rangle \tau^2$. Solid lines, forward dispersion ($\tau > 0$); dotted lines, backward dispersion ($\tau < 0$). Colours represent different initial wall-normal planes y_0. (b) Difference between $\langle \delta x^2 \rangle(\tau)$ for $\tau > 0$ and $\tau < 0$ compensated by $2\tau^3$ and non-dimensionalised in wall units. Dashed lines correspond to the streamwise contribution to the Lagrangian power $\langle v_x a_x \rangle$ evaluated from tracer data at $\tau = 0$.

plateau at $\overline{u_x a_x}$, represented by dashed lines in fig. 4.5b.

The short-time estimation (4.14) is valid for all wall distances according to fig. 4.5b. In the case of $y_0^+ = 232$, $\overline{u_x a_x} \approx 0$ leading to a nearly time-symmetric mean-square displacement at short time lags. As shown in fig. 4.4, $\overline{u_x a_x}$ is weakly positive at larger wall distances, and therefore tracers travel slightly longer distances when tracked forwards in time, which is confirmed by fig. 4.5b. As discussed in section 4.4, this reflects the fact that tracers gain kinetic energy on average far from the wall.

Up to this point we have only explained the temporal asymmetry of $\langle \delta x^2 \rangle$ in terms of the short-time Taylor expansion (4.14). A qualitative description can be made regarding the asymmetry at longer times by taking into account the mean Lagrangian power profiles in fig. 4.4. For tracers initially located near the wall, the negative gap between forward and backward displacements can be expected to increase as long as tracers stay within a region of negative $\overline{u_x a_x}$, i.e. within $y^+ < 200$. In fig. 4.5b, it is shown that for particles initially located at $y^+ = 18$, the gap increases fastest for short time lags, while at later times the gap keeps increasing at a lower rate. This may be explained by particles migrating on average away from the wall where the mean Lagrangian power is weaker, leading to a slower rate of change of the mean tracer kinetic energy and thus to a slower growth of the forwards-backwards gap. As seen in fig. 4.5b, this is not the case for tracers released at $y^+ = 67$, where the compensated gap increases at some intermediate time lag. This may reflect the fact that some particles migrate towards the wall where the mean Lagrangian power is strongly negative. In this case, the average kinetic energy lost by the subset of particles migrating towards the wall

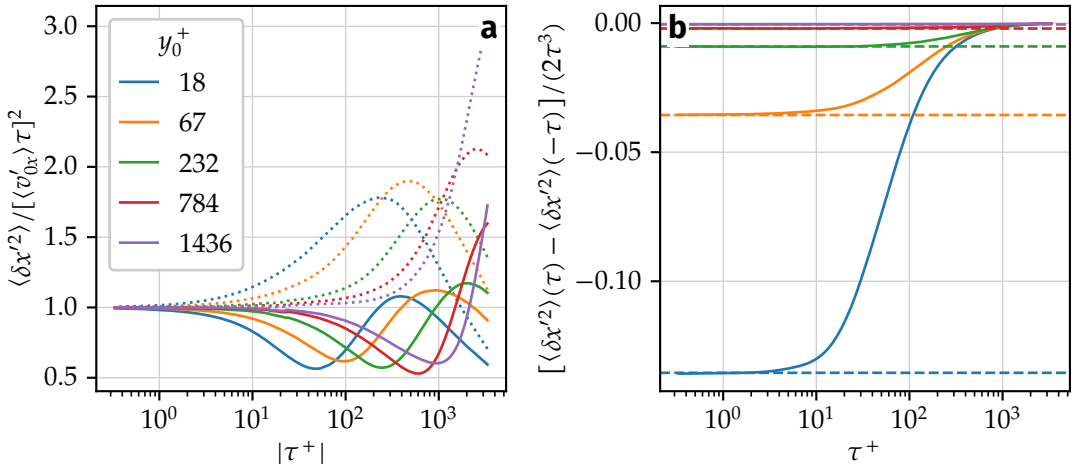

Figure 4.6. Streamwise mean-square dispersion in the channel. Equivalent of fig. 4.5 for the mean-square dispersion $\langle \delta x'^2 \rangle$. In (a), the ballistic short-time approximation is given by $\langle \delta x'^2 \rangle \approx \langle v'^2_{0x} \rangle \tau^2$. In (b), dashed lines correspond to the streamwise velocity-acceleration covariance $\overline{u'_x a'_x}$ evaluated at each initial wall distance. See fig. 4.5 for more details.

would strongly contribute to the temporal asymmetry after the initial ballistic regime. In comparison, the positive contribution of the particles migrating towards the channel centre to the mean kinetic energy would be much weaker, since the mean Lagrangian power is only weakly positive at $y^+ > 200$ (fig. 4.4a).

We now briefly comment on the general long-time behaviour of the mean-square displacement curves in fig. 4.5a. The interpretation is similar to that of the mean displacement $\langle \delta x \rangle$ (section 4.2). At long times, the streamwise displacement of tracers initially located close to the wall is accelerated compared to their initial ballistic regime since their average velocity increases (fig. 4.3). The opposite occurs with tracers initially located near the channel centre, i.e. their average velocity decreases to match the bulk velocity U_b at long times.

4.5.2 Mean-square streamwise dispersion

We now consider the mean-square dispersion $\langle \delta x'^2 \rangle$, i.e. the variance of the streamwise tracer dispersion in the channel quantifying the streamwise particle spread over time. The time evolution of $\langle \delta x'^2 \rangle$, for positive and negative time lags, is presented in fig. 4.6a compensated by the ballistic regime associated to eq. (4.16). The curves display a clear ballistic regime at short times, which has however a shorter characteristic duration than for $\langle \delta x^2 \rangle$, discussed above. This difference is explained by the fact that the fluctuating tracer velocity changes more abruptly, in relative terms, than its total velocity.[6] As for

[6] In other words, a change in the streamwise velocity of a fluid particle, $\delta v_x = v_x(t+\tau) - v_x(t)$, results in a more important relative modification of the particle fluctuating velocity than of its total velocity, i.e. $|\delta v'_x / v'_x| \gg |\delta v_x / v_x|$. At short time lags τ, this can be proved by noting that $\delta v'_x \approx \delta v_x$ and $|v_x| \approx |U(y) + v'_x| \gg |v'_x|$. This is valid as long as tracers stay in the same region of the channel where

$\langle \delta x^2 \rangle$, we find that the characteristic time of validity of the ballistic regime grows with wall distance, as do the turbulence time scales in the channel (fig. 3.12).

At longer times, a clear divergence between positive and negative time lags is observed. For all initial wall distances, tracers spread faster over the streamwise direction when tracked backwards in time. This is qualitatively consistent with the short-time estimation (4.17) and the observation that the streamwise velocity-acceleration covariance $\overline{u_x' a_x'}$ is negative everywhere in the channel (fig. 4.4).

The temporal asymmetry is quantified in fig. 4.6b, where the difference between forward and backward mean-square dispersion compensated by $2\tau^3$ is plotted. The short-time plateaus confirm that the estimation (4.17) correctly predicts the time asymmetry at short time lags, and therefore that the velocity-acceleration covariance determines the irreversibility of the streamwise dispersion. In all cases, the gap between backward and forward dispersion increases at faster rate for small time increments and slows down for larger time lags.

4.5.3 Mean-square wall-normal displacement

The wall-normal motion of tracer particles has been initially described in section 4.1 in terms of the average displacement $\langle \delta y \rangle(\tau, y_0)$. It has been shown that tracers drift on average towards the channel centre, consistently with the hypothesis that tracers lose memory of their initial positions over time and tend asymptotically to a uniform distribution across the channel at infinite time lags. This hypothesis is evaluated here in terms of the expected values of the wall-normal mean-square displacement $\langle \delta y^2 \rangle$ and dispersion $\langle \delta y'^2 \rangle$.

The asymptotically uniform distribution of tracers across the channel can be expressed as the uniform PDF describing the wall-normal location y of a tracer,

$$P(y) = \frac{1}{2h} \quad \text{for} \quad y \in [0, 2h], \tag{4.21}$$

where h is the channel half-width. From eq. (4.21), the expected value of y^2 is $\langle y^2 \rangle = 4h^2/3$. From here, it is readily shown that the asymptotic expected values of δy^2 and $\delta y'^2$ are given by

$$\langle \delta y^2 \rangle = \frac{h^2}{3} + (h - y_0)^2 \quad \text{and} \quad \langle \delta y'^2 \rangle = \frac{h^2}{3}. \tag{4.22}$$

The time evolution of $\langle \delta y^2 \rangle$ and $\langle \delta y'^2 \rangle$ for different initial wall distances y_0 is presented in fig. 4.7. The ballistic regime predicted by eqs. (4.13) and (4.16) is recovered at short times for all wall distances. At long times, the curves tend to the asymptotic values given by eq. (4.22), which are represented by horizontal dashed lines in the figure. Results are shown for positive and negative time lags, although the difference between both is barely visible suggesting that wall-normal dispersion is symmetric in time. This is consistent with the negligible contribution of $\overline{u_y a_y}$ to the Lagrangian

the mean velocity $U(y)$ does not change significantly.

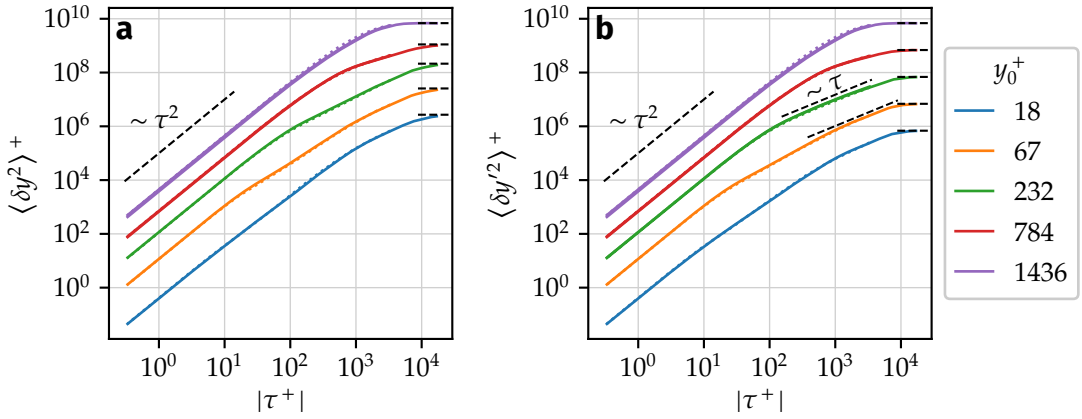

Figure 4.7. (a) Wall-normal mean-square displacement $\langle \delta y^2 \rangle$. (b) Wall-normal mean-square dispersion $\langle \delta y'^2 \rangle$. Solid lines, forward dispersion ($\tau > 0$); dotted lines, backward dispersion ($\tau < 0$). Forward dispersion curves are obtained from longer-extent dataset DS2. Horizontal dashed lines on the top right represent the asymptotic estimations (4.22). Quantities are non-dimensionalised in wall units. Curves are shifted vertically by increments of one decade for clarity.

power (fig. 4.4), to which is associated a negligible τ^3 term in eq. (4.14). Interestingly, for initial locations in the logarithmic layer ($y_0^+ = 67$ and 232 in the figure), the diffusive regime $\langle \delta y'^2 \rangle \sim \tau$ predicted by Taylor is observed at intermediate times before reaching the asymptotic state mentioned above. This may be explained by tracers staying within the logarithmic region, where the wall-normal velocity variance $\overline{u_y'^2}$ is maximum and nearly constant (see fig. 3.2b), before leaving towards either the inner or the outer layer where the intensity of the wall-normal velocity fluctuations (and thus the dispersion rate) is lower.

Comparison between fig. 4.7(a) and (b) shows that the time evolutions of $\langle \delta y^2 \rangle$ and $\langle \delta y'^2 \rangle$ are very similar. In other words, the mean-square displacement $\langle \delta y^2 \rangle$ is mainly determined by the spreading of tracers over the wall-normal direction and not so much by the mean drift $\langle \delta y \rangle$. The latter, as seen in section 4.1, evolves very slowly in time. A rough comparison of the length scales associated to the mean drift and to the mean dispersion is as follows. From fig. 4.1, it is seen that on average, tracers near the wall require $\tau^+ \sim 1000$ to travel a distance $\langle \delta y \rangle^+ \sim 200$. Over the same time, fig. 4.7 gives a mean-square dispersion of $\langle \delta y'^2 \rangle^+ \sim 10^5$ for particles initially located at $y_0^+ = 18$, i.e. a spreading of $\sqrt{10^5} \approx 300$ wall units. Hence, dispersion acts faster than mean drift for particles initially located near the wall. Further away from the wall, the difference between the evolution rates of dispersion and drift is expected to grow as mean drift becomes slower (fig. 4.1).

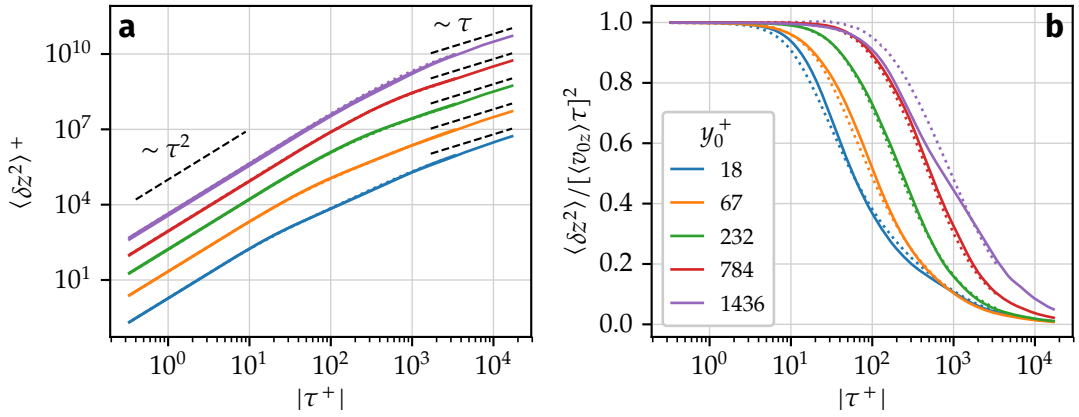

Figure 4.8. Spanwise mean-square displacement $\langle \delta z^2 \rangle$ (a) non-dimensionalised in wall units, and (b) compensated by the ballistic short-time approximation $\langle \delta z^2 \rangle \approx \langle v_{0z}^2 \rangle \tau^2$. Solid lines, forward dispersion ($\tau > 0$); dotted lines, backward dispersion ($\tau < 0$). In (a), curves are shifted vertically by increments of one decade for clarity.

4.5.4 Mean-square spanwise dispersion

Finally, the mean-square dispersion in the spanwise direction is represented in fig. 4.8a. Noting that the mean displacement $\langle \delta z \rangle$ is zero due to $z \leftrightarrow -z$ symmetry in the channel, the mean-square displacement $\langle \delta z^2 \rangle$ and the mean-square dispersion $\langle \delta z'^2 \rangle$ are equal and therefore only one of them is represented in the figure. At long times, the curves tend to the normally-diffusive regime first predicted by Taylor [175], i.e. $\langle \delta z^2 \rangle \sim \tau$. As for the other displacement components, a clear ballistic regime is observed at short times. The time of validity of this ballistic regime is roughly equal to that observed for the streamwise mean-square dispersion (fig. 4.6a). This is clearer in fig. 4.8b where the mean-square dispersion is compensated by the short-time ballistic regime.

Similarly to the case of the wall-normal dispersion, $\langle \delta z^2 \rangle$ does not display significant time asymmetry, which is again consistent with the approximately zero value of $\overline{u_z a_z}$ in the channel (fig. 4.4). Differences between backward and forward dispersion are more visible in fig. 4.8b due to the chosen normalisation, but they are negligible and most likely a result of the finite size of the statistical sample.

4.6 Conclusion

Single-tracer dispersion in turbulent channel flow at $Re_\tau = 1440$ is described in this chapter. The time asymmetry of dispersion is analysed with regard to the average fluxes of kinetic energy across the channel which are a sign of the irreversibility of this kind of flow, and which distinguish wall-bounded turbulence from homogeneous turbulent flows.

As opposed to HIT where there are no preferential directions, in wall-bounded turbulence there exists an average tracer drift. The most evident average drift is related

to the effect of the mean flow which advects tracers at high speed in the streamwise direction. As described in section 4.1, tracers are also affected by a (much slower) average advection in the wall-normal direction due to the cumulative effect of the velocity fluctuations in that direction. Tracers drift on average towards the channel centre, since they tend to distribute uniformly across the channel at very long times as they lose memory of their initial locations. However, the precise mechanisms explaining this wall-normal drift are not understood at this point. A better understanding of this phenomenon is relevant for modelling the dispersion of tracers, and more concretely, it would lead to improvements of the ballistic particle pair dispersion model introduced later in chapter 5 by properly accounting for the absolute drift of particle pairs.

The irreversibility of wall-bounded turbulent flows is reflected on the time asymmetry of the streamwise motion of tracers in the channel. For instance, tracers located near the wall at a reference time t_0 travel on average longer distances when tracked backwards in time than forwards (fig. 4.2a). Furthermore, groups of tracers probed at any fixed wall distance spread over larger streamwise distances for negative time lags (fig. 4.6).

In section 4.2, the first observation is associated to a non-zero value of the average streamwise acceleration, although this is only valid at very short times, and in regions of strong average acceleration, i.e. near the wall. A more complete explanation is given in section 4.3 in terms of the average flux of total kinetic energy in the channel. In statistically stationary channel flow turbulence, even though the mean energy content is constant in time, energy is mainly injected far from the wall where the mean velocity is higher, and is dissipated mainly in the near-wall region due to viscous stresses. This imbalance implies that, close to the wall where dissipation is more important, tracers lose kinetic energy on average, while the opposite occurs far from the wall. This is quantified by the mean Lagrangian power $\overline{\Pi} = \overline{\boldsymbol{u} \cdot \boldsymbol{a}}$, which is negative close to the wall and slightly positive near the channel centre. As a result, on average tracers see an ever-decreasing streamwise convection speed as long as they stay within the near-wall region, leading to the observed temporal asymmetry.

The second observation mentioned above is explained in section 4.3 by linking the short-time temporal asymmetry of the mean tracer spreading rate in the streamwise direction, to the velocity-acceleration covariance $\overline{\boldsymbol{u}' \cdot \boldsymbol{a}'}$, which is itself negative all across the channel, and approximately equal to $-\varepsilon$ in the logarithmic and outer regions of the channel. This suggests that the mean spreading rate decreases over time due to turbulent energy dissipation, while TKE production does not play a role on tracer dispersion. This finding differentiates the present flow from HIT where Galilean-invariant single-particle statistics (such as the mean-square dispersion) are time-symmetric.

Temporal asymmetry is not observed in wall-normal and spanwise dispersion statistics. This is consistent with the contributions of the respective components to $\overline{\boldsymbol{u} \cdot \boldsymbol{a}}$ and $\overline{\boldsymbol{u}' \cdot \boldsymbol{a}'}$ being negligible compared to the streamwise contributions. Additionally, the expected long-time behaviour of wall-normal and spanwise dispersion statistics is evaluated from numerical data. In the wall-normal direction, the expectation is that tracers become uniformly distributed across the channel at very long times, which is expressed by an asymptotic mean-square dispersion $\langle \delta y'^2 \rangle = h^2/3$. Due to isotropy in the

spanwise direction, the normally-diffusive regime $\langle \delta z'^2 \rangle \sim \tau$ predicted by Taylor [175] is expected in z. The available data confirms the tendency towards these two regimes at asymptotically long times.

To improve the understanding of Lagrangian kinetic energy dynamics and their link to tracer dispersion, it may be instructive to analyse the average evolution of Lagrangian power along tracer paths, $\langle \boldsymbol{v} \cdot \boldsymbol{a} \rangle(\tau, y_0)$, as well as the evolution of the velocity-acceleration variance $\langle \boldsymbol{v}' \cdot \boldsymbol{a}' \rangle(\tau, y_0)$. As an additional perspective, the present analysis may be completed by studying the temporal evolution of the crossed streamwise–wall-normal component of the single particle dispersion (or displacement) tensor $\langle \delta x' \delta y' \rangle$. This component is expected to be non-zero, and may be affected by the temporal irreversibility of wall-bounded turbulence.

5 Relative dispersion of particle pairs

The description of tracer dispersion in turbulent channel flows is expanded in the present chapter by analysing the separation dynamics of pairs of fluid particles over time. Due to its direct relation to turbulent mixing and to the dissipation of scalar fluctuations, the relative dispersion problem is relevant for practical applications such as the growth of a cloud of pollutant in the atmosphere [149, 155]. Since the seminal work of Richardson [146] in 1926, relative dispersion in turbulent flows has been the subject of numerous studies. However, up to this day definite answers to some of the questions derived from Richardson's work have not been provided even in the ideal setting of homogeneous isotropic turbulence. In particular, no clear consensus exists regarding the conditions of validity of the enhanced pair separation dynamics described by Richardson.

In this chapter, we present relative dispersion statistics in a turbulent channel flow obtained from DNS at $Re_\tau = 1440$. This Reynolds number, although still moderate, is significantly higher than previous relative dispersion studies in wall-bounded turbulence [134], and thus the expectation is that a higher degree of scale separation shall provide a clearer identification of the different dispersion regimes in inhomogeneous flows. In the following, the time asymmetry of relative dispersion in wall-bounded turbulence is considered and its short-time behaviour is contrasted to the case of HIT [79]. The anisotropy of pair dispersion is then studied via the relative dispersion tensor. A preliminary model for the dispersion of tracer pairs in inhomogeneous flows is introduced, based on the ballistic cascade phenomenology proposed by Bourgoin [29]. The present chapter is adapted from our article 'Relative Dispersion of Particle Pairs in Turbulent Channel Flow' [135].

The outline of this chapter is as follows. Relative dispersion investigations in isotropic and anisotropic turbulent flows relevant in the context of the present work are presented in section 5.1. The numerical approach for obtaining relative dispersion statistics in channel flow simulations is then described in section 5.2. In section 5.3, forwards and backwards in time mean-square dispersion statistics are presented. Their short-time evolution is analysed including relevant dispersion time scales, as well as their time asymmetry and their dependence on the initial particle pair spatial configuration. To characterise the influence of mean shear on relative dispersion, pair separation is decomposed in section 5.4 into contributions by the mean and fluctuating velocity fields, and the mean-square dispersion induced by the fluctuating flow is studied. The anisotropy of pair separation is then analysed in section 5.5 in terms of the relative dispersion tensor, describing the mean-square separation in each direction and the relation between separation components. Then, the ballistic dispersion model by Bourgoin [29] is adapted to inhomogeneous flows in section 5.6 and assessed

against our channel flow DNS results. Finally, section 5.7 is devoted to conclusions and perspectives.

5.1 Introduction

5.1.1 Relative dispersion in isotropic turbulent flows

In turbulent flows, the spreading of a cloud of passive scalar about its centre of mass can be described by the statistics of relative dispersion between fluid particle pairs [13, 155]. As first described by Richardson [146], turbulent motion can greatly enhance the pair separation process. In his seminal paper, Richardson proposed that the separation of two tracers in turbulent flows can be described (in a statistical sense) by a diffusive process with a scale-dependent diffusion coefficient $K(D)$, where $D = |\boldsymbol{x}^B - \boldsymbol{x}^A|$ is the separation between the two particles. When D is in the inertial subrange ($\eta \ll D \ll L$, where $\eta = (\nu^3/\varepsilon)^{1/4}$ is the Kolmogorov length scale and L is the characteristic size of the largest turbulent eddies), Richardson found from measurements that the diffusion coefficient $K(D)$ is proportional to $D^{4/3}$. This is since then known as Richardson's 4/3 law. As later shown by Obukhov [121], the same relation can be derived from dimensional arguments in the framework of Kolmogorov's K41 local isotropy theory [83] leading to $K \sim \varepsilon^{1/3} D^{-4/3}$. In principle, this relation cannot be valid at short times following the identification of the particle pairs, when dispersion also depends on the initial separation D_0 [12], which has to be additionally accounted for in the dimensional arguments.

A consequence of Richardson's law is that the mean-square separation between two particles is expected to grow as

$$\langle D^2(t) \rangle = g \varepsilon t^3 \tag{5.1}$$

when D is in the inertial subrange. Equation (5.1) is referred to as Richardson–Obukhov law [149]. Here, g is known as Richardson's constant and is expected to have a universal value. As mentioned above, the Richardson–Obukhov regime cannot be expected to hold at short times when the initial separation D_0 must be taken into account. This dependency on the initial separation is described by Batchelor's regime [12], which expresses that the short-term mean-square change of separation between particle pairs is ballistic,

$$\langle \boldsymbol{R}^2(t) \rangle = \langle (\boldsymbol{D}(t) - \boldsymbol{D}_0)^2 \rangle = \langle \delta \boldsymbol{v}_0^2 \rangle t^2 \quad \text{for} \quad t \ll t_B. \tag{5.2}$$

Here $\boldsymbol{D}(t)$ is the instantaneous particle separation vector and $\boldsymbol{D}_0 = \boldsymbol{D}(0)$, $\delta \boldsymbol{v}_0$ is the initial relative velocity between the particles, and t_B is a characteristic time scale of the ballistic regime, which may be related to the characteristic time scales of the turbulent flow. Batchelor's regime can be derived from the Taylor expansion of $\boldsymbol{D}(t)$ about $t = 0$. The Lagrangian average $\langle \cdot \rangle$, introduced in section 3.3 in the context of single-particle statistics, denotes here an ensemble of particle pairs initially separated by $\boldsymbol{D}_0$. In HIT, if $D_0 = |\boldsymbol{D}_0|$ is within the inertial subrange, the ballistic time t_B may be

estimated to be proportional to the eddy-turnover time at the scale D_0, resulting in the Batchelor time scale $t_E = {D_0}^{2/3}\varepsilon^{-1/3}$ [12]. Here, the initial mean square relative velocity $\langle \delta v_0^2 \rangle$ is nothing else than the Eulerian second-order velocity structure function $S_2(\boldsymbol{x}, \boldsymbol{r}) = \overline{[\boldsymbol{u}(\boldsymbol{x}+\boldsymbol{r}, t) - \boldsymbol{u}(\boldsymbol{x}, t)]^2}$ evaluated at the separation $\boldsymbol{r} = \boldsymbol{D}_0$. In HIT, if the distance $r = |\boldsymbol{r}|$ is in the inertial range, K41 theory predicts a structure function of the form $S_2(r) = \frac{11}{3} C_2 (\varepsilon r)^{2/3}$. Here C_2 is Kolmogorov's constant for the longitudinal second-order velocity structure function [55] which has the well-accepted value of $C_2 \approx 2.1$ in high-Reynolds numbers homogeneous isotropic flows [172].

It is important to note that the ballistic regime (5.2) is a purely kinematic relation, as it is derived from a Taylor expansion and makes no assumptions on the underlying flow. Moreover, it is exactly valid for the *change* of separation $\boldsymbol{R}(t) = \boldsymbol{D}(t) - \boldsymbol{D}_0$ and *not* for the separation $\boldsymbol{D}(t)$ itself. Some authors have attempted to identify the ballistic separation regime using the relation $\langle \boldsymbol{D}^2(t) \rangle - \boldsymbol{D}_0^2 \approx \langle \delta v_0^2 \rangle t^2$. This relation is derived from the Taylor expansion of $\boldsymbol{D}(t)$ under the additional assumption that $\langle \boldsymbol{D}_0 \cdot \delta \boldsymbol{v}_0 \rangle = 0$, i.e. that the initial separation and the initial relative velocity are uncorrelated [149]. This was originally assumed by Batchelor [12] and is expected to hold in isotropic turbulence. However, as first verified by Ouellette et al. [128] in a von Kármán turbulent flow between two counter-rotating impellers, this term cannot be neglected in anisotropic flows. That is, if $\langle \boldsymbol{D}^2 \rangle - \boldsymbol{D}_0^2$ is plotted instead of $\langle \boldsymbol{R}^2 \rangle$, the universal t^2 scaling at very short times is lost, as it is polluted by the additional $\langle \boldsymbol{D}_0 \cdot \delta \boldsymbol{v}_0 \rangle$ term.

Relative dispersion of particle pairs has been extensively investigated in isotropic flows [149, 155]. These studies show that the initial particle separation is extremely influential in relative separation statistics at short times, and on the time scales determining the transition from the ballistic to Richardson–Obukhov regime. Using PTV in a nearly isotropic flow at $Re_\lambda = 815$, Bourgoin et al. [30] experimentally showed that Batchelor's regime (5.2) governs pair separation over several time decades, while signs of Richardson–Obukhov regime (5.1) were not observed for any of the initial pair separations D_0. The authors concluded that even larger turbulence levels are required to achieve Richardson–Obukhov super-diffusive regime. Indeed, this regime requires the existence of an intermediate time range in which the following two conditions are simultaneously satisfied: (i) the initial separation D_0 has been forgotten ($t \gg t_B$), and (ii) particle separation remains small enough for their trajectories to remain correlated ($D(t) \ll L$). The second condition is equivalent to $t \ll T_L$ where T_L is the Lagrangian integral time scale [149]. This implies a large separation of scales requiring very high Reynolds number turbulent flows. We finally note that at long times $t \gg T_L$, the motion of the particles in a pair becomes decorrelated and their mean-square separation follows twice Taylor's [175] prediction [see also eq. (1.6)],

$$\langle D(t)^2 \rangle \approx 4 \overline{u_i'^2} T_L t \quad \text{for} \quad t \gg T_L. \tag{5.3}$$

Experimentally, Ott and Mann [126] observed a Richardson–Obukhov regime in the inertial range at $Re_\lambda \approx 100$ provided that a temporal offset is applied to eq. (5.1), i.e. $\langle D(t)^2 \rangle = g\varepsilon(t - T_0)^3$. The authors chose the offset T_0 by a fit of their data, finding a Richardson constant $g \approx 0.5$. This value is consistent with more recent experimental

and numerical studies in HIT [18, 25, 27, 34, 75]. Boffetta and Sokolov [27] found great uncertainty in their estimation of g, which they attributed to turbulence intermittency. They improved their estimation by using exit-time statistics, in which statistics are gathered over particle pairs separated at the same scales (see also Biferale et al. [23]). Exit-time statistics reduce crossover effects related to averaging over separations belonging to different length scales. Also in HIT, Rast and Pinton [145] studied pair dispersion in a point-vortex flow model by analysing the time scale t_d during which individual particle pairs remain together before their separation increases significantly. The authors suggested that pair separation may be understood as an average over particle pairs which separately follow Richardson–Obukhov scaling, but each after a different time delay t_d.

Relative dispersion in isotropic turbulence is known to be a time-asymmetric process. That is, when fluid particles are tracked backwards in time (conditioned to an imposed *final* separation), they separate faster on average than in the forward case [18, 34, 158]. Recently, Bragg et al. [32] and Jucha et al. [79] associated this temporal asymmetry at short times to the irreversibility of turbulence, which can be understood as the directionality of the turbulent energy cascade (from large to small scales in 3D turbulence). Bragg et al. [32] also considered the separation of inertial particles, and noted that the ratio of backward to forward mean-square separation may be up to an order of magnitude larger than for fluid particles in isotropic turbulence. Inertial particles were found to experience an additional source of irreversibility arising from the non-local contribution of their velocity dynamics.

5.1.2 Relative dispersion in shear and wall-bounded flows

Fewer studies have been devoted to the case of anisotropic and inhomogeneous turbulent flows. In inhomogeneous flows, the relative dispersion problem is more complex, since the statistics depend not only on the magnitude, but also on the orientation of the initial separation $\boldsymbol{D}_0$ and on the initial particle pair position $\boldsymbol{x}_0$. Moreover, particles do not separate equally in each direction. Therefore, the mean-square separation $\langle \boldsymbol{R}^2(t) \rangle$ can be generalised into a relative dispersion tensor $\Delta_{ij}(t) = \langle R_i(t) R_j(t) \rangle$ [13, 109] containing more than a single independent component (as opposed to the isotropic case).

The dispersion of tracer pairs in a homogeneous shear flow was studied using DNS by Shen and Yeung [165]. The authors observed that particles separate faster when they are initially oriented in the cross-stream direction, i.e. in the direction of the mean velocity gradient. This is simply explained by particles being initially located in regions of different mean velocities, and thus being separated by the mean shear from the beginning. More generally, mean shear enhances particle dispersion in the streamwise direction. In stationary homogeneous shear flow, it was suggested by Corrsin [44] (see also Squires and Eaton [169] and Monin and Yaglom [108, p. 558]) that the streamwise mean-square particle displacement (defined in section 4.3) increases at asymptotically

long times as

$$\langle \delta x^2 \rangle(t) \approx \frac{2}{3} S^2 \overline{u_y'^2} T_{L,y} t^3 \quad \text{for} \quad t \gg T_{L,y}, \tag{5.4}$$

where $S = \mathrm{d}U/\mathrm{d}y$ is the mean shear rate and $T_{L,y}$ is the Lagrangian integral time scale associated to the cross-stream velocity component u_y. In analogy to the case of isotropic turbulence, this asymptotic regime leads to an asymptotic streamwise mean-square particle separation $\Delta_{xx}(t) \approx (4/3) S^2 \overline{u_y'^2} T_{L,y} t^3$. The regime $\Delta_{xx} \sim t^3$ was observed at long times by Shen and Yeung [165] for their largest initial separations, $D_0 = 64\eta$. In the cross-stream and spanwise directions, the mean-square separation is expected to asymptotically evolve linearly with time consistently with Taylor's prediction. This was however not exactly observed in the simulations of Shen and Yeung [165] due to deviation of their simulated flow away from statistical stationarity. Indeed, homogeneous shear flows are inherently non-stationary as a consequence of being spatially unbounded, since the largest turbulent scales grow over time as mean shear deforms the fluid [169].

To study the impact of shear on a passively advected non-reactive scalar, Celani et al. [39] considered a simple flow model given by the superposition between a linear shear and an isotropic turbulent velocity field obeying K41 scaling. The authors described the existence of a temporal transition between a first stage of separation, where turbulent fluctuations dominate and Richardson's law can be expected to hold, and a second stage where shear becomes dominant. The transition is expected to happen at a crossover time which is proportional to the characteristic time scale of the shear.

More recently, Pitton et al. [134] studied the separation of fluid and inertial particle pairs in a turbulent channel flow using DNS at a low friction-Reynolds number $Re_\tau = 150$. Consistently with the studies mentioned above, the authors observed that mean shear induces a super-diffusive regime at large times, when particle separation becomes of the order of the largest scales of the flow. Arguably due to an insufficient separation of scales, the Richardson–Obukhov regime was not clearly identified. Pitton et al. [134] removed the effect of mean shear by tracking fluid and inertial particles which followed the fluctuating velocity field only. The authors found that, although pair separation is importantly reduced at long times compared to the case with mean shear, separation in the streamwise direction remains dominant over the wall-normal and spanwise separations. Since the authors considered the mean-square separation $\langle \boldsymbol{D}^2(t) \rangle$ as opposed to the mean-square change of separation $\langle \boldsymbol{R}^2(t) \rangle$, their results do not display a clear Batchelor regime (see eq. (5.2) and discussion in section 5.1.1).

5.2 Particle pair datasets

Dispersion of particle pairs is studied in this work by DNS of turbulent channel flow at $Re_\tau = 1440$ described in chapter 2. In particular, simulation parameters are listed in table 2.1 and Lagrangian particle tracking algorithms are described in section 2.2. In the following we describe the two fluid-particle datasets, labelled DS1 and DS2, from

Table 5.1. Particle pair datasets. y_0^+, nominal initial wall distance; D_0, initial pair separation distance; $\boldsymbol{e}_0$, initial pair orientation; $T^+_{\max}$, maximum time lag of statistics; bw, backward dispersion; N_p, number of particles in dataset; N_p / set, number of particles sharing the same initial configuration (same y_0^+ and, for DS2, same D_0 and $\boldsymbol{e}_0$).

Dataset	y_0^+	D_0/η	$\boldsymbol{e}_0$	$T^+_{\max}$	bw	N_p total	N_p / set
DS1	20 to 1000	< 16	any	5.3×10^3	yes	2×10^6	$> 17\,000$
DS2	3 to 1440	1, 4, 16, 64	$\boldsymbol{e}_x, \boldsymbol{e}_y, \boldsymbol{e}_z$	1.7×10^4	no	$\sim 3.2 \times 10^6$	20 093

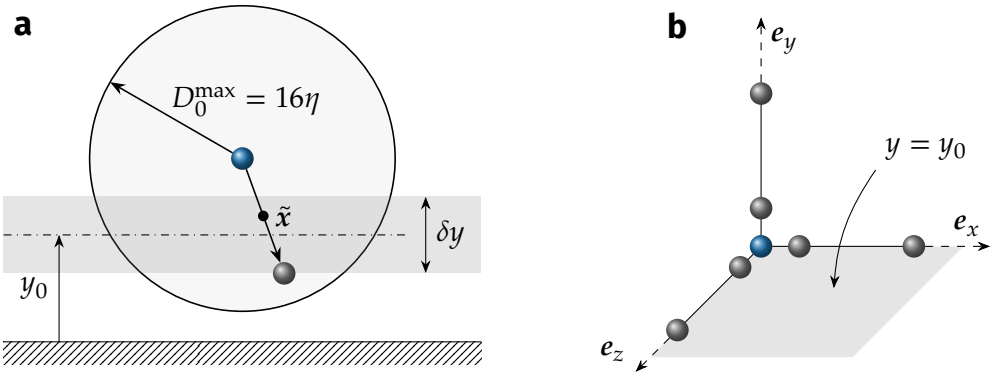

Figure 5.1. Schematic of particle pair datasets DS1 and DS2. (a) Particle pairs in dataset DS1 have initial separations $|\boldsymbol{D}_0| < 16\eta$. Their centroid $\tilde{\boldsymbol{x}}$ is located within wall-normal bins $y = y_0 \pm \delta y/2$ with $\delta y = 8\eta$ (filled rectangle). (b) In dataset DS2, oriented particle clusters are initialised at chosen wall distances y_0. The central particle (blue) is paired with every satellite particle (grey) in the cluster. In the schematic, 6 different pairs are formed which count towards different initial configurations $(y_0, \boldsymbol{D}_0)$.

which relative dispersion statistics are computed. These datasets respectively serve the purposes of comparing backwards and forwards in time dispersion statistics, and of characterising the effect of the initial particle pair spatial configuration as well as the asymptotic long-time dispersion regimes. Dataset properties are summarised in table 5.1, and their respective configurations are sketched in fig. 5.1.

The dataset DS1 consists of 2×10^6 fluid particles initialised at random positions in the domain. During post-processing, particle pairs are identified at chosen times t_0 according to the criterion described further below. Then, statistics are computed over the temporal range $t \in [t_0 - T/2, t_0 + T/2]$. This naturally allows to obtain backward and forward dispersion statistics, and is similar to the approach used by Berg et al. [18] and more recently by Buaria et al. [34] to study backward dispersion in HIT. The temporal window length T and the spacing between two reference times t_0 are chosen respectively as $T^+ \approx 1.1 \times 10^4$ and $\Delta t_0^+ \approx 1.3 \times 10^{-3}$.

The criterion for particle pair identification in dataset DS1 is as follows. Pairs separated by $|\boldsymbol{D}_0| < D_0^{\max}$ at t_0 are identified such that their centroids are located within bins of wall-normal distance $y = y_0 \pm \delta y/2$, as sketched in fig. 5.1a. The maximum pair separation is taken as $D_0^{\max} = 16\eta$, where the Kolmogorov length scale η, which in-

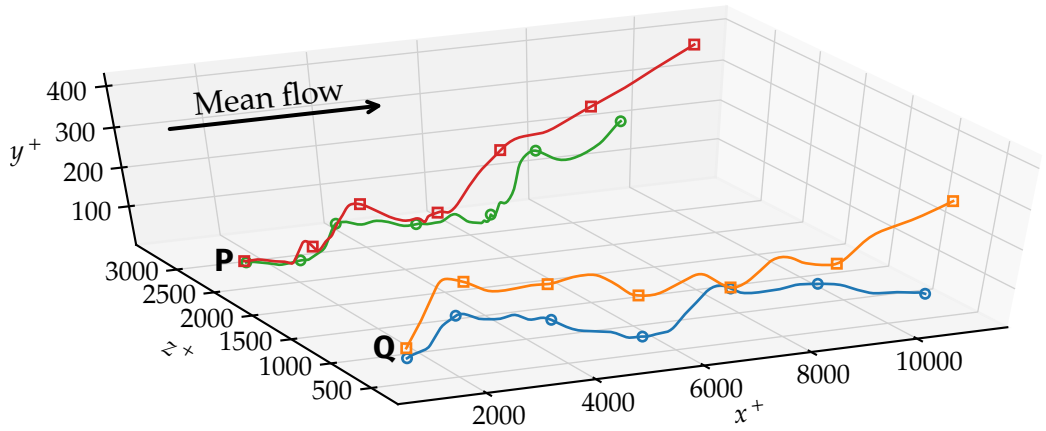

Figure 5.2. Sample trajectories of two particle pairs from dataset DS2. Trajectories are shown over $t^+ = 600$. Markers are drawn every $\Delta t^+ = 100$. In both cases, the initial pair wall distance is $y_0^+ = 18$ and the initial separation is $D_0 = 16\eta$ ($D_0^+ = 27$). Pairs P and Q are initially oriented in the spanwise (z) and wall-normal (y) directions, respectively.

creases with wall distance, is defined as $\eta = (\nu^3/\varepsilon)^{1/4}$. Here, the mean turbulent energy dissipation rate is estimated as $\varepsilon = \nu\overline{(\partial_j u_i')(\partial_j u_i')}$, where $\boldsymbol{u}'(\boldsymbol{x}, t)$ is the instantaneous fluctuating velocity field. The mean dissipation profile $\varepsilon(y)$ has been computed in the Eulerian frame from the same DNS. Pair dispersion statistics are computed over sets of particle pairs identified at the same reference wall distance y_0. In wall units, the positions $y_0^+ = 20, 60, 200, 600$ and 1000 are chosen (the channel centre is at $y^+ = 1440$). The bin widths are taken as $\delta y = 8\eta$. The Kolmogorov length scale ranges from $\eta^+ \approx 1.72$ at $y^+ = 20$ to $\eta^+ \approx 5.31$ at $y^+ = 1000$ (see fig. A.3 in appendix A.2). Consequently, particles in the $y_0^+ = 20$ group may actually be located within $0 < y^+ < 40$ at the reference time t_0. Due to the evolution of η with wall distance and to the above pair selection scheme, the total number of statistical samples (particle pairs) is lower for particle sets near the wall. Concretely, the total number of identified particle pairs varies from roughly 1.7×10^4 samples at $y_0^+ = 20$, to 1.5×10^6 samples at $y_0^+ = 1000$. The dataset DS1 has already been used to study the acceleration of Lagrangian tracers in the same turbulent channel flow (see chapter 3 and Stelzenmuller et al. [174]), as well as for the analysis of backwards and forwards single-particle dispersion statistics (chapter 4).

A disadvantage of dataset DS1 is that the exact spatial configuration of the particle pairs at time t_0 (initial position and separation vector) is not prescribed. In particular, particle pairs with different initial orientations $\boldsymbol{e}_0$ and separations $D_0 < 16\eta$ are averaged together. This dataset is therefore not adapted for studying the influence of the anisotropic Eulerian structure of the flow on pair separation, which, as shown in the next sections, has a great impact on the short-time separation statistics. For this reason, a second dataset labelled DS2 is generated. Particles in dataset DS2 are initialised at chosen locations in order to characterise the influence of the initial configuration of the pairs on relative dispersion. Each initial configuration is defined by 3 parameters:

(i) the initial wall distance y_0^+ of one of the particles in the pair, (ii) the separation distance D_0 between the two particles, and (iii) the orientation of the particle pair $\boldsymbol{e}_0$, so that the initial pair separation vector is $\boldsymbol{D}_0 = D_0\boldsymbol{e}_0$. The particle arrangement is sketched in fig. 5.1b. In the simulations, 10 initial wall distances y_0^+ are chosen ranging from 3 to 1440, combined with separations $D_0/\eta = 1$, 4, 16 and 64, and orientations in the three Cartesian directions ($\boldsymbol{e}_0 \in \{\boldsymbol{e}_x, \boldsymbol{e}_y, \boldsymbol{e}_z\}$). This results in 120 different initial configurations. For each parameter combination, the size of the statistical sample (i.e. the number of particle pairs) is roughly 20 000. Only forward dispersion statistics are obtained from this dataset. Applying the same approach to backward dispersion would require the storage of an exceedingly large amount of Eulerian velocity fields, with a prohibitive cost in terms of storage memory [158]. The present scheme is similar to the 'tetrahedron' particle pair arrangement used by Shen and Yeung [165] in a homogeneous turbulent shear flow DNS and by Pitton et al. [134] in a turbulent channel flow DNS.

In fig. 5.2, the trajectories of two pairs of particles initialised near the wall are shown. At the initial time, both particle pairs differ only in the orientation $\boldsymbol{e}_0$ of their initial separation, namely pair P is oriented in the spanwise direction, and pair Q in the wall-normal direction. At the initial stages of separation, mean shear has no influence on the separation of pair P as both particles are at the same wall distance y^+. As long as their wall-normal separation D_y stays relatively small, turbulent fluctuations dominate particle separation over mean shear. The case of pair Q is different, since the two particles are initially in regions of different mean velocity, and therefore mean shear effects are important from the start. As can be seen from fig. 5.2, under the influence of mean shear, particles in pair Q separate faster than those in pair P following their release, reaching larger separations D at short times. At larger times, the influence of the initial orientation is less noticeable, as observed from the comparable separations of pairs P and Q at the end of their trajectories ($t^+ = 600$).

5.3 Mean-square separation

In this section, we consider the mean-square change of separation between two particles $\langle \boldsymbol{R}^2(t) \rangle = \langle (\boldsymbol{D}(t) - \boldsymbol{D}_0)^2 \rangle$, as given by eq. (5.2) describing Batchelor's regime. We recall that $\boldsymbol{D}(t)$ is the instantaneous separation vector and $\boldsymbol{D}_0 = \boldsymbol{D}(0)$ is the initial separation. In HIT, two-particle Lagrangian statistics depend on two scalar parameters: the initial pair separation distance $D_0 = |\boldsymbol{D}_0|$ and time t. In statistically stationary channel flow, as already discussed in section 3.3 for single-particle Lagrangian statistics, the initial position of the pair relative to the walls needs to be taken into account as a consequence of statistical inhomogeneity. This is done here by fixing the wall-normal position y_0 of one of the particles in the pair.[1] Moreover, due to anisotropy, the full initial separation vector $\boldsymbol{D}_0$ must be retained, as opposed to only its magnitude D_0. This dependency on

[1] This is not the only possible choice. For instance, one can instead choose the initial distance between the wall and the pair centroid, $y_c = (y^A + y^B)/2$, where A and B denote the two particles in a pair. This is done in section 5.6 where a model for the mean-square pair separation is introduced.

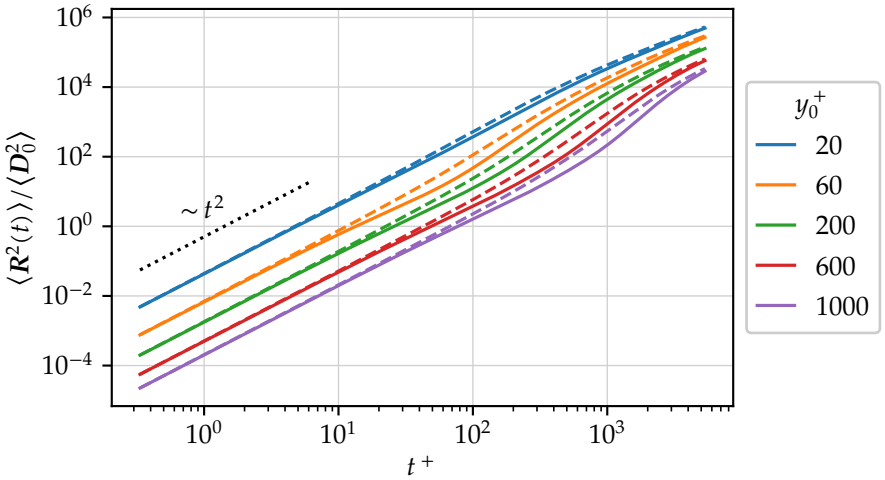

Figure 5.3. Backward and forward mean-square change of separation $\langle \boldsymbol{R}^2 \rangle$ normalised by the initial mean-square separation $\langle \boldsymbol{D}_0^2 \rangle$. Particle pairs are initially separated by $D_0 < 16\eta$ (dataset DS1). Different colours correspond to different initial wall distances y_0^+. Solid lines: forward dispersion. Dashed lines: backward dispersion.

$\boldsymbol{D}_0$ is alternatively written as a simultaneous dependency on the distance D_0 and on the orientation $\boldsymbol{e}_0$, where $\boldsymbol{D}_0 = D_0 \boldsymbol{e}_0$ and $|\boldsymbol{e}_0| = 1$. To summarise, two-particle Lagrangian statistics depend on the parameter set $(t, y_0, \boldsymbol{D}_0)$, where y_0 is the wall-normal position of the first particle in the pair at $t = 0$, and $\boldsymbol{D}_0$ is their separation vector at the same instant, pointing from the first to the second particle. To simplify the notations, the dependency on y_0 and $\boldsymbol{D}_0$ is omitted from the equations (e.g. we write $\langle \boldsymbol{R}^2(t) \rangle$ instead of $\langle \boldsymbol{R}^2 \rangle (t, y_0, \boldsymbol{D}_0)$). We note that, as described in section 5.2, statistics obtained from dataset DS1 include contributions from all possible orientations $\boldsymbol{e}_0$, from all separations in $D_0/\eta \in [0, 16]$, and from a range of initial wall-normal distances $y_0^* = y_0 \pm 4\eta$.

Figure 5.3 shows the time evolution of the mean-square change of separation $\langle \boldsymbol{R}^2 \rangle$ for initial separations $D_0 < 16\eta$, for different initial positions y_0, and for particles tracked both backwards and forwards in time (dataset DS1). As stated above, statistics are averaged among all initial separation vectors $\boldsymbol{D}_0$ within a sphere of radius 16η. At short times, the ballistic regime predicted by eq. (5.2) is recovered for both backward and forward separations, and for all wall distances. Following this initial regime, a growing gap is observed at intermediate times between backward and forward dispersion, with the former being faster than the latter. This time asymmetry is qualitatively consistent with observations in 3D HIT as described in section 5.1.1 [18, 32, 79, 158].

In the following sections, first the short-time ballistic dispersion regime is analysed. By considering the Taylor expansion of the separation at short times (section 5.3.1), the influence of the second-order Eulerian velocity structure function S_2 and of the crossed velocity-acceleration structure function S_{au} is emphasised. The evolution of these structure functions in the channel is discussed in section 5.3.2. In section 5.3.3, a suitable definition of the ballistic time scale is introduced, which leads in section 5.3.4

to a proper short-time normalisation of the mean-square dispersion curves shown in fig. 5.3. The temporal asymmetry of pair dispersion in the present flow is then addressed in section 5.3.5, followed by the influence of the initial separation distance and orientation in section 5.3.6.

5.3.1 Short-time dispersion

To understand the observed short-time ballistic regime and the deviation that follows, we consider the Taylor expansion of the separation between two particles at short times,

$$\boldsymbol{D}(t) = \boldsymbol{D}_0 + \delta\boldsymbol{v}_0 t + \frac{1}{2}\delta\boldsymbol{a}_0 t^2 + \mathcal{O}(t^3), \tag{5.5}$$

where $\delta\boldsymbol{v}_0 = \boldsymbol{v}_0^B - \boldsymbol{v}_0^A$ and $\delta\boldsymbol{a}_0 = \boldsymbol{a}_0^B - \boldsymbol{a}_0^A$ are respectively the relative particle velocity and acceleration at $t = 0$ (superscripts identify particles in the pair). As a result, the short-time mean-square change of separation is expressed as

$$\langle \boldsymbol{R}^2(t) \rangle = \langle \delta v_0^2 \rangle t^2 + \langle \delta\boldsymbol{v}_0 \cdot \delta\boldsymbol{a}_0 \rangle t^3 + \mathcal{O}(t^4) \quad \text{for} \quad t \ll t_B, \tag{5.6}$$

where the time scale t_B characterises the duration of the short-time regime. At the leading order, the mean-square separation follows Batchelor's regime introduced in eq. (5.2), during which particles travel at their initial velocities [12]. As discussed in section 5.1.1, the mean-square initial relative velocity $\langle \delta v_0^2 \rangle$ is equal to the second-order Eulerian structure function $S_2(\boldsymbol{x}_0, \boldsymbol{D}_0) = \overline{\delta\boldsymbol{u}^2}(\boldsymbol{x}_0, \boldsymbol{D}_0) = \overline{[\boldsymbol{u}(\boldsymbol{x}_0 + \boldsymbol{D}_0, t) - \boldsymbol{u}(\boldsymbol{x}_0, t)]^2}$, where $\boldsymbol{u}(\boldsymbol{x}, t)$ is the Eulerian velocity field, and $\boldsymbol{x}_0$ is the initial position of the first particle in the pair. In channel flow, due to statistical homogeneity in the streamwise and spanwise directions, the dependency of S_2 on $\boldsymbol{x}_0$ reduces to a dependency on the wall-normal distance y_0. In stationary HIT, S_2 only depends on the separation $D_0 = |\boldsymbol{D}_0|$. Moreover, when this separation is within the inertial subrange, K41 theory predicts the well-known relation

$$S_2(D_0) = \frac{11}{3} C_2 (\varepsilon D_0)^{2/3}, \tag{5.7}$$

where $C_2 \approx 2.1$ is Kolmogorov's constant for the longitudinal second-order velocity structure function [137, 172].

At the next order, the ballistic term in eq. (5.6) is corrected by a t^3 term whose coefficient $\langle \delta\boldsymbol{v}_0 \cdot \delta\boldsymbol{a}_0 \rangle$ is equal to the crossed velocity-acceleration structure function $S_{au}(\boldsymbol{x}_0, \boldsymbol{D}_0) = \overline{\delta\boldsymbol{u} \cdot \delta\boldsymbol{a}}(\boldsymbol{x}_0, \boldsymbol{D}_0)$. In 3D turbulence, under the conditions of local homogeneity and stationarity and if the spatial increment $r = |\boldsymbol{r}|$ is in the inertial subrange, the velocity-acceleration structure function is given by

$$S_{au}(\boldsymbol{x}, \boldsymbol{r}) = -[\varepsilon(\boldsymbol{x}) + \varepsilon(\boldsymbol{x} + \boldsymbol{r})] = -2\varepsilon_p(\boldsymbol{x}, \boldsymbol{r}), \tag{5.8}$$

where ε_p is the mean turbulent dissipation rate averaged among the two probed positions [51, 63, 98]. This relation is exact in the limit of infinite Reynolds numbers, and is the Lagrangian equivalent of Kolmogorov's 4/5 law [55]. The negative sign of S_{au} is associated with the direction of the turbulent cascade, from large to small scales

in 3D turbulence. Thus, under the assumptions for eq. (5.8), the t^3 term of eq. (5.6) is negative for forward dispersion ($t > 0$) and positive for backward dispersion ($t < 0$). As first suggested by Jucha et al. [79], this explains the short-time temporal asymmetry of relative dispersion in isotropic flows. The t^3 term is reminiscent of Richardson–Obukhov super-diffusive regime in which $\langle \boldsymbol{R}^2 \rangle \sim t^3$ [eq. (5.1)]. However, eq. (5.6) cannot explain Richardson dispersion as it is only valid at short times. Moreover, for forward dispersion the t^3 term in eq. (5.6) is negative and thus leads to a *deceleration* of the pair separation rate, opposing the expected effect of Richardson dispersion.

5.3.2 Structure functions S_2 and S_{au}

To characterise the short-time dispersion regime eq. (5.6) in the channel, we investigate the evolution of the structure functions S_2 and S_{au} with wall distance and with spatial increment. To our knowledge, only few studies in the literature have dealt with Eulerian structure functions in wall-bounded flows. Moreover, studies characterising the crossed velocity-acceleration structure function S_{au} in such flows are non-existent. Relevant works have focused on the logarithmic region of boundary layers, and have mainly considered the second-order streamwise velocity structure function $S_{xx}(y, \boldsymbol{r}) = \overline{\delta u_x^2}(y, \boldsymbol{r})$, and only for streamwise separations (i.e. $\boldsymbol{r} = r\boldsymbol{e}_x$) [7, 45, 166]. Recently, Yang et al. [200] proposed scalings for the complete fluctuating velocity structure function tensor $S'_{ij}(y, \boldsymbol{r}) = \overline{\delta u'_i \delta u'_j}(y, \boldsymbol{r})$ in the logarithmic region, derived from a model based on Townsend's attached-eddy hypothesis [103, 181]. However, when considering spanwise separations ($\boldsymbol{r} = r\boldsymbol{e}_z$), their predicted scalings do not match the results from channel flow DNS at moderate Reynolds number [95]. A very recent extension of the same model [201], this time accounting for wall-normal and spanwise velocity fluctuations in the logarithmic region, may provide improved predictions for the velocity structure functions in wall-bounded turbulence.

We estimate S_2 and S_{au} across the channel from Lagrangian data at $t = 0$ when particles of dataset DS2 are released. The estimation is performed over all initial particle configurations, namely for a range of wall distances $y = y_0$ and spatial displacement vectors $\boldsymbol{r} = \boldsymbol{D}_0$. We stress that the statistics are obtained *a posteriori* from a single flow snapshot, and more converged statistics could be computed from a new DNS. The evolution with wall distance of the structure functions, for different increments $\boldsymbol{r} = r\boldsymbol{e}_r$, is given in fig. 5.4. Since S_{au} is mostly negative (as expected in homogeneous flows), we plot $-S_{au}$ instead.

In the near-wall region, the structure functions display a strong dependency on the orientation of the increment $\boldsymbol{r}$. This strong anisotropy is a clear manifestation of the complexity of near-wall turbulence, which is characterised by the presence of preferentially-oriented motions including quasi-streamwise vortices and the associated sweeps and streaks [147]. Moreover, mean shear is important in this region, i.e. the mean streamwise velocity $U(y)$ changes quickly with wall distance. For this reason, S_2 is expected to be larger for spatial offsets in the wall-normal direction ($\boldsymbol{r} = r_y\boldsymbol{e}_y$), since in this case it includes a contribution of the mean velocity increment $\delta U = U(y+r_y) - U(y)$. This is confirmed by the curves in fig. 5.4. Moreover, near the wall S_2 is larger for

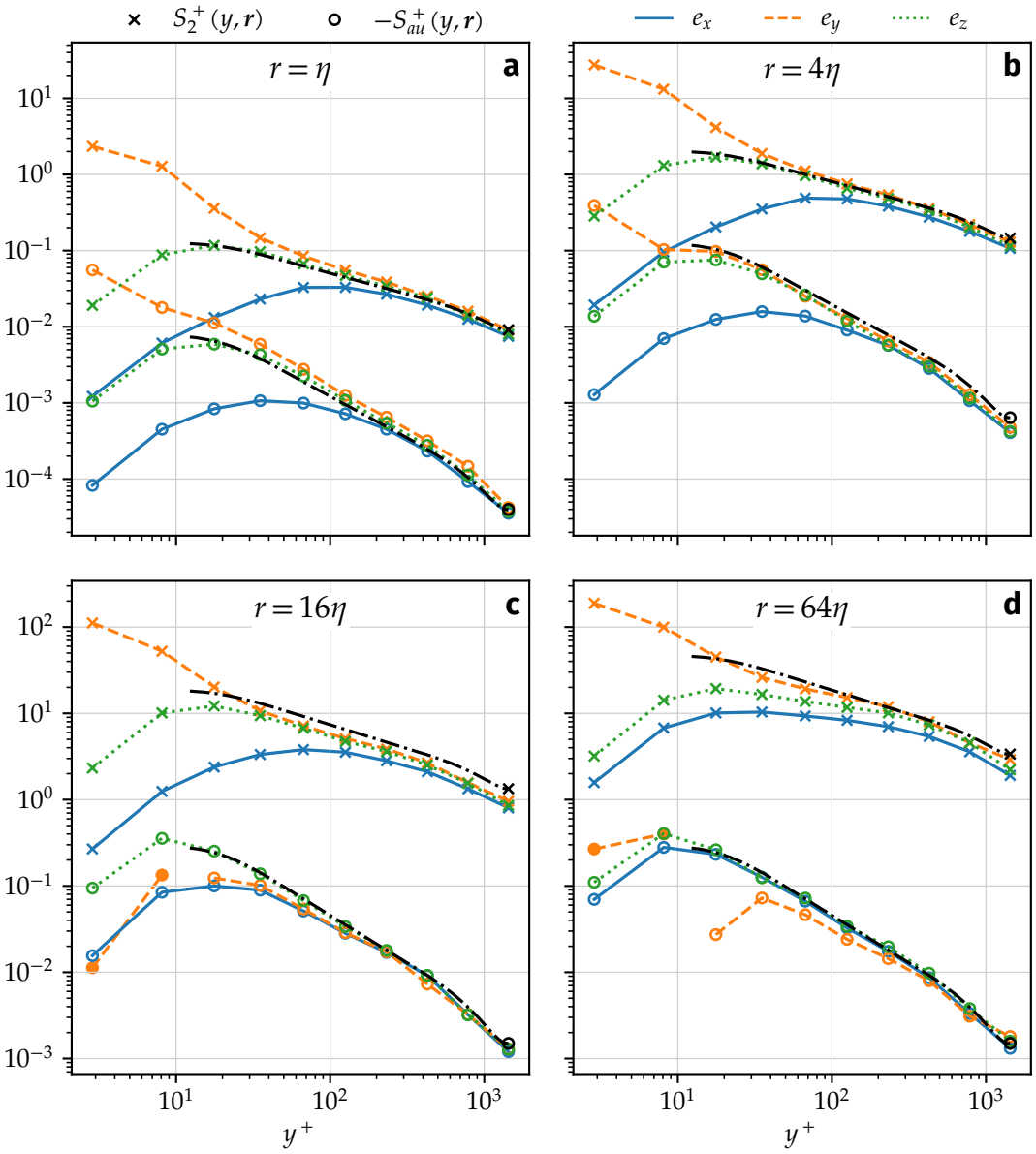

Figure 5.4. Structure functions $S_2(y,\boldsymbol{r})$ (crosses) and $-S_{au}(y,\boldsymbol{r})$ (circles) in wall units, for all initial configurations of dataset DS2. Subfigures (a) through (d) present statistics for spatial increments $r/\eta = 1$, 4, 16 and 64, respectively. Increments are oriented in the streamwise ($\boldsymbol{e}_x$, solid lines), wall-normal ($\boldsymbol{e}_y$, dashed lines) and spanwise ($\boldsymbol{e}_z$, dotted lines) directions. Filled circles represent positive values of S_{au}. Black dash-dotted lines represent isotropic estimations of S_2 and S_{au}. For small separations (subfigures a-b), the dissipation-range estimations $S_2' = r^2/(3\tau_\eta^2)$ and $S_{au} = \beta r^2/(3\tau_\eta^3)$ are plotted, with $\beta = -0.16$. For large separations (subfigures c-d), the inertial-range estimations $S_2 = \frac{11}{3}C_2(\varepsilon r)^{2/3}$ and $S_{au} = -2\varepsilon$ are plotted, with $C_2 = 2.1$.

spanwise than for streamwise displacements, with a difference that is more pronounced with smaller separations r. This is due to the effect of streaks and quasi-streamwise vortices, which induce a fluctuating velocity field that is correlated over longer distances in the streamwise direction (see e.g. Robinson [147]). Hence, the velocity increment between two points in the near-wall region is weaker if the points are aligned in the streamwise direction (since both points are likely to be found within the same coherent structure) than in the spanwise direction.

As seen in fig. 5.4, the velocity-acceleration structure function S_{au} is also anisotropic near the wall. For small separations ($r/\eta = 1$ and 4), its behaviour is similar to that of S_2 in that its absolute value is larger for wall-normal displacements and smaller for streamwise displacements. As mentioned above, S_{au} is mostly negative. Positive values are obtained in a few extreme cases where one of the probed locations is at $y^+ < 10$ while the other is at $y^+ + r_y^+$ with $r_y/\eta \geq 16$ ($r_y^+ \gtrsim 25$). In these cases the velocity and acceleration increments relate the flow in the viscous sublayer (or the beginning of the buffer layer) with that at the beginning of the logarithmic region. Since these regions have very different dynamics, homogeneity is not expected to hold on the resulting two-point statistics. Furthermore, in these cases S_{au} is dominated by the scalar product between the mean velocity and mean acceleration increments, $\delta\overline{\boldsymbol{u}} \cdot \delta\overline{\boldsymbol{a}} = \delta\overline{u_x}\delta\overline{a_x}$.[2] As seen in section 3.2 (fig. 3.3; see also [174, 202]), in the buffer layer and the beginning of the logarithmic region the mean streamwise acceleration $\overline{a_x}(y)$ is an increasing function of wall distance, similarly to the mean velocity $\overline{u_x}(y) = U(y)$. This results in a positive product $\delta\overline{u_x}\delta\overline{a_x}$ when locations across the buffer layer are sampled.

Away from the wall, the structure functions become nearly independent of the displacement orientation, suggesting a return to isotropy towards the bulk of the channel. Still, a slight difference persists for S_2 at nearly all wall distances, with the streamwise orientation resulting in a weaker structure function. This may be associated with the persistence of very-large-scale motions in the channel [167]. A similar behaviour is observed for S_{au} at the smallest separations $r/\eta = 1$ and 4.

Dissipation-range estimations In fig. 5.4, the S_2 profiles obtained from our DNS at the small separations $r/\eta = 1$ and 4 are compared with the dissipation-range estimation for the fluctuating part of the structure function, $S_2'(r) \approx \frac{1}{3}\overline{(\partial_j u_i')(\partial_j u_i')}r^2$, which is derived from the first-order Taylor expansion $\delta u_i' \approx \boldsymbol{r} \cdot \boldsymbol{\nabla} u_i'$ and the isotropy assumption. The estimation above can be expressed in terms of the mean turbulent dissipation rate $\varepsilon = \nu\overline{(\partial_j u_i')(\partial_j u_i')}$, which varies with wall distance. This leads to $S_2(r) \approx \varepsilon r^2/(3\nu) = r^2/(3\tau_\eta^2)$, where $\tau_\eta = (\nu/\varepsilon)^{1/2}$ is the Kolmogorov time scale. For the two small separations, the computed S_2 profiles closely match the prediction, suggesting that separations up to 4η are not within the inertial subrange. Similarly, the behaviour of S_{au} over dissipation-range increments r can be approximated by $S_{au}(r) \approx \frac{1}{3}\overline{(\partial_j u_i)(\partial_j a_i)}r^2$. From K41-like dimensional considerations, one has $\overline{(\partial_j u_i)(\partial_j a_i)} = \beta\varepsilon/\eta^2$ with β a non-dimensional constant. This ultimately leads to the

[2] Note that the velocity-acceleration structure function follows the Reynolds decomposition $S_{au} = \overline{\delta\boldsymbol{u} \cdot \delta\boldsymbol{a}} = \delta\overline{\boldsymbol{u}} \cdot \delta\overline{\boldsymbol{a}} + \overline{\delta\boldsymbol{u}' \cdot \delta\boldsymbol{a}'}$.

dissipation-range estimation $S_{au}(r) \approx \beta r^2/(3\tau_\eta^3)$. The value $\beta = -0.16$ is found to fit the $\langle \delta \boldsymbol{v}_0 \cdot \delta \boldsymbol{a}_0 \rangle$ data at the smallest separation $r = \eta$. For $r = 4\eta$, the prediction slightly overestimates the results obtained from tracer data in the bulk of the channel, hinting the transition from the dissipative to the inertial regime.

Inertial-range estimations Furthermore, we compare the larger separations $r/\eta = 16$ and 64 with the inertial-range K41 prediction for locally isotropic turbulence, $S_2(r) = \frac{11}{3} C_2 (\varepsilon r)^{2/3}$, with $C_2 = 2.1$. In the channel, the local isotropy hypothesis is more likely to hold in the logarithmic and outer regions. In the bulk of the channel, the obtained S_2 profiles follow the same evolution with wall distance as the K41 prediction. However, in general the prediction slightly overestimates the numerical results. This difference may be interpreted as a finite-Reynolds number effect, leading to an insufficient scale separation and the absence of a proper inertial range. Indeed, at the present Taylor-scale Reynolds number, $Re_\lambda \sim 100$, the Kolmogorov constant C_2 is expected to be lower than the chosen (and well-accepted) value of $C_2 = 2.1$ [172].

Similarly, to verify the validity of relation (5.8), the obtained S_{au} profiles at separations 16η and 64η are compared with $-2\varepsilon(y)$. For non-zero wall-normal displacements $r_y = \boldsymbol{r} \cdot \boldsymbol{e}_y$, one has $\varepsilon(y) \neq \varepsilon_p(y, \boldsymbol{r})$, and therefore this comparison is not exactly equivalent to eq. (5.8) when wall-normal orientations are considered. Remarkably, the prediction holds almost exactly over a wide range of wall distances. This is especially true for spanwise increments, for which a good agreement is found at nearly all wall distances.

Integral-scale structure functions We finally comment on the value of the structure functions S_2 and S_{au} for integral-scale separations. In channel flow, the velocity structure function can be decomposed as

$$S_2(y, \boldsymbol{r}) = \overline{S_2}(y, \boldsymbol{r}) + S_2'(y, \boldsymbol{r}) \tag{5.9}$$

$$= \left[\overline{u_x}(y + r_y) - \overline{u_x}(y)\right]^2 + \overline{u_i' u_i'}(y) + \overline{u_i' u_i'}(y + r_y) - 2\overline{u_i'(\boldsymbol{x}, t) u_i'(\boldsymbol{x} + \boldsymbol{r}, t)}, \tag{5.10}$$

where $r_y = \boldsymbol{r} \cdot \boldsymbol{e}_y$. For integral-scale separations $\boldsymbol{r}$, the last term in eq. (5.10) vanishes as the velocity fluctuations become uncorrelated. Hence, S_2 is given by contributions of mean shear and of the velocity variances (or equivalently, of the mean TKE $\bar{k} = \overline{u_i' u_i'}/2$) at the two probed locations. In the particular case of wall-parallel offsets ($r_y = 0$), eq. (5.10) reduces to $S_2 = 2\overline{u_i' u_i'}(y) = 4\bar{k}(y)$, as in homogeneous flows.

Similarly, the velocity-acceleration structure function can be decomposed as $S_{au} = \overline{S_{au}} + S_{au}'$, with

$$\overline{S_{au}}(y, \boldsymbol{r}) = \left[\overline{u_x}(y + r_y) - \overline{u_x}(y)\right] \left[\overline{a_x}(y + r_y) - \overline{a_x}(y)\right], \tag{5.11}$$

$$S_{au}'(y, \boldsymbol{r}) = \overline{u_i' a_i'}(y) + \overline{u_i' a_i'}(y + r_y) - \overline{u_i'(\boldsymbol{x}, t) a_i'(\boldsymbol{x} + \boldsymbol{r}, t)} - \overline{u_i'(\boldsymbol{x} + \boldsymbol{r}, t) a_i'(\boldsymbol{x}, t)}. \tag{5.12}$$

For large-enough separations, the last two terms in eq. (5.12) vanish.[3] Moreover, as discussed in section 4.4, the velocity-acceleration covariance is $\overline{u_i' a_i'}(y) \approx -\varepsilon$ in most of the channel, more precisely for $y^+ \gtrsim 20$ (see also fig. B.2 in appendix B.2). For wall-parallel displacements ($r_y = 0$), $\overline{S_{au}} = 0$ and therefore $S_{au}(y, \boldsymbol{r}) \approx -2\varepsilon(y)$ in most of the channel. This is verified in fig. 5.4d, where this equality holds throughout the channel for offsets $r = 64\eta$ in the streamwise and spanwise directions. Even in the case of wall-normal offsets, S_{au} is close to -2ε in the logarithmic and outer layers, implying that the contribution of $\overline{S_{au}}$ is relatively weak. To summarise, the observation that $\overline{u_i' a_i'} \approx -\varepsilon$ in most of the channel allows to generalise eq. (5.8), initially valid for inertial-range spatial increments, beyond the inertial range and up to integral-scale increments.

5.3.3 Ballistic time scale

As seen in section 5.3.1, the structure functions S_2 and S_{au} described in the previous section are relevant to the initial ballistic regime given by eq. (5.6). Here, we assess possible definitions of the characteristic duration t_B of the ballistic regime. Originally, Batchelor [12] assumed this time as proportional to the eddy-turnover time at scale D_0, i.e. $t_E = D_0^{2/3}\varepsilon^{-1/3}$ [55] when the separation D_0 is in the inertial range.

An alternative proposed by Bitane et al. [25] is to consider the time t_0 over which the two leading-order terms of eq. (5.6) have the same magnitude,

$$t_0 = \langle \delta v_0^2 \rangle / |\langle \delta v_0 \cdot \delta a_0 \rangle| = S_2(\boldsymbol{x}_0, \boldsymbol{D}_0) / |S_{au}(\boldsymbol{x}_0, \boldsymbol{D}_0)| \,. \tag{5.13}$$

This characteristic time naturally describes the duration of the short-time regime, since for $t \ll t_0$ the t^2 term is dominant and thus ballistic separation takes place, while for $t \approx t_0$ this term is overtaken by subleading-order terms and thus the Taylor expansion (5.6) is no longer valid [25]. The characteristic time t_0 may be approximated by the dissipation- and inertial-range predictions for S_2 and S_{au} introduced in section 5.3.2. For separations D_0 in the dissipation and inertial ranges, these estimations are respectively given by

$$t_D = \frac{\tau_\eta}{\beta} \quad \text{and} \quad t_I = \frac{11}{6} C_2 D_0^{2/3} \varepsilon_p^{-1/3}. \tag{5.14}$$

We note that, in homogeneous flows (where $\varepsilon_p = \varepsilon$), t_I is proportional to the eddy-turnover time t_E.

The time scales t_0, t_D and t_I are computed for each of the initial configurations of dataset DS2. The results for the pairs initially oriented in the spanwise direction ($\boldsymbol{e}_0 = \boldsymbol{e}_z$) are shown in fig. 5.5. Also plotted are the mean shear time scale across the channel, $T_S(y) = [\mathrm{d}U(y)/\mathrm{d}y]^{-1}$, and the Lagrangian integral time scale $T_L(y)$. In fact,

[3] In fact, the Eulerian two-point cross-correlation between velocity and acceleration components is expected to decay over lengths smaller than the integral length scale, since the acceleration is a small-scale quantity. For a qualitative comparison between velocity and acceleration length scales, see their respective Eulerian auto-correlations in fig. 2.2.

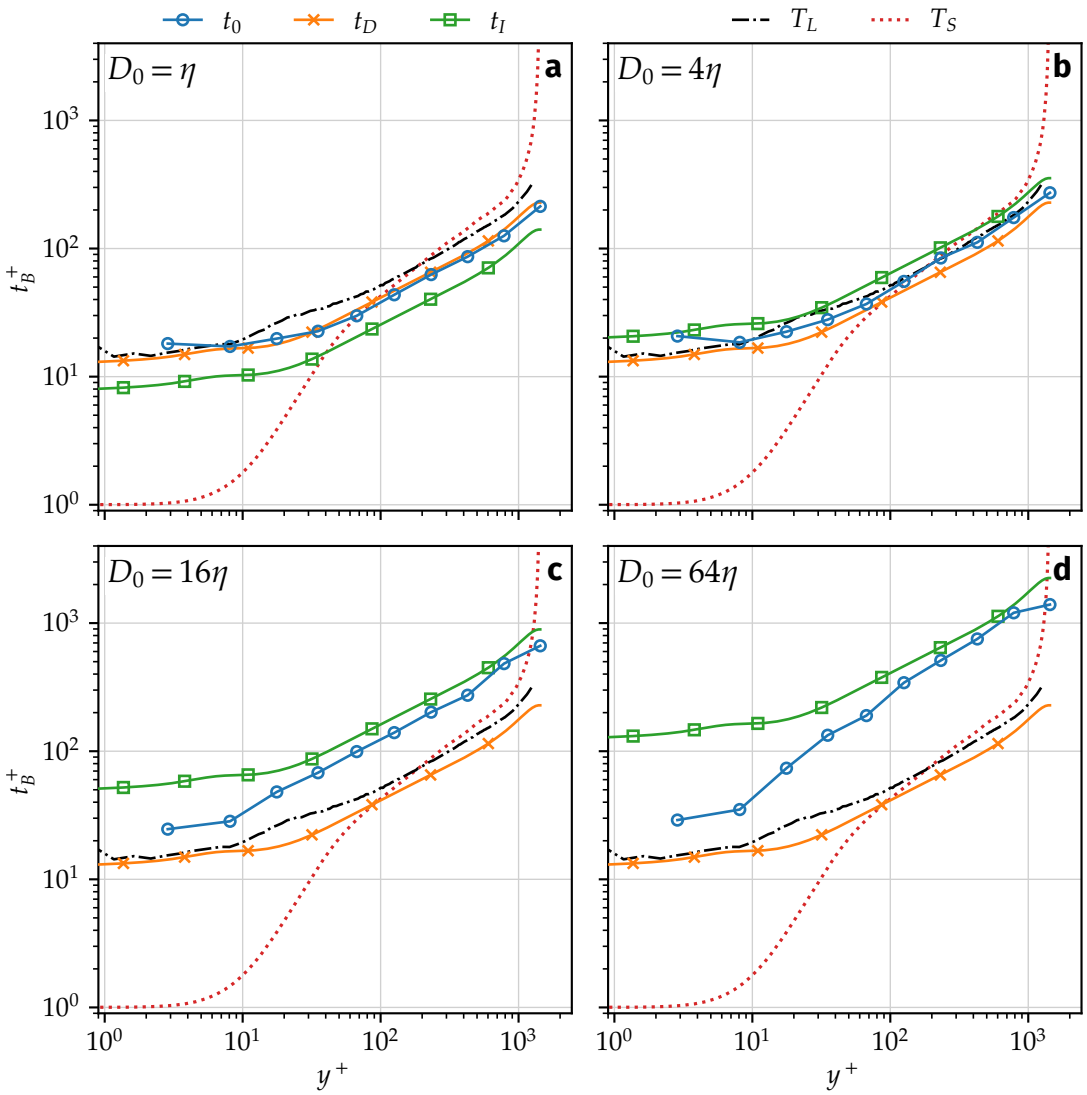

Figure 5.5. Characteristic ballistic time scales in wall units along the channel width, for different initial separations D_0 in the spanwise direction ($\boldsymbol{e}_0 = \boldsymbol{e}_z$). Subfigures (a) through (d) present initial separations $D_0/\eta = 1, 4, 16, 64$. Results are obtained from dataset DS2. Circles, $t_0 = \langle \delta v_0^2 \rangle / |\langle \delta \boldsymbol{v}_0 \cdot \delta \boldsymbol{a}_0 \rangle|$; crosses, dissipation-range estimation $t_D = \tau_\eta / \beta$; squares, inertial-range estimation $t_I = \frac{11}{6} C_2 D_0^{2/3} \varepsilon_p^{-1/3}$. Non-dimensional constants are $C_2 = 2.1$ and $\beta = -0.16$. Also represented are the Lagrangian integral time scale T_L (black dashed lines) and the mean shear time scale $T_S = (\mathrm{d}U/\mathrm{d}y)^{-1}$ (red dotted lines).

as shown in section 3.5 (see also Stelzenmuller et al. [174]), due to anisotropy a different Lagrangian integral time scale $T_{L,i}$ can be defined for each velocity component. In fig. 5.5, we take T_L as the quadratic mean among the three components, $T_L^2 = T_{L,i}T_{L,i}/3$.

As shown in fig. 5.5, the dissipation-range estimation $t_D = \tau_\eta/\beta$ matches the ballistic time t_0 over all wall distances for the smallest separation. This is expected since the value of β was chosen to match the behaviour of S_{au} at $D_0 = \eta$ in section 5.3.2. For $D_0 = 4\eta$, there is still good agreement between both time scales, even though a weak departure from dissipation-range scaling is observed. This departure is consistent with observations in section 5.3.2 concerning the validity of the dissipation-range estimation of S_{au} at $D_0 = 4\eta$. The agreement between t_0 and t_D shows the relevance of the characteristic dissipation time τ_η on the ballistic separation regime for small initial separations. As expected, for the larger initial separations $D_0/\eta = 16$ and 64, the dissipation-range prediction t_D loses validity due to transition from dissipative to inertial scales.

For $D_0/\eta = 16$ and 64, the inertial-range estimation t_I differs from t_0 in the near-wall region, where the isotropy hypothesis implied by t_I is far from being valid. Away from the wall, both time scales display a similar evolution with wall distance. In particular, in the logarithmic region they are approximately proportional, i.e. their curves present a nearly constant gap consistently with the difference observed between the velocity structure function S_2 and its isotropic inertial-range estimation (fig. 5.4(c-d)). As discussed in section 5.3.2, a lower value of the Kolmogorov constant C_2 would narrow the gap between the estimated and observed velocity structure functions.

When compared to the Lagrangian integral time scale T_L, the ballistic time t_0 is of the same order of magnitude for small separations, and considerably larger for large separations. This suggests that the scale separation needed for observing Richardson's super-diffusive regime is not achieved in the present flow, since an intermediate time range between t_0 and T_L does not exist. We also compare t_0 with the characteristic time of the mean shear T_S, which gives an indication of the time needed for mean shear to govern the relative dispersion process. As shown in fig. 5.5, this time scale is small near the wall, where the mean velocity gradient is most intense, and grows far from the wall as shear decreases. For separations $D_0/\eta = 1$ and 4, T_S is smaller than t_0 in the near-wall region (up to $y^+ \approx 80$). For larger separations, $T_S < t_0$ everywhere in the channel. In these cases, mean shear is expected to influence relative dispersion statistics from the beginning of the separation process.

5.3.4 Normalised mean-square separation

The time scales t_D and t_I introduced in the previous section are constructed from assumptions on the underlying turbulent flow, namely local homogeneity and isotropy as well as initial separations falling either in the dissipative or the inertial subrange. In contrast, t_0 is obtained according to purely kinematic considerations, and it is chosen in the following as the characteristic ballistic time. Using t_0, eq. (5.6) can be normalised

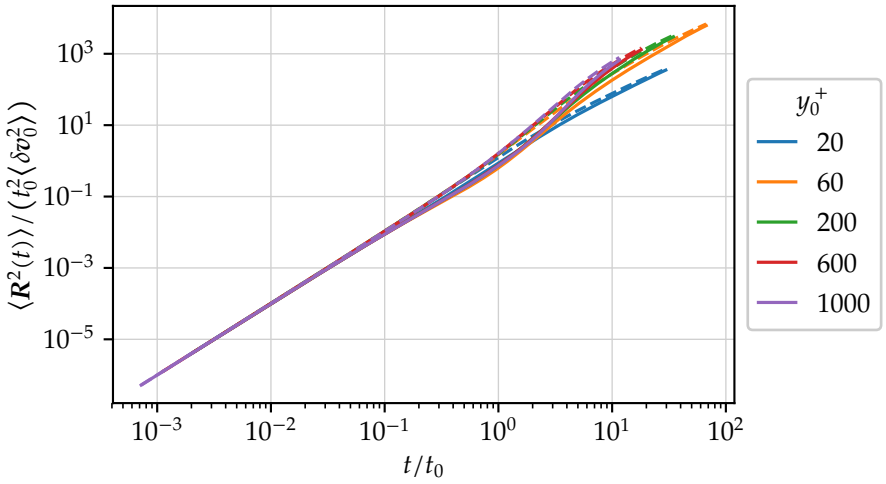

Figure 5.6. Backward and forward mean-square change of separation $\langle \boldsymbol{R}^2 \rangle$ normalised by the structure function $\langle \delta v_0^2 \rangle$ and the ballistic time scale $t_0 = \langle \delta v_0^2 \rangle / |\langle \delta v_0 \cdot \delta a_0 \rangle|$. Pairs are initially separated by $D_0 < 16\eta$ (dataset DS1). Solid lines: forward dispersion. Dashed lines: backward dispersion.

as

$$\frac{\langle \boldsymbol{R}^2 \rangle}{\langle \delta \boldsymbol{v}_0^2 \rangle t_0^2} = \left(\frac{t}{t_0}\right)^2 + s\left(\frac{t}{t_0}\right)^3 + \mathcal{O}(t^4) \quad \text{for} \quad t \ll t_0, \tag{5.15}$$

where $s \in \{-1, 1\}$ is the sign of $\langle \delta v_0 \cdot \delta a_0 \rangle$.

In fig. 5.6, dispersion curves of fig. 5.3 are normalised against the expected ballistic regime according to eq. (5.15). Under this scaling, forward dispersion curves associated to different wall distances collapse for times up to $t \approx 2t_0$, emphasising the relevance of the proposed scaling. At longer times, the separation rate increases for pairs that are initially far from the wall. A remarkable t^2 ballistic regime is observed for all wall distances. Starting from $t \approx 0.1t_0$, the separation rate becomes slightly slower than ballistic for forward dispersion, and slightly faster for backward dispersion, consistently with a negative sign of the t^3 term in eq. (5.15). Starting from $y_0^+ = 60$, normalised curves differ only slightly, consistently with the decay of inhomogeneity and anisotropy far from the wall.

Figure 5.7 plots the local scaling exponents of $\langle \boldsymbol{R}^2(t) \rangle$, i.e. the local slope of the curves shown in fig. 5.6, for forward and backward dispersion. An initial plateau with a value of 2, corresponding to the ballistic regime, is recovered for both forward and backward dispersion. A deviation from this regime is observed as early as $|t|/t_0 \approx 0.01$. As already seen in fig. 5.6 and as discussed in more detail in section 5.3.5, the deviation is given by a separation rate that decreases in the forward case, and increases in the backward case. The early deviation from the ballistic regime can be associated to the purely kinematic effect of the t^3 term in eq. (5.15) provided that $s = -1$ (i.e. $\langle \delta v_0 \cdot \delta a_0 \rangle < 0$). This is confirmed by the comparison between the numerical results and the truncated Taylor expansion of $\langle \boldsymbol{R}^2(t) \rangle$ in the figure.

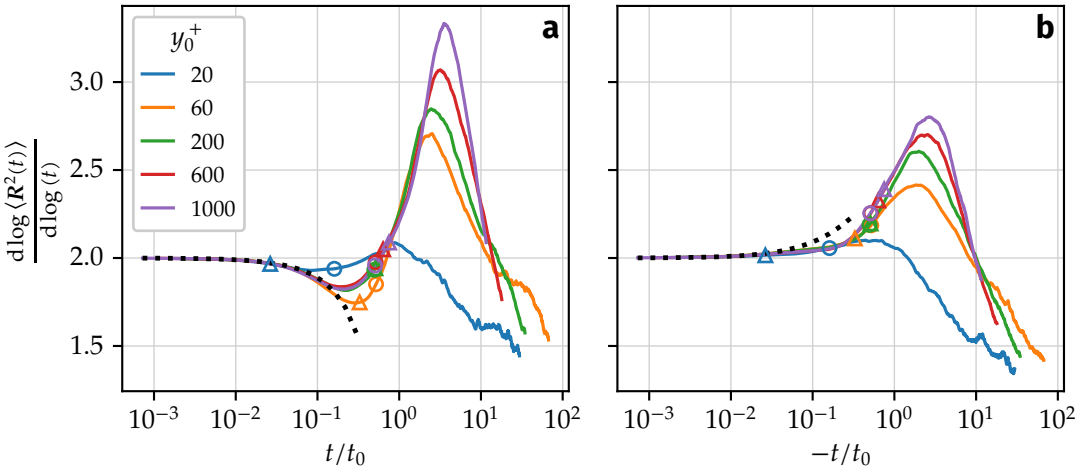

Figure 5.7. Local scaling exponents of the mean-square change of separation $\langle \boldsymbol{R}^2(t)\rangle$. (a) Forward dispersion. (b) Backward dispersion. Pairs are initially separated by $D_0 < 16\eta$ (dataset DS1). The dotted line represents the truncated Taylor expansion $\langle \boldsymbol{R}^2(t)\rangle = \langle \delta v_0^2\rangle t^2 + \langle \delta v_0 \cdot \delta a_0\rangle t^3$ assuming $\langle \delta v_0 \cdot \delta a_0\rangle < 0$. For each initial wall distance y_0^+, markers indicate the local value of the Lagrangian integral time scale T_L (circles) and of the mean shear time scale T_S (triangles).

At intermediate times, all cases present an increasing separation rate that ends with a peak. As described further below, this increased separation rate is explained by the enhancing effect of mean shear on the streamwise pair separation. Except for the smallest initial wall distance $y_0^+ = 20$, the peak is found at $2 < |t|/t_0 < 5$. The local separation rate reaches larger values in the forward case than in the backward one. A possible interpretation is that, since backward dispersion is faster, integral-scale separations are reached earlier for negative time lags than for positive ones, and thus less time is spent in the intermediate super-diffusive regime for negative lags. In some cases, the local scaling exponents reach values around 3, in accordance with Richardson's t^3 super-diffusive regime. However, Richardson dispersion is not expected in the present flow due to the absence of sufficient scale separation and because of the interference of mean shear since the early stages of dispersion, as discussed in section 5.3.3. As seen in fig. 5.7, the peaks of the local separation rate occur at times larger than the Lagrangian integral time scale T_L (represented by circles in the figure), and therefore the accelerated dispersion cannot be attributed to Richardson's regime, which occurs in the inertial range of scales. More likely, the rapid separation rate is caused by mean shear as suggested above and as observed for fluid and inertial particles by Pitton et al. [134] in channel flow. This regime is also comparable to the long-time t^3 streamwise separation rate expected in homogeneous shear flow [165, 169], as discussed in section 5.1.2. However, as opposed to homogeneous shear flow, in channel flow the mean velocity gradient is not constant and actually changes sign at the channel centre. This implies that at sufficiently long times for particles to cross the channel centre, the shear-induced separation rate is expected to decrease, which is precisely the long-time behaviour observed in fig. 5.7.

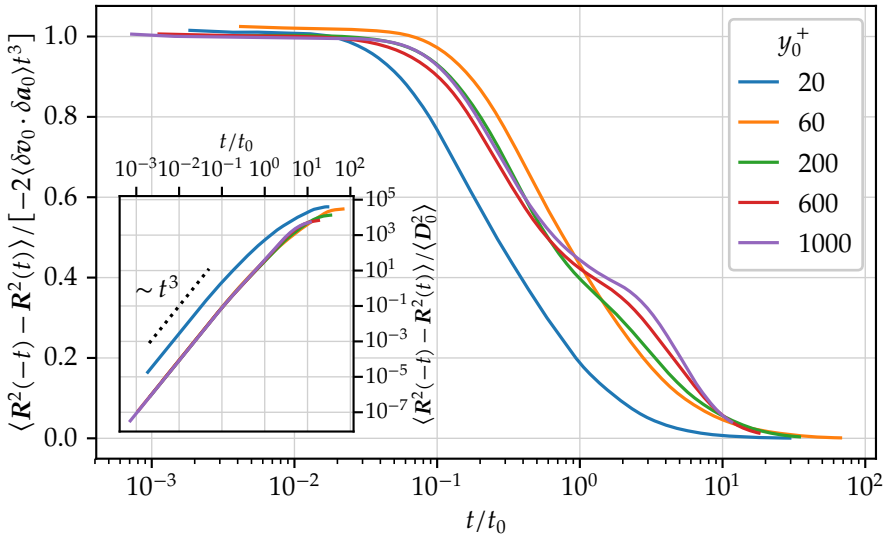

Figure 5.8. Difference between backward and forward mean-square separation compensated by $-2\langle \delta \boldsymbol{v}_0 \cdot \delta \boldsymbol{a}_0\rangle t^3$. Pairs are initially separated by $D_0 < 16\eta$ (dataset DS1). Inset: mean-square separation difference compensated by the initial mean-square separation $\langle \boldsymbol{D}_0^2\rangle$.

5.3.5 Temporal asymmetry

The results presented above show that relative dispersion is time-asymmetric in turbulent channel flows. Moreover, fig. 5.7 suggests that the time asymmetry at short times can be explained by the subleading-order term describing the deviation from ballistic separation in eq. (5.6). This idea was first proposed by Jucha et al. [79], who considered the difference between forward and backward mean-square separation at short times,

$$\langle \boldsymbol{R}^2(t)\rangle - \langle \boldsymbol{R}^2(-t)\rangle = 2\langle \delta \boldsymbol{v}_0 \cdot \delta \boldsymbol{a}_0\rangle t^3 + \mathcal{O}(t^5) \quad \text{for} \quad t \ll t_0, \tag{5.16}$$

which is readily obtained from the expansion (5.6). As discussed in section 5.3.1, the structure function $S_{au} = \langle \delta \boldsymbol{v}_0 \cdot \delta \boldsymbol{a}_0\rangle$ is equal to $-2\varepsilon_p$ under local homogeneity conditions and for separations in the inertial range [63]. In section 5.3.2 we have shown that this relation is approximately verified in the logarithmic and outer regions of the channel for large-enough separations ($D_0 \geq 16\eta$). Even for smaller separations and near-wall locations, S_{au} is generally negative, except in a few extreme cases where the average fields $\overline{u_i}$ and $\overline{a_i}$ dominate the velocity and acceleration increments. Furthermore, in light of the relation $\overline{u_i' a_i'} \approx -\varepsilon$ in the channel (section 4.4), we have argued in section 5.3.2 that the estimate $S_{au} \approx -2\varepsilon_p$ holds in the channel even for integral-scale separations. As a result, the t^3 term in eq. (5.16) is generally negative for $t > 0$, and therefore particles separate faster backwards than forwards in time as in the isotropic case [79].

The difference between backward and forward mean-square separations is plotted

in fig. 5.8 compensated by $2\langle \delta v_0 \cdot \delta a_0 \rangle t^3$. As predicted by eq. (5.16), a plateau with a value of 1 is initially found for all initial wall distances. A deviation from this plateau is observed starting from $t = 0.05 t_0$, which is quantitatively consistent with results in HIT [79]. This departure may be explained by the neglected t^5 term in eq. (5.16), or by a loss of memory of the initial particle pair properties as scales larger than D_0 are sampled. In the inset of fig. 5.8, the difference between backward and forward statistics is normalised by the initial mean-square separation $\langle \boldsymbol{D}_0^2 \rangle$. The positive sign of this difference at all times confirms that backward dispersion evolves at faster rate than forward dispersion for all initial positions. Moreover, starting from $y_0^+ = 60$, similarity of the temporal asymmetry with wall distance is observed. The gap between negative and positive time lags grows at faster rate at short times, where its evolution is described by eq. (5.16), while at very long times it tends to a constant value.

5.3.6 Influence of the initial separation

Up to this point, we have presented relative dispersion statistics averaged over all possible initial orientations $\boldsymbol{e}_0$ and over all separations in $D_0 < 16\eta$. As already observed in section 5.3.2, the structure functions characterising the short-time regime given by eq. (5.6) are strongly anisotropic near the wall, and therefore relative dispersion statistics are expected to depend on the initial pair orientation in that region. Moreover, the structure function S_2 governing the initial ballistic separation typically increases with the separation in the dissipative and inertial scales (as confirmed by fig. 5.4), and therefore an influence of D_0 on the statistics is also expected. To characterise the impact of the precise initial pair configuration on the dispersion, we consider here the DS2 dataset, described in section 5.2, in which particles are initialised according to chosen combinations of the initial wall-normal location y_0 and initial pair separation vector $\boldsymbol{D}_0$.

In fig. 5.9, the mean-square change of separation $\langle \boldsymbol{R}^2 \rangle$ is shown for a range of initial wall-normal positions y_0, separation distances D_0, and separation orientations $\boldsymbol{e}_0$. As stated above, initial orientation plays an important role for particles initialised near the wall (subfigures a-b), while its impact is weaker far from the wall (subfigures c-d). In all cases, the initial ballistic separation is more effective when the initial separation D_0 is larger, consistently with the increasing behaviour of S_2 with spatial increment. As expected, particles separate faster at short times when they are oriented in the wall-normal direction, in which case mean shear enhances pair separation from the beginning. As mentioned in section 5.1.2, similar observations were made in a homogeneous shear flow by Shen and Yeung [165], who found that particles separate faster when they are initially oriented in the cross-stream direction. Regarding the wall-parallel directions, in which mean shear does not have an influence at short times, spanwise orientations are found to lead to faster ballistic separations than streamwise separations. Again, this can be seen in terms of the structure function S_2, which is larger for spanwise than for streamwise increments (fig. 5.4). As discussed in section 5.3.2, near the wall this is explained by the presence of streaks and quasi-streamwise vortices, which imply weaker velocity increments between two points aligned in the streamwise

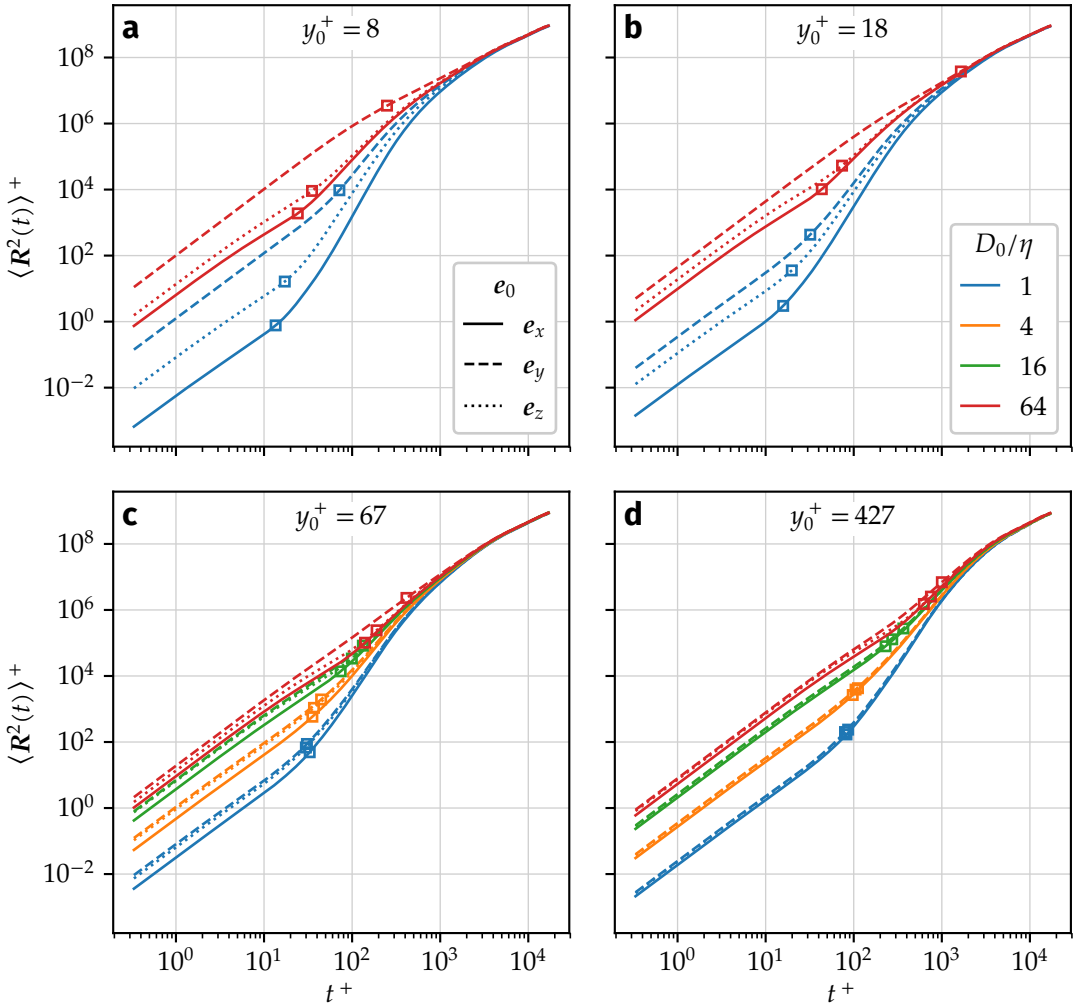

Figure 5.9. Forward mean-square change of separation for different initial configurations, in wall units. Pairs are initially located at $y_0^+ = 8$, 18, 67 and 427 (subfigures (a) to (d)). Line styles represent the initial pair orientation: streamwise, solid lines; wall-normal, dashed lines; spanwise, dotted lines. Line colours represent different initial separations D_0/η. Squares indicate the ballistic time t_0 associated to each initial condition. Results are obtained from dataset DS2.

direction than in the spanwise direction (in other words, velocity stays correlated for longer distances in the streamwise direction).

At very long times, the mean-square separation no longer depends on the initial pair configuration. The curves from all the initial configurations collapse due to loss of memory of the initial condition. An intermediate time range connects the initial ballistic regime, strongly dependent on the initial configuration, and the long-time dispersion regime, independent of the initial configuration. The ballistic time scale t_0, represented by squares over each curve of fig. 5.9, suitably represents the transition from ballistic separation to the intermediate regime. The latter is described as a super-diffusive process which separates particles faster than the initial ballistic regime, as already observed in section 5.3.4 for pairs with initial separations $D_0 < 16\eta$. In fig. 5.9, the slope of the intermediate regime is steeper when the initial ballistic regime is slower, that is, when the structure function $S_2(y_0, \boldsymbol{D}_0)$ is weaker. This is the case for small separations D_0, as well as for wall-parallel orientations, in which case the contribution of mean shear to S_2 is zero.

5.4 Mean shear influence

In order to characterise the influence of mean shear on relative dispersion in the channel, the time evolution of the particle pair separation is decomposed into a separation induced by the mean velocity field, $\overline{\boldsymbol{R}}(t)$, and a separation due to the fluctuating velocity field, $\boldsymbol{R}'(t)$. This decomposition is introduced in section 5.4.1. Then, in section 5.4.2, short-time dispersion is described based on the Taylor expansion of $\boldsymbol{R}'(t)$, in an analogous manner to the short-time description of the total separation (section 5.3.1). Finally, in section 5.4.3, the time asymmetry of the fluctuation-induced separation $\boldsymbol{R}'$ is discussed.

5.4.1 Decomposition of the mean-square separation

By definition, the velocity of a fluid particle is $\boldsymbol{v}(t) = \boldsymbol{u}(\boldsymbol{x}(t), t)$, where $\boldsymbol{u}(\boldsymbol{x}, t)$ is the Eulerian velocity field and $\boldsymbol{x}(t)$ is the instantaneous particle position. The tracer velocity may be decomposed into contributions by the Eulerian mean and fluctuating velocity fields, $\overline{\boldsymbol{u}}(\boldsymbol{x})$ and $\boldsymbol{u}'(\boldsymbol{x}, t)$. Their contributions, denoted $\boldsymbol{U}(t)$ and $\tilde{\boldsymbol{v}}(t)$, are given by

$$\boldsymbol{v}(t) = \boldsymbol{U}(t) + \tilde{\boldsymbol{v}}(t) = \overline{\boldsymbol{u}}(\boldsymbol{x}(t)) + \boldsymbol{u}'(\boldsymbol{x}(t), t). \tag{5.17}$$

We stress that $\tilde{\boldsymbol{v}}$ is the Eulerian fluctuation of the velocity $\boldsymbol{u}$ evaluated at the tracer position. From a Lagrangian viewpoint, as discussed in section 3.4 in the context of Lagrangian correlation functions, $\tilde{\boldsymbol{v}}$ is *not* the true velocity fluctuation, since its Lagrangian mean $\langle \tilde{\boldsymbol{v}}(t) \rangle$ is generally non-zero for $t \neq 0$. Hence, the choice of notation is made to avoid confusion with the Lagrangian fluctuation defined in section 3.4.

Similarly to $\boldsymbol{v}(t)$, the relative velocity between two tracers, $\delta\boldsymbol{v}(t) = \boldsymbol{v}^B(t) - \boldsymbol{v}^A(t)$, can

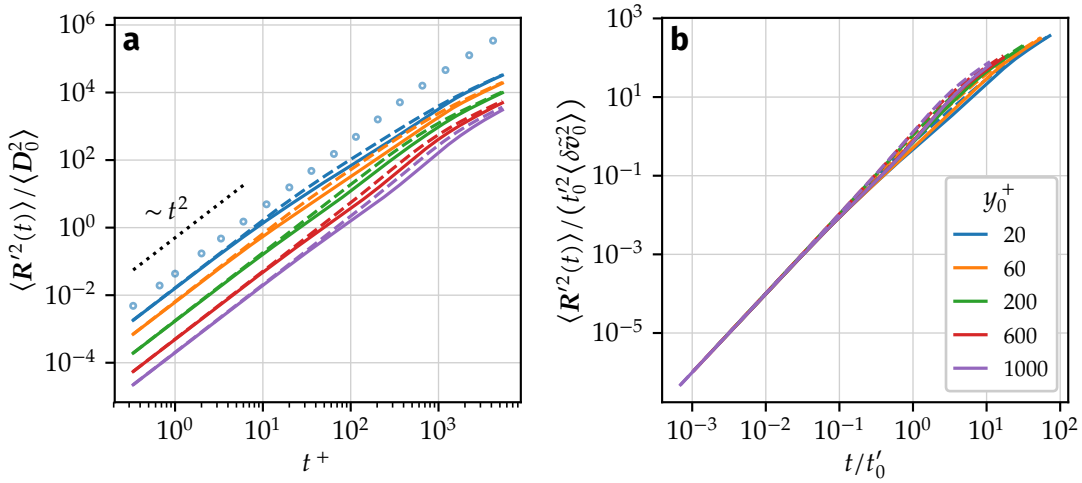

Figure 5.10. Backward and forward mean-square change of separation due to the fluctuating flow $\langle \boldsymbol{R}'^2 \rangle$, normalised (a) by the initial mean-square separation $\langle \boldsymbol{D}_0^2 \rangle$ and (b) by the structure function $\langle \delta\tilde{v}_0^2 \rangle$ and the ballistic time scale $t_0' = \langle \delta\tilde{v}_0^2 \rangle / |\langle \delta\tilde{v}_0 \cdot \delta\tilde{a}_0 \rangle|$. Particle pairs are initially separated by $D_0 < 16\eta$ (dataset DS1). Solid lines: forward dispersion. Dashed lines: backward dispersion. In (a), circles represent the total mean-square separation $\langle \boldsymbol{R}^2(t) \rangle$ for $y_0^+ = 20$ and $t > 0$.

be decomposed as

$$\delta \boldsymbol{v}(t) = \delta \boldsymbol{U}(t) + \delta \tilde{\boldsymbol{v}}(t) \tag{5.18}$$

$$= \left[\overline{\boldsymbol{u}}\left(\boldsymbol{x}^B(t)\right) - \overline{\boldsymbol{u}}\left(\boldsymbol{x}^A(t)\right) \right] + \left[\boldsymbol{u}'\left(\boldsymbol{x}^B(t), t\right) - \boldsymbol{u}'\left(\boldsymbol{x}^A(t), t\right) \right], \tag{5.19}$$

where $\boldsymbol{x}^A(t)$ and $\boldsymbol{x}^B(t)$ are the instantaneous positions of the two tracers. Noting that the change of separation $\boldsymbol{R}(t) = \boldsymbol{D}(t) - \boldsymbol{D}_0$ between two tracers over time is the integral of their relative velocity $\delta \boldsymbol{v}(t)$, from eq. (5.18) $\boldsymbol{R}(t)$ can be decomposed as

$$\boldsymbol{R}(t) = \overline{\boldsymbol{R}}(t) + \boldsymbol{R}'(t) = \int_0^t \delta \boldsymbol{U}(\tau)\, \mathrm{d}\tau + \int_0^t \delta \tilde{\boldsymbol{v}}(\tau)\, \mathrm{d}\tau, \tag{5.20}$$

where $\overline{\boldsymbol{R}}(t)$ and $\boldsymbol{R}'(t)$ are the separations induced by the mean and fluctuating velocity fields, respectively.

Furthermore, we denote by $\tilde{\boldsymbol{a}}(t)$ the material derivative of $\tilde{\boldsymbol{v}}$,

$$\tilde{\boldsymbol{a}}(t) = \frac{\mathrm{D}\tilde{\boldsymbol{v}}(t)}{\mathrm{D}t} = \boldsymbol{a}(t) - (\boldsymbol{v}(t) \cdot \boldsymbol{\nabla})\, \overline{\boldsymbol{u}}(\boldsymbol{x}(t)), \tag{5.21}$$

where $\boldsymbol{a}(t) = \mathrm{D}\boldsymbol{v}/\mathrm{D}t$ is the total tracer acceleration. We note that $\tilde{\boldsymbol{a}}$ differs from the fluctuating fluid acceleration at the tracer position, which is instead given by $a_i'(t) = a_i(t) - \partial_j \overline{u_i u_j}(\boldsymbol{x}(t))$. In channel flow, the mean velocity field takes the form $\overline{\boldsymbol{u}}(\boldsymbol{x}) =$

$U(y)\boldsymbol{e}_x$, and therefore eq. (5.21) writes

$$\tilde{\boldsymbol{a}}(t) = \boldsymbol{a}(t) - v_y(t)\frac{\mathrm{d}U(y(t))}{\mathrm{d}y}\boldsymbol{e}_x, \tag{5.22}$$

where $y(t)$ and $v_y(t)$ are the wall-normal particle position and velocity, respectively. The last term in eq. (5.22) is the contribution of the Eulerian mean velocity field to the acceleration of a tracer. Concretely, mean shear accelerates the tracer in the streamwise direction if the latter moves in the direction of the mean velocity gradient (e.g. $v_y > 0$ in the lower half of the channel). Hence, $\tilde{\boldsymbol{a}}$ can be interpreted as the contribution of the Eulerian fluctuating velocity field to the fluid particle acceleration.

The time evolution of the mean-square separation induced by the fluctuating velocity field is plotted in fig. 5.10a for pairs initially separated by $D_0 < 16\eta$ (dataset DS1). Compared to the total mean-square separation $\langle \boldsymbol{R}^2 \rangle$ (fig. 5.3), $\langle \boldsymbol{R}'^2 \rangle$ is about one order of magnitude weaker at very long times ($t^+ \approx 5000$). When the influence of mean shear is removed, the super-diffusive regime at intermediate times is considerably weaker. Concerning the initial ballistic regime, the difference between $\langle \boldsymbol{R}^2 \rangle$ and $\langle \boldsymbol{R}'^2 \rangle$ is more pronounced when pairs are initially located close to the wall. For $y_0^+ = 20$, $\langle \boldsymbol{R}^2 \rangle$ (represented by circles in the figure) evolves considerably faster than $\langle \boldsymbol{R}'^2 \rangle$ during the ballistic regime, implying that $\langle \delta v_0^2 \rangle > \langle \delta \tilde{v}_0^2 \rangle$. This is a result of mean shear having a dominant role on the separation dynamics in the near-wall region, where the mean velocity gradient is most intense. For larger wall distances, the influence of mean shear on the ballistic regime is much weaker, implying that away from the wall the initial separation regime (or equivalently the structure function S_2) is governed by turbulent fluctuations.

Similarly to the total relative dispersion described in the previous sections, relative dispersion induced by the fluctuating flow is a time-asymmetric process, with backward dispersion being faster than forward dispersion. As before, this asymmetry is first evidenced as a deviation from the initial ballistic separation. The gap between backward and forward dispersion increases at intermediate times, and then decreases at very long times. The present results confirm that the temporal asymmetry of relative dispersion in turbulent channel flow is a consequence of the irreversibility of turbulent fluctuations, as is in isotropic flows [79].

5.4.2 Short-time dispersion

Similarly to the case of the total relative dispersion (section 5.3.1), the mean-square separation due to the fluctuating flow can be expanded at short times as

$$\langle \boldsymbol{R}'^2(t) \rangle = \langle \delta \tilde{\boldsymbol{v}}_0^2 \rangle t^2 + \langle \delta \tilde{\boldsymbol{v}}_0 \cdot \delta \tilde{\boldsymbol{a}}_0 \rangle t^3 + \mathcal{O}(t^4) \quad \text{for} \quad t \ll t'_0, \tag{5.23}$$

where $\delta \tilde{\boldsymbol{v}}_0 = \delta \tilde{\boldsymbol{v}}(0)$ and $\delta \tilde{\boldsymbol{a}}_0 = \delta \tilde{\boldsymbol{a}}(0)$, with $\delta \tilde{\boldsymbol{a}}(t) = \tilde{\boldsymbol{a}}^B(t) - \tilde{\boldsymbol{a}}^A(t)$. According to eq. (5.23), the separation $\boldsymbol{R}'(t)$ is also expected to follow an initial ballistic growth, although the characteristic duration of this regime is not necessarily the same as for the total change of separation $\boldsymbol{R}(t)$. Consistently with the discussion in section 5.3.3, the ballistic time

scale associated to $\boldsymbol{R}'$ is defined here as $t'_0 = \langle \delta\tilde{v}_0^2 \rangle / |\langle \delta\tilde{v}_0 \cdot \delta\tilde{a}_0 \rangle|$. In fig. 5.10b, forward and backward $\langle \boldsymbol{R}'^2(t) \rangle$ curves of subfigure (a) are normalised according to the short time regime (5.23). The collapse of the curves confirms the validity of the above expansion and of the chosen time scale.

Structure functions As for the total mean-square separation, the coefficients governing the short-time expansion eq. (5.23) are Eulerian structure functions evaluated at the initial particle pair configuration. Since $\tilde{v}$ is the fluctuating velocity field at the position of a tracer, $\langle \delta\tilde{v}_0^2 \rangle$ is equal to the fluctuating velocity structure function $S'_2(y_0, \boldsymbol{D}_0)$ already introduced in section 5.3.2 [eq. (5.9)]. The case of $\langle \delta\tilde{v}_0 \cdot \delta\tilde{a}_0 \rangle$ is more subtle, since $\tilde{a}$ differs from the fluctuating fluid acceleration $\boldsymbol{a}'$, and therefore $\langle \delta\tilde{v}_0 \cdot \delta\tilde{a}_0 \rangle$ is not equal to the structure function S'_{au} defined in eq. (5.12). Instead, $\langle \delta\tilde{v}_0 \cdot \delta\tilde{a}_0 \rangle$ is given by the structure function

$$\tilde{S}_{au}(\boldsymbol{x}, \boldsymbol{r}) = \overline{\left[u'_i(\boldsymbol{x}+\boldsymbol{r}, t) - u'_i(\boldsymbol{x}, t) \right] \left[\frac{\mathrm{D}u'_i}{\mathrm{D}t}(\boldsymbol{x}+\boldsymbol{r}, t) - \frac{\mathrm{D}u'_i}{\mathrm{D}t}(\boldsymbol{x}, t) \right]}. \tag{5.24}$$

In particular, for integral-range separations $|\boldsymbol{r}| \gg L$, the fluctuations at the two probed locations become decorrelated. Noting that $u'_i \, \mathrm{D}u'_i/\mathrm{D}t$ is the material derivative of the TKE $k(\boldsymbol{x}, t)$, this leads to

$$\tilde{S}_{au}(\boldsymbol{x}, \boldsymbol{r}) \approx \overline{\frac{\mathrm{D}k}{\mathrm{D}t}}(\boldsymbol{x}) + \overline{\frac{\mathrm{D}k}{\mathrm{D}t}}(\boldsymbol{x}+\boldsymbol{r}) \quad \text{for} \quad |\boldsymbol{r}| \gg L. \tag{5.25}$$

The quantity $\overline{\mathrm{D}k/\mathrm{D}t}(\boldsymbol{x})$ represents the average rate of change of TKE among fluid particles instantaneously located at $\boldsymbol{x}$. As shown in appendix B.2 (see fig. B.2), this quantity is close to zero in most of the channel except for $y^+ < 40$, implying that tracers on average do not gain or lose TKE in the logarithmic and outer layers. Most importantly for the present study, this implies that $\tilde{S}_{au} \approx 0$ for sufficiently large initial particle pair separations. This can be contrasted with the relation $S_{au} \approx -2\varepsilon_p$, which, as discussed in section 5.3.2, is valid both for inertial- and integral-scale separations in the channel. The relation $\tilde{S}_{au} \approx 0$ at large separations ultimately indicates that, according to the short-time expansion (5.23), $\langle \boldsymbol{R}'^2(t) \rangle$ is not expected to be time-asymmetric if the initial pair separation D_0 is in the integral scales. This is consistent with the case of isotropic turbulence, where particle separation is not time-asymmetric for paired trajectories that are completely uncorrelated.

Local scaling exponents The local scaling exponents of $\langle \boldsymbol{R}'^2(t) \rangle$ are shown in fig. 5.11 with time normalised by t'_0. As with $\langle \boldsymbol{R}^2(t) \rangle$ (fig. 5.3), for all wall distances the initial ballistic regime is followed by a decelerated separation rate in the forward case, and by an accelerated separation rate in the backward case, which are both explained by a negative value of $\langle \delta\tilde{v}_0 \cdot \delta\tilde{a}_0 \rangle$ in eq. (5.23). The observed behaviour closely follows the truncated Taylor expansion of $\langle \boldsymbol{R}'^2(t) \rangle$ at short times. Consistently with previous observations, comparison with fig. 5.7 indicates that the super-diffusive regime at

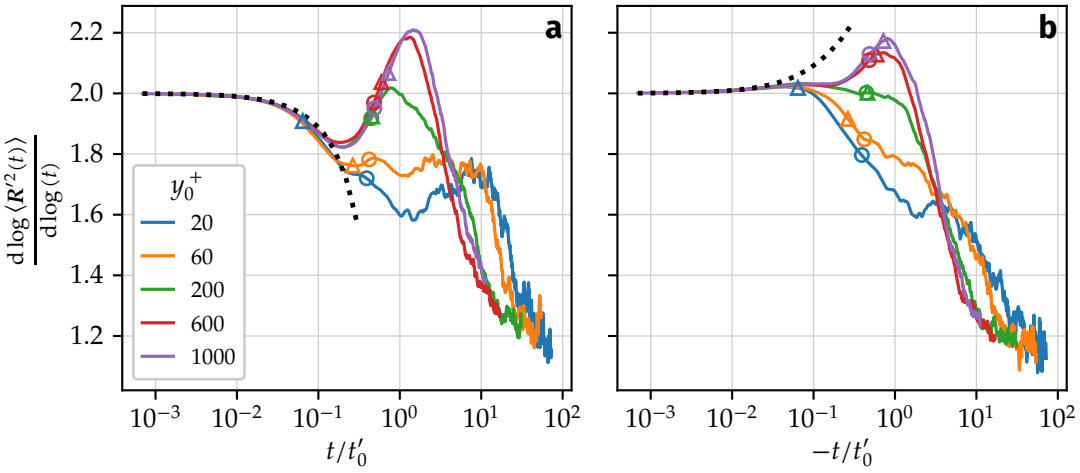

Figure 5.11. Local scaling exponents of the mean-square separation by the fluctuating flow $\langle \boldsymbol{R}'^2(t)\rangle$. (a) Forward dispersion. (b) Backward dispersion. Pairs are initially separated by $D_0 < 16\eta$ (dataset DS1). The dotted line represents the truncated Taylor expansion $\langle \boldsymbol{R}'^2(t)\rangle = \langle \delta\tilde{\boldsymbol{v}}_0^2\rangle t^2 + \langle \delta\tilde{\boldsymbol{v}}_0 \cdot \delta\tilde{\boldsymbol{a}}_0\rangle t^3$ assuming $\langle \delta\tilde{\boldsymbol{v}}_0 \cdot \delta\tilde{\boldsymbol{a}}_0\rangle < 0$. For each initial wall distance y_0^+, markers indicate the local value of the Lagrangian integral time scale T_L (circles) and of the mean shear time scale T_S (triangles).

intermediate times is remarkably weaker for $\langle \boldsymbol{R}'^2(t)\rangle$ than for the total separation $\langle \boldsymbol{R}^2(t)\rangle$, with maximum values that barely exceed the initial ballistic separation $\langle \boldsymbol{R}'^2\rangle \sim t^2$. This confirms that the intermediate super-diffusive regime observed in the previous sections, approaching a Richardson-like scaling $\langle \boldsymbol{R}^2\rangle \sim t^3$, is due to mean shear and not to Richardson's law. At very long times, the average separation rate decreases continuously. It may be predicted that the diffusion by the fluctuating flow should tend to a normally-diffusive process as in HIT [175], which would correspond to a scaling $\langle \boldsymbol{R}'^2\rangle \sim t$. However, the available data is insufficient to verify this statement.

5.4.3 Temporal asymmetry

Analogously to the case of $\langle \boldsymbol{R}^2(t)\rangle$ given by eq. (5.16), following eq. (5.23) the temporal asymmetry of $\langle \boldsymbol{R}'^2(t)\rangle$ is described at short times by

$$\langle \boldsymbol{R}'^2(t)\rangle - \langle \boldsymbol{R}'^2(-t)\rangle = 2\langle \delta\tilde{\boldsymbol{v}}_0 \cdot \delta\tilde{\boldsymbol{a}}_0\rangle t^3 + \mathcal{O}(t^5) \quad \text{for} \quad t \ll t'_0. \tag{5.26}$$

As noted above, for a given initial pair configuration $(y_0, \boldsymbol{D}_0)$, $\langle \delta\tilde{\boldsymbol{v}}_0 \cdot \delta\tilde{\boldsymbol{a}}_0\rangle$ is equal to the Eulerian structure function $\tilde{S}_{au}(y, \boldsymbol{r})$ (defined in eq. (5.24)) evaluated at $y = y_0$ and $\boldsymbol{r} = \boldsymbol{D}_0$. The validity of this analytical prediction is verified from simulation data in fig. 5.12, where the difference $\langle \boldsymbol{R}'^2(t)\rangle - \langle \boldsymbol{R}'^2(-t)\rangle$ is plotted compensated by $2\langle \delta\tilde{\boldsymbol{v}}_0 \cdot \delta\tilde{\boldsymbol{a}}_0\rangle t^3$. The expected plateau at 1 is recovered for times $t \lesssim 0.1t'_0$, similarly to the case of $\langle \boldsymbol{R}^2\rangle$ (fig. 5.8), and consistently with equivalent results in HIT [32, 79]. Namely, Jucha et al. [79] plotted the compensated difference as given in fig. 5.12 using DNS and experimental HIT data at different Reynolds numbers ranging from $Re_\lambda = 200$ to 690.

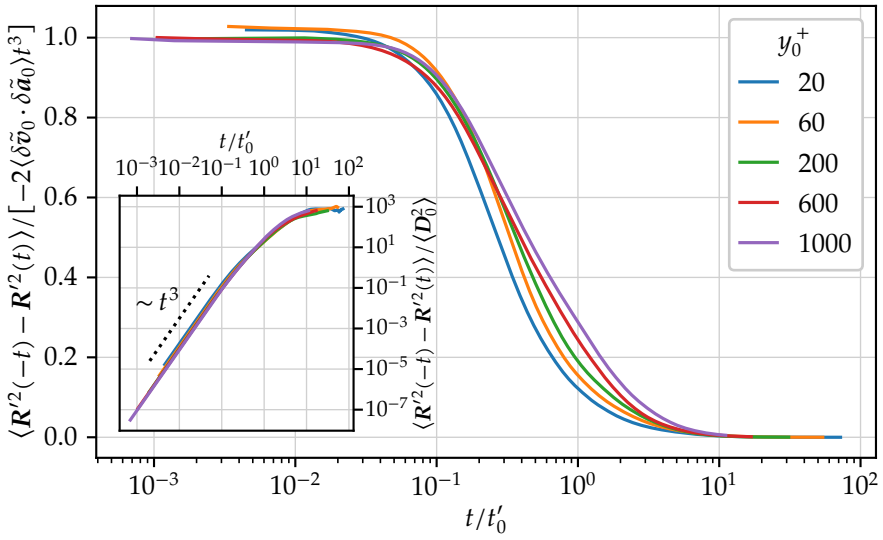

Figure 5.12. Difference between backward and forward mean-square separation by the fluctuating flow, compensated by $-2\langle \delta\tilde{v}_0 \cdot \delta\tilde{a}_0\rangle t^3$. Pairs are initially separated by $D_0 < 16\eta$ (dataset DS1). Inset: mean-square separation difference compensated by the initial mean-square separation $\langle \boldsymbol{D}_0^2\rangle$.

All their data showed a clear plateau up to $t \approx t_E/10$, where t_E is the eddy-turnover time at the scale D_0 (introduced in section 5.3.3). Here, the plateau is observed even close to the wall, where the flow is strongly anisotropic. Interestingly, for $y_0^+ = 20$, the curve closely matches the behaviour at larger wall distances, which was not the case for $\langle \boldsymbol{R}^2\rangle$ shown in fig. 5.8. More generally, the spread of the curves associated to different y_0^+ is reduced with respect to those obtained for $\langle \boldsymbol{R}^2\rangle$ (fig. 5.8), emphasising the impact of mean shear on $\langle \boldsymbol{R}^2\rangle$, at relatively short times close to the wall and at larger times away from the wall. This is confirmed in the inset of fig. 5.12, where the backwards-forwards difference compensated by the initial mean-square separation $\langle \boldsymbol{D}_0^2\rangle$ collapses for the different initial wall distances. We note that, as described in section 5.2, the initial wall distance of particles in the $y_0^+ = 20$ set is actually within $0 < y^+ < 40$. Therefore, the present data does not allow for a finer description of the temporal asymmetry of pair dispersion close to the wall, where the Eulerian flow structure changes rapidly with y^+.

The contributions of the three separation components to the backwards-forwards difference are plotted in fig. 5.13 for the initial wall distances $y_0^+ = 60$ and 600. For $y_0^+ = 60$, backward dispersion is faster than forwards in the three directions at short times, indicating that the contribution of each component to the structure function $\tilde{S}_{au}$ is negative. However, this difference is dominated by the streamwise separation, which is approximately equal to the total difference at all times. Meanwhile, the differences in the wall-normal and spanwise directions stay small and even change sign after the initial regime. In the case of $y_0^+ = 600$, the three separation components contribute nearly equally to the backwards-forwards difference at short times, indicating that

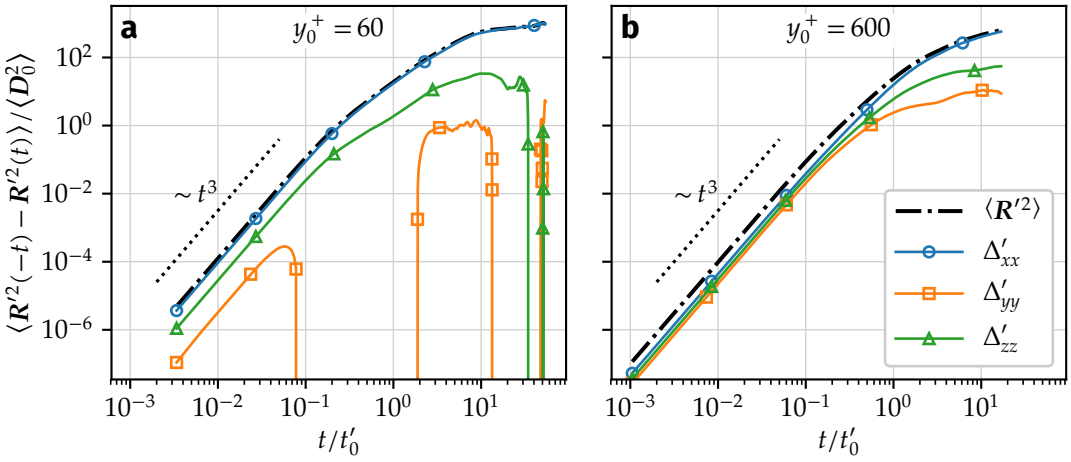

Figure 5.13. Difference between backward and forward mean-square separation by the fluctuating flow by separation component, compensated by $\langle \boldsymbol{D}_0^2 \rangle$. Initial wall distances are (a) $y_0^+ = 60$ and (b) $y_0^+ = 600$. The black dashed line is the total difference $\langle \boldsymbol{R}'^2(-t) \rangle - \langle \boldsymbol{R}'^2(t) \rangle$. Pairs are initially separated by $D_0 < 16\eta$ (dataset DS1).

$\tilde{S}_{au}(y, \boldsymbol{r})$ is nearly isotropic in this region of the channel. For the three components, the difference stays positive at all times (meaning that particle pairs separate over longer distances backwards in time in the three directions), although the streamwise separation dominates at long times.

5.5 Relative dispersion tensor

Until now, we have mostly considered statistics related to the change of separation distance between a pair of particles, $|\boldsymbol{R}(t)| = |\boldsymbol{D}(t) - \boldsymbol{D}_0|$. However, the statistics of separation between two particles in inhomogeneous and anisotropic flows present an anisotropic evolution in time. In the particular case of shear flows, the presence of mean shear enhances particle separation in the streamwise direction, while it does not have a direct effect in the other directions.

The anisotropy of relative dispersion can be investigated in terms of the relative dispersion tensor [13, 109],

$$\Delta_{ij}(t) = \langle R_i(t) R_j(t) \rangle, \tag{5.27}$$

where $R_i(t) = D_i(t) - D_i(0)$ is the i-th component of $\boldsymbol{R}(t)$. The trace of Δ_{ij} is equal to the mean-square change of separation, $\Delta_{ii}(t) = \langle \boldsymbol{R}^2(t) \rangle$. By construction, Δ_{ij} is a symmetric tensor. In channel flow, due to the statistical symmetry $z \leftrightarrow -z$, its non-diagonal components Δ_{xz} and Δ_{yz} are zero. As a consequence, the relative dispersion tensor contains a single independent non-diagonal component, $\Delta_{xy} = \Delta_{yx}$. Each component of the relative dispersion tensor depends on the initial wall distance y_0 and on the initial pair separation vector $\boldsymbol{D}_0$.

The short-time evolution of $\langle \boldsymbol{R}^2(t) \rangle$ as predicted by expansion (5.6) can be general-

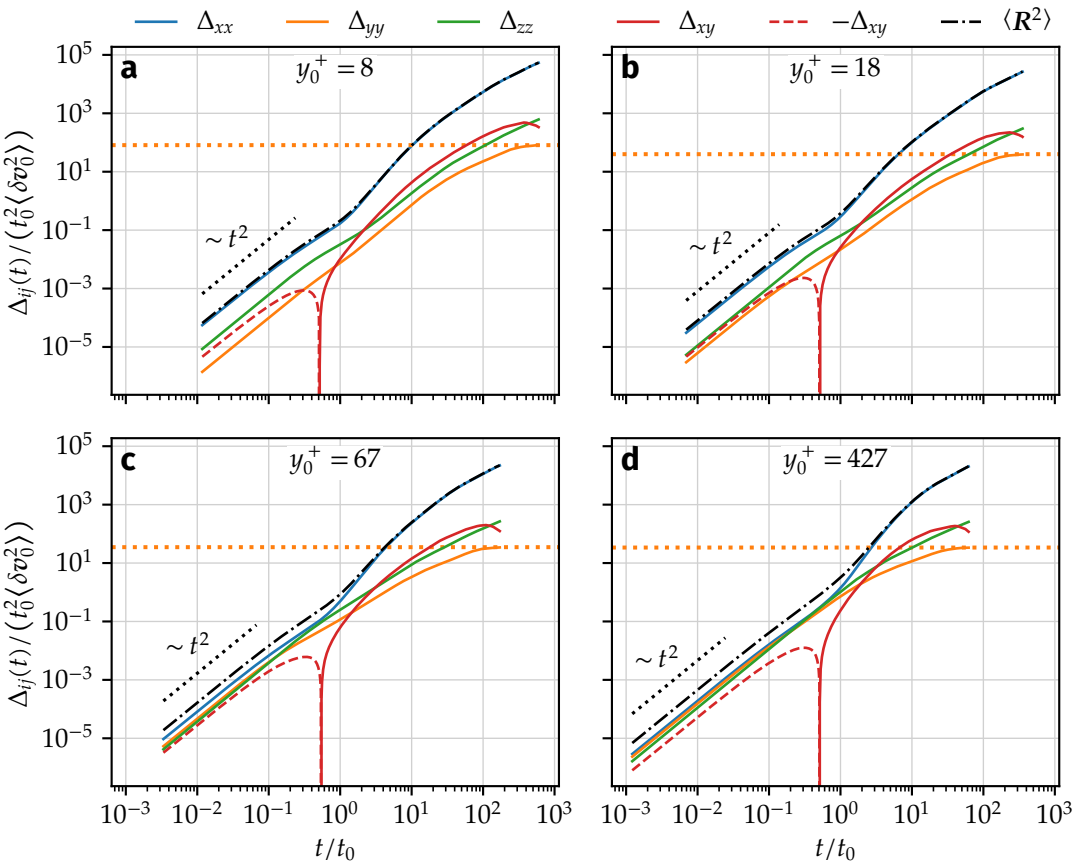

Figure 5.14. Components of the relative dispersion tensor Δ_{ij}, compensated by the mean-square initial relative velocity $\langle \delta v_0^2 \rangle$ and the characteristic ballistic time t_0. Pairs are initially located at $y_0^+ = 8$, 18, 67 and 427 (subfigures (a) to (d)). The initial separation vector is $\boldsymbol{D}_0 = 16\eta \boldsymbol{e}_z$. The total mean-square separation $\Delta_{ii} = \langle \boldsymbol{R}^2 \rangle$ is also represented. Dotted horizontal lines mark the level $\Delta_{ij} = 2h^2/3$, where h is the channel half-width. Negative values of Δ_{xy} are represented by dashed lines. Results are obtained from dataset DS2.

ised to

$$\Delta_{ij}(t) = \langle \delta v_{0i} \delta v_{0j} \rangle t^2 + \left(\langle \delta v_{0i} \delta a_{0j} \rangle + \langle \delta v_{0j} \delta a_{0i} \rangle \right) \frac{t^3}{2} + \mathcal{O}(t^4) \quad \text{for} \quad t \ll t_0. \tag{5.28}$$

Hence, each component of Δ_{ij} independently follows an initial ballistic regime according to the velocity structure function tensor

$$\langle \delta v_{0i} \delta v_{0j} \rangle = S_{ij}(\boldsymbol{x}_0, \boldsymbol{D}_0) = \overline{\delta u_i(\boldsymbol{x}_0, \boldsymbol{D}_0, t)\, \delta u_j(\boldsymbol{x}_0, \boldsymbol{D}_0, t)}, \tag{5.29}$$

where $\delta u_i(\boldsymbol{x}, \boldsymbol{r}, t) = u_i(\boldsymbol{x} + \boldsymbol{r}, t) - u_i(\boldsymbol{x}, t)$. At the next order, the t^3 term is governed by the symmetric part of the crossed velocity-acceleration structure function tensor, $\langle \delta v_{0i} \delta a_{0j} \rangle = \overline{\delta u_i(\boldsymbol{x}_0, \boldsymbol{D}_0, t)\, \delta a_j(\boldsymbol{x}_0, \boldsymbol{D}_0, t)}$.

5.5.1 Short-time dispersion

The temporal evolution of the Δ_{ij} components is shown in fig. 5.14 for particle pairs initially separated in the spanwise direction by $D_0 = 16\eta$, for different initial wall distances y_0. Because of the spanwise initial alignment of the pairs, mean shear does not play a role during the initial ballistic separation. As predicted by eq. (5.28), a ballistic separation is observed for each component of Δ_{ij}. This ballistic regime is anisotropic, i.e. it displays different separation rates in each direction. As expected, the anisotropy of the short-time separation is stronger near the wall ($y_0^+ = 8$ and 18), where tracers separate faster in the streamwise direction, while separation in the other directions is comparatively negligible. (note that the curves for Δ_{xx} and the trace $\langle \boldsymbol{R}^2 \rangle$ are nearly superposed at all times). The strong anisotropy near the wall can be explained by the effect of near-wall streaks. These are elongated regions in the streamwise direction, carrying low-speed and high-speed fluid alternating in the spanwise direction [147]. Two tracers initially belonging to two neighbouring streaks (a high-speed streak next to a low-speed streak), experience a rapid streamwise separation due to the velocity difference between the streaks.

As expected, short-time statistics approach isotropy as particles are released further away from the wall. This is consistent with the observations in section 5.4.3 (see fig. 5.13), in which the temporal asymmetry of the short-time dispersion is close to isotropy far from the wall. In all cases, for each diagonal component of Δ_{ij}, the ballistic separation is immediately followed by a short-lived deceleration of the separation rate. Following eq. (5.28) and consistently with the observations from previous sections, this deceleration is associated with a negative value of the component-wise crossed structure function $\langle \delta v_{0i} \delta a_{0i} \rangle$ (where repeated indices do not imply summation).

5.5.2 Intermediate and long-time dispersion

At intermediate times starting from $t \approx t_0$, Δ_{xx} displays an accelerated separation rate, while Δ_{yy} and Δ_{zz} evolve at slower rates compared to the initial ballistic regime. The rapid separation in the streamwise direction can be attributed to the effect of mean shear. The shear-dominated separation is most effective until $t \approx 10t_0$, where it is characterised by a steep slope of the Δ_{xx} evolution. This is consistent with the duration of the super-diffusive regime observed for $\langle \boldsymbol{R}^2 \rangle$, as discussed in section 5.3.4 (fig. 5.7).

Concerning the wall-normal component Δ_{yy}, an estimate can be made for its asymptotic long-time behaviour noting that the wall-normal pair separation is limited to $|D_y| \leq 2h$ (where h is the channel half-width) due to confinement by the channel walls. As discussed in section 4.5.3 in the context of single-particle displacements, under the assumption of loss of memory of the initial particle position, the wall-normal position of a single particle obeys a uniform distribution at long times, described by the PDF $P_y(y) = 1/(2h)$ for $0 \leq y \leq 2h$. Furthermore, the trajectories of two paired particles are expected to decorrelate over sufficiently long times. As a consequence, the joint PDF describing the wall-normal positions of the two particles, $P_{yy}(y_1, y_2)$, becomes equal to $P_y(y_1)P_y(y_2)$. Under these assumptions, the asymptotic wall-normal mean-square

separation is given by

$$\langle D_y^2 \rangle = \int_0^{2h} \int_0^{2h} (y_2 - y_1)^2 P_{yy}(y_1, y_2)\, \mathrm{d}y_1\, \mathrm{d}y_2 = \frac{2}{3} h^2. \tag{5.30}$$

This estimation can be extended to the wall-normal component of the dispersion tensor, i.e. $\Delta_{yy} \approx 2h^2/3$, provided the initial wall-normal pair separation is small compared to the channel dimensions, $|D_{0y}| \ll h$. In fig. 5.14, this estimate (represented by dotted horizontal lines) accurately predicts the behaviour of Δ_{yy} at long times. We have verified this to be the case for $t^+ > 1 \times 10^4$ for all y_0^+ (not shown here). This is consistent with results in fig. 5.9 showing that after $t^+ \approx 1 \times 10^4$, statistics no longer depend on the initial particle pair configuration.

5.5.3 Time evolution of cross-term Δ_{xy}

We finally discuss the evolution of the non-diagonal term Δ_{xy} shown in fig. 5.14, which may yield additional insight on the mechanisms of pair separation in wall-bounded turbulence. Initially, Δ_{xy} evolves ballistically with an increasingly negative value at all wall distances. Following eq. (5.28), this corresponds to a negative value of the structure function $S_{xy}(y, \boldsymbol{r})$, in this case for $\boldsymbol{r} = 16\eta \boldsymbol{e}_z$. This is consistent with the model of Yang et al. [200] (briefly discussed in section 5.3.2), predicting a structure function S_{xy}^+ between -1 and -2 when the two probed locations are within the logarithmic region. The ballistic regime ends with a deviation of Δ_{xy} towards positive values, resulting from a positive value of the t^3 term in eq. (5.28). This leads to a change of sign of Δ_{xy}, which becomes positive at $t \approx t_0/2$ for all initial wall distances.

At intermediate times, Δ_{xy} displays a rapid growth, coinciding with the super-diffusive growth of Δ_{xx}. As for Δ_{xx}, this is explained by the influence of mean shear. To illustrate this, one can consider a pair of tracers A and B initially located in the lower half of the channel ($0 < y_0 < h$). At some point, even if the tracers are initially close, their wall-normal separation $|D_y| = |y_B - y_A|$ will grow due to turbulent diffusion until $|D_y|$ becomes large enough for mean shear to become important. Without loss of generality, we assume that particle B is further away from the wall than particle A, i.e. $D_y > 0$. Hence, as long as the particles stay within the lower half of the channel, particle B is located in a region of faster average flow than A, and thus their streamwise separation D_x grows rapidly due to mean shear. The result is a product $D_x D_y$ which rapidly grows over time as long as D_y remains positive. This is no longer valid once a tracer crosses the channel centre, which explains the decelerated growth of Δ_{xy} at later times.

5.6 Ballistic dispersion model

The presented results confirm that the ballistic separation of particle pairs is a universal property of relative dispersion, which is not limited to isotropic turbulence (or even to turbulent flows, for that matter). This makes ballistic motion a fundamental aspect

of relative dispersion, which can not only explain the separation of particle pairs at short times following their release, but may also give an explanation for the long-time dispersion including Richardson's explosive separation regime. This is precisely the path taken by several authors, who have attempted to model relative dispersion in isotropic flows based on the idea of subsequent ballistic separations to obtain a description of the long-time dispersion dynamics [29, 50, 168, 178].

In the following we consider the iterative ballistic model proposed by Bourgoin [29] for isotropic turbulence, and we propose a simple extension to anisotropic flows accounting for mean shear and finite-Reynolds effects. Bourgoin's ballistic model is briefly described in section 5.6.1. In section 5.6.2, an extension of the model to anisotropic flows is formulated. The model is compared to our channel flow DNS results in section 5.6.3. Finally, potential model improvements are discussed in section 5.6.4.

5.6.1 Ballistic cascade model in isotropic turbulence

Bourgoin [29] formulated the ballistic cascade in turbulent flows as a simple iterative model illustrated by fig. 5.15. Starting from an initial separation D_0 within the inertial subrange, the mean-square separation $\langle \boldsymbol{D}^2 \rangle$ is incremented at each iteration by a ballistic assumption according to

$$D_{k+1}^2 = D_k^2 + S_2(D_k) t_k^{*2}(D_k) \quad \text{for} \quad k = 0, 1, 2, \dots, \tag{5.31}$$

where D_k^2 is the mean-square separation at iteration k. Here, $S_2(D_k) = \frac{11}{3} C_2 (\varepsilon D_k)^{2/3}$ is the isotropic second-order Eulerian velocity structure function for a separation D_k in the inertial subrange, as introduced in section 5.1.1. The duration of the k-th iteration is given by $t_k^* = \alpha t_k$, where $t_k = S_2(D_k)/(2\varepsilon)$ is a characteristic time of the ballistic regime (equal to t_I as defined in eq. (5.14)), and α is a non-dimensional positive constant referred to as the persistence parameter. A value $\alpha < 1$ expresses that the actual duration of the ballistic separation regime is smaller than the characteristic time t_0, as observed in isotropic turbulent flows [25, 30] and in the present channel flow (see e.g. fig. 5.7). In the above model, the total time elapsed by the end of iteration k is $T_{k+1} = \sum_{n=0}^{k} t_n^*(D_k)$ (fig. 5.15).

Besides Kolmogorov's constant C_2, which has the well-accepted value $C_2 \approx 2.1$ in high-Reynolds numbers flows [172], α is the only free parameter of the model. By analytically relating C_2 and α to Richardson's constant, Bourgoin [29] found $\alpha = 0.12$ as the value that best matches the well-accepted Richardson constant in 3D turbulence, $g \approx 0.55$ [149]. With this value of the persistence parameter, the ballistic cascade model reproduces with great accuracy the DNS results from Bitane et al. [25] in HIT at $Re_\lambda = 730$, with initial particle separations D_0 ranging from 2η to 48η.

The model described by eq. (5.31) is symmetric in time, i.e. it predicts the same separation rates for forward and backward dispersion. Bourgoin [29] also proposed a time-asymmetric extension of the model by including the t^3 term in the Taylor expansion (5.6), associated to the crossed velocity-acceleration structure function S_{au}. This refined model captures a ratio between backward and forward Richardson constants

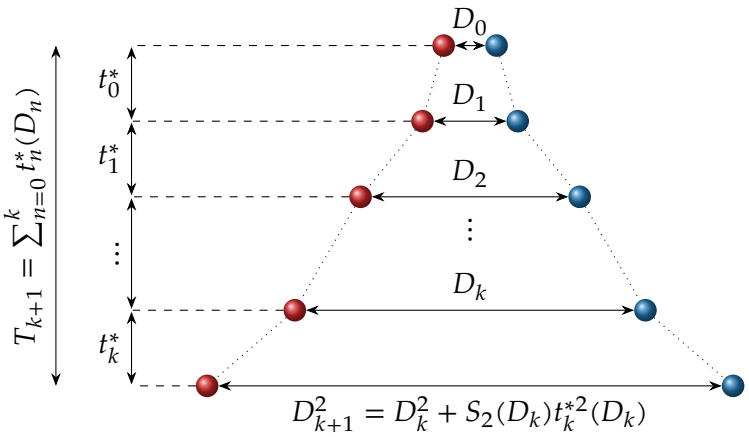

Figure 5.15. Schematic of the iterative ballistic cascade model proposed by Bourgoin [29]. At each iteration k, the mean-square particle pair separation grows ballistically from D_k^2 to D_{k+1}^2 during a time $t_k^*(D_k)$, with a growth rate given by $S_2(D_k)$ [eq. (5.31)]. Figure adapted from Bourgoin [29].

$g_{\mathrm{bw}}/g_{\mathrm{fw}} = 1.9$, consistent with available experimental and numerical results [18, 32].

The model (5.31) implies that the ballistic separation is approximated by $\langle \boldsymbol{D}^2(t) \rangle - \boldsymbol{D}_0^2 \approx S_2(D_0)t^2$ at short times. As discussed in section 5.1.1, this relation is exact only if $\langle \boldsymbol{D}_0 \cdot \delta\boldsymbol{v}_0 \rangle = 0$, i.e. if the initial separation and the initial relative velocity are uncorrelated. This is generally not true in anisotropic flows [128], in which case a (possibly small) approximation error is incurred by the model at short times. As also discussed by Bourgoin [29], a stronger approximation implied by the model is that, over time, the full distribution of particle pair separations is replaced by its second-order moment, i.e. the mean-square separation $\langle \boldsymbol{D}^2 \rangle$. In reality, over time different particle pairs have different separations, and thus their ballistic growth rate should be obtained from the two-point statistics at their own instantaneous separation. This suggests a probabilistic approach, such as the one proposed by Thalabard et al. [178], in which the full distribution of particle pair separations is modelled. Nevertheless, as mentioned above, the approximations made by Bourgoin's iterative model are sufficient to accurately describe mean-square separation statistics observed in simulations and, in the case of the time-asymmetric model extension, the ratio between backward and forward Richardson constants.

5.6.2 Ballistic cascade model in inhomogeneous turbulence

As shown in the previous sections, the mean-square separation of particle pairs in channel flow is accurately described at short times by an average ballistic separation. Therefore, a model based on a succession of ballistic separations seems suitable for predicting pair dispersion statistics in the present flow. In this section, such a model is proposed based on Bourgoin's approach, which is adapted to account for the effect of an inhomogeneous mean velocity field $\boldsymbol{U}(\boldsymbol{x})$. The model is also adjusted to account

for the transition from inertial- to integral-scale separations at sufficiently long times. In addition to the mean velocity field, the present model requires as input the mean turbulent dissipation rate $\varepsilon(\boldsymbol{x})$.

In contrast to the isotropic model, where the output is the (mean-squared) separation $D(t)$, the present model needs to keep track of the full mean separation vector $\boldsymbol{D}(t)$ and of the absolute particle pair position in order to account for anisotropy and inhomogeneity. The position of the pair is determined here by the particle pair centroid $\tilde{\boldsymbol{x}}(t) = (\boldsymbol{x}^A(t) + \boldsymbol{x}^B(t))/2$, where $\boldsymbol{x}^A$ and $\boldsymbol{x}^B$ are the positions of the two particles. In channel flow, due to homogeneity in the streamwise and spanwise directions, only the wall-normal component $\tilde{y} = \tilde{\boldsymbol{x}} \cdot \boldsymbol{e}_y$ needs to be considered. Moreover, the model requirements reduce to the mean streamwise velocity profile across the channel $U(y)$, and the mean turbulent dissipation rate $\varepsilon(y)$. The model is started with the initial particle pair configuration, determined by the initial separation vector $\boldsymbol{D}_0$ and the wall-normal centroid position $\tilde{y}_0 = (y_0^A + y_0^B)/2$.

We model the time evolution of the mean-square separation vector $\langle \boldsymbol{D}^2 \rangle$ and the mean position of the pair centroid $\tilde{\boldsymbol{x}}$ iteratively. As a first approximation, the centroid is kept fixed over time, i.e. $\tilde{\boldsymbol{x}}_k = \tilde{\boldsymbol{x}}_0$ at every iteration k. This will be improved in future versions of the model, by taking into account the drift of the particle pair centroid based on the single-particle dispersion statistics presented in chapter 4. At iteration k, the mean-square separation in each direction $i \in \{x, y, z\}$ is incremented according to

$$D^2_{k+1,i} = D^2_{k,i} + S_{2i}(\tilde{\boldsymbol{x}}_k, \boldsymbol{D}_k)\, t^{*2}_k(\tilde{\boldsymbol{x}}_k, \boldsymbol{D}_k) \quad \text{for} \quad k = 0, 1, 2, \dots, \tag{5.32}$$

where $D^2_{k,i}$ is the mean-square separation in the i-th direction at iteration k. The total mean-square separation is then $D^2_k = D^2_{k,x} + D^2_{k,y} + D^2_{k,z}$.

The structure function S_{2i} is associated to the velocity component u_i. Applying the Reynolds decomposition, S_{2i} can be written as the superposition of a mean and a fluctuating component,

$$S_{2i}(\tilde{\boldsymbol{x}}_k, \boldsymbol{D}_k) = \overline{S}_{2i}(\tilde{\boldsymbol{x}}_k, \boldsymbol{D}_k) + S'_{2i}(\tilde{\boldsymbol{x}}_k, \boldsymbol{D}_k). \tag{5.33}$$

The mean component is readily obtained from the mean velocity field,

$$\overline{S}_{2i}(\tilde{\boldsymbol{x}}_k, \boldsymbol{D}_k) = \left[U_i(\boldsymbol{x}^B_k) - U_i(\boldsymbol{x}^A_k)\right]^2, \tag{5.34}$$

where $\boldsymbol{x}^A_k$ and $\boldsymbol{x}^B_k$ are the modelled positions of the two particles,

$$\boldsymbol{x}^A_k = \tilde{\boldsymbol{x}}_k - \frac{\boldsymbol{D}_k}{2} \quad \text{and} \quad \boldsymbol{x}^B_k = \tilde{\boldsymbol{x}}_k + \frac{\boldsymbol{D}_k}{2}. \tag{5.35}$$

Meanwhile, the fluctuating component S'_{2i} is estimated so as to account for the transition from inertial- to integral-scale separations. In the inertial range, S'_{2i} is assumed to be

isotropic and thus it is estimated as [137]

$$S_{2i}^{I}(\tilde{\boldsymbol{x}}_k, \boldsymbol{D}_k) = C_2 \left(\varepsilon(\tilde{\boldsymbol{x}}_k)\,|\boldsymbol{D}_k|\right)^{2/3} \left(\frac{4}{3} - \frac{1}{3}\frac{D_{k,i}^2}{|\boldsymbol{D}_k|^2}\right), \tag{5.36}$$

which is directly related to expression (5.7) for the total structure function S_2. As discussed in section 5.3.2 [eq. (5.10)], for integral-scale separations, the velocity fluctuations at the two locations become decorrelated and the structure function S'_{2i} is given by the sum of the velocity variances at the two positions,

$$S_{2i}^{L}(\tilde{\boldsymbol{x}}_k, \boldsymbol{D}_k) = \overline{u_i'^2}(\boldsymbol{x}_k^A) + \overline{u_i'^2}(\boldsymbol{x}_k^B), \tag{5.37}$$

where $\overline{u_i'^2}$ is the variance of the velocity component u_i.

Noting that the velocity structure function typically increases with the spatial increment (or equivalently, the velocity auto-correlation decreases with distance), it is reasonable to model S'_{2i} as an increasing function of the separation $|\boldsymbol{D}_k|$. Hence, we choose to implicitly model the transition from inertial- to integral-scale separations by taking

$$S'_{2i}(\tilde{\boldsymbol{x}}_k, \boldsymbol{D}_k) = \min\left\{S_{2i}^{I}(\tilde{\boldsymbol{x}}_k, \boldsymbol{D}_k),\, S_{2i}^{L}(\tilde{\boldsymbol{x}}_k, \boldsymbol{D}_k)\right\}, \tag{5.38}$$

that is, the transition happens when the components of the separation vector $\boldsymbol{D}_k$ become large enough for the inertial-scale estimation S_{2i}^{I} to overcome the integral-scale structure function S_{2i}^{L}. A weakness of this model is that it predicts a sharp transition between scales, given by an abrupt (non-differentiable) structure function at the separation where the transition happens, whereas the structure function should be a smooth function of the separation. This is illustrated by fig. 5.16, which compares the structure functions S'_{2i} obtained from eq. (5.38) with their values in channel flow DNS, for separations $\boldsymbol{D}_k$ in the spanwise direction. For small separations, the overestimation of S'_{2i} by the model is explained both by dissipative-scale separations not being included in the model, and by the lack of sufficient scale separation at the present Reynolds number, as discussed in section 5.3.2. In the figure, the fluctuating value of S'_{2x} from DNS at large separations is a numerical artefact due to the finite domain size in the spanwise direction, as discussed in section 2.1.4.2.

We finally note that, according to eq. (5.38), the three separation components D_i may transition to the integral scales at different times. This is not an issue since, in inhomogeneous flows, the characteristic size of the integral scales generally depends on the considered orientation.

As in the original model by Bourgoin [29], the iteration time is taken as $t_k^* = \alpha t_k$,

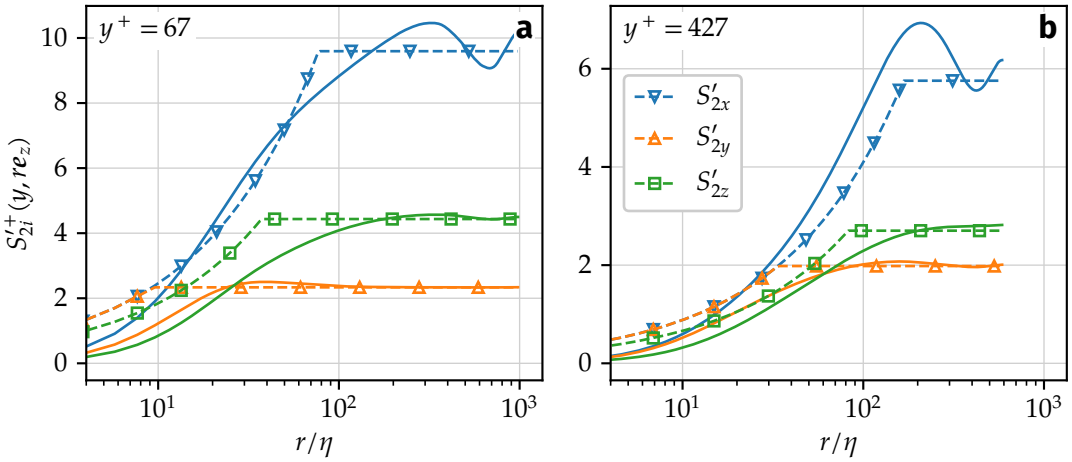

Figure 5.16. Modelled and computed velocity structure functions $S'_{2i}(y, \boldsymbol{r})$ in wall units, for (a) $y^+ = 67$ and (b) $y^+ = 427$. Spatial increments are in the spanwise direction, $\boldsymbol{r} = r\boldsymbol{e}_z$. Dashed lines with markers, modelled structure functions according to eq. (5.38); solid lines, channel flow DNS at $Re_\tau = 1440$.

with the ballistic time scale estimated as[4]

$$t_k(\tilde{\boldsymbol{x}}_k, \boldsymbol{D}_k) = \frac{S_2(\tilde{\boldsymbol{x}}_k, \boldsymbol{D}_k)}{2\varepsilon(\tilde{\boldsymbol{x}}_k)} = \frac{1}{2\varepsilon(\tilde{\boldsymbol{x}}_k)} \sum_{i=1}^{3} S_{2i}(\tilde{\boldsymbol{x}}_k, \boldsymbol{D}_k). \tag{5.39}$$

Here, the structure functions S_{2i} are determined from eqs. (5.33), (5.34) and (5.38). The estimation (5.39) is obtained from definition (5.13) for the ballistic time scale, along with the assumption that the crossed velocity-acceleration structure function is given by $S_{au}(\tilde{\boldsymbol{x}}_k, \boldsymbol{D}_k) = -2\varepsilon(\tilde{\boldsymbol{x}}_k)$. The value of the persistence parameter $\alpha = 0.12$ is kept unchanged from the isotropic model. Finally, the time elapsed by the end of iteration k is $T_k = \sum_{n=0}^{k} t_k^*(\tilde{\boldsymbol{x}}_n, \boldsymbol{D}_n)$.

As described above, a limitation of the present model is that the centroid position $\tilde{\boldsymbol{x}}_k$ stays fixed over time. Since the mean turbulent dissipation rate is always evaluated at $\tilde{\boldsymbol{x}}_k$ [eqs. (5.36) and (5.39)], the effective dissipation also stays constant in time, as in the isotropic model. In fact, the present model falls back to the isotropic model when a constant mean velocity field is imposed (i.e. in the absence of mean shear), as long as separations stay within the inertial subrange. A stronger limitation of the inhomogeneous model is that it does not account for the presence of solid boundaries and thus for wall confinement in wall-bounded flows. In other words, the model allows particles to travel beyond walls. When a particle crosses a channel wall, the mean velocity at its position is taken as $\boldsymbol{U} = 0$. Further work is required to properly

[4] In our publication [135] a different definition was used, with S'_{2i} instead of S_{2i}. As a consequence, the model results presented in this work differ from those of the article and are closer to the DNS statistics. The present definition yields a longer duration of each ballistic iteration, and is consistent with the ballistic regime being determined by the full relative particle velocity and not only by its fluctuating component.

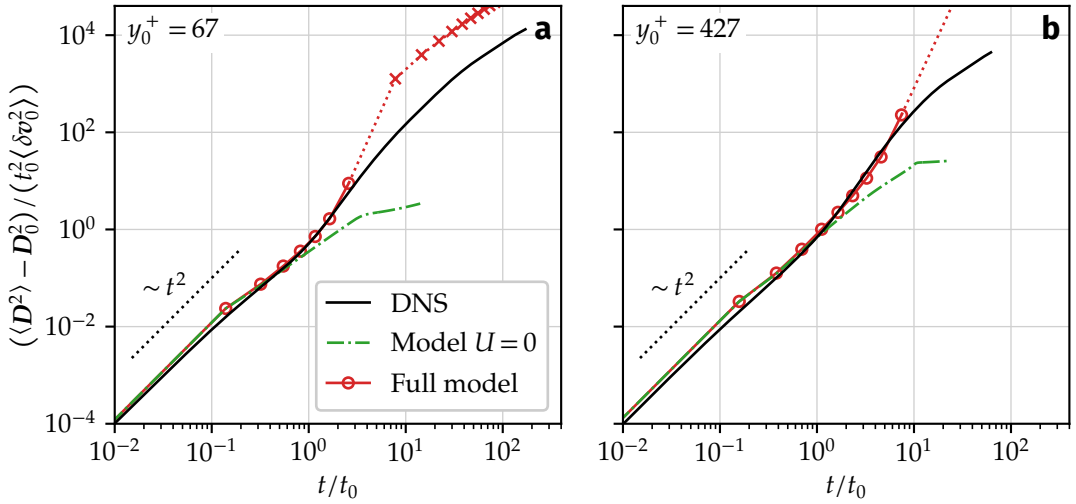

Figure 5.17. Inhomogeneous ballistic cascade model compared to pair dispersion statistics obtained from DNS. Particle pairs are initially located at (a) $y_0^+ = 67$ and (b) $y_0^+ = 427$. The initial separation vector is $\boldsymbol{D}_0 = 16\eta \boldsymbol{e}_z$. Black solid line, DNS results; dash-dotted line, ballistic model with zero velocity profile; line with markers, full ballistic model with velocity profile $U(y)$. Markers are drawn at every ballistic iteration. Dotted lines and crosses are drawn once one of the modelled particles has crossed the channel walls.

account for wall confinement.

5.6.3 Application to turbulent channel flow

The model formulated above is tested in the channel flow configuration, using as input a mean velocity profile $U(y)$, velocity variance profiles $\overline{u_i'^2}(y)$, and a mean turbulent dissipation rate profile $\varepsilon(y)$ obtained from our DNS at $Re_\tau = 1440$ (profiles are plotted in appendix A, figs. A.1 and A.3). We test two initial configurations, corresponding to initial wall distances $y_0^+ = 67$ and 427. In both cases the initial particle separation is $\boldsymbol{D}_0 = 16\eta \boldsymbol{e}_z$. The DNS results obtained from these two cases have been analysed in previous sections (see e.g. fig. 5.14(c-d)). Since the present model assumes isotropy to estimate inertial-range structure functions (eq. (5.36)), model predictions are expected to be more accurate for particles initialised far from the wall where anisotropy is weaker. Furthermore, the chosen initial separation $D_0 = 16\eta$ is considered favourable for testing the model since, as shown in fig. 5.4, the velocity structure function S_2 closely matches the inertial-range isotropic behaviour predicted by K41 theory. This is not the case for smaller separations including $D_0/\eta = 1$ and 4. For these separations, the model should be extended by including dissipation-range structure function estimations such as the ones proposed in section 5.3.2.

A comparison between the model and DNS results is shown in fig. 5.17 for the two chosen initial configurations. Also shown is a variant of the model with a zero mean velocity profile ($U(y) = 0$), so that mean shear effects are neglected. As mentioned

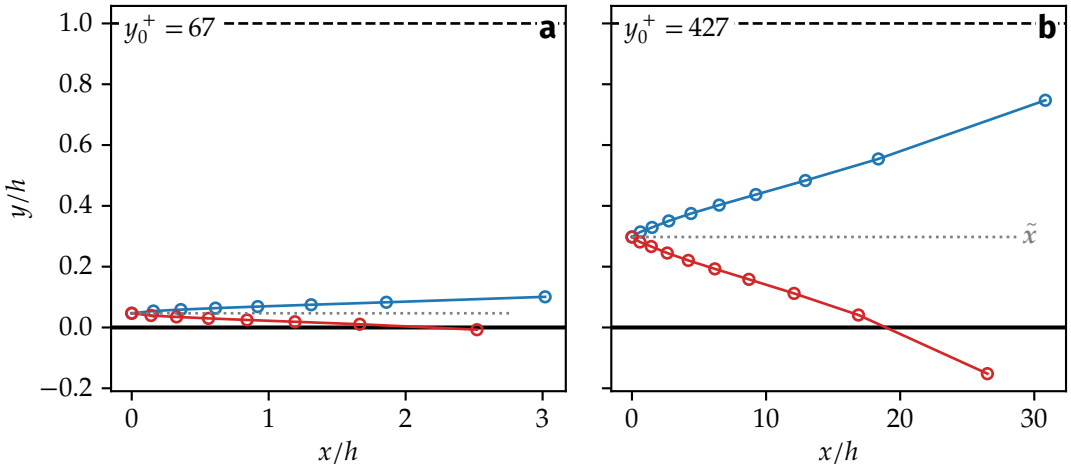

Figure 5.18. Trajectories of modelled particle pairs projected on a x-y plane. Initial configurations are as in fig. 5.17. Markers are drawn at every ballistic iteration. The pair centroid $\tilde{x}$, represented by a dotted line, is advected by the mean streamwise velocity $U(\tilde{x})$. The lower wall and the channel centreline are represented by solid and dashed lines, respectively.

above, this variant is equivalent to Bourgoin's isotropic model as long as separations stay within the inertial subrange. Figure 5.17 is complemented by fig. 5.18 illustrating the modelled particle pair trajectories for the two initial configurations, up to the moment a particle crosses the wall. In fig. 5.17, the full model closely predicts the DNS data during the first few ballistic iterations. Up to $t \approx t_0$, the two model variants closely match, suggesting that turbulent fluctuations dominate the separation over mean shear. At later times, the full model accurately describes the transition to the shear-dominated separation regime, in which the separation rate is accelerated with respect to the initial t^2 scaling. Contrarily to the results presented by Bourgoin [29], here the zero-shear model does not show evidence of Richardson's t^3 regime due to lack of scale separation, since particle pairs do not spend enough time in the inertial subrange.

For both initial wall distances, the model slightly overpredicts the separation at the first iteration compared to the DNS data. This is explained by inaccuracies in the prediction of the structure functions S_{2i}. This is clearer in fig. 5.19, where each component of the modelled and computed mean-square separation is separately plotted compensated by the initial ballistic regime in t^2. For both initial wall distances, the model overpredicts the initial ballistic regime (and therefore S_{2i}) in the wall-normal and spanwise directions. The ballistic streamwise separation is correctly predicted at very short times for $y_0^+ = 67$. However, this seems to be coincidental as the same separation is overestimated at $y_0^+ = 427$, where the model is expected to be more accurate due to return to isotropy far from the wall. The overprediction of S_{2i} can be explained by the relatively small Reynolds number of the present flow ($Re_\lambda^{\max} \sim 100$). As discussed in section 5.3.2, a lower value of the Kolmogorov constant C_2 would fit more closely the velocity structure functions in the channel. This can be expected to

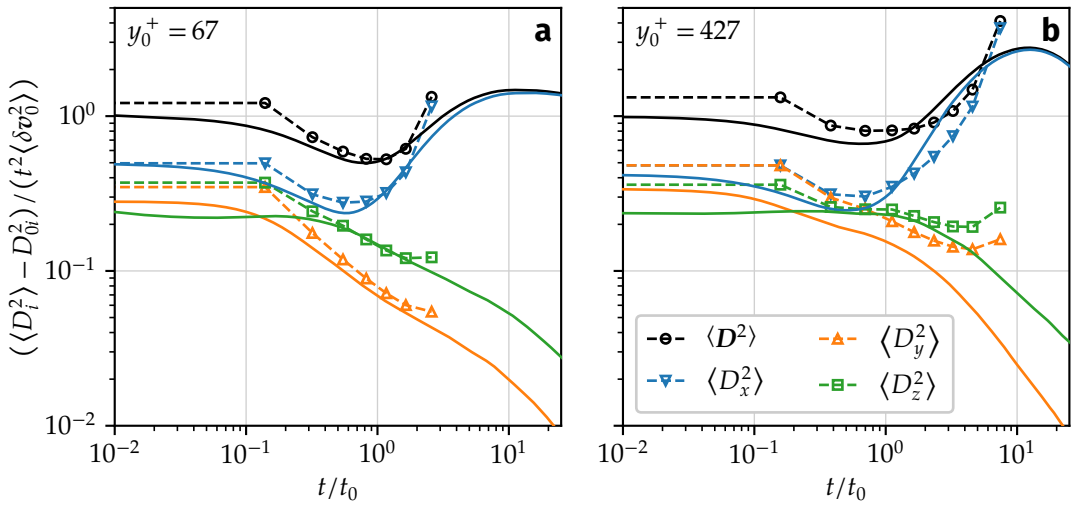

Figure 5.19. Modelled mean-square separation in each direction compared with DNS statistics. Results are compensated by $t^2\langle \delta v_0^2 \rangle$, so that the ballistic regime appears as a plateau. Initial configurations are as in fig. 5.17. Dashed lines with markers, full model; solid lines, DNS results. Markers are drawn at every ballistic iteration.

improve the comparisons with DNS data.

At intermediate times, fig. 5.19 shows that the model qualitatively captures the decreasing separation rates in the wall-normal and spanwise directions, as well as the hierarchy of separations in the different directions ($D_x^2 > D_z^2 > D_y^2$) and the explosion of the streamwise separations due to mean shear. Moreover, it accurately predicts the time where the transition to the shear-dominated regime occurs.

The inhomogeneous model strongly departs from the DNS data at long times. This is explained by the model not accounting for the presence of walls, which limit the wall-normal motion of particles. As a result, over time the model overestimates the wall-normal particle separation D_y. This is more visible in fig. 5.19b, where at long times the modelled D_y displays a growth rate faster than t^2. In turn, this results in an overestimation of the separation by mean shear, since the mean velocity difference increases with D_y as long as particles do not cross the channel centreline.

5.6.4 Discussion and perspectives

As shown above, the inhomogeneous ballistic model proposed here is capable of qualitatively describing aspects of pair dispersion in channel flow turbulence at short and intermediate times, including not only the initial ballistic regime, but also the transition from turbulence- to shear-dominated diffusion regimes. However, the model has several shortcomings. First, it overpredicts the initial ballistic separation regime, which is explained above by an overestimation of the velocity structure functions S_{2i} due to finite-Reynolds number effects. Secondly, the model does not account for the presence of solid walls and therefore it strongly overestimates the wall-normal particle

separation at intermediate and long times, while allowing particles to cross beyond walls.

The presence of solid boundaries may be partially modelled by estimating the drift of the particle pair centroid $\tilde{\boldsymbol{x}}$ away from walls. In channel flow, the modelled particle pair centroid should drift at long times towards the channel centre, in agreement with single-tracer displacement statistics (see section 4.1). However, modelling the evolution of $\tilde{\boldsymbol{x}}$ would only delay particles from reaching (and crossing) the walls without completely preventing it, since particles would still be allowed to separate indefinitely in the wall-normal direction. Consequently, an additional restriction on the wall-normal particle separation D_y needs to be included. In the channel, D_y^2 must be bounded by, and tend to, the long-term asymptotic wall-normal separation $D_y^2 = 2h^2/3$ (eq. (5.30)). Therefore, the model may be extended by adding a repulsive response from walls which would negate a fraction of the particle wall-normal motion. The intensity of the response would increase with the proximity of particles to the walls. However, the issue of quantifying such a response in a way that is consistent with observed Lagrangian dispersion statistics in the channel has not been resolved at present time.

Further extensions to improve the predictive capabilities of the model in finite-Reynolds numbers inhomogeneous flows are possible. To properly estimate the ballistic dynamics at small separations, dissipative-scale structure function estimations (such as the ones proposed in section 5.3.2 for the present flow) may be introduced into the model. On the other hand, a tensor formulation of the model, based on the short-time ballistic evolution of the dispersion tensor components (eq. (5.28)), may improve relative dispersion predictions in general anisotropic flows. In the channel, this would require an additional model for the S_{xy} structure function briefly discussed in section 5.5.3. This must be complemented with anisotropy corrections for the diagonal components of S_{ij}, which are presently assumed to be isotropic for inertial-range separations (eq. (5.36)). Approaches based on Townsend's attached-eddy hypothesis [181], such as the one proposed by Yang et al. [200], could be a good starting point for estimating the required structure functions.

5.7 Conclusion

In this chapter we study the relative dispersion of tracer pairs in a turbulent channel flow from direct numerical simulations. Statistics are conditioned on the initial particle pair wall distance y_0 and initial separation vector $\boldsymbol{D}_0 = D_0\boldsymbol{e}_0$. At short times following their release, particle pair separation statistics are determined by the Eulerian flow structure at their initial locations. In particular, their mean-square change of separation $\langle \boldsymbol{R}^2 \rangle$ follows an initial ballistic growth, $\langle \boldsymbol{R}^2 \rangle \approx S_2(y_0, \boldsymbol{D}_0)t^2$, where $S_2(y, \boldsymbol{r})$ is the Eulerian second-order velocity structure function at a wall distance y and spatial increment $\boldsymbol{r}$. At the next order, the crossed velocity-acceleration structure function $S_{au}(y, \boldsymbol{r})$ governs the deviation from the initial ballistic separation at short times. In our simulations, the ballistic regime and the deviation that follows are invariably observed and linked to S_2

and S_{au}, for all the analysed initial wall distances and initial separation vectors. This confirms the robustness of the short-time ballistic regime, which is based purely on kinematic considerations, consistently with observations in isotropic flows [25, 30].

The characteristic duration of the initial regime is accurately described in our simulations by the ballistic time scale $t_0 = S_2/|S_{au}|$ first proposed by Bitane et al. [25]. However, due to the relative complexity of wall-bounded flows at finite Reynolds numbers, accurate estimates of S_2 and S_{au} are not easily obtained, especially near the wall where the flow is strongly anisotropic and driven by coherent turbulent structures. We show that isotropic estimations of S_2 and S_{au} describe reasonably well the observed statistics in the logarithmic and outer layers (fig. 5.4), although improvements can be made to account for the persistence of small-scale anisotropy, large- and very-large-scale motions, and finite Reynolds number effects. Nevertheless, the relation $S_{au}(y, \boldsymbol{r}) = -2\varepsilon$, expected to hold for inertial-scale increments $|\boldsymbol{r}|$ at large Reynolds numbers if the flow is locally homogeneous [63], is accurate in most of the channel for large-enough increments. More generally, S_{au} is negative for nearly all the considered initial particle pair configurations.

Consistently with studies in isotropic turbulence, tracers separate faster when tracked backwards in time than forwards. At short times, this time asymmetry is explained by negative values of S_{au} [79]. The time-asymmetric behaviour persists when only the separation by the fluctuating flow is considered, confirming that the asymmetry is linked to the irreversibility of turbulent fluctuations.

Mean shear drives particle separation at intermediate and long times starting from $t \approx t_0$. Its effect is to enhance the streamwise particle separation when particle pairs find themselves in regions of the channel with different mean velocities. This shear-induced super-diffusive regime is more effective at intermediate times, and slows down at long times as particles cross the channel centreline where the mean velocity gradient direction is reversed. At intermediate times, the separation rate is higher in cases where the initial ballistic regime is less effective. This is the case for small initial separations D_0, as well as for wall-parallel orientations (fig. 5.9), in which cases mean shear has a negligible effect on the initial separation dynamics. Conversely, when the ballistic regime is driven by mean shear, the separation rate at intermediate times is lower.

The anisotropy of pair dispersion is characterised by the relative dispersion tensor Δ_{ij}. Each tensor component separately follows a ballistic growth at short times. The dominant role of mean shear is described by an increasing rate of change of the streamwise mean-square separation Δ_{xx} and of the cross-term Δ_{xy} at intermediate times following the ballistic growth (fig. 5.14). At the chosen initial separation ($\boldsymbol{D}_0 = 16\eta\boldsymbol{e}_z$), Δ_{xy} is negative at small times as a consequence of the local Eulerian flow structure, while it becomes positive and rapidly grows at later times due to mean shear. Meanwhile, the wall-normal and spanwise separation rates decrease following the initial ballistic regime. Due to wall confinement in the channel, Δ_{yy} tends to an asymptotic value $2h^2/3$ at long times.

Finally, a simple model for the mean-square separation in inhomogeneous flows is introduced based on the ballistic cascade phenomenology proposed by Bourgoin [29] for isotropic turbulence, which relies on the robustness of ballistic pair separations in

turbulent flows. The present model further accounts for the presence of mean shear through an imposed mean velocity field, as well as for integral-scale separations. The model correctly predicts the initial stages of separation in channel flow for inertial-range initial separations, including the ballistic regime and the subsequent transition to the shear-dominated separation. However, the agreement remains mostly qualitative, and further refinements to the estimation of structure functions are needed to improve model predictions. More importantly, the present model does not account for the presence of walls, effectively allowing particles to cross solid boundaries. This very strong limitation needs to be corrected in future developments of the model.

The present study leaves unanswered questions regarding the impact of the properties of wall-bounded turbulence on relative dispersion. Besides their implicit effect on the structure functions governing the short-time separations, the effect on dispersion of near-wall structures such as quasi-streamwise vortices, responsible for sweep and ejection events, has not been considered explicitly. The role of these structures will be examined in future studies via statistics conditioned to the occurrence of such events. Furthermore, the determination of pair separation PDFs may yield a more complete description of relative dispersion in the channel. Forthcoming studies will also deal with Lagrangian dispersion of fluid particle tetrads as well as with relative dispersion of inertial particles.

6 Conclusion and perspectives

The Lagrangian perspective can provide important insight on the temporal evolution of turbulent flows and on the dispersion of species resulting from their chaotic motion. In wall-bounded turbulence, the Lagrangian properties of the flow are determined not only by random turbulent motion, but also by wall confinement, which limits the motion of Lagrangian tracers in the wall-normal direction; by preferentially oriented coherent motions near the wall, which contribute to the anisotropy of Lagrangian statistics; and by mean shear, which strongly enhances the relative separation between tracers. The effect of these characteristic properties of wall turbulence on different Lagrangian observables is described and quantified in the present investigation, with a focus on the properties of the Lagrangian acceleration and of tracer dispersion in confined wall-bounded flows. The moderate Reynolds number $Re_\tau = 1440$ chosen for this study allows to observe, in addition to a near-wall region dominated by viscous shear and coherent motions, a significant outer region where mean shear is the main source of anisotropy.

In the inner region of the flow, Lagrangian acceleration statistics are consistent with previous observations in wall-bounded turbulence at lower Reynolds number. Namely, the acceleration is strongly anisotropic, and is highly intermittent due to the dominant influence of coherent structures inducing helical trajectories associated to strong centripetal accelerations. In the buffer layer, while the wall-normal and spanwise acceleration components are strongly influenced by quasi-streamwise vortices, negative streamwise accelerations are commonly associated to increasing viscous shear as tracers move towards the wall. The outer region of the flow is dominated by large-scale mean shear. It is shown that mean shear is responsible for small-scale anisotropy of the Lagrangian acceleration statistics even near the channel centre, in contradiction with the idea of a return to isotropy, which is commonly applied in numerous subgrid-scale models for turbulent flows in LES. This is suggested by the Lagrangian cross-correlations between streamwise and wall-normal acceleration, which become non-zero after a short time lag $\tau \sim \tau_\eta$ with a sign that is consistent with the direction of mean shear.

In wall-bounded turbulence, the inner region acts as a sink of total kinetic energy which is injected mainly in the outer region of the flow. As a consequence, on average tracers located in the inner region lose kinetic energy over time. As demonstrated in this study, this has a clear impact on tracer trajectories: when tracers are conditioned to a chosen near-wall location, they travel shorter streamwise distances on average when they are tracked forwards in time than backwards. Evidence of time irreversibility is also observed in the spreading of particles in the streamwise direction, quantified by the variance of the streamwise displacement $\langle \delta x'^2 \rangle$. For all wall distances, tracers spread

over longer distances when they are tracked backwards in time. This observation is linked to the dynamics of turbulent kinetic energy in wall turbulence. In particular, away from the inner region, the difference between backward and forward spreads at short times grows proportionally to the mean turbulent kinetic energy dissipation rate ε.

As shown by previous studies, mean shear greatly influences the relative separation of pairs of tracers in wall-bounded and shear flows. This influence is evident at intermediate times following the release of particle pairs, after the initial ballistic separation that is determined by the initial relative velocity of the pair. By decomposing the relative separation into components due to the mean and the fluctuating velocity fields, we show that, in the present flow, mean shear is responsible for the accelerated separation rate observed at intermediate times. The separation rate is comparable to that predicted by Richardson's law in high Reynolds number turbulent flows, although the mechanisms are not the same, and thus the observed behaviour cannot be related to Richardson's law. By quantifying the time scales associated to relative dispersion, we estimate that much larger Reynolds numbers are required to expect Richardson's law in our flow. The long-time limit of relative dispersion is also explored. At long times, the enhancing effect of mean shear slows down due to tracers crossing the channel centreline where mean shear changes direction.

The time asymmetry of pair dispersion is also investigated. Pairs of tracers separate faster when they are tracked backwards in time than forwards. As in three-dimensional HIT, this is explained at short times by the negative value of the crossed velocity-acceleration structure function $S_{au}(y, \boldsymbol{r})$, which is equal to -2ε under local homogeneity conditions for spatial increments $|\boldsymbol{r}|$ in the inertial range. This relation is verified away from the inner region for sufficiently large initial particle separations.

Taking into account the dominant role of mean shear on relative dispersion, a simple model the mean-square particle separation in the channel is proposed. The model describes relative dispersion as a sequence of discrete ballistic separations, and is based on a similar formulation for isotropic flows. Besides considering the existence of a non-uniform mean velocity field, the proposed model accounts for the transition from inertial- to integral-scale particle separations. The model correctly reproduces the transition to the shear-dominated separation regime. However, the model fails at later times since it does not currently account for confinement by the walls.

Perspectives

The present investigation highlights the effect of certain statistical quantities, such as the mean velocity profile, on the dispersion of Lagrangian particles. In contrast, the effect of coherent motions on tracer dispersion has not been explored with much detail in this work. Coherent motions can be expected to have a dominant role on tracer dispersion, especially for particles located in the inner region. In the buffer layer, sweeps and ejections are associated to wall-normal displacement of tracers. These features are usually produced by quasi-streamwise vortices, and therefore tracers initially caught

in an ejection may be expected to describe, at later (and earlier) times, a spiralling motion along one of these structures. In addition, tracers captured by quasi-streamwise vortices may have longer residence times in the near-wall region, while other tracers may spread faster towards the outer region of the flow. An interesting question concerns the characteristic residence time of tracers in the near-wall region as a consequence of coherent motions. We have also hinted that the short-time relative separation of tracers near the wall is determined by the typical structure of the coherent motions in the inner region. For instance, two tracers caught respectively in an ejection and a neighbouring sweep event will quickly separate in the streamwise and wall-normal directions, at least at short times. On the other hand, if the tracers are within the same quasi-streamwise vortex, chances are that their separation will remain bounded over relatively long times comparable to the typical life time of such structures. A more precise characterisation of the influence of coherent structures on the relative separation of particles is needed to understand the Lagrangian dynamics of near-wall turbulence.

It is clear that small-scale coherent motions influence the geometry of Lagrangian paths. This influence may be quantified in terms of the curvature and torsion of Lagrangian trajectories in space, as it has been done in HIT [33, 42, 159, 198] and more recently in different inhomogeneous rotating flows [5], where these parameters have been linked to the presence of small-scale vortices. Alternatively, the changes of direction of Lagrangian paths over variable time lags τ have been studied in HIT [28] and in rotating Rayleigh–Bénard convection [6]. In wall turbulence, an important question is how mean shear and near-wall coherent motions influence the topology of Lagrangian paths, and how their impact compares to the effect of vortex filaments in isotropic turbulence. In the outer region of the flow, the evidence of small-scale anisotropy presented in this work suggests a preferential direction of curvature of Lagrangian paths. This could also be verified by a geometric study of tracer trajectories.

Finally, as mentioned in the introduction, a logical extension of the present work concerns the dynamics of inertial particles in wall-bounded turbulence. A first step in this direction would be to consider small heavy inertial particles (e.g. small solid particles in air), which have been extensively studied in many turbulent flow configurations, including isotropic turbulence and wall-bounded flows [87]. Such particles are simple to model in numerical simulations since they can be smaller than the smallest scales of the flow, and thus they see a uniform flow around them which is not affected by their presence. Despite the considerable amount of work on this issue, most available particle-laden simulations in wall-bounded flows are at relatively low Reynolds numbers. Moreover, to our knowledge the time asymmetry of particle dispersion statistics has not been considered in this kind of flow. In wall turbulence, heavy particles are known to migrate on average towards the wall where the turbulent kinetic energy is lower, a phenomenon known as turbophoresis [87]. This clearly represents an additional source of time asymmetry which is not present in the case of fluid tracers. In this regard, an interesting question is whether inertial particle statistics are affected by the same sources of time asymmetry as fluid tracers, and how this effect compares to (or interacts with) that of turbophoresis.

As a follow-up question, the dynamics of finite-size particles in wall-bounded tur-

bulence may also be considered. This problem is interesting not only as a point of comparison with tracers and smaller particles, but also from a modelling standpoint. Indeed, predicting the motion of finite-size particles represents a significant challenge when the particle size is larger than the smallest turbulent scales, since (i) particles larger than the smallest scales of motion clearly perturb the surrounding flow, and (ii) the motion of a real particle is determined by the average force applied by the fluid on its surface, which cannot simply be replaced by a fluid property evaluated at an infinitesimal point, i.e. at the particle centre. In this regard, previous numerical studies in wall-bounded turbulence exist. One approach is to fully resolve the boundary of each individual particle, which yields a correct representation of the physics, but is very costly from a computational standpoint, and thus it is limited to a relatively small number of particles. For these reasons, it would be interesting to determine whether an accurate simplified description of finite-size particles can be made using a point-particle model. Such model may rely on Faxén corrections, which have already been used in HIT [36, 65], as well as on additional lift forces on the particles, including the Magnus effect resulting from their own rotation, and Saffman lift resulting from the shear around them.

Alternatively, a promising development regarding the modelling of large inertial particles was recently made by Barge [11], based on the point-particle model previously proposed by Gorokhovski and Zamansky [60] to simulate particles with diameter $d_p > \eta$ in LES. The model supposes that the force applied by the flow on a particle follows K41 scaling. Hence, if the particle diameter is in the inertial range, the particle acceleration is written in terms of d_p and of the local dissipation rate at the particle position ε_d. Barge applied this model to an isotropic turbulence DNS at $Re_\lambda = 90$ using particle diameters up to 41η and different particle densities, and was able to reproduce the particle acceleration PDFs obtained by Qureshi et al. [143] in a wind tunnel using a wide variety of particle sizes and densities. The question of whether this model can be applied or adapted to wall-bounded turbulence remains currently unanswered.

A Single-point statistics at $Re_\tau = 1440$

A.1 Velocity and acceleration statistics

In figs. A.1 and A.2, single-point single-time velocity and acceleration statistics at $Re_\tau = 1440$ obtained both from Eulerian fields and from Lagrangian particle data are compared.

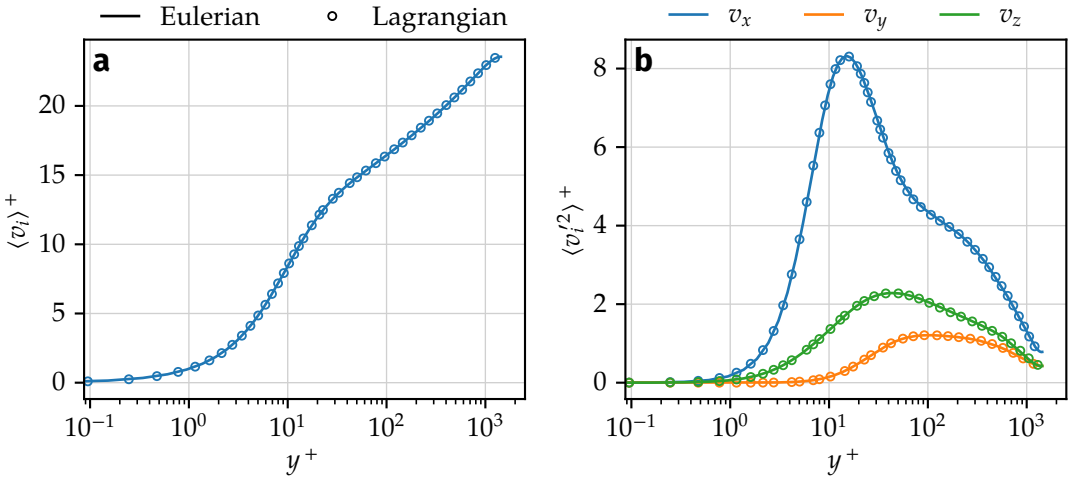

Figure A.1. (a) Velocity mean and (b) variance profiles obtained from Eulerian fields and from Lagrangian particle data at $Re_\tau = 1440$.

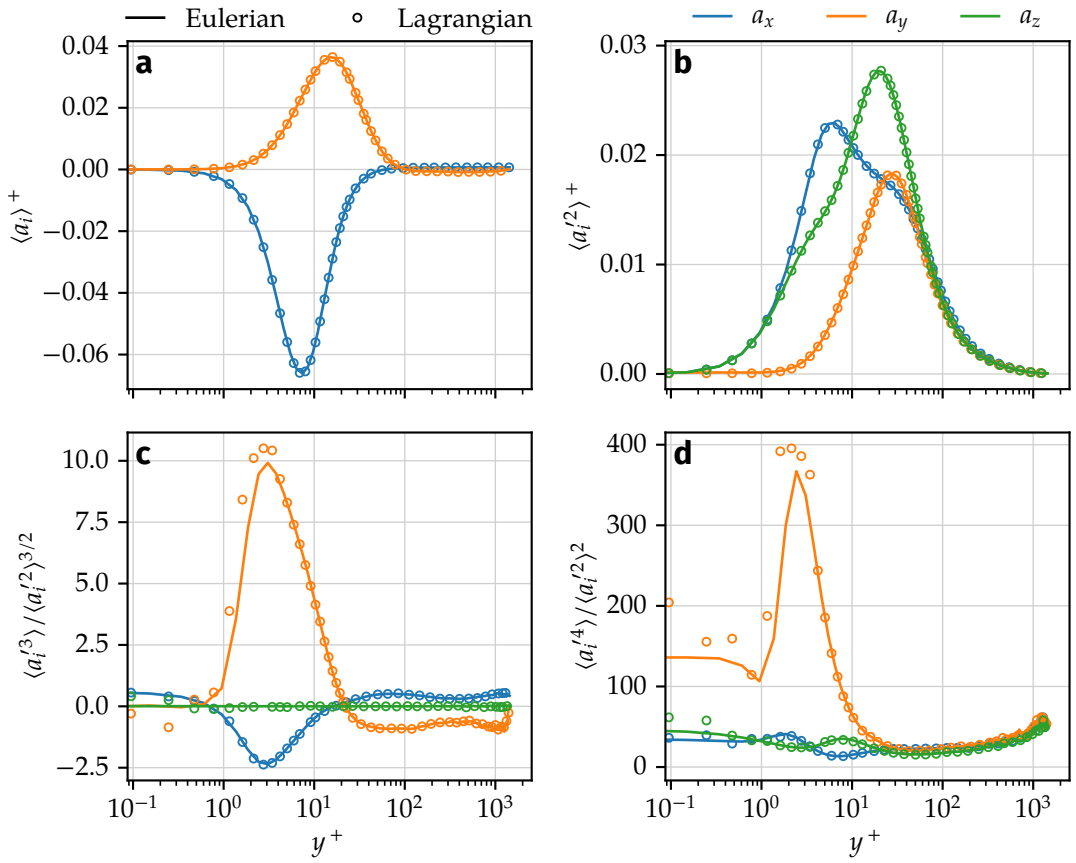

Figure A.2. (a) Acceleration mean, (b) variance, (c) skewness and (d) flatness profiles obtained from Eulerian fields and from Lagrangian particle data at $Re_\tau = 1440$.

A.2 Dissipation and turbulent scales

Figure A.3a shows the turbulent and total mean kinetic energy dissipation rates across the channel width at $Re_\tau = 1440$, respectively defined as

$$\varepsilon(y) = \nu \overline{\frac{\partial u_i'}{\partial x_j} \frac{\partial u_i'}{\partial x_j}} \quad \text{and} \quad \varepsilon_T(y) = \nu \overline{\frac{\partial u_i}{\partial x_j} \frac{\partial u_i}{\partial x_j}}. \tag{A.1}$$

The above definition of ε, used throughout this document, is actually referred to as the *pseudo-dissipation* by Pope [137]. The real turbulent kinetic energy dissipation rate is given by

$$\varepsilon_R = 2\nu \overline{s_{ij}' s_{ij}'} = \varepsilon + \nu \frac{\partial^2 \overline{u_i' u_j'}}{\partial x_i \partial x_j}, \tag{A.2}$$

where $s_{ij}' = (\partial_j u_i' + \partial_i u_j')/2$ is the fluctuating rate of strain [137, p. 124]. In channel flow, the above expression simplifies to

$$\varepsilon_R(y) = \varepsilon(y) + \nu \frac{\mathrm{d}^2 \overline{u_y'^2}}{\mathrm{d}y^2}. \tag{A.3}$$

We have verified in our $Re_\tau = 1440$ simulations that ε and the real kinetic dissipation ε_R are virtually equivalent, with a maximum relative difference of about 0.1 %.

Also shown in fig. A.3a are the Kolmogorov length and time scales

$$\eta(y) = \left(\frac{\nu^3}{\varepsilon}\right)^{1/4} \quad \text{and} \quad \tau_\eta(y) = \sqrt{\frac{\nu}{\varepsilon}}. \tag{A.4}$$

Figure A.3b plots the Taylor-scale Reynolds number across the channel width, estimated as

$$Re_\lambda(y) = k \left(\frac{20}{3\nu\varepsilon}\right)^{1/2}, \tag{A.5}$$

where $k = \overline{u_i' u_i'}/2$ is the turbulent kinetic energy.

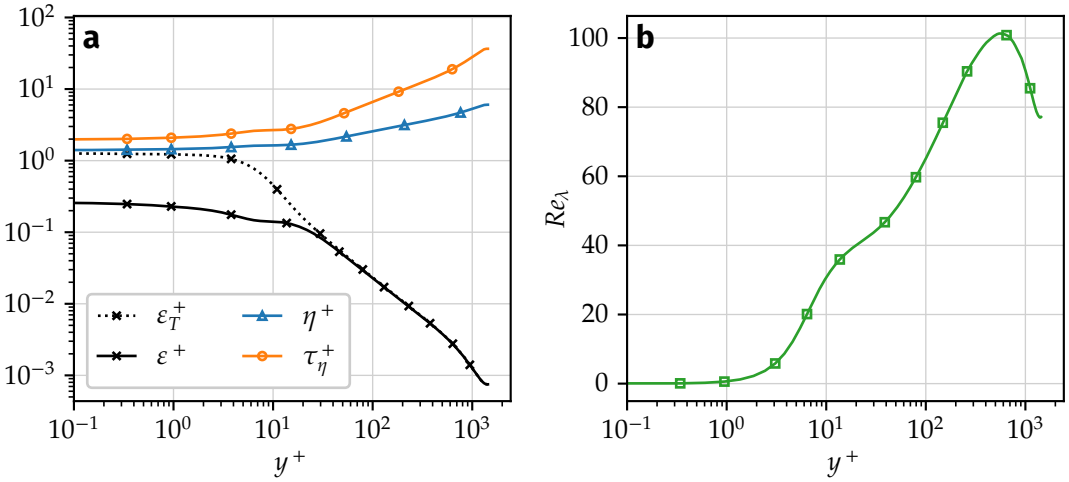

Figure A.3. (a) Mean turbulent kinetic energy dissipation rate (ε), total mean kinetic energy dissipation rate (ε_T), and Kolmogorov length and time scales (η and τ_η) across the channel width for $Re_\tau = 1440$. Quantities are non-dimensionalised in wall units. (b) Taylor-scale Reynolds number across the channel width.

B Mean Lagrangian dynamics of kinetic energy

In this appendix, the average rate of change of total and turbulent kinetic energy along tracer paths in turbulent channel flows is described in terms of kinetic energy budgets and of related quantities including the Lagrangian power $\overline{\boldsymbol{u}\cdot\boldsymbol{a}}$ and the velocity-acceleration covariance $\overline{\boldsymbol{u}'\cdot\boldsymbol{a}'}$.

Appendix B.1 presents the budgets of total kinetic energy $E = |\boldsymbol{u}|^2/2$, whose average rate of change along Lagrangian paths is given by the mean Lagrangian power $\overline{\Pi} = \overline{\mathrm{D}E/\mathrm{D}t} = \overline{\boldsymbol{u}\cdot\boldsymbol{a}}$. Then, appendix B.2 relates the average rate of change of turbulent kinetic energy $k = |\boldsymbol{u}'|^2/2$ along Lagrangian paths to the velocity-acceleration covariance $\overline{\boldsymbol{u}'\cdot\boldsymbol{a}'}$. An expression for the latter is obtained based on the TKE budget across the channel.

B.1 Total kinetic energy budget

An evolution equation for the total kinetic energy per unit mass $E(\boldsymbol{x},t) = |\boldsymbol{u}|^2/2$ can be derived from the momentum equation (1.2b) (see e.g. [137, p. 123]),

$$\frac{\mathrm{D}E}{\mathrm{D}t} = -\frac{1}{\rho}\boldsymbol{u}\cdot\boldsymbol{\nabla}p + \nu\boldsymbol{u}\cdot\nabla^2\boldsymbol{u} + \boldsymbol{u}\cdot\boldsymbol{f} \tag{B.1}$$

$$= -\frac{1}{\rho}\boldsymbol{\nabla}\cdot(p\boldsymbol{u}) + \nu\nabla^2 E - \nu\frac{\partial u_i}{\partial x_j}\frac{\partial u_i}{\partial x_j} + \boldsymbol{u}\cdot\boldsymbol{f}. \tag{B.2}$$

In channel flow, the driving force is the mean pressure gradient $\boldsymbol{f} = -\boldsymbol{\nabla}p_0/\rho = G_p\delta_{ix}/\rho$, while the fluctuating pressure p is periodic in the streamwise and spanwise directions. Equation (B.2) can be averaged in those directions and time to yield an expression for the average variation of kinetic energy along tracer paths (the *mean Lagrangian power*) as a function of wall distance,

$$\overline{\frac{\mathrm{D}E}{\mathrm{D}t}}(y) = \Pi_{\mathrm{in}}(y) - \varepsilon_T(y) + T(y), \tag{B.3}$$

where the input power Π_{in} corresponds to the average work done by the driving force per unit time,

$$\Pi_{\mathrm{in}}(y) = \overline{\boldsymbol{u}\cdot\boldsymbol{f}} = \frac{G_p}{\rho}\overline{u_x}(y), \tag{B.4}$$

and $T(y) = \nu\,\mathrm{d}^2\overline{E}(y)\big/\mathrm{d}y^2$ represents mean kinetic energy diffusion by viscous effects. The pressure term in eq. (B.2) vanishes when the kinetic energy equation is integrated along the periodic directions, as can be shown by application of the divergence theorem

combined with the periodicity of $p\boldsymbol{u}$.

Equation (B.3) can be averaged in y to obtain the global mean energy budget in the channel,

$$\frac{1}{2h}\int_0^{2h}\overline{\frac{\mathrm{D}E}{\mathrm{D}t}}(y)\,\mathrm{d}y = \frac{1}{2h}\int_0^{2h}\left[\Pi_{\mathrm{in}}(y)-\varepsilon_T(y)\right]\mathrm{d}y + \frac{\nu}{2h}\left[\frac{\mathrm{d}\overline{E}}{\mathrm{d}y}(2h)-\frac{\mathrm{d}\overline{E}}{\mathrm{d}y}(0)\right]. \tag{B.5}$$

The left-hand side term is zero due to statistical stationarity (the global kinetic energy content is conserved over time). The rightmost term also vanishes since wall-normal energy gradients are zero at the walls.[1] The resulting equation is a balance between the globally averaged energy production and dissipation,

$$\frac{1}{2h}\int_0^{2h}\Pi_{\mathrm{in}}(y)\,\mathrm{d}y = \frac{1}{2h}\int_0^{2h}\varepsilon_T(y)\,\mathrm{d}y\,. \tag{B.6}$$

To summarise, the mean kinetic energy dissipation rate ε_T must exactly compensate the mean input power Π_{in} when globally averaged in the channel. The diffusion term $T(y)$ in eq. (B.3) redistributes kinetic energy along the wall-normal direction, and it does not contribute to the global energy balance.

Finally, it is worth noting that the rate of change of kinetic energy can be written in terms of the fluid velocity and acceleration,

$$\frac{\mathrm{D}E}{\mathrm{D}t} = \frac{\mathrm{D}\boldsymbol{u}^2}{\mathrm{D}t} = \boldsymbol{u}\cdot\frac{\mathrm{D}\boldsymbol{u}}{\mathrm{D}t} = \boldsymbol{u}\cdot\boldsymbol{a}. \tag{B.7}$$

In other words, the kinetic energy of a fluid particle changes over time as the product $\boldsymbol{v}\cdot\boldsymbol{a}$, where $\boldsymbol{v}$ and $\boldsymbol{a}$ are the particle velocity and acceleration.

The mean kinetic energy budget (B.3) is evaluated in fig. B.1a. The diffusion term T mainly redistributes energy from the buffer layer to the viscous subregion, where energy is strongly dissipated by viscous shear. The sum of the terms in eq. (B.3) is shown to match the mean rate of change of kinetic energy $\overline{\mathrm{D}E/\mathrm{D}t} = \overline{\boldsymbol{u}\cdot\boldsymbol{a}}$, thus validating the expression obtained for the energy budget.

The same curves are shown in fig. B.1b premultiplied by wall distance, so that the area under the curves effectively represent integrated quantities in the chosen semi-log representation. From the premultiplied curves, it is clearly seen that most of the energy production happens far from the wall, where the mean streamwise velocity is more intense. Energy dissipation peaks at $y^+ \approx 7$, although dissipation occurs everywhere in the channel. Globally, it is found that production and dissipation rates compensate each other (the corresponding filled areas have the same surface), and thus the global balance (B.6) is verified. Near the channel centre, the imbalance between production and dissipation leads to positive values of the mean Lagrangian power $\overline{\boldsymbol{u}\cdot\boldsymbol{a}}$, meaning that on average, fluid particles in that region gain energy over time. The opposite is true in the buffer layer (i.e. $\overline{\boldsymbol{u}\cdot\boldsymbol{a}} < 0$), which is explained both by a negligible energy

[1] To prove this, one can consider the wall-normal derivative of the instantaneous energy, $\partial_y E(\boldsymbol{x},t) = \partial_y(u_i u_i)/2 = u_i\partial_y u_i$. At the walls, $u_i = 0$ and therefore $\partial_y E = 0$.

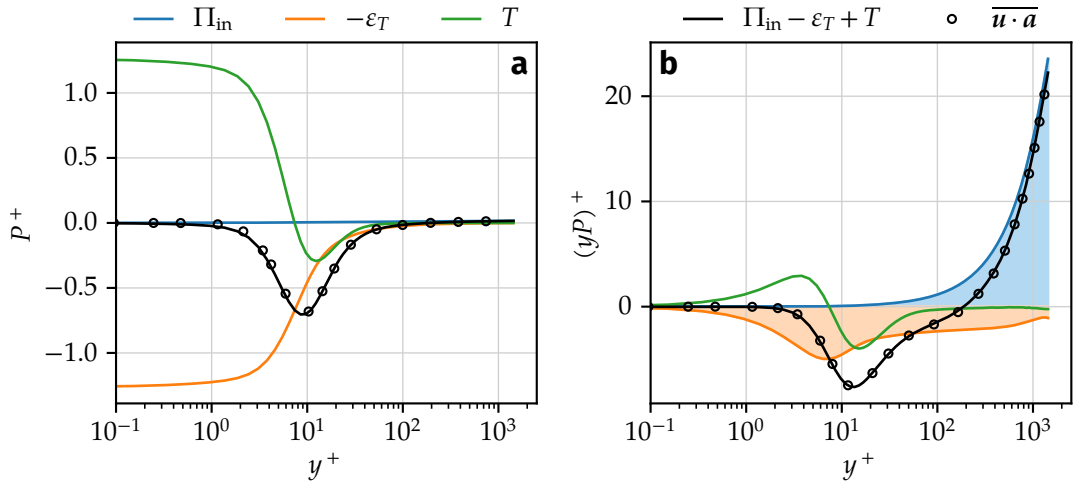

Figure B.1. Mean kinetic energy budget in the channel for $Re_\tau = 1440$. (a) Terms of the mean kinetic energy budget (B.3) (coloured lines) and their sum (black line). Black circles represent the mean Lagrangian power $\overline{\boldsymbol{u} \cdot \boldsymbol{a}}$. Quantities are non-dimensionalised in wall units. (b) Same curves premultiplied by y^+, so that the area under the curves equals integrated quantities. Filled areas represent the integrated production and dissipation terms appearing in the global kinetic energy budget (B.6).

production rate Π_{in}, and by the average redistribution of energy towards the viscous subregion by the diffusion term T.

B.2 Lagrangian dynamics of the turbulent kinetic energy

B.2.1 Decomposition of $\overline{\mathrm{D}k/\mathrm{D}t}$

As discussed in section 4.4 and in appendix B.1, the product $\boldsymbol{v} \cdot \boldsymbol{a}$ describes the instantaneous rate of change of the total kinetic energy of a fluid particle with velocity $\boldsymbol{v}$ and acceleration $\boldsymbol{a}$. Hence, the mean Lagrangian power $\Pi(y) = \overline{\boldsymbol{u} \cdot \boldsymbol{a}}(y)$ indicates whether fluid particles located at a wall distance y either gain or lose kinetic energy on average. Analogously, the velocity-acceleration covariance $\overline{\boldsymbol{u}' \cdot \boldsymbol{a}'}$ (also discussed in section 4.4) can be linked to the mean temporal variation of the instantaneous TKE $k = |\boldsymbol{u}'|^2/2$ of a tracer particle, although the connection is not as straightforward as that between $\overline{\boldsymbol{u} \cdot \boldsymbol{a}}$ and the total kinetic energy in anisotropic flows.

To construct a relation between the covariance $\overline{\boldsymbol{u}' \cdot \boldsymbol{a}'}$ and the TKE, we start by writing

the fluctuating acceleration a_i' according to

$$a_i' = a_i - \overline{a_i} \tag{B.8}$$
$$= \frac{\mathrm{D}u_i}{\mathrm{D}t} - \overline{\frac{\mathrm{D}u_i}{\mathrm{D}t}} \tag{B.9}$$
$$= \frac{\partial}{\partial t}(u_i - \overline{u_i}) + \frac{\partial}{\partial x_j}\left(u_i u_j - \overline{u_i u_j}\right) \tag{B.10}$$
$$= \frac{\partial u_i'}{\partial t} + \frac{\partial}{\partial x_j}\left(u_i' u_j + \overline{u_i} u_j' - \overline{u_i' u_j'}\right), \tag{B.11}$$

where we have used the incompressibility condition $\partial_j u_j = 0$. This result can be used to express the rate of change of the fluctuating velocity along tracer paths in terms of a_i',

$$\frac{\mathrm{D}u_i'}{\mathrm{D}t} = \frac{\partial u_i'}{\partial t} + \frac{\partial}{\partial x_j}\left(u_i' u_j\right) \tag{B.12}$$
$$= a_i' + \frac{\partial}{\partial x_j}\left(\overline{u_i' u_j'} - \overline{u_i} u_j'\right). \tag{B.13}$$

Noting that the rate of change of the TKE along tracer paths is $\mathrm{D}k/\mathrm{D}t = u_i' \,\mathrm{D}u_i'/\mathrm{D}t$, from eq. (B.13) one can write

$$\frac{\mathrm{D}k}{\mathrm{D}t} = u_i' a_i' + u_i' \frac{\partial}{\partial x_j}\left(\overline{u_i' u_j'} - \overline{u_i} u_j'\right) \tag{B.14}$$
$$= u_i' a_i' + \frac{\partial}{\partial x_j}\left(u_i' \overline{u_i' u_j'}\right) - \overline{u_i' u_j'} \frac{\partial u_i'}{\partial x_j} - u_i' u_j' \frac{\partial \overline{u_i}}{\partial x_j}, \tag{B.15}$$

where the incompressibility condition $\partial_j u_j' = 0$ has been applied.

Finally, eq. (B.15) can be ensemble-averaged to obtain the mean Lagrangian rate of change of TKE,

$$\overline{\frac{\mathrm{D}k}{\mathrm{D}t}} = \overline{u_i' a_i'} - \overline{u_i' u_j'} \frac{\partial \overline{u_i}}{\partial x_j} = \overline{u_i' a_i'} + \mathcal{P}. \tag{B.16}$$

Hence, the variations of TKE along fluid particle paths are determined by contributions from the velocity-acceleration covariance $\overline{\boldsymbol{u}' \cdot \boldsymbol{a}'}$ and from the turbulent kinetic energy production term $\mathcal{P} = -\overline{u_i' u_j'} \partial_j \overline{u_i}$, which is typically positive and transfers kinetic energy from the mean flow to the velocity fluctuations [137, p. 125].

In turbulent channel flow, the mean velocity gradient is given by the mean shear $\partial_j \overline{u_i} = \mathrm{d}U/\mathrm{d}y \, \delta_{ix}\delta_{jy}$, where $U(y)$ is the mean streamwise velocity. Therefore, the production term is $\mathcal{P} = -\overline{u_x' u_y'} \,\mathrm{d}U/\mathrm{d}y$, and eq. (B.16) writes

$$\overline{\frac{\mathrm{D}k}{\mathrm{D}t}} = \overline{u_i' a_i'} - \overline{u_x' u_y'} \frac{\mathrm{d}U}{\mathrm{d}y}. \tag{B.17}$$

As we shall see below, the production term is associated to the TKE gained or lost by a fluid particle when it moves in the direction perpendicular to the mean shear, i.e. away from or towards the wall. Meanwhile, the velocity-acceleration covariance expresses that a fluid particle gains (or loses) TKE when it accelerates in the same (or opposite) direction as its fluctuating velocity v' relative to the local mean flow. A negative value of $\overline{u_i' a_i'}$ would then indicate that the acceleration tends to act opposite to the fluctuating velocity, thus suppressing turbulent fluctuations. As shown below (fig. B.2), this is found to be the case in the whole channel.

To better understand the decomposition (B.17), one can consider a fluid particle moving between two infinitesimally close instants t and $t + \delta t$ with a wall-normal velocity v_y. The streamwise velocity of the particle at the two instants is then

$$v_x(t) = U(y(t)) + v_x'(t), \tag{B.18}$$
$$v_x(t + \delta t) = U(y(t + \delta t)) + v_x'(t + \delta t), \tag{B.19}$$

where $y(t)$ is the instantaneous particle wall-normal position, and v_x' is the fluctuating streamwise velocity at the particle position. During an infinitesimal time δt, the particle moves by $\delta y = v_y(t)\delta t$ in the wall-normal direction, and thus $U(y(t + \delta t)) = U(y + v_y(t)\delta t) = U(y) + v_y(t)\delta t \frac{\mathrm{d}U(y)}{\mathrm{d}y}$. Hence, by subtracting eqs. (B.18) and (B.19) and rearranging terms, one finds

$$\delta v_x' = \delta v_x - v_y \delta t \frac{\mathrm{d}U}{\mathrm{d}y}, \tag{B.20}$$

where $\delta v_x = v_x(t + \delta t) - v_x(t)$ and similarly for $\delta v_x'$. Finally, one can multiply by $v_x'/\delta t$ and replace $\delta/\delta t$ by the Lagrangian derivative $\mathrm{D}/\mathrm{D}t$ to find

$$v_x' \frac{\mathrm{D}v_x'}{\mathrm{D}t} = v_x' a_x - v_x' v_y \frac{\mathrm{d}U}{\mathrm{d}y}, \tag{B.21}$$

where we have additionally applied the definition of the acceleration $a_x = \mathrm{D}v_x/\mathrm{D}t$. The left-hand side of eq. (B.21) is nothing else than the variation of the streamwise velocity contribution to the particle TKE. The first term on the right-hand side is the contribution to the TKE by the variation of the total particle streamwise velocity over time (i.e. its streamwise acceleration). The second term is the variation of TKE when the particle moves in the cross-stream direction, in which case the local mean velocity U changes and hence there is an exchange between the particle fluctuating kinetic energy and its mean kinetic energy. For instance, assuming that its total velocity v_x stays constant, a tracer having a velocity deficit relative to the mean flow ($v_x' < 0$) gains kinetic energy when it moves to a region of faster mean velocity, since its velocity deficit increases and so does $v_x'^2$. In wall-bounded turbulence, this is precisely the mechanism behind ejections of 'pockets' of slow fluid away from the wall (section 1.2.4). This mechanism is at the core of the TKE production by the mean flow, which is on average represented by the production term $\mathcal{P}$. Finally, the streamwise contribution to eq. (B.17)

can be recovered by ensemble-averaging eq. (B.21) at a fixed wall distance. This is readily verified noting that $v_y = v'_y$ and $\overline{v'_x a_x} = \overline{v'_x a'_x}$ (since $\overline{v'_x \overline{a_x}} = 0$).

B.2.2 Turbulent kinetic energy budget

It is interesting to contrast eq. (B.17) with the turbulent kinetic energy budget that can be derived from the Navier–Stokes equations [see e.g. 100, 137],

$$\frac{\bar{\mathrm{D}}\overline{k}}{\bar{\mathrm{D}}t}(y) = 0 = \mathscr{P} - \varepsilon + \nu\frac{\mathrm{d}^2\overline{k}}{\mathrm{d}y^2} - \frac{\mathrm{d}}{\mathrm{d}y}\overline{u'_y k} - \frac{1}{\rho}\frac{\mathrm{d}}{\mathrm{d}y}\overline{u'_y p'}, \tag{B.22}$$

where $\bar{\mathrm{D}}Q/\bar{\mathrm{D}}t = \partial_t Q + \overline{u_j}\partial_j Q$ represents the rate of change of a quantity Q along the path of an 'average' tracer moving with the mean flow velocity. The terms on the right-hand side of eq. (B.22) respectively represent TKE production, TKE dissipation, viscous diffusion, turbulent transport, and pressure transport. It is readily shown that

$$\overline{\frac{\mathrm{D}k}{\mathrm{D}t}} = \frac{\bar{\mathrm{D}}\overline{k}}{\bar{\mathrm{D}}t} + \frac{\partial}{\partial x_j}\overline{u'_j k} = \frac{\bar{\mathrm{D}}\overline{k}}{\bar{\mathrm{D}}t} + \frac{\mathrm{d}}{\mathrm{d}y}\overline{u'_y k}. \tag{B.23}$$

Hence, the mean variation of TKE along tracer paths is given by

$$\overline{\frac{\mathrm{D}k}{\mathrm{D}t}} = \mathscr{P} - \varepsilon + \nu\frac{\mathrm{d}^2\overline{k}}{\mathrm{d}y^2} - \frac{1}{\rho}\frac{\mathrm{d}}{\mathrm{d}y}\overline{u'_y p'}. \tag{B.24}$$

It follows from eqs. (B.17) and (B.24) that the velocity-acceleration covariance can be written as

$$\overline{u'_i a'_i} = -\varepsilon + \nu\frac{\mathrm{d}^2\overline{k}}{\mathrm{d}y^2} - \frac{1}{\rho}\frac{\mathrm{d}}{\mathrm{d}y}\overline{u'_y p'}. \tag{B.25}$$

B.2.3 Profiles at $Re_\tau = 1440$

The mean Lagrangian derivative of the TKE along the channel width for $Re_\tau = 1440$ is shown in fig. B.2a, along with the two terms of its decomposition (B.17). The global variation of TKE in the channel, $\int_0^{2h} \overline{\mathrm{D}k/\mathrm{D}t}\,\mathrm{d}y$, has been verified to be zero, consistently with the statistical stationarity of the flow. The mean variation of TKE along fluid particle paths is close to zero in most of the channel, except for the near-wall region up to $y^+ \approx 40$, where turbulent kinetic energy is transferred from the viscous region to the buffer layer. Away from the wall, the two contributions from the velocity-acceleration covariance and from TKE production cancel each other out, meaning that tracers on average do not gain or lose TKE. In the logarithmic region, it is verified that turbulent energy production and dissipation rates are nearly equal (see e.g. [94, 137, p. 281]). This is seen more clearly in fig. B.2b where curves are normalised by ε. Hence, $\overline{u'_i a'_i} \approx -\varepsilon$ results in a mean particle TKE variation that is close to zero in that region. Moreover, under this normalisation, a small negative value of $\overline{\mathrm{D}k/\mathrm{D}t}$ is visible near the channel centre where dissipation reaches its minimum. This is a result of both the Reynolds

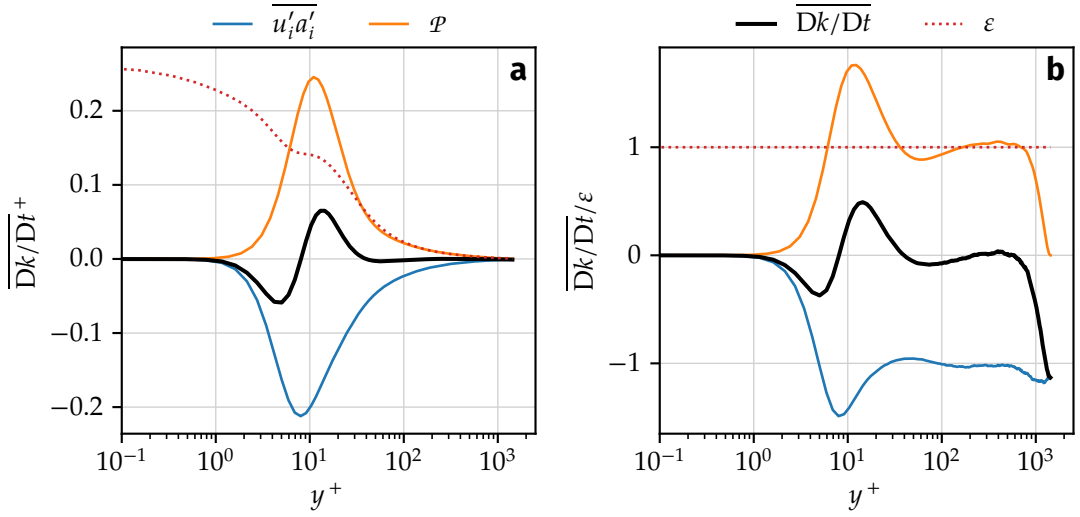

Figure B.2. Mean Lagrangian derivative of the turbulent kinetic energy, $\overline{\mathrm{D}k/\mathrm{D}t}$, across the channel, for $Re_\tau = 1440$. Data is non-dimensionalised (a) in wall-units and (b) by the mean turbulent dissipation rate $\varepsilon(y)$. Also shown is ε (dotted lines), as well as the contributions of the velocity-acceleration covariance $\overline{u_i' a_i'}$ and of the turbulent kinetic energy production $\mathcal{P}$ (eq. (B.17)). The term $\overline{\mathrm{D}k/\mathrm{D}t}$ is computed here using eq. (B.17), and its integral along the channel width is verified to be zero.

stresses and the mean shear dropping to zero at the centre due to flow symmetry, while the $\overline{u_i' a_i'}$ contribution is non-zero in that region, instead keeping a value close to $-\varepsilon$.

Bibliography

[1] H. Abe, H. Kawamura and Y. Matsuo, 'Direct numerical simulation of a fully developed turbulent channel flow with respect to the Reynolds number dependence', J. Fluids Eng **123**, 382–393 (2001) (cit. on pp. 50, 105).

[2] R. J. Adrian, C. D. Meinhart and C. D. Tomkins, 'Vortex organization in the outer region of the turbulent boundary layer', J. Fluid Mech. **422**, 1–54 (2000) (cit. on pp. 24, 27).

[3] R. J. Adrian and J. Westerweel, *Particle Image Velocimetry*, Cambridge Aerospace Series 30 (Cambridge University Press, 2011), 558 pp. (cit. on p. 3).

[4] R. J. Adrian, 'Hairpin vortex organization in wall turbulence', Phys. Fluids **19**, 041301 (2007) (cit. on pp. 24, 25, 27).

[5] K. M. J. Alards, H. Rajaei, L. Del Castello, R. P. J. Kunnen, F. Toschi and H. J. H. Clercx, 'Geometry of tracer trajectories in rotating turbulent flows', Phys. Rev. Fluids **2**, 044601 (2017) (cit. on p. 161).

[6] K. M. J. Alards, H. Rajaei, R. P. J. Kunnen, F. Toschi and H. J. H. Clercx, 'Directional change of tracer trajectories in rotating Rayleigh-Bénard convection', Phys. Rev. E **97**, 063105 (2018) (cit. on p. 161).

[7] R. A. Antonia, T. Zhou and G. P. Romano, 'Second- and third-order longitudinal velocity structure functions in a fully developed turbulent channel flow', Phys. Fluids **9**, 3465 (1998) (cit. on p. 125).

[8] W. J. Baars, N. Hutchins and I. Marusic, 'Reynolds number trend of hierarchies and scale interactions in turbulent boundary layers', Phil. Trans. R. Soc. A **375**, 20160077 (2017) (cit. on p. 21).

[9] S. Balachandar and J. K. Eaton, 'Turbulent dispersed multiphase flow', Annu. Rev. Fluid Mech. **42**, 111–133 (2010) (cit. on p. 33).

[10] B. Balakumar and R. Adrian, 'Large- and very-large-scale motions in channel and boundary-layer flows', Phil. Trans. R. Soc. A **365**, 665–681 (2007) (cit. on p. 27).

[11] A. Barge, 'Propriétés lagrangiennes de l'accélération turbulente des particules fluides et inertielles dans un écoulement avec un cisaillement homogène : DNS et nouveaux modèles de sous-maille de LES', PhD thesis (Lyon, 12th June 2018) (cit. on p. 162).

[12] G. K. Batchelor, 'The application of the similarity theory of turbulence to atmospheric diffusion', Q.J.R. Meteorol. Soc. **76**, 133–146 (1950) (cit. on pp. 116, 117, 124, 129).

[13] G. K. Batchelor, 'Diffusion in a field of homogeneous turbulence: II. The relative motion of particles', Math. Proc. Cambridge Philos. Soc. **48**, 345–362 (1952) (cit. on pp. 116, 118, 143).

[14] J. Bec, L. Biferale, M. Cencini, A. S. Lanotte and F. Toschi, 'Effects of vortex filaments on the velocity of tracers and heavy particles in turbulence', Phys. Fluids **18**, 081702 (2006) (cit. on pp. 11, 13, 14).

[15] L. H. Benedict and R. D. Gould, 'Towards better uncertainty estimates for turbulence statistics', Exp. Fluids **22**, 129–136 (1996) (cit. on p. 74).

[16] R. Benzi, L. Biferale, R. Fisher, D. Q. Lamb and F. Toschi, 'Inertial range Eulerian and Lagrangian statistics from numerical simulations of isotropic turbulence', J. Fluid Mech. **653**, 221–244 (2010) (cit. on p. 10).

[17] R. Benzi, S. Ciliberto, R. Tripiccione, C. Baudet, F. Massaioli and S. Succi, 'Extended self-similarity in turbulent flows', Phys. Rev. E **48**, R29 (1993) (cit. on p. 11).

[18] J. Berg, B. Lüthi, J. Mann and S. Ott, 'Backwards and forwards relative dispersion in turbulent flow: An experimental investigation', Phys. Rev. E **74**, 016304 (2006) (cit. on pp. 118, 120, 123, 148).

[19] J. Berg, S. Ott, J. Mann and B. Lüthi, 'Experimental investigation of Lagrangian structure functions in turbulence', Phys. Rev. E **80**, 026316 (2009) (cit. on p. 11).

[20] P. S. Bernard, M. F. Ashmawey and R. A. Handler, 'An analysis of particle trajectories in computer-simulated turbulent channel flow', Physics of Fluids A: Fluid Dynamics **1**, 1532–1540 (1989) (cit. on p. 29).

[21] J. Bezanson, A. Edelman, S. Karpinski and V. B. Shah, 'Julia: A fresh approach to numerical computing', SIAM Rev. **59**, 65–98 (2017) (cit. on p. 48).

[22] L. Biferale, G. Boffetta, A. Celani, B. J. Devenish, A. Lanotte and F. Toschi, 'Multifractal statistics of Lagrangian velocity and acceleration in turbulence', Phys. Rev. Lett. **93**, 064502 (2004) (cit. on p. 11).

[23] L. Biferale, G. Boffetta, A. Celani, B. J. Devenish, A. Lanotte and F. Toschi, 'Lagrangian statistics of particle pairs in homogeneous isotropic turbulence', Phys. Fluids **17**, 115101 (2005) (cit. on p. 118).

[24] L. Biferale, G. Boffetta, A. Celani, A. Lanotte and F. Toschi, 'Particle trapping in three-dimensional fully developed turbulence', Phys. Fluids **17**, 021701 (2005) (cit. on pp. 11, 13).

[25] R. Bitane, H. Homann and J. Bec, 'Time scales of turbulent relative dispersion', Phys. Rev. E **86**, 045302 (2012) (cit. on pp. 118, 129, 147, 156).

[26] G. Boffetta, F. De Lillo and S. Musacchio, 'Lagrangian statistics and temporal intermittency in a shell model of turbulence', Phys. Rev. E **66**, 066307 (2002) (cit. on p. 10).

[27] G. Boffetta and I. M. Sokolov, 'Relative dispersion in fully developed turbulence: The Richardson's law and intermittency corrections', Phys. Rev. Lett. **88**, 094501 (2002) (cit. on p. 118).

[28] W. J. T. Bos, B. Kadoch and K. Schneider, 'Angular statistics of Lagrangian trajectories in turbulence', Phys. Rev. Lett. **114**, 214502 (2015) (cit. on p. 161).

[29] M. Bourgoin, 'Turbulent pair dispersion as a ballistic cascade phenomenology', J. Fluid Mech. **772**, 678–704 (2015) (cit. on pp. 115, 147, 148, 150, 153, 156).

[30] M. Bourgoin, N. T. Ouellette, H. Xu, J. Berg and E. Bodenschatz, 'The role of pair dispersion in turbulent flow', Science **311**, 835–838 (2006) (cit. on pp. 117, 147, 156).

[31] J. P. Boyd, *Chebyshev and Fourier Spectral Methods*, Second Edition (Dover Publications, Mineola, N.Y, 3rd Dec. 2001), 688 pp. (cit. on pp. 36, 38, 44).

[32] A. D. Bragg, P. J. Ireland and L. R. Collins, 'Forward and backward in time dispersion of fluid and inertial particles in isotropic turbulence', Phys. Fluids **28**, 013305 (2016) (cit. on pp. 118, 123, 141, 148).

[33] W. Braun, F. De Lillo and B. Eckhardt, 'Geometry of particle paths in turbulent flows', J. Turbul. **7**, N62 (2006) (cit. on p. 161).

[34] D. Buaria, B. L. Sawford and P. K. Yeung, 'Characteristics of backward and forward two-particle relative dispersion in turbulence at different Reynolds numbers', Phys. Fluids **27**, 105101 (2015) (cit. on pp. 118, 120).

[35] M. Buffat, L. Le Penven and A. Cadiou, 'An efficient spectral method based on an orthogonal decomposition of the velocity for transition analysis in wall bounded flow', Comput. Fluids **42**, 62–72 (2011) (cit. on pp. 35, 39, 42–44).

[36] E. Calzavarini, R. Volk, M. Bourgoin, E. Lévêque, J.-F. Pinton and F. Toschi, 'Acceleration statistics of finite-sized particles in turbulent flow: the role of Faxén forces', J. Fluid Mech. **630**, 179–189 (2009) (cit. on p. 162).

[37] C. Canuto, M. Y. Hussaini, A. Quarteroni and T. A. Zang, *Spectral Methods in Fluid Dynamics* (Springer Berlin Heidelberg, Berlin, Heidelberg, 1988) (cit. on pp. 36, 37, 39).

[38] D. R. Carlson, S. E. Widnall and M. F. Peeters, 'A flow-visualization study of transition in plane Poiseuille flow', J. Fluid Mech. **121**, 487–505 (1982) (cit. on p. 19).

[39] A. Celani, M. Cencini, M. Vergassola, E. Villermaux and D. Vincenzi, 'Shear effects on passive scalar spectra', J. Fluid Mech. **523**, 99–108 (2005) (cit. on p. 119).

[40] L. Chen, S. W. Coleman, J. C. Vassilicos and Z. Hu, 'Acceleration in turbulent channel flow', J. Turbul. **11**, N41 (2010) (cit. on p. 46).

[41] J.-I. Choi, K. Yeo and C. Lee, 'Lagrangian statistics in turbulent channel flow', Phys. Fluids **16**, 779–793 (2004) (cit. on pp. 29, 30, 58, 62, 66, 79, 80, 95).

[42] Y. Choi, Y. Park and C. Lee, 'Helicity and geometric nature of particle trajectories in homogeneous isotropic turbulence', Int. J. Heat Fluid Flow **31**, 482–487 (2010) (cit. on p. 161).

[43] J. W. Cooley and J. W. Tukey, 'An algorithm for the machine calculation of complex Fourier series', Math. Comp. **19**, 297–301 (1965) (cit. on p. 38).

[44] S. Corrsin, 'Progress Report on Some Turbulent Diffusion Research', in *Advances in Geophysics*, Vol. 6, edited by H. E. Landsberg and J. Van Mieghem (Elsevier, 1st Jan. 1959), pp. 161–164 (cit. on pp. 15, 118).

[45] P. A. Davidson and P.-Å. Krogstad, 'A universal scaling for low-order structure functions in the log-law region of smooth- and rough-wall boundary layers', J. Fluid Mech. **752**, 140–156 (2014) (cit. on p. 125).

[46] R. B. Dean, 'Reynolds number dependence of skin friction and other bulk flow variables in two-dimensional rectangular duct flow', J. Fluids Eng. **100**, 215–223 (1978) (cit. on pp. 20, 72).

[47] J. W. Deardorff and R. L. Peskin, 'Lagrangian statistics from numerically integrated turbulent shear flow', Phys. Fluids **13**, 584–595 (1970) (cit. on pp. 28, 31).

[48] B. Efron and R. J. Tibshirani, *An Introduction to the Bootstrap* (Springer US, Boston, MA, 1993) (cit. on p. 74).

[49] V. Eswaran and S. B. Pope, 'An examination of forcing in direct numerical simulations of turbulence', Comput. Fluids **16**, 257–278 (1988) (cit. on p. 14).

[50] T. Faber and J. C. Vassilicos, 'Turbulent pair separation due to multiscale stagnation point structure and its time asymmetry in two-dimensional turbulence', Phys. Fluids **21**, 015106 (2009) (cit. on p. 147).

[51] G. Falkovich, K. Gawędzki and M. Vergassola, 'Particles and fields in fluid turbulence', Rev. Mod. Phys. **73**, 913 (2001) (cit. on pp. 101, 124).

[52] G. Falkovich, H. Xu, A. Pumir, E. Bodenschatz, L. Biferale, G. Boffetta, A. S. Lanotte and F. Toschi, 'On Lagrangian single-particle statistics', Phys. Fluids **24**, 055102 (2012) (cit. on p. 101).

[53] B. A. Finlayson, *The Method of Weighted Residuals and Variational Principles* (Society for Industrial and Applied Mathematics, Philadelphia, PA, 18th Dec. 2013) (cit. on p. 36).

[54] M. Frigo and S. G. Johnson, 'The design and implementation of FFTW3', Proc. IEEE **93**, 216–231 (2005) (cit. on p. 46).

[55] U. Frisch, *Turbulence: The Legacy of A.N. Kolmogorov*, 1st ed. (Cambridge University Press, 30th Nov. 1995) (cit. on pp. 9, 11, 84, 117, 124, 129).

[56] N. Furuichi, Y. Terao, Y. Wada and Y. Tsuji, 'Further experiments for mean velocity profile of pipe flow at high Reynolds number', Phys. Fluids **30**, 055101 (2018) (cit. on p. 20).

[57] M. Gad-el-Hak and P. R. Bandyopadhyay, 'Reynolds number effects in wall-bounded turbulent flows', Appl. Mech. Rev **47**, 307–365 (1994) (cit. on p. 21).

[58] S. Gerashchenko, N. S. Sharp, S. Neuscamman and Z. Warhaft, 'Lagrangian measurements of inertial particle accelerations in a turbulent boundary layer', J. Fluid Mech. **617**, 255–281 (2008) (cit. on p. 32).

[59] F. S. Godeferd and L. Lollini, 'Direct numerical simulations of turbulence with confinement and rotation', J. Fluid Mech. **393**, 257–308 (1999) (cit. on p. 39).

[60] M. Gorokhovski and R. Zamansky, 'Lagrangian simulation of large and small inertial particles in a high Reynolds number flow: Stochastic simulation of subgrid turbulence/particle interactions', in Proceedings of the Summer Program, Center for Turbulence Research, Stanford University (2014), pp. 37–46 (cit. on p. 162).

[61] M. Guala, S. E. Hommema and R. J. Adrian, 'Large-scale and very-large-scale motions in turbulent pipe flow', J. Fluid Mech. **554**, 521–542 (2006) (cit. on p. 27).

[62] S. Herpin, M. Stanislas, J. M. Foucaut and S. Coudert, 'Influence of the Reynolds number on the vortical structures in the logarithmic region of turbulent boundary layers', J. Fluid Mech. **716**, 5–50 (2013) (cit. on p. 26).

[63] R. J. Hill, 'Opportunities for use of exact statistical equations', J. Turbul. **7**, N43 (2006) (cit. on pp. 124, 134, 156).

[64] R. J. Hill and S. T. Thoroddsen, 'Experimental evaluation of acceleration correlations for locally isotropic turbulence', Phys. Rev. E **55**, 1600–1606 (1997) (cit. on pp. 30, 45).

[65] H. Homann and J. Bec, 'Finite-size effects in the dynamics of neutrally buoyant particles in turbulent flow', J. Fluid Mech. **651**, 81–91 (2010) (cit. on p. 162).

[66] H. Homann and F. Laenen, 'SoAx: A generic C++ Structure of Arrays for handling particles in HPC codes', Comput. Phys. Commun. **224**, 325–332 (2018) (cit. on p. 67).

[67] S. Hoyas and J. Jiménez, 'Scaling of the velocity fluctuations in turbulent channels up to $Re_\tau = 2003$', Phys. Fluids **18**, 011702 (2006) (cit. on pp. 53, 54, 70).

[68] S. Hoyas and J. Jiménez, 'Reynolds number effects on the Reynolds-stress budgets in turbulent channels', Phys. Fluids **20**, 101511 (2008) (cit. on p. 105).

[69] Z. Hu, C. L. Morfey and N. D. Sandham, 'Wall pressure and shear stress spectra from direct simulations of channel flow', AIAA J. **44**, 1541–1549 (2006) (cit. on pp. 53, 54, 57, 70).

[70] P. D. Huck, N. Machicoane and R. Volk, 'Production and dissipation of turbulent fluctuations close to a stagnation point', Phys. Rev. Fluids **2**, 084601 (2017) (cit. on pp. 105, 106).

[71] P. D. Huck, 'Particle dynamics in turbulence: from the role of inhomogeneity and anisotropy to collective effects', PhD thesis (ENS de Lyon, Université de Lyon, 6th Dec. 2017) (cit. on pp. 95, 105).

[72] M. Hultmark, M. Vallikivi, S. C. C. Bailey and A. J. Smits, 'Turbulent pipe flow at extreme Reynolds numbers', Phys. Rev. Lett. **108**, 094501 (2012) (cit. on p. 20).

[73] J. C. R. Hunt, A. A. Wray and P. Moin, 'Eddies, streams, and convergence zones in turbulent flows', in Proceedings of the Summer Program 1988, Center for Turbulence Research, Stanford University (1st Dec. 1988) (cit. on p. 26).

[74] N. Hutchins, K. Chauhan, I. Marusic, J. Monty and J. Klewicki, 'Towards reconciling the large-scale structure of turbulent boundary layers in the atmosphere and laboratory', Bound.-Layer Meteorol. **145**, 273–306 (2012) (cit. on p. 21).

[75] T. Ishihara and Y. Kaneda, 'Relative diffusion of a pair of fluid particles in the inertial subrange of turbulence', Phys. Fluids **14**, L69 (2002) (cit. on p. 118).

[76] J. Jiménez, 'Cascades in wall-bounded turbulence', Annu. Rev. Fluid Mech. **44**, 27–45 (2012) (cit. on p. 21).

[77] J. Jiménez, 'Coherent structures in wall-bounded turbulence', J. Fluid Mech. **842**, P1 (2018) (cit. on pp. 16, 23).

[78] J. Jiménez and A. A. Wray, 'On the characteristics of vortex filaments in isotropic turbulence', J. Fluid Mech. **373**, 255–285 (1998) (cit. on p. 26).

[79] J. Jucha, H. Xu, A. Pumir and E. Bodenschatz, 'Time-reversal-symmetry breaking in turbulence', Phys. Rev. Lett. **113**, 054501 (2014) (cit. on pp. 95, 115, 118, 123, 125, 134, 135, 139, 141, 156).

[80] J. Kim, 'Progress in pipe and channel flow turbulence, 1961–2011', J. Turbul. **13**, N45 (2012) (cit. on p. 21).

[81] J. Kim, P. Moin and R. Moser, 'Turbulence statistics in fully developed channel flow at low Reynolds number', J. Fluid Mech. **177**, 133–166 (1987) (cit. on pp. 29, 50).

[82] S. J. Kline, W. C. Reynolds, F. A. Schraub and P. W. Runstadler, 'The structure of turbulent boundary layers', J. Fluid Mech. **30**, 741 (1967) (cit. on p. 24).

[83] A. N. Kolmogorov, 'The local structure of turbulence in incompressible viscous fluid for very large Reynolds numbers', Dokl. Akad. Nauk SSSR **30**, 301–305 (1941) (cit. on pp. 8, 84, 87, 116).

[84] A. N. Kolmogorov, 'Dissipation of energy in locally isotropic turbulence', Dokl. Akad. Nauk SSSR **32**, 16–18 (1941) (cit. on p. 11).

[85] K. Kontomaris, T. J. Hanratty and J. B. McLaughlin, 'An algorithm for tracking fluid particles in a spectral simulation of turbulent channel flow', J. Comput. Phys. **103**, 231–242 (1992) (cit. on pp. 29, 30).

[86] Q. Koziol and D. Robinson, *HDF5*, [Computer Software], Mar. 2018 (cit. on p. 48).

[87] J. G. M. Kuerten, 'Point-particle DNS and LES of particle-laden turbulent flow - a state-of-the-art review', Flow Turbul. Combust., 1–25 (2016) (cit. on p. 161).

[88] J. G. M. Kuerten and J. J. H. Brouwers, 'Lagrangian statistics of turbulent channel flow at $Re_\tau = 950$ calculated with direct numerical simulation and Langevin models', Phys. Fluids **25**, 105108 (2013) (cit. on p. 30).

[89] A. La Porta, G. A. Voth, A. M. Crawford, J. Alexander and E. Bodenschatz, 'Fluid particle accelerations in fully developed turbulence', Nature **409**, 1017–1019 (2001) (cit. on pp. 11, 12, 90, 91, 93).

[90] J. H. LaCasce, 'Statistics from Lagrangian observations', Prog. Oceanogr. **77**, 1–29 (2008) (cit. on p. 7).

[91] S. Laizet and N. Li, 'Incompact3d: A powerful tool to tackle turbulence problems with up to $O(10^5)$ computational cores', Int. J. Numer. Meth. Fluids **67**, 1735–1757 (2011) (cit. on p. 46).

[92] J. M. Lawson, E. Bodenschatz, C. C. Lalescu and M. Wilczek, 'Bias in particle tracking acceleration measurement', Exp. Fluids **59**, 172 (2018) (cit. on p. 73).

[93] C. Lee, K. Yeo and J.-I. Choi, 'Intermittent nature of acceleration in near wall turbulence', Phys. Rev. Lett. **92**, 144502 (2004) (cit. on pp. 13, 30, 45, 50, 52, 71, 76, 82, 85, 94).

[94] M. Lee and R. D. Moser, 'Direct numerical simulation of turbulent channel flow up to $Re_\tau \approx 5200$', J. Fluid Mech. **774**, 395–415 (2015) (cit. on pp. 22, 105, 172).

[95] A. Lozano-Durán and J. Jiménez, 'Effect of the computational domain on direct simulations of turbulent channels up to $Re_\tau = 4200$', Phys. Fluids **26**, 011702 (2014) (cit. on pp. 28, 51, 125).

[96] P. Luchini, 'Universality of the turbulent velocity profile', Phys. Rev. Lett. **118**, 224501 (2017) (cit. on p. 19).

[97] N. Malaya, K. W. Schulz and R. Moser, 'Petascale I/O using HDF-5', in Proceedings of the 2010 TeraGrid Conference, TG '10 (2010), 11:1–11:4 (cit. on p. 47).

[98] J. Mann, S. Ott and J. S. Andersen, *Experimental study of relative, turbulent diffusion*, Technical report Risø-R-1036(EN) (Risø National Laboratory, Roskilde, Denmark, Sept. 1999) (cit. on p. 124).

[99] P. Manneville, 'On the transition to turbulence of wall-bounded flows in general, and plane Couette flow in particular', Eur. J. Mech. B Fluids **49**, 345–362 (2015) (cit. on p. 19).

[100] N. N. Mansour, J. Kim and P. Moin, 'Reynolds-stress and dissipation-rate budgets in a turbulent channel flow', J. Fluid Mech. **194**, 15–44 (1988) (cit. on pp. 105, 172).

[101] I. Marusic, B. J. McKeon, P. A. Monkewitz, H. M. Nagib, A. J. Smits and K. R. Sreenivasan, 'Wall-bounded turbulent flows at high Reynolds numbers: Recent advances and key issues', Phys. Fluids **22**, 065103 (2010) (cit. on pp. 21–23, 27, 54).

[102] I. Marusic and R. J. Adrian, 'The Eddies and Scales of Wall Turbulence', in *Ten Chapters in Turbulence*, edited by P. A. Davidson, Y. Kaneda and K. R. Sreenivasan (Cambridge University Press, Cambridge, 2012), pp. 176–220 (cit. on pp. 21, 24–26).

[103] I. Marusic and J. P. Monty, 'Attached eddy model of wall turbulence', Annu. Rev. Fluid Mech. **51**, 49–74 (2019) (cit. on pp. 16, 125).

[104] B. J. McKeon, 'The engine behind (wall) turbulence: perspectives on scale interactions', J. Fluid Mech. **817** (2017) (cit. on p. 16).

[105] Y. Mito and T. J. Hanratty, 'Use of a modified Langevin equation to describe turbulent dispersion of fluid particles in a channel flow', Flow Turbul. Combust. **68**, 1–26 (2002) (cit. on p. 30).

[106] R. J. Moffat, 'Describing the uncertainties in experimental results', Exp. Therm. Fluid Sci. **1**, 3–17 (1988) (cit. on p. 74).

[107] P. Moin and K. Mahesh, 'Direct numerical simulation: a tool in turbulence research', Annu. Rev. Fluid Mech. **30**, 539–578 (1998) (cit. on p. 36).

[108] A. S. Monin and A. M. Yaglom, *Statistical Fluid Mechanics: Mechanics of Turbulence*, Vol. 1 (MIT Press, Cambridge, Massachusetts, 1971), 764 pp. (cit. on pp. 1, 15, 118).

[109] A. S. Monin and A. M. Yaglom, *Statistical Fluid Mechanics: Mechanics of Turbulence*, Vol. 2 (MIT Press, Cambridge, Massachusetts, 1975), 874 pp. (cit. on pp. 9, 45, 118, 143).

[110] J. Montagnier, A. Cadiou, M. Buffat and L. Le Penven, 'Towards petascale spectral simulations for transition analysis in wall bounded flow', Int. J. Numer. Meth. Fluids **72**, 709–723 (2013) (cit. on p. 46).

[111] J. P. Monty, J. A. Stewart, R. C. Williams and M. S. Chong, 'Large-scale features in turbulent pipe and channel flows', J. Fluid Mech. **589**, 147–156 (2007) (cit. on pp. 27, 28, 51).

[112] J. P. Monty, 'Developments in smooth wall turbulent duct flows', PhD thesis (University of Melbourne, 2005), 272 pp. (cit. on pp. 20, 22, 72).

[113] N. Mordant, A. M. Crawford and E. Bodenschatz, 'Experimental Lagrangian acceleration probability density function measurement', Phys. D **193**, 245–251 (2004) (cit. on pp. 66, 73).

[114] N. Mordant, J. Delour, E. Léveque, A. Arnéodo and J.-F. Pinton, 'Long time correlations in Lagrangian dynamics: A key to intermittency in turbulence', Phys. Rev. Lett. **89**, 254502 (2002) (cit. on p. 10).

[115] N. Mordant, P. Metz, O. Michel and J.-F. Pinton, 'Measurement of Lagrangian velocity in fully developed turbulence', Phys. Rev. Lett. **87**, 214501 (2001) (cit. on p. 10).

[116] N. Mordant, J.-F. Pinton and F. Chillà, 'Characterization of turbulence in a closed flow', J. Phys. II France **7**, 1729–1742 (1997) (cit. on p. 14).

[117] N. Mordant, A. M. Crawford and E. Bodenschatz, 'Three-dimensional structure of the Lagrangian acceleration in turbulent flows', Phys. Rev. Lett. **93**, 214501 (2004) (cit. on pp. 13, 84, 90, 91, 93).

[118] N. Mordant, E. Lévêque and J.-F. Pinton, 'Experimental and numerical study of the Lagrangian dynamics of high Reynolds turbulence', New J. Phys. **6**, 116 (2004) (cit. on pp. 10, 11, 52, 71, 80, 82, 93).

[119] R. D. Moser, P. Moin and A. Leonard, 'A spectral numerical method for the Navier–Stokes equations with applications to Taylor–Couette flow', J. Comput. Phys. **52**, 524–544 (1983) (cit. on pp. 39, 40, 42, 43).

[120] H. M. Nagib and K. A. Chauhan, 'Variations of von Kármán coefficient in canonical flows', Phys. Fluids **20**, 101518 (2008) (cit. on p. 22).

[121] A. M. Obukhov, 'On the distribution of energy in the spectrum of turbulent flow', Izv Akad Nauk SSSR **5**, 453–66 (1941) (cit. on p. 116).

[122] J. L. G. Oliveira, C. W. M. van der Geld and J. G. M. Kuerten, 'Lagrangian velocity and acceleration statistics of fluid and inertial particles measured in pipe flow with 3D particle tracking velocimetry', Int. J. Multiph. Flow **73**, 97–107 (2015) (cit. on p. 31).

[123] R. Örlü, T. Fiorini, A. Segalini, G. Bellani, A. Talamelli and P. H. Alfredsson, 'Reynolds stress scaling in pipe flow turbulence—first results from CICLoPE', Phil. Trans. R. Soc. A **375**, 20160187 (2017) (cit. on p. 20).

[124] S. A. Orszag, 'Accurate solution of the Orr–Sommerfeld stability equation', J. Fluid Mech. **50**, 689–703 (1971) (cit. on p. 19).

[125] S. A. Orszag, 'On the elimination of aliasing in finite-difference schemes by filtering high-wavenumber components', J. Atmos. Sci. **28**, 1074–1074 (1971) (cit. on p. 44).

[126] S. Ott and J. Mann, 'An experimental investigation of the relative diffusion of particle pairs in three-dimensional turbulent flow', J. Fluid Mech. **422**, 207–223 (2000) (cit. on p. 117).

[127] R. Ouchene, J. I. Polanco, I. Vinkovic and S. Simoëns, 'Acceleration statistics of prolate spheroidal particles in turbulent channel flow', J. Turbul. **19**, 827–848 (2018) (cit. on p. 33).

[128] N. T. Ouellette, H. Xu, M. Bourgoin and E. Bodenschatz, 'An experimental study of turbulent relative dispersion models', New J. Phys. **8**, 109 (2006) (cit. on pp. 117, 148).

[129] N. T. Ouellette, H. Xu, M. Bourgoin and E. Bodenschatz, 'Small-scale anisotropy in Lagrangian turbulence', New J. Phys. **8**, 102 (2006) (cit. on p. 14).

[130] R. L. Panton, 'Overview of the self-sustaining mechanisms of wall turbulence', Prog. Aerosp. Sci. **37**, 341–383 (2001) (cit. on p. 25).

[131] F. Pasquarelli, A. Quarteroni and G. Sacchi-Landriani, 'Spectral approximations of the Stokes problem by divergence-free functions', J. Sci. Comput. **2**, 195–226 (1987) (cit. on pp. 39, 40).

[132] D. Pekurovsky, 'P3DFFT: A Framework for Parallel Computations of Fourier Transforms in Three Dimensions', SIAM J. Sci. Comput. **34**, C192–C209 (2012) (cit. on p. 46).

[133] S. Pirozzoli, M. Bernardini and P. Orlandi, 'Passive scalars in turbulent channel flow at high Reynolds number', J. Fluid Mech. **788**, 614–639 (2016) (cit. on p. 36).

[134] E. Pitton, C. Marchioli, V. Lavezzo, A. Soldati and F. Toschi, 'Anisotropy in pair dispersion of inertial particles in turbulent channel flow', Phys. Fluids **24**, 073305 (2012) (cit. on pp. 31, 62, 115, 119, 122, 133).

[135] J. I. Polanco, I. Vinkovic, N. Stelzenmuller, N. Mordant and M. Bourgoin, 'Relative dispersion of particle pairs in turbulent channel flow', Int. J. Heat Fluid Flow **71**, 231–245 (2018) (cit. on pp. 115, 151).

[136] S. B. Pope, 'Lagrangian PDF methods for turbulent flows', Annu. Rev. Fluid Mech. **26**, 23–63 (1994) (cit. on p. 71).

[137] S. B. Pope, *Turbulent Flows* (Cambridge University Press, 10th Aug. 2000), 810 pp. (cit. on pp. 6, 8, 9, 18, 25, 27, 105, 124, 150, 165, 167, 170, 172).

[138] S. B. Pope, 'A stochastic Lagrangian model for acceleration in turbulent flows', Phys. Fluids **14**, 2360–2375 (2002) (cit. on p. 71).

[139] S. B. Pope, 'Simple models of turbulent flows', Phys. Fluids **23**, 011301 (2011) (cit. on pp. 7, 8).

[140] A. Pumir and B. I. Shraiman, 'Persistent Small Scale Anisotropy in Homogeneous Shear Flows', Phys. Rev. Lett. **75**, 3114–3117 (1995) (cit. on p. 84).

[141] A. Pumir, H. Xu, G. Boffetta, G. Falkovich and E. Bodenschatz, 'Redistribution of kinetic energy in turbulent flows', Phys. Rev. X **4**, 041006 (2014) (cit. on pp. 95, 102).

[142] A. Pumir, H. Xu and E. D. Siggia, 'Small-scale anisotropy in turbulent boundary layers', J. Fluid Mech. **804**, 5–23 (2016) (cit. on p. 84).

[143] N. M. Qureshi, U. Arrieta, C. Baudet, A. Cartellier, Y. Gagne and M. Bourgoin, 'Acceleration statistics of inertial particles in turbulent flow', Eur. Phys. J. B **66**, 531–536 (2008) (cit. on p. 162).

[144] M. P. Rast and J.-F. Pinton, 'Point-vortex model for Lagrangian intermittency in turbulence', Phys. Rev. E **79**, 046314 (2009) (cit. on p. 13).

[145] M. P. Rast and J.-F. Pinton, 'Pair dispersion in turbulence: The subdominant role of scaling', Phys. Rev. Lett. **107**, 214501 (2011) (cit. on p. 118).

[146] L. F. Richardson, 'Atmospheric diffusion shown on a distance-neighbour graph', Proc. R. Soc. Lond. Ser. A **110**, 709–737 (1926) (cit. on pp. 31, 115, 116).

[147] S. K. Robinson, 'Coherent motions in the turbulent boundary layer', Annu. Rev. Fluid Mech. **23**, 601–639 (1991) (cit. on pp. 125, 127, 145).

[148] V. Sabel'nikov, A. Chtab-Desportes and M. Gorokhovski, 'New sub-grid stochastic acceleration model in LES of high-Reynolds-number flows', Eur. Phys. J. B **80**, 177–187 (2011) (cit. on pp. 71, 89).

[149] J. P. L. C. Salazar and L. R. Collins, 'Two-particle dispersion in isotropic turbulent flows', Annu. Rev. Fluid Mech. **41**, 405–432 (2009) (cit. on pp. 115–117, 147).

[150] M. Samie, I. Marusic, N. Hutchins, M. K. Fu, Y. Fan, M. Hultmark and A. J. Smits, 'Fully resolved measurements of turbulent boundary layer flows up to $Re_\tau = 20\,000$', J. Fluid Mech. **851**, 391–415 (2018) (cit. on pp. 22, 23, 54).

[151] M. Sano and K. Tamai, 'A universal transition to turbulence in channel flow', Nat. Phys. **12**, 249–253 (2016) (cit. on p. 19).

[152] Y. Sato and K. Yamamoto, 'Lagrangian measurement of fluid-particle motion in an isotropic turbulent field', J. Fluid Mech. **175**, 183–199 (1987) (cit. on p. 6).

[153] B. L. Sawford, 'Reynolds number effects in Lagrangian stochastic models of turbulent dispersion', Phys. Fluids A **3**, 1577–1586 (1991) (cit. on pp. 8, 9, 71, 87, 89).

[154] B. L. Sawford, P. K. Yeung, M. S. Borgas, P. Vedula, A. L. Porta, A. M. Crawford and E. Bodenschatz, 'Conditional and unconditional acceleration statistics in turbulence', Phys. Fluids **15**, 3478–3489 (2003) (cit. on p. 88).

[155] B. Sawford, 'Turbulent relative dispersion', Annu. Rev. Fluid Mech. **33**, 289–317 (2001) (cit. on pp. 115–117).

[156] B. L. Sawford and P. K. Yeung, 'Kolmogorov similarity scaling for one-particle Lagrangian statistics', Phys. Fluids **23**, 091704 (2011) (cit. on p. 88).

[157] B. L. Sawford and P. K. Yeung, 'Direct numerical simulation studies of Lagrangian intermittency in turbulence', Phys. Fluids **27**, 065109 (2015) (cit. on pp. 10, 62, 66).

[158] B. L. Sawford, P. K. Yeung and M. S. Borgas, 'Comparison of backwards and forwards relative dispersion in turbulence', Phys. Fluids **17**, 095109 (2005) (cit. on pp. 33, 118, 122, 123).

[159] A. Scagliarini, 'Geometric properties of particle trajectories in turbulent flows', J. Turbul. **12**, N25 (2011) (cit. on p. 161).

[160] D. Schanz, S. Gesemann and A. Schröder, 'Shake-The-Box: Lagrangian particle tracking at high particle image densities', Exp. Fluids **57**, 70 (2016) (cit. on p. 32).

[161] P. J. Schmid and D. S. Henningson, *Stability and Transition in Shear Flows*, red. by J. E. Marsden and L. Sirovich, Vol. 142, Applied Mathematical Sciences (Springer New York, New York, NY, 2001) (cit. on pp. 39, 42).

[162] A. Schröder, R. Geisler, K. Staack, G. E. Elsinga, F. Scarano, B. Wieneke, A. Henning, C. Poelma and J. Westerweel, 'Eulerian and Lagrangian views of a turbulent boundary layer flow using time-resolved tomographic PIV', Exp. Fluids **50**, 1071–1091 (2011) (cit. on p. 32).

[163] A. Schröder, D. Schanz, R. Geisler and S. Gesemann, 'Investigations of coherent structures in near-wall turbulence and large wall-shear stress events using Shake-The-Box', in 18th International Symposium on the Application of Laser and Imaging Techniques to Fluid Mechanics (2016) (cit. on p. 32).

[164] Z.-S. She, E. Jackson and S. A. Orszag, 'Intermittent vortex structures in homogeneous isotropic turbulence', Nature **344**, 226–228 (1990) (cit. on p. 12).

[165] P. Shen and P. K. Yeung, 'Fluid particle dispersion in homogeneous turbulent shear flow', Phys. Fluids **9**, 3472–3484 (1997) (cit. on pp. 15, 31, 62, 79, 118, 119, 122, 133, 135).

[166] C. M. de Silva, I. Marusic, J. D. Woodcock and C. Meneveau, 'Scaling of second- and higher-order structure functions in turbulent boundary layers', J. Fluid Mech. **769**, 654–686 (2015) (cit. on p. 125).

[167] A. J. Smits, B. J. McKeon and I. Marusic, 'High–Reynolds number wall turbulence', Annu. Rev. Fluid Mech. **43**, 353–375 (2011) (cit. on pp. 20, 22, 24, 27, 51, 127).

[168] I. M. Sokolov, J. Klafter and A. Blumen, 'Ballistic versus diffusive pair dispersion in the Richardson regime', Phys. Rev. E **61**, 2717–2722 (2000) (cit. on p. 147).

[169] K. D. Squires and J. K. Eaton, 'Lagrangian and Eulerian statistics obtained from direct numerical simulations of homogeneous turbulence', Phys. Fluids A **3**, 130–143 (1991) (cit. on pp. 15, 118, 119, 133).

[170] K. R. Sreenivasan, 'The turbulent boundary layer', in *Frontiers in Experimental Fluid Mechanics*, edited by M. Gad-el-Hak, Lecture Notes in Engineering (Springer Berlin Heidelberg, Berlin, Heidelberg, 1989), pp. 159–209 (cit. on p. 24).

[171] K. R. Sreenivasan and R. A. Antonia, 'The phenomenology of small-scale turbulence', Annu. Rev. Fluid Mech. **29**, 435–472 (1997) (cit. on p. 12).

[172] K. R. Sreenivasan, 'On the universality of the Kolmogorov constant', Phys. Fluids **7**, 2778–2784 (1995) (cit. on pp. 117, 124, 128, 147).

[173] N. Stelzenmuller, 'A Lagrangian study of inhomogeneous turbulence', PhD thesis (Université Grenoble Alpes, 20th Oct. 2017) (cit. on pp. 28, 71–73, 81, 104).

[174] N. Stelzenmuller, J. I. Polanco, L. Vignal, I. Vinkovic and N. Mordant, 'Lagrangian acceleration statistics in a turbulent channel flow', Phys. Rev. Fluids **2**, 054602 (2017) (cit. on pp. 71, 121, 127, 131).

[175] G. I. Taylor, 'Diffusion by continuous movements', Proc. London Math. Soc. **s2-20**, 196–212 (1922) (cit. on pp. 7, 101, 111, 113, 117, 141).

[176] H. Tennekes, 'Eulerian and Lagrangian time microscales in isotropic turbulence', J. Fluid Mech. **67**, 561–567 (1975) (cit. on p. 4).

[177] H. Tennekes and J. L. Lumley, *A First Course in Turbulence* (MIT Press, 1972), 320 pp. (cit. on pp. 5, 7, 15, 21, 22).

[178] S. Thalabard, G. Krstulovic and J. Bec, 'Turbulent pair dispersion as a continuous-time random walk', J. Fluid Mech. **755**, R4 (2014) (cit. on pp. 147, 148).

[179] F. Toschi, L. Biferale, G. Boffetta, A. Celani, B. J. Devenish and A. Lanotte, 'Acceleration and vortex filaments in turbulence', J. Turbul. **6**, N15 (2005) (cit. on pp. 12, 52, 66, 71, 82, 93).

[180] F. Toschi and E. Bodenschatz, 'Lagrangian properties of particles in turbulence', Annu. Rev. Fluid Mech. **41**, 375–404 (2009) (cit. on pp. 5, 9, 10, 33, 87, 88).

[181] A. A. Townsend, *The Structure of Turbulent Shear Flow*, 2nd ed. (Cambridge University Press, Cambridge, UK, 1976) (cit. on pp. 125, 155).

[182] A. Tsinober, P. Vedula and P. K. Yeung, 'Random Taylor hypothesis and the behavior of local and convective accelerations in isotropic turbulence', Phys. Fluids **13**, 1974–1984 (2001) (cit. on p. 46).

[183] T. Tsukahara and T. Ishida, 'The lower bound of subcritical transition in plane Poiseuille flow', in EUROMECH Colloquium EC565, Subcritical Transition to Turbulence (2014), p. 83 (cit. on p. 19).

[184] M. Vallikivi and A. J. Smits, 'Fabrication and characterization of a novel nanoscale thermal anemometry probe', J. Microelectromech. Syst. **23**, 899–907 (2014) (cit. on p. 23).

[185] M. Van Dyke, *An Album of Fluid Motion* (Parabolic Press, Stanford, California, 1982), 176 pp. (cit. on p. 4).

[186] M. van Hinsberg, J. Thije Boonkkamp, F. Toschi and H. Clercx, 'On the efficiency and accuracy of interpolation methods for spectral codes', SIAM J. Sci. Comput. **34**, B479–B498 (2012) (cit. on p. 62).

[187] E. van Sebille et al., 'Lagrangian ocean analysis: Fundamentals and practices', Ocean Model. **121**, 49–75 (2018) (cit. on pp. 7, 8).

[188] P. Vedula and P. K. Yeung, 'Similarity scaling of acceleration and pressure statistics in numerical simulations of isotropic turbulence', Phys. Fluids **11**, 1208–1220 (1999) (cit. on pp. 30, 45).

[189] G. A. Voth, A. La Porta, A. M. Crawford, J. Alexander and E. Bodenschatz, 'Measurement of particle accelerations in fully developed turbulence', J. Fluid Mech. **469**, 121–160 (2002) (cit. on pp. 11, 12).

[190] G. A. Voth, K. Satyanarayan and E. Bodenschatz, 'Lagrangian acceleration measurements at large Reynolds numbers', Phys. Fluids **10**, 2268–2280 (1998) (cit. on pp. 11, 14).

[191] G. A. Voth and A. Soldati, 'Anisotropic particles in turbulence', Annu. Rev. Fluid Mech. **49**, 249–276 (2017) (cit. on p. 33).

[192] R. J. E. Walpot, C. W. M. van der Geld and J. G. M. Kuerten, 'Determination of the coefficients of Langevin models for inhomogeneous turbulent flows by three-dimensional particle tracking velocimetry and direct numerical simulation', Phys. Fluids **19**, 045102 (2007) (cit. on p. 31).

[193] Q. Wang, K. D. Squires and X. Wu, 'Lagrangian statistics in turbulent channel flow', Atmos. Environ. **29**, 2417–2427 (1995) (cit. on p. 95).

[194] J. D. Wilson and B. L. Sawford, 'Review of Lagrangian stochastic models for trajectories in the turbulent atmosphere', Bound.-Layer Meteorol. **78**, 191–210 (1996) (cit. on p. 7).

[195] X. Wu and P. Moin, 'Direct numerical simulation of turbulence in a nominally zero-pressure-gradient flat-plate boundary layer', J. Fluid Mech. **630**, 5–41 (2009) (cit. on p. 26).

[196] H. Xu, A. Pumir, G. Falkovich, E. Bodenschatz, M. Shats, H. Xia, N. Francois and G. Boffetta, 'Flight-crash events in turbulence', Proc. Natl. Acad. Sci. **111**, 7558–7563 (2014) (cit. on pp. 95, 101, 102).

[197] H. Xu, M. Bourgoin, N. T. Ouellette and E. Bodenschatz, 'High order Lagrangian velocity statistics in turbulence', Phys. Rev. Lett. **96**, 024503 (2006) (cit. on pp. 10, 11).

[198] H. Xu, N. T. Ouellette and E. Bodenschatz, 'Curvature of Lagrangian trajectories in turbulence', Phys. Rev. Lett. **98**, 050201 (2007) (cit. on p. 161).

[199] Y. Yamamoto and Y. Tsuji, 'Numerical evidence of logarithmic regions in channel flow at $Re_\tau = 8000$', Phys. Rev. Fluids **3**, 012602 (2018) (cit. on pp. 20, 22).

[200] X. I. A. Yang, R. Baidya, P. Johnson, I. Marusic and C. Meneveau, 'Structure function tensor scaling in the logarithmic region derived from the attached eddy model of wall-bounded turbulent flows', Phys. Rev. Fluids **2**, 064602 (2017) (cit. on pp. 125, 146, 155).

[201] X. I. A. Yang, R. Baidya, Y. Lv and I. Marusic, 'Hierarchical random additive model for the spanwise and wall-normal velocities in wall-bounded flows at high Reynolds numbers', Phys. Rev. Fluids **3**, 124606 (2018) (cit. on p. 125).

[202] K. Yeo, B.-G. Kim and C. Lee, 'On the near-wall characteristics of acceleration in turbulence', J. Fluid Mech. **659**, 405–419 (2010) (cit. on pp. 30, 45, 50, 54–57, 70, 71, 75, 76, 82, 90, 91, 94, 127).

[203] P. K. Yeung, 'One- and two-particle Lagrangian acceleration correlations in numerically simulated homogeneous turbulence', Phys. Fluids **9**, 2981 (1997) (cit. on pp. 13, 15).

[204] P. K. Yeung, 'Lagrangian characteristics of turbulence and scalar transport in direct numerical simulations', J. Fluid Mech. **427**, 241–274 (2001) (cit. on p. 5).

[205] P. K. Yeung, 'Lagrangian investigations of turbulence', Annu. Rev. Fluid Mech. **34**, 115–142 (2002) (cit. on pp. 2, 5, 87).

[206] P. K. Yeung and S. B. Pope, 'Lagrangian statistics from direct numerical simulations of isotropic turbulence', J. Fluid Mech. **207**, 531–586 (1989) (cit. on pp. 6, 13, 29, 62, 66, 80, 84, 85).

[207] R. Zamansky, I. Vinkovic and M. Gorokhovski, 'Acceleration statistics of solid particles in turbulent channel flow', Phys. Fluids **23**, 113304 (2011) (cit. on p. 66).

[208] R. Zamansky, I. Vinkovic and M. Gorokhovski, 'Acceleration in turbulent channel flow: universalities in statistics, subgrid stochastic models and an application', J. Fluid Mech. **721**, 627–668 (2013) (cit. on pp. 71, 89).

[209] E.-S. Zanoun, F. Durst and H. Nagib, 'Evaluating the law of the wall in two-dimensional fully developed turbulent channel flows', Phys. Fluids **15**, 3079 (2003) (cit. on p. 20).

[210] E.-S. Zanoun, H. Nagib and F. Durst, 'Refined c_f relation for turbulent channels and consequences for high-Re experiments', Fluid Dyn. Res. **41**, 021405 (2009) (cit. on p. 20).